Université de Montréal

Detector dose response to megavoltage photon beams coupled to magnetic fields

par
Yunuen Cervantes Espinosa

Département de Physique
Faculté des arts et des sciences

Thèse présentée à la Faculté des études supérieures
en vue de l'obtention du grade de Philosophiæ Doctor (Ph.D.)
en Physique option
en physique medicale

Août, 2021

© Yunuen Cervantes Espinosa, 2021.

Université de Montréal
Faculté des études supérieures

Cette thèse intitulée:

Detector dose response to megavoltage photon beams coupled to magnetic fields

présentée par:

Yunuen Cervantes Espinosa

a été évaluée par un jury composé des personnes suivantes:

Claude Leroy,	président-rapporteur
Hugo Bouchard,	directeur de recherche
Simon Duane,	codirecteur
Jean-François Carrier,	membre du jury
Bryan Muir,	examinateur externe
Antonella Badia,	représentant du doyen de la FES

Thèse acceptée le: .....

RÉSUMÉ

La radiothérapie guidée par résonance magnétique promet une administration de dose plus précise que les techniques conventionnelles puisqu'elle permet une visualisation en temps réel des structures internes avant et pendant le traitement. Cependant, la dosimétrie doit être réalisée en présence de champs magnétiques. Alors que le champ magnétique n'affecte pas le transport des particules neutres, il affecte le transport des particules chargées secondaires en raison de la force de Lorentz, qui modifie le champ de rayonnement et la réponse de dose du détecteur. Cette thèse vise à comprendre l'effet du champ magnétique sur la réponse de dose du détecteur, à la caractériser et à fournir des facteurs de correction de qualité prenant en compte l'impact du champ magnétique.

Dans le premier article, quatre chambres d'ionisation à petite cavité ont été caractérisées via des simulations de Monte Carlo et des mesures expérimentales. Il a été constaté que le champ magnétique accentuait tous les détails géométriques. Une description précise du volume sensible effectif est cruciale dans les simulations. De plus, la géométrie modélisée doit être aussi proche que possible de la géométrie réelle, y compris les couches d'air internes. Des facteurs de correction de qualité tenant compte du champ magnétique et de son incertitude du budget d'incertitude sont présentés pour différentes configurations.

Le deuxième article a évalué l'effet du champ magnétique sur les facteurs de perturbation de cinq détecteurs à petite cavité, dont trois détecteurs à petite cavité et deux détecteurs à semi-conducteurs. Les facteurs de perturbation des composants structurels, les facteurs de moyenne de densité et de volume ont été déterminés pour différentes tailles de champ et orientations. De plus, des facteurs de correction de qualité ont été calculés dans les mêmes conditions. Les résultats montrent que le champ magnétique a un impact significatif sur le facteur de perturbation de la densité dans les chambres d'ionisation. En revanche, son impact est plus prononcé dans les composants structurels des détecteurs semi-conducteurs.

L'objectif du troisième article était de fournir plus d'informations sur la com-

préhension de la relation dose-réponse des détecteurs dans les champs magnétiques via des calculs de spectres de fluence électronique. La fluence des électrons différentiel en énergie dans la cavité du détecteur peut être fortement modifiée dans les champs magnétiques, et les perturbations de fluence sont généralement plus évidentes pour les électrons de faible énergie. Ces calculs ont montré l'interaction entre plusieurs facteurs qui rendent les effets de perturbation imprévisibles dans le faisceau de photons couplé aux champs magnétiques : 1) orientation du détecteur et du champ magnétique, 2) taille et forme de la cavité, 3) composants structurels, 4) couche d'air entre le détecteur et le milieu et leur asymétrie, et 5) l'énergie.

mots clés : Radiotherapie, champs magnétiques, simulations Monte Carlo, dosimétrie de référence, chambre d'ionisation, petits champs, fluence électronique, facteurs de correction de qualité, facteurs de perturbation, volume mort

ABSTRACT

Magnetic resonance-guided radiation therapy promises more accurate dose delivery than conventional techniques by allowing real-time visualization of internal structures before and during treatment. However, the dosimetry must be performed in the presence of magnetic fields. While the magnetic field does not affect the transport of uncharged particles, it affects the transport of secondary charged particles due to the Lorentz force, which modifies the radiation field and the detector dose response. This thesis aims to understand the effect of the magnetic field on detector dose response, characterize it, and provide quality correction factors accounting for the impact of the magnetic field.

In the first article, four small-cavity ionization chambers were characterized via Monte Carlo simulations and experimental measurements. It was found that the magnetic field emphasized all the geometrical details. An accurate description of the effective sensitive volume is crucial in the simulations. Also, the modelled geometry must be as close as possible to the actual geometry, including the internal air layers. Quality correction factors accounting for the magnetic field and its uncertainty budget uncertainty are presented for different configurations.

The second article evaluated the magnetic field effect on perturbation factors of five small volume detectors, including three ionization chambers and two solid-state detectors. The perturbation factors from extracameral components, density and volume averaging factors were determined for different field sizes and orientation setups. Additionally, quality correction factors were calculated in the same conditions. Results show that the magnetic field significantly impacts the density perturbation factor in the ionization chambers. In contrast, its impact is more pronounced in the extracameral components in the solid-state detectors.

The purpose of the third article was to provide more insight into the understanding of detector dose-response in magnetic fields via calculations of electron fluence spectra. The electron fluence differential in energy in the detector cavity can be severely modified in magnetic fields, and fluence perturbations are generally

more evident for low-energy electrons. These calculations showed the interplay between multiple factors that make the perturbation effects unpredictable in photon beams coupled to magnetic fields: 1) detector and magnetic field orientation, 2) cavity size and shape, 3) extracameral components, 4) air gaps and their asymmetry, and 5) energy.

Keywords: Radiotherapy, magnetic fields, Monte Carlo simulations, reference dosimetry, ionization chamber, small fields, electron fluence, quality correction factors, perturbation factors, dead volume

CONTENTS

RÉSUMÉ . . . . . **iii**

ABSTRACT . . . . . **v**

CONTENTS . . . . . **vii**

LIST OF FIGURES . . . . . **xiv**

LIST OF ABBREVIATIONS . . . . . **xxii**

NOTATION . . . . . **xxiv**

ACKNOWLEDGMENTS . . . . . **xxx**

CHAPTER 1: INTRODUCTION **1**

1.1 Background 1

1.1.1 Motivation 1

1.1.2 The context of radiation therapy 1

1.1.3 Magnetic resonance imaging-guided radiation therapy . . . 2

1.1.4 Impact of the magnetic field on reference dosimetry 5

1.2 Objectives 8

1.3 Structure of the thesis 9

CHAPTER 2: THEORY **10**

2.1 Radiation transport 10

2.1.1 Interactions of particles with matter 10

2.1.2 Radiation transport equation 17

2.1.3 Radiation transport in the presence of an external magnetic field 20

2.2 Monte Carlo method for radiation transport 23

2.2.1 Simulation of radiation transport 23

2.2.2 Radiation transport in magnetic fields 24
2.2.3 Fano test 29
2.3 Radiation dosimetry 30
2.3.1 Radiation detectors 30
2.3.2 Reference dosimetry protocols 36
2.3.3 Towards reference dosimetry in the presence of magnetic fields 41

CHAPTER 3: INTRODUCTION TO ARTICLE 1 48
3.1 Context 48
3.2 Uncertainty budget 49
3.2.1 Definitions 49
3.2.2 Absorbed dose ratio relative to dose in the absence of magnetic fields 50
3.2.3 Mathematical derivations 51
3.3 Complementary information to materials and methods 58
3.3.1 Experimental setup 58
3.3.2 Intrinsic response 59
3.4 Results and impact 59
3.5 Contributions 60

CHAPTER 4: SMALL-CAVITY CHAMBER DOSE RESPONSE IN MEGAVOLTAGE PHOTON BEAMS COUPLED TO MAGNETIC FIELDS 62
4.1 Introduction 64
4.2 Materials and Methods 67
4.2.1 The IAEA-AAPM formalism 67
4.2.2 Experimental measurements 70
4.2.3 Numerical methods 71
4.2.4 Uncertainty analysis 74
4.3 Results 77
4.3.1 Numerical models 77

4.3.2 Small-cavity ion chamber response in the presence of magnetic fields . . . 79
4.3.3 Verification of manufacturing details with micro-CT measurements . . . 83
4.3.4 Generated data with uncertainty budget . . . 85
4.3.5 Quality correction factors . . . 86
4.4 Discussion . . . 87
4.4.1 Comparison with other studies . . . 87
4.4.2 Impact of geometry discrepancies . . . 90
4.4.3 Recommendations for determination of quality correction factors . . . 92
4.5 Conclusion . . . 92

CHAPTER 5: INTRODUCTION TO ARTICLE 2 . . . 94
5.1 Context . . . 94
5.2 Results and impact . . . 95
5.3 Contributions . . . 100

CHAPTER 6: DETECTOR PERTURBATION AND QUALITY CORRECTION FACTORS IN MAGNETIC RESONANCE GUIDED RADIATION THERAPY SMALL PHOTON BEAMS . . . 102
6.1 Introduction . . . 104
6.2 Materials and Methods . . . 107
6.2.1 Dosimetry formalism . . . 107
6.2.2 Decomposition of the perturbation factors . . . 107
6.2.3 Quality correction factors . . . 109
6.2.4 Monte Carlo simulations . . . 109
6.2.5 Uncertainty analysis . . . 111
6.3 Results . . . 112
6.3.1 Perturbation factors in the absence of magnetic fields . . . 112

6.3.2 Effect of the magnetic field on the perturbation factors . . . 117
6.3.3 Quality correction factors . . . 118
6.4 Discussion . . . 119
6.4.1 Perturbation factors in the absence of magnetic fields . . . 119
6.4.2 Effect of the magnetic field on the perturbation factors . . . 122
6.5 Suitability for clinical environment . . . 127
6.6 Conclusion . . . 128

CHAPTER 7: INTRODUCTION TO ARTICLE 3 . . . 130
7.1 Context . . . 130
7.2 Supplementary theory . . . 131
7.3 Results and impact . . . 132
7.3.1 Farmer chamber . . . 133
7.3.2 Small-cavity chambers . . . 133
7.3.3 Solid-state detectors . . . 134
7.3.4 Air gaps . . . 134
7.3.5 Impact . . . 134
7.4 Supplementary results . . . 136
7.5 Contributions . . . 136

CHAPTER 8: MONTE CARLO INVESTIGATION OF ELECTRON FLUENCE PERTURBATION IN MR-GUIDED RADIOTHERAPY BEAMS USING SIX COMMERCIAL RADIATION DETECTORS . . . 139
8.1 Introduction . . . 141
8.2 Materials and Methods . . . 143
8.2.1 Theory . . . 143
8.2.2 Monte Carlo calculations . . . 148
8.3 Results and discussion . . . 153
8.3.1 Validation of Monte Carlo calculations of electron fluence in the presence of magnetic fields . . . 153

8.3.2 Electron fluence in ionization chambers 154
8.3.3 Effect of detector geometry and density 159
8.3.4 Effect of the cavity size 163
8.3.5 Air gap effect on electron fluence spectrum 166
8.3.6 Solid-state detectors 169
8.4 Discussion 172
8.5 Conclusion 173

Appendix 175
8.A Magnetic-field term in the radiation transport equation 175
8.B Radiation transport equation for the electron fluence spectrum . . 175

CHAPTER 9: CONCLUSION 179

BIBLIOGRAPHY 184

LIST OF TABLES

4.I Maximal percentage difference in relative dose response between experiments and Monte Carlo simulations in the parallel orientation. 80

4.II Maximal percentage difference in relative dose response between experiments and Monte Carlo simulations in the perpendicular orientation. 83

4.III Uncertainty budget of chamber relative response estimated from various sources of uncertainty for the parallel orientation. . . . 87

4.IV Uncertainty budget of chamber relative response estimated from various sources of uncertainty for the perpendicular orientation. 87

4.V Estimated quality correction factors of four chamber models with two magnetic field strengths in each orientation 87

5.I Percentage of maximal variation with respect to unity of the perturbation factors in orientation 1. 99

6.I Calculated quality correction factors for the PTW60012 in a 1.5 T magnetic field, in four orientations, for multiple square field sizes. Uncertainties are estimated using the method described in section 6.2.5. 119

6.II Calculated quality correction factors for the PTW60019 in a 1.5 T magnetic field, in four orientations, for multiple square field sizes. Uncertainties are estimated using the method described in section 6.2.5. 119

6.III Calculated quality correction factors for the PTW31010 in a 1.5 T magnetic field, in four orientations, for multiple square field sizes. Uncertainties are estimated using the method described in section 6.2.5. 120

6.IV Calculated quality correction factors for the PTW31021 in a 1.5 T magnetic field, in four orientations, for multiple square field sizes. Uncertainties are estimated using the method described in section 6.2.5. 120
6.V Calculated quality correction factors for the PTW31022 in a 1.5 T magnetic field, in four orientations, for multiple square field sizes. Uncertainties are estimated using the method described in section 6.2.5. 121

7.I Percentage of total electron fluence variation due to the magnetic field in the detectors. 133
7.II Ratio of dose in the PTW30013 cavity with different air gap thickness relative to that with no air gap. 135
7.III Ratio of dose in the PTW31010 cavity with different air gap thickness relative to that with no air gap. 135

8.I Detector specifications, taken from the manufacturer catalogue. 149
8.II Percentage of total electron fluence variation due to the magnetic field in the ionization chambers. 159
8.III Percentage of total electron fluence variation due to the magnetic field in the ionization chambers surrounded by an air gap. The uncertainty is below 0.01% in all cases. 169

LIST OF FIGURES

1.1 The two configurations of MRI-linac devices. 3
1.2 Current MRI-linac systems. 4
1.3 Schematic diagram of the Unity MRI-linac. 5
1.4 Electron trajectories in water in the absence and presence of a magnetic field, taken from simulations of a 6 MeV pencil photon beam irradiating water performed in the user code *egs_chamber* (EGSnrc). 7

2.1 Dominant photon-matter interactions in RT energies. 11
2.2 Photon-matter interactions 12
2.3 Diagram the main types of interactions of charged particles with an atom, depending on the impact parameter, b, relative to the atomic radius, r_a. 14
2.4 Diagram illustrating the fluence, f_i, in the solid angle, $d\Omega$. . . 18
2.5 In vacuum, the electron trajectory follows a circular trajectory due to the Lorentz force 21
2.6 In a medium, as the electron loses energy due to interaction with the medium, the electron path describes a spiral with decreasing radius due to the Lorentz force 22
2.7 CH step in the presence of electromagnetic fields in EGSnrc . 28
2.8 Cavity ionization chamber 32
2.9 A p-n junction in a diode 33
2.10 Beam calibration diagram 37
2.11 Nonstandard reference dosimetry routes 41
2.12 Illustration of the impact of the magnetic field orientation on the secondary electrons 42
2.13 Detector orientations in reference dosimetry 44
2.14 Illustration of the modeled air gaps surrounding the chamber. 45

4.1 Diagram of the experimental setup 71
4.2 Chamber orientations 73
4.3 Validation of the beam model 77
4.4 Dead volume calculation and model 78
4.5 Experimental relative response of PTW31010, PTW31016, PTW31021 and PTW31022 for parallel orientation. 80
4.6 Simulated relative response normalised to experimental relative response for the parallel orientation 81
4.7 Experimental relative response of PTW31010, PTW31016, PTW31021 and PTW31022 for perpendicular orientation. 82
4.8 Simulated relative response normalised to experimental relative response for the perpendicular orientation. 84
4.9 Micro-CT image of PTW31010, PTW31021 and PTW31016 . 86

5.1 Density perturbation factor in the absence and presence of magnetic fields 96
5.2 Overall perturbation factor in the absence and presence of magnetic fields 97
5.3 Volume averaging perturbation factor in the absence and presence of magnetic fields 98
5.4 Quality correction factors accounting for the magnetic field effect as a function of field size for four orientations. 100

6.1 Decomposition of perturbation factors using an arbitrary, yet consistent, route. The perturbation factors on top of the arrows corresponds to the ratio of each adjacent cavity dose. . . 109

6.2 Diagrams of the chamber setup: a) detector axis perpendicular to the magnetic field and parallel to the beam; b)detector axis perpendicular to the magnetic field and perpendicular to the beam with the Lorentz force pointing secondary electrons towards the stem on average; c)detector axis perpendicular to the magnetic field and perpendicular to the beam with the Lorentz force pointing secondary electrons towards the tip on average; d)detector axis parallel to the magnetic field and perpendicular to the beam. 111

6.3 On the left side, P_ρ of solid-state detectors for four orientations as function of the field sizes at 0 T. On the right side, the effect of the magnetic on P_ρ as a function of the field size. 113

6.4 On the left side,P_ρ of ionization chambers for four orientations as function of the field sizes at 0 T. On the right side, the effect of the magnetic on P_ρ as a function of the field size. 113

6.5 On the left side, P_{MC} of solid-state detectors for four orientations as function of the field sizes at 0 T. On the right side, the effect of the magnetic on P_{MC} as a function of the field size. . 114

6.6 On the left side, the overall perturbation factor of ionization chambers, for four orientations as function of the field sizes at 0 T. On the right side, the effect of the magnetic on P_{MC} as a function of the field size. 115

6.7 On the left side, the volume averaging factor of solid-state detectors for four orientations as function of the field sizes at 0 T. On the right side, the effect of the magnetic on P_{vol} as a function of the field size. 116

6.8 On the left side, the volume averaging factor of ionization chambers for four orientations as function of the field sizes at 0 T. On the right side, the effect of the magnetic on P_{vol} as a function of the field size. 116

6.9 Illustration of ERE using a dose map of a 2×2 cm^2 field irradiating a $10 \times 10 \times 10$ cm^3 water phantom with a rectangular cavity in the center made of a) air and b) diamond at 1.5 T. . 124

7.1 The electron fluence spectral differences due to the magnetic field in each semiflex 3D PTW31021 chamber geometry considered in the parallel orientation row and perpendicular orientations 137

7.2 The electron fluence spectral differences due to the magnetic field in each pinpoint 3D PTW31022 chamber geometry considered in the parallel orientation and perpendicular orientation 138

8.1 Diagram of three orientations for ionization chambers and one orientation for the solid-state detectors. 1) The chamber axis is parallel to the magnetic field, 2a) the chamber axis is perpendicular to the magnetic field and the Lorentz force ($\mathbf{F}_\mathrm{L}$) points towards the stem, 2b) the chamber axis is perpendicular to the magnetic field with $\mathbf{F}_\mathrm{L}$ pointing towards the tip and 3) the solid-state detector axis is perpendicular to the magnetic field and parallel to the beam. 149

8.2 Scheme of the three detector geometries where the electron fluence is calculated. On the left, the full detector, on the middle the bare cavity with artificial water w^*, having the same atomic properties as water with the electron density of the original sensitive volume material, and on the right, the bare cavity filled with water. 151

8.3 Illustration of the modeled air gaps surrounding the chamber in the parallel orientation. 152

8.4 Normalized electron fluence simulated with `cavity` (EGSnrc) in a water voxel of 1 mm^3 at 0 T and 1.5 T. 154

8.5 In the top row, Monte Carlo calculated electron fluence spectra per total incident photon fluence, at 0 T and 1.5 T, in each ionization chamber (from left to right: PTW30013, PTW31010, PTW31021 and PTW31022), in the parallel orientation. In the bottom row, the corresponding electron fluence differences due to the presence of the magnetic field in each field size and chamber model. The vertical dashed line is at the energy at which the gyration radius equals the cavity diameter, explained in section 8.3.4. 155

8.6 In the top row, Monte Carlo calculated electron fluence spectra per total incident photon fluence, at 0 T and 1.5 T, in each ionization chamber (from left to right: PTW30013, PTW31010, PTW31021 and PTW31022), in the perpendicular orientation 2a ($\mathbf{F}_{\mathrm{L}} \rightarrow$ stem). In the bottom row, the corresponding electron fluence differences due to the presence of the magnetic field in each field size and chamber model. The vertical dashed line is at the energy at which the gyration radius equals the cavity diameter, explained in section 8.3.4. 156

8.7 In the top row, Monte Carlo calculated electron fluence spectra per total incident photon fluence, at 0 T and 1.5 T, in each ionization chamber (from left to right: PTW30013, PTW31010, PTW31021 and PTW31022), in the perpendicular orientation 2b ($\mathbf{F}_{\mathrm{L}} \rightarrow$ tip). In the bottom row, the corresponding electron fluence differences due to the presence of the magnetic field in each field size and chamber model. The vertical dashed line is at the energy at which the gyration radius equals the cavity diameter, explained in section 8.3.4. 157

8.8 The electron fluence spectral differences due to the magnetic field in each Farmer-type chamber geometry considered in the parallel orientation on the top row and perpendicular orientations with $\mathbf{F}_{\mathrm{L}}$ pointing towards the stem on the middle row and $\mathbf{F}_{\mathrm{L}}$ pointing towards the tip on the bottom row. The geometries are: the Farmer type chamber (left), the bare cavity with artificial water (middle) and the bare cavity filled with water (right) at 0 T and 1.5 T for fields of 10×10 cm ^{2} and 3×3 cm^2. The first vertical dashed line (at 0.50 MeV) is at the energy at which $\Delta = 0$, , explained in section 8.3.4. 160

8.9 The electron fluence spectral differences due to the magnetic field in each semiflex chamber geometry considered in the parallel orientation on the top row and perpendicular orientations with $\mathbf{F}_{\mathrm{L}}$ pointing towards the stem on the middle row and $\mathbf{F}_{\mathrm{L}}$ pointing towards the tip on the bottom row. The geometries are: chamber (left), the bare cavity with artificial water (middle) and the bare cavity filled with water (right) at 0 T and 1.5 T for fields of 10×10 cm ^{2} and 1×1 cm^2. The vertical dashed line is at the energy at which the gyration radius equals the cavity thickness, explained in section 8.3.4. On the left, an illustration of the sensitive volume in the smallest field size in each orientation. 162

8.10 Electrons entering an infinite slab at the same position in a vacuum in the presence of an external 1.5 T magnetic field. E_{ERE} is the energy at which the gyration radius equals the cavity thickness. On the left, electrons with enough energy to fully traverse the slab. On the right, electrons with energy to return to the incident wall. 164

8.11 Illustration of each chamber sensitive volume inside the smallest field. The dimensions of the sensitive volume and the field are to scale. 164
8.12 Symmetrical air gaps around chambers PTW30013 (left) and PTW31010 (right) at 1.5 T. In the top row, the electron fluence spectra per total incident photon fluence in the chamber for air gaps of different thickness. In the bottom row, the effect of the air gap is evaluated with respect to no air gap in the electron fluence in the presence of magnetic fields. 167
8.13 Asymmetrical air gaps around the Farmer-type chamber at 0 T (left) and at 1.5 T (right). In the top row, the electron fluence spectra per total incident photon fluence in the chamber for air gaps of different thickness. In the bottom row, the effect of the air gap is evaluated with respect to no air gap. 168
8.14 Asymmetrical air gaps around the PTW31010 chamber at 0 T (left) and at 1.5 T (right). In the top row, the electron fluence spectra per total incident photon fluence in the chamber for air gaps of different thickness. In the bottom row, the effect of the air gap is evaluated with respect to no air gap. 169
8.15 Ratio of dose in the cavity with an air gap relative to that with no air gap at 0 T and 1.5 T for chambers PTW30013 (left) and PTW31010 (right) 170

8.16 In the top row, the electron fluence per incident photon fluence for the full solid-state detector (top left), for the bare cavity with artificial water (top middle) and for the bare cavity filled with water (top right) at 0 T and 1.5 T for square irradiation beams of 10×10 cm^2 and 1×1 cm^2. In the bottom row, the relative difference between the electron fluence at 0 T and 1.5 T for each field size and each geometry considered. The vertical dashed line is at the energy at which the gyration radius equals the cavity thickness, explained in section 8.3.4. 171

LIST OF ABBREVIATIONS

AAPM	American Association of Physicists in Medicine
BTE	Boltzmann transport equation
CE	Central electrode
CH	Condensed history
CoP	Code of Practice
CPE	Charged particle equilibrium
CSE	Cross-section enhancement
CSDA	Continuous-slowing-down approximation
DV	Dead volume
ERE	Electron return effect
FFF	Flattening-filter-free
IAEA	International Atomic Energy Agency
IGRT	Image-guided radiation therapy
IMRT	Intensity-modulated radiation therapy
Kerma	Kinetic energy released per unit mass
LCPE	Lateral charged particle equilibrium
Linac	Linear accelerator
MC	Monte Carlo
MRgRT	Magnetic resonance-guided radiation therapy
MRI	Magnetic resonance imaging
MRI-Linac	Magnetic resonance imaging integrated to a linear accelerator

MV	Megavoltage
msr	machine-specific reference
NPL	National Physical Laboratory
OARs	Organs at risk
pcsr	plan-class specfic reference
PDD	Percentage depth dose
RT	Radiation therapy
SBRT	Stereotactic body radiation therapy
SDD	Source-to-surface distance
SID	Source-to-isocenter distance
SRT	Stereotactic radiation therapy
VRT	Variance reduction technique

NOTATION

A	atomic mass
A	area
b	impact parameter
$\vec{B}$	magnetic field
c	speed of light in vacuum
$C(\beta)$	shell correction factor in the stopping power
C_{inc}	constant factors in the Klein-Nishina cross section times electron density
d	cavity diameter
D_{det}	absorbed dose in the detector sensitive volume
D_{exp}	experimental absorbed dose
D_{med}	absorbed dose to medium
D_{num}	Monte Carlo simulated absorbed dose
$D_{w,Q_i}^{f_i}$	absorbed dose to water for a field f_i and beam quality Q_i
e	elementary electric charge
E	kinetic energy
$\vec{E}$	electric field
E_b	binding Energy
E_{tot}	total energy
$\dot{f}$	flux or fluence rate
$\vec{F}$	force vector
f_B	field size f couple to a magnetic field $\vec{B}$
f_e	electron fluence spectra differential in energy
$f_i(\vec{r},\vec{p})$	fluence differential in energy of particle type i and direction corresponding to the number of particles at position $\vec{r}$ with momentum $\vec{p}$ per unit energy, per unit area perpendicular to $\hat{\boldsymbol{u}}$ and per unit solid angle $d\hat{\boldsymbol{u}} = sin\theta d\theta d\phi$
$F_i(\vec{r},p)$	spectral distribution of a given f_i integrated over all directions

F_i^{tot}	total incident energy fluence of particle type i
$\vec{F}_L$	Lorentz force
$f_{\text{med, det, Q}}$	cavity theory factor ($D_{\text{med}}/D_{\text{det}}$) for radiation quality Q
f_{msr}	machine-specfic reference field
f_{pcsr}	plan class specfic reference field
f_{ref}	reference field
h	Plank constant
I	mean excitation energy
$\mathcal{I}\{f;\vec{r}\}$	Interaction term independent of time
k_Q or k_{Q,Q_0}	beam quality correction factor for the differences between the reference beam quality at the primary standards laboratory Q_0 and the beam quality Q of the conventional reference field at the hospital
$k_{Q_2,Q_1}^{f_2,f_1}$	quality correction factor from field size f_1 to f_2 and from beam quality Q_1 to Q_2
$k_{Q_B,Q}^{f_B,f}$, k_{Q_B} or $k_B^{Q_{msr}}$	quality correction factor accounting for the magnetic field effect
$[L_\Delta(E)/\rho]_{\text{det}}$	mass electronic restricted stopping power
m	mass
M	detector reading
m_e	electron mass
M_Q^f	corrected charge reading for a f field and beam quality Q
$M_{Q_{msr}}^{f_{msr}}$	corrected charge reading for a msr field and beam quality Q_{msr}
M_{raw}	raw charged measurement in ionization chambers
N	number of particles

$n(\vec{r},\vec{p},t)$	particle number distribution at a time t, corresponding to the number of particles with momentum $\vec{p}$ at position $\vec{r}$ per unit volume, momentum and solid angle
$n(E)$	dose spectrum
N_A	Avogadro's constant
$N_{D,w}^{^{60}Co}$	absorbed dose to water calibration factor for an ionization chamber located under reference conditions in a ^{60} Co radiation beam
$N_{D,\mathrm{w},Q_i}^{f_i}$	calibration coefficient specific for field size f_i and beam quality Q_i
$\vec{p}$	vector corresponding to the particle momentum
P	pressure
P	total perturbation factor
P_{elec}	electrometer correction factor
P_{ext}	extracameral perturbation factor
P_{ion}	recombination correction factor
P_{MC}	overall perturbation factor
P_{med}	medium perturbation factor
P_{pol}	polarity correction factor
P_{TP}	temperature-pressure correction factor
P_{vol}	volume averaging perturbation factor
P_ρ	density perturbation factor
q	particle charge
Q	beam quality
Q_B	beam quality in the presence of a magnetic field $\vec{B}$
Q_{msr}	machine-specfic reference quality beam
Q_{pcsr}	plan class specfic reference quality beam
$\vec{r}$	vector corresponding to the particle position in space
R or r_g	gyration radius of charged particles subjected to a magnetic field of strength B
r_a	atomic radius

r_e	electron radius
R_{exp}	ratio of experimental absorbed dose with and without magnetic field
$\vec{r}_{f,em}$	final particle position after a CH step in electromagnetic fields
R_{num}	ratio of numerical absorbed dose with and without magnetic field
$R_{Q_i}^{f_i}$	chamber intrinsic response for the field size f_i and the beam quality Q_i
$\vec{r}_0$	initial particle position before a CH step
s	path travelled by the particle between time 0 and t
$S(E)$	unrestricted stopping power
S/ρ	mass stopping power
S_{el}/ρ	mass electronic stopping power
$S(\vec{r},\vec{p})$	external source term
t	time
T	kinetic energy
T	temperature
$\hat{\boldsymbol{u}}$	unit vector in the direction of the particle momentum
$\vec{u}_0$	initial direction of particle motion
$\vec{v}$	velocity vector
V	volume
V_H	normal operating voltage for ionization chambers
V_L	reduced operating voltage for ionization chambers
W	transferred energy by a particle in a collision
Z	atomic number
$\%dd(10)_x$	photon component of the photon beam percentage depth dose at 10 cm depth in a 10 $\times$ 10 cm^2 field on the surface of a water phantom at SSD=100 cm

β	speed in units of c, $\beta = v/c$
γ	Lorentz relativistic factor $\gamma = 1/\sqrt{1-\beta^2}$
$\delta(\beta)$	density effect correction factor
Δ	energy loss cut-off for inelastic collisions
Δl	pathlength correction
δ_{data}	error coming from physical data
$\delta_{\text{Fano}}(B)$	algorithmic error from MC simulation
$\delta_{\text{geom}}(B)$	error cause by difference between blueprints and actual chamber design
$\delta_{\text{rep}}(B)$	error associated with measurement repeatability
$\delta_{\text{setup}}(B)$	error associated with measurement setup error
$\delta_{\text{stat}}(B)$	statistical uncertainty from MC simulation
$\Delta\vec{u}$	total angular deflection
$\Delta\vec{u}_{\text{med}}$	angular deflection due to elastic and inelastic scattering in a medium
$\Delta\vec{u}_{\text{em}}$	angular deflection due to the electromagnetic field
ϵ_{data}	error from physical data used in the radiation transport algorithm in the absorbed dose ratio with and without magnetic field
ϵ_{Fano}	algorithmic error from MC simulation in the absorbed dose ratio with and without magnetic field
ϵ_{geom}	error caused by difference between blueprints and actual chamber design in the absorbed dose ratio with and without magnetic field
ϵ_{rep}	error associated with measurement repeatability in the absorbed dose ratio with and without magnetic field
ϵ_{setup}	error associated with measurement setup error in the absorbed dose ratio with and without magnetic field
ϵ_{stat}	statistical error from MC simulation in the absorbed dose ratio with and without magnetic field
κ	initial photon energy in units of electron rest energy
κ_0	initial photon energy

ν	photon frequency
ρ	mass density
σ	cross section
Σ	macroscopic cross section
σ_{data}	physical data uncertainty
σ_{DV}	dead volume uncertainty
σ_{geo}	geometry uncertainty
σ_{Fano}	Fano uncertainty
σ_{ph}	photoelectric effect cross section
σ_{pp}	pair production cross section
σ_{print}	blueprints uncertainty
σ_{rep}	experimental repeatability uncertainty
σ_{setup}	experimental setup uncertainty
σ_{stat}	Monte Carlo statistical uncertainty
σ_{th}	Thomson cross section
τ	kinetic energy of a charged particle in units of its rest energy
Ω	solid angle

ACKNOWLEDGMENTS

My Ph.D. studies became a reality thanks to a scholarship provided by CONACyT and to being accepted into the medical physics program at Université de Montréal. I am grateful for these formative years that have been full of challenges, knowledge, and experiences.

First of all, I would like to thank Hugo Bouchard, I am genuinely thankful for the time and knowledge shared with me, the opportunities you gave me, the support and understanding these years, especially during the pandemic when things got tough.

I acknowledge Simon Duane and Ilias Billas for the secondments at NPL, which were fundamental in my Ph.D. research and in my formation as a scientist. Thanks to Simon for the opportunities, discussion and feedback. To Ilias for his support, collaboration and friendship. To David Shipley for all the technical help at NPL. To my office mates Hannah Cook, Michael McManus, Daniela Botnariuc, Reem Al-Samarraie, Sam Flynn, and Charles Fekete for becoming my friends, for the meals and beers and for showing me a bit of London. Finally, to Esther Bär for being there in different moments of my Ph.D., especially when the pandemic hit London, and I was far away from home. Still, I never felt alone, thanks to her, Charles and Tommy.

Sur cette note, je tiens à remercier à Stéphane Bedwani pour son soutien au CHUM et à mes collègues de bureau: Daniel Ahumada, Mikael Simard, Arthur Lalonde, Charlotte Remy, Jasmine Duchaine, Caroline Laplante, Andréanne Lapointe et Mathilde Wahl pour les lunch et la camaraderie. Un gros merci à Jasmine qui est devenue une collaboratrice et une amie.

I am truly grateful to Francisco Berumen Murillo for all the support, motivation, understanding, and love, even when our time zones were different. Me siento muy afortunada de estar contigo, no hay más palabras que decir, las sabes todas.

Gracias a mi mamá, mi papá, a Efraín y a mi familia por estar siempre conmigo (aunque esten lejos), por todo su apoyo y por su amor. Los extraño constantemente, esto es para ustedes.

Gabrielle and Rosa, thank you for welcoming me to Montreal with open arms and making me feel at home. Thanks to all my friends who have been there in one way or another. Especially to my oldest friends, Claudia, Fany, Pily and David, for the (almost) daily conversations and laughs and for being my support group.

CHAPTER 1

INTRODUCTION

1.1 Background

1.1.1 Motivation

Cancer is a leading cause of death worldwide; almost ten million deaths related to cancer occurred in 2020 [1]. In Canada, cancer is the leading cause of death, accounting for 29.6% of all deaths [2]. Radiation therapy (RT) is an essential tool in cancer treatment; approximately 50% of all cancer patients receive it during their course of treatment. RT contributes to 40% of curative treatments for cancer world-wide [3].

1.1.2 The context of radiation therapy

RT uses high doses of ionizing radiation to kill cancer cells. In the human body, ionizing radiation can be deposited directly into the DNA or into a critical cellular component, killing or damaging the cell at different levels. The radiation can also indirectly interact with the body by ionizing the water molecules and producing free radicals. These are highly reactive and can damage cellular components, or they can produce additional free radicals. The human body is mostly water; hence indirect interactions are the most probable [4].

In RT, the radiation beam can be delivered internally or externally to the cancer lesion. In internal RT, such as brachytherapy, the radiation is delivered by radioactive sources placed inside the body. In external RT, the radiation beams are produced by an external machine and delivered to the patient. The most common used forms of radiation are X-rays, γ-rays and high-energy (4 MeV -25 MeV) electron beams, but other particles such as protons or heavy ions are also used. External RT treatments are one of the common clinical approach [3, 5].

The use of radiation in medicine began shortly after the discovery of x-rays in

1895 [6] and of radioactivity in 1896 [7]. External RT began with superficial and orthovoltage therapy with x-ray tubes [8]. In the early 1950s, megavoltage (MV) photon beams began to be used with the development of clinical linear accelerators (linac) and with the introduction of cobalt-60 teletherapy machines which emit gamma rays of 1.17 and 1.33 MeV [8, 9]. The design of linacs has evolved and improved since they first appear. In modern linacs, electrons are accelerated with radio frequency electromagnetic waves and strike a target of high-Z material to produce a spectrum of x-ray energies [10]. Each linac has a unique radiation beam with a specific energy spectrum.

In the last three decades, technological advances in RT aim to deliver the radiation more accurately and conformal to the cancer lesion sparing as much healthy tissue as possible. Among the most relevant are: 1) intensity-modulated radiation therapy (IMRT), where dose varies inside the radiation field, 2) stereotactic radiation therapy (SRT) and stereotactic body radiation therapy (SBRT) treatments which are very conformal to the lesion target and have a steep dose gradient outside the target, 3) particle beam therapy, particularly proton therapy, where there is a significant reduction in the radiation dose to the healthy tissue [11], and 4) image-guided radiation therapy (IGRT) where the integration of imaging systems to the radiation device allows better control, accuracy and precision of dose delivery [12].

IGRT treatments track variations in the shape, position, and movement of the target volume, allowing the adaptation of treatment plans to these variations. Magnetic resonance imaging (MRI) has been used for a long time in RT. MRI has excellent soft-tissue contrast without delivering any radiation dose to the patient. In the last decade, several designs integrating MRI systems to linacs (MRI-linacs) have been developed [13, 14, 15, 16, 17, 18]. This thesis focuses on this technology, specifically on the effect of the magnetic field on dose distribution and measurement.

1.1.3 Magnetic resonance imaging-guided radiation therapy

Currently, there are two MRI-linac systems commercially available, the MRIdian® from ViewRay (ViewRay Inc., Oakwood, USA) and the Unity® from Elekta (Elekta

Instrument AB Stockholm, Sweden). In these systems, the magnetic field is always perpendicular to the irradiation beam, as illustrated on the left of figure 1.1 . Other prototypes, so-called in-line systems, where the beam is parallel to the magnetic field, are under research by the Australian Magnetic Resonance Imaging-linac program [17] and the MagnetTx Aurora ® by the University of Alberta [18]. The devices are shown in figure 1.2. Part of this research project was performed using the Elekta Unity MRI-Linac; thus, this device is described in more detail. The in-line systems are beyond the scope of this thesis.

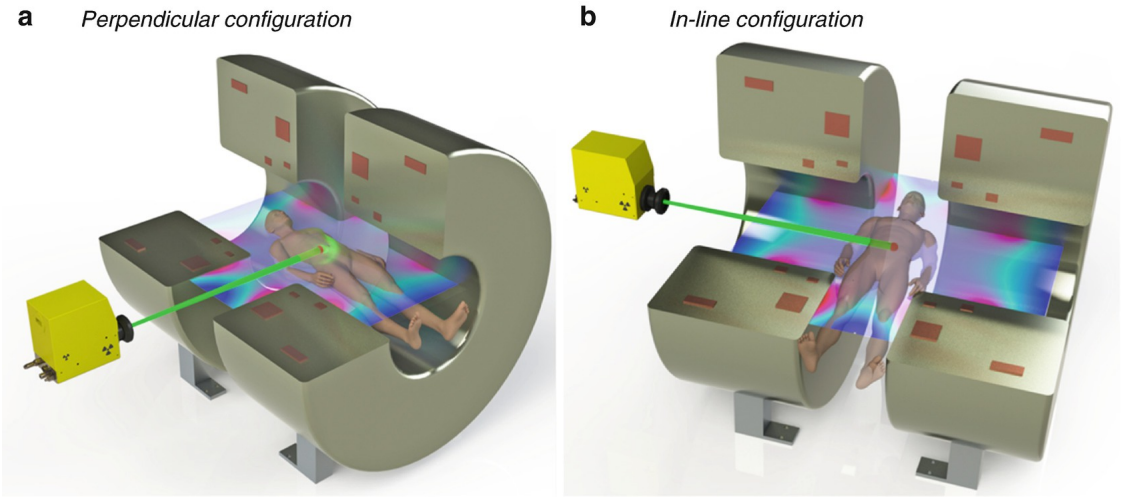

Figure 1.1 – The two configurations of MRI-linac devices: a) The radiation beam is perpendicular to the magnetic field, corresponding to Elekta Unity® and Viewray MRIdian® configuration. b) The radiation beam is parallel to the magnetic field, corresponding to the Australian Magnetic Resonance Imaging-linac program and the MagnetTx Aurora® by the University of Alberta. Figure taken from reference [19].

The first commercially available device was Viewray's MRIdian, consisting of a 0.35 T MR scanner surrounded by a ring-gantry with three equidistant ^{60}Co sources, each head is equipped with independent doubly focused multileaf collimators [15]. The first patient was treated in 2014 at Washington University [16]. In the latest version of the MRIdian, the ^{60}Co sources were replaced by 6 MV flattening-filter-free (FFF) linac [21].

The first clinical MRI-linac prototype was developed by a collaboration be-

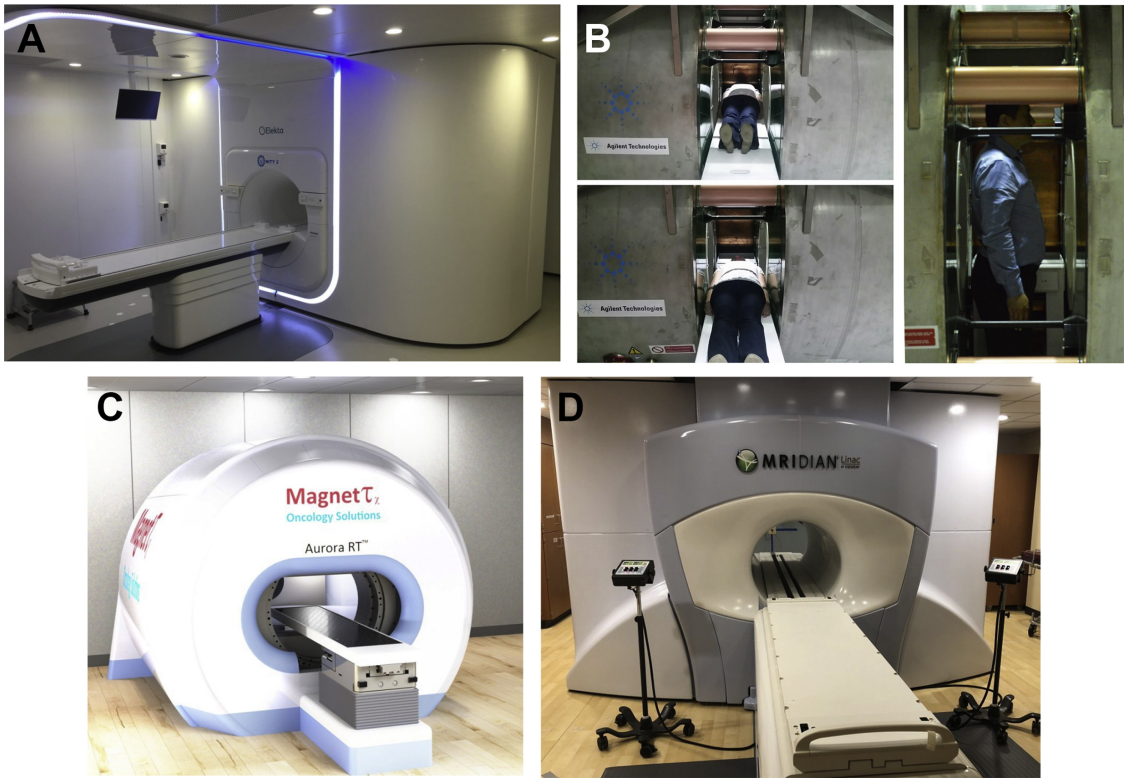

Figure 1.2 – (a) Elekta's 1.5 T Unity® system at University Medical Centre in Utrecht, The Netherlands. (b) The Australian MRI-linac, (left) supine positioning and (right) standing positioning that is possible with this open system. (c) The Aurora-RT® system at the University of Alberta. (d) Viewray's MRIdian® system at Washington University in St Louis, USA. Figure taken from reference [20].

tween the University Medical Center Utrecht, Elekta, and Philips (Koninklijke Philips N.V., Amsterdam, Netherlands) [22, 13]. In 2017, the first-in-man study was performed on the prototype combining a 1.5 T MRI scanner with a 7 MV FFF linear accelerator [14]. This prototype evolved into the Elekta Unity MRI-linac, released for clinical use in 2018. The first patient was treated in the same year at the University Medical Center Utrecht [23].

The integration of an MRI with a linac poses many technological challenges. The main technical difficulty is the magnetic interaction between the two systems: the MRI components scatter and attenuate the beam and the magnetic field changes the trajectory of the secondary electrons while the metal components of the linac

perturb the magnetic field homogeneity inside the MRI [24, 25]. These difficulties were overcome by adopting the active shielding method of the magnet. The active shielding provides a low magnetic field in a toroid around the magnet where the sensitive linac components are placed. The linac is mounted on a gantry ring surrounding the 1.5 T magnet, as illustrated in figure 1.3 [25, 26]. The radiation beam travels through a homogeneous part of the cryostat free of super-conducting coils [26]. Additionally, a radio-frequency cage is integrated into the MR scanner to isolate it from the linac interference [27].

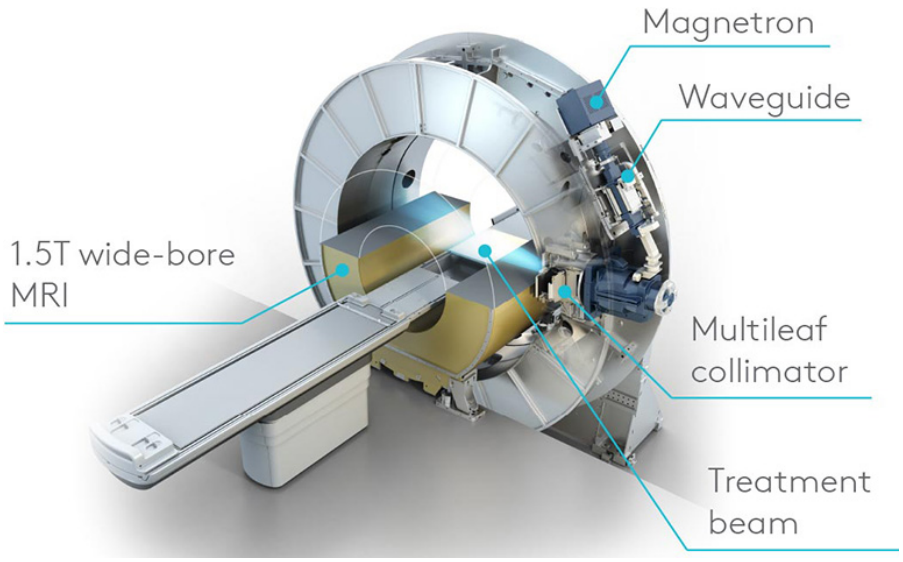

Figure 1.3 – Schematic diagram of the Unity MRI-linac, taken from reference [27].

1.1.4 Impact of the magnetic field on reference dosimetry

RT relies on accurate dose delivery to the target volume; an overall accuracy of 5%-7% in dose delivery at the 95% confidence level is recommended [5, 28]. In particular, the combined uncertainty for ionization chamber reference dosimetry in external beam radiotherapy is between 1.6% and 2.6% with k=1 [29]. To achieve this, linacs are calibrated to deliver a specific dose under standard conditions following accepted dosimetry protocols or Code of Practice (CoP). National

and international organizations issue these protocols, so standard procedures are adopted nationally, regionally or globally. This allows reliable comparison of reference dosimetry data and outcomes of RT treatments between different institutions [30].

In the reference dosimetry protocols, the absorbed dose is determined at a reference point in a phantom (usually made of water) irradiated by a beam of quality, Q, under specific reference conditions. Examples of reference conditions are the reference point 10 cm depth, the source-to-surface distance (SSD) equal to 100 cm and a 10×10 cm^2 field. Radiation dosimeters provide a reading, M, proportional to the dose deposited by the radiation beam in the dosimeter's sensitive volume [30]. Ionization chambers are the preferred reference radiation dosimeter in RT. For external RT with high-energy photon beams, two of the most important protocols for clinical reference dosimetry are: one from the task group TG-51 [31, 32] from the American Association of Physicists in Medicine (AAPM), commonly referred to as TG-51, and the Technical Reports Series No. 398, or TRS-398, [33] from the International Atomic Energy Agency (IAEA).

In MRI-linacs, the magnetic field is always present, which impacts the reference dosimetry measurements. The magnetic field does not affect the photon beam, nor does it impact the photon-matter interactions in the energy range of interest [34]. However, the secondary charged particles produced by the photon beam are affected by it, and their trajectories are impacted by the Lorentz force. Figure 1.4 depicts electrons travelling through water in the absence and presence of a magnetic field. This affects the radiation field and the detector dose response, introducing some differences from conventional reference dosimetry.

The magnetic field introduces significant effects on the reference field, such as the compression of the build-up region, asymmetry in the penumbra and in dose profiles, among others explained in more detail in section 2.3.3.2. One important effect is the so-called electron return effect (ERE) which occurs in interfaces between high and low-density media, for instance, water-air interfaces. Depending on the strength of the magnetic field and on the energy of the secondary electrons,

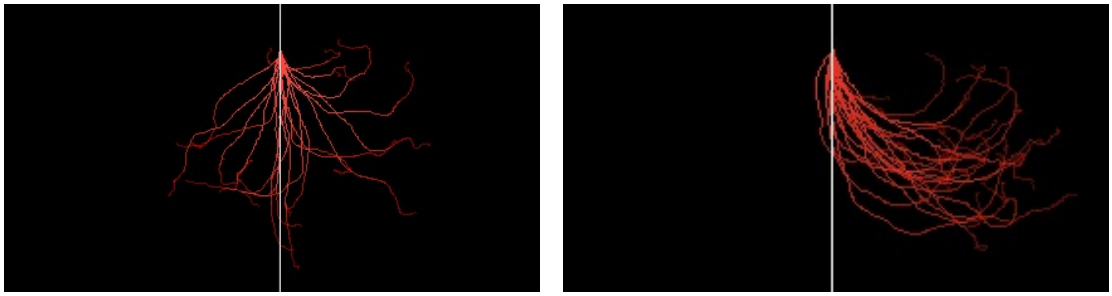

(a) 0 T **(b)** 1.5 T

Figure 1.4 – Electron trajectories in water in the absence and presence of a magnetic field, taken from simulations of a 6 MeV pencil photon beam irradiating water performed in the user code *egs_chamber* (EGSnrc).

they can return from the low-density medium to the high-density region and deposit their energy there, creating a high dose region at the end of the high-density region [13].

The detector response is impacted by the magnetic field. Situations that generally are neglected in conventional dosimetry become an issue in magnetic fields. First, detector orientation with respect to the magnetic field is relevant since charged particles are deflected towards different components of the detector, perturbing the detector response differently [35]. Secondly, small air gaps surrounding the detector could also potentially impact the detector response in magnetic fields [36, 37, 38]. Finally, Monte Carlo (MC) simulations of detector response are also impacted by the magnetic field; a higher level of detail and precision is required for the detector geometry model, including an accurate definition of the active sensitive volume [39, 40, 41].

Currently, there are no available reference dosimetry protocols for the MRI-linacs, although there is a global effort with several groups working towards this goal. This thesis contributes to that effort.

1.2 Objectives

This thesis is composed of three articles, the objectives of each article are presented in the following. In the first article, the impact of the magnetic field on small-cavity response was studied. Objectives were as follows:

1. To characterize small-cavity detector response in the presence of magnetic fields using four commercial small-cavity ionization chambers in two configurations, using Monte Carlo simulations and experimental measurements.
2. To calculate quality correction factors, k_{Q_B}, accounting for the effect of the magnetic field.
3. To provide a detailed uncertainty budget for k_{Q_B}.

The second article studies the interplay of the magnetic field effect on detector dose response and the effect of reducing the irradiation field size in these conditions. The specific objectives of this article were:

1. To provide physical insights on the effects of magnetic fields on detector response in different irradiation field sizes.
2. To calculate perturbation factors and quality correction factors of several detectors irradiated by beams of multiple field sizes in the presence of magnetic fields.
3. To determine the conditions that minimize perturbations on detector response.

The third article explains the underlying physics behind the magnetic field effect on detector response by calculating the electron fluence rather than the dose in different detectors. Objectives of this article were:

1. To study the behaviour of electron spectra and restrictions of Fano's theorem in the presence of magnetic fields
2. To characterize the variations in electron spectra in the presence of magnetic fields in six detectors in different irradiation conditions.

1.3 Structure of the thesis

In chapter two, the theory relevant to reference dosimetry in the presence of magnetic fields is presented. The first article entitled "small-cavity chamber dose response in megavoltage photon beams coupled to magnetic field" is introduced in chapter three and presented in chapter four. Additionally, in chapter three, supplementary calculations for the uncertainty budget are also explained. The second article entitled "Detector perturbation and quality correction factors in magnetic resonance-guided radiation therapy small photon beams" is introduced in chapter five and presented in chapter six. The third article entitled "Monte Carlo investigation of electron fluence perturbation in MR-guided radiotherapy beams using six commercial radiation detectors" is introduced in chapter seven and presented in chapter eight. Finally, the conclusions of the thesis are presented in chapter nine.

CHAPTER 2

THEORY

2.1 Radiation transport

2.1.1 Interactions of particles with matter

As particles travel through matter, they interact with the atomic electrons and nuclei of the medium. Neutral particles, such as photons, rarely interact with matter, whereas charged particles interact with almost every atom along its path, losing energy or changing direction in each interaction [42, 30]. In photon-matter interactions, in the RT energy range, photons indirectly deposit their energy through four photon-matter interaction processes: pair production, incoherent (Compton) and coherent (Rayleigh) scattering, and the photoelectric effect, explained in section 2.1.1.1. These interactions produce secondary charged particles such as electrons and positrons. As these secondary charged particles traverse matter, they lose energy via inelastic collisions with atomic electrons or by radiation processes [42, 30]. In section 2.1.1.2, the electron-matter interactions are explained in detail.

2.1.1.1 Photon interactions with matter

The likelihood of the different processes through which a photon interacts with matter depends on the initial photon energy and on the atomic number (Z) of the absorbing medium. In external RT, the energies of interest are between 10 keV and 25 MeV [30] where the dominant photon-matter interactions are photoelectric absorption at lower energies, the Compton scattering at intermediate energies and pair production at higher energies, as shown in figure 2.1 [42, 30].

A low-energy photon can also interact with the medium via Rayleigh or coherent scattering in which the whole atom elastically scatters the incident photon. Thus, there is no energy transferred, no ionization, nor excitation of the atom, and this is why this process is not relevant in RT. Rayleigh scattering occurs more frequently

at lower energies and in high-Z materials.

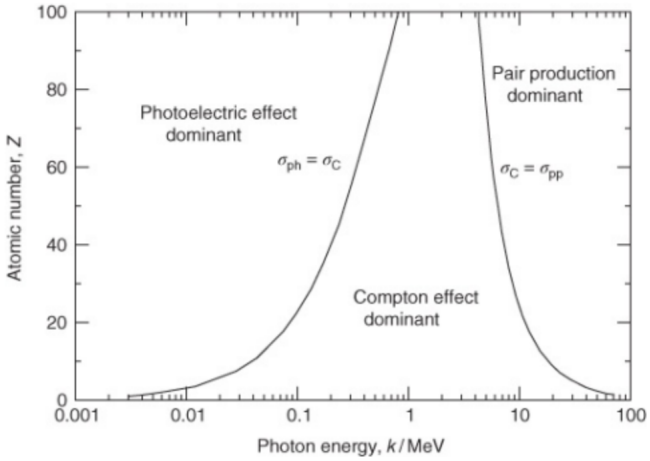

Figure 2.1 – The relative importance of the three principal interactions of photons with matter as a function of the medium atomic number and photon energy. Taken from reference [30].

Photoelectric effect

An incident photon with energy $h\nu$ interacts with an inner atomic shell electron with binding energy E_b, this interaction can only occur if $h\nu > E_b$. The photon is absorbed, the electron gains the photon energy and is ejected with a kinetic energy of $T = h\nu - E_b$, as illustrated in 2.2a. The photoelectric effect cross section, σ_{ph}, strongly depends on the atomic number and on the energy of the incident photon. The proportionality to these factors is given by: $\sigma_{\text{ph}} \propto \frac{Z^n}{(h\nu)^m}$, where $m = 3.5$ and $n = 4$ for low Z materials, and $n = 4.8$ for high Z [42, 30].

Compton scattering

Compton scattering occurs when an incident photon with initial energy $h\nu$ collides with an atomic electron. This electron is considered free, i.e. its binding energy is negligible compared to the projectile's kinetic energy. After the collision, the electron scatters at angle ϕ with kinetic energy T, and the photon scatters at an angle θ with a lower energy $h\nu'$, as shown in figure 2.2b. Due to energy

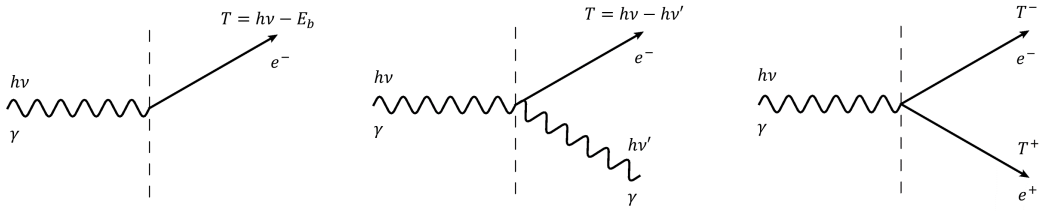

(a) Photoelectric effect **(b)** Compton scattering **(c)** Pair production

Figure 2.2 – An incident photon with $h\nu$ energy interacts with the medium mainly via three interaction process: photoelectric effect, Compton scattering and pair production.

conservation, the energy transferred to the electron is:

$$T = h\nu - h\nu' = h\nu - \frac{h\nu}{1 + \frac{h\nu}{m_e c^2}(1 - \cos\theta)}. \tag{2.1}$$

with m_e is the electron mass. The right part of equation 2.1 is obtained with the conservation of momentum in the parallel and perpendicular components. Backscattering of the photon and forward scattering of the electron, i.e. $\theta = \pi$ and $\phi = 0$, results in the maximal energy transferred to the electron:

$$T_{\max} = h\nu - \frac{h\nu}{1 + \frac{2h\nu}{m_e c^2}}. \tag{2.2}$$

In general, electrons can only scatter in the forward hemisphere, i.e. $-\pi/2 \leq \phi \leq \pi/2$, in a Compton event. For low-energy photons ($\sim$0.01 MeV), the electron receives practically no energy, the photon energy remains almost the same ($h\nu \approx h\nu)'$, and the photon scatters in the forward direction [30].

The probability that a Compton interaction occurs was first approximated by Thomson, as : $\sigma_{th} = (8\pi r_e^2)/3 = 6.65 \times 10^{-25}$ cm$^2/e^-$ [42]. This value is independent of the energy, and it is only a good approximation for low photon energies (< 0.01 MeV). In 1929, Klein and Nishina improved Thomson's cross-section by applying

Dirac's relativistic theory. In the Klein-Nishina (KN) treatment, the electrons are assumed to be unbound and at rest. Hence, the KN cross-section is independent of the atomic number [30].

Pair production

The photon interacts with the electromagnetic field of the atomic nucleus. It is completely absorbed, releasing all of its energy ($h\nu$), and an electron-positron pair is produced with kinetic energies T^- and T^+, respectively, as illustrated in figure 2.2c. The pair production process can only occur if the photon energy is at least $2m_ec^2 = 1.022$ MeV. The electron and the positron do not necessarily receive equal kinetic energy; the average kinetic energy is $\overline{T} = (h\nu - 1.022 \text{ MeV})/2$. The pair production cross-section per atom σ_{pp} is proportional to Z^2 and independent of the photon energy [42, 30].

It is also possible but less probable that the photon interacts with the force field of an atomic electron. In such a way that the atomic electron acquires significant kinetic energy and is ejected along with the created positron-electron pair, this process is called "triplet production". The photon energy threshold for this interaction is 2.044 MeV [42, 30].

2.1.1.2 Interactions of charged particles with matter

As charged particles traverse matter, there are Coulomb interactions between them and the atoms, atomic electrons or atomic nuclei. This leads to the loss of their energy and to changes in their direction. The medium gains its energy as atoms become ionized or excited. There are two basic interaction processes of charged particles with matter: collisions and radiative processes such as bremsstrahlung and positron annihilation [42, 30].

In external RT, electrons are the primary charged particle of interest. Contrary to photons, which interact relatively infrequently with atoms, electrons interact with almost every atom along its pathway, losing energy almost continuously. This

lead to a theory for electron energy loss known as the continuous-slowing-down approximation (CSDA) [42, 30].

Electronic collisions

In a classical approach, electronic collisions can be characterized by the impact parameter, b, which is the closest perpendicular distance between the electron path and the atom center. Electronic collisions can be classified into different types, such as elastic or inelastic, by directly comparing the impact parameter and the atomic radius, r_a, as shown in figure 2.3 [30].

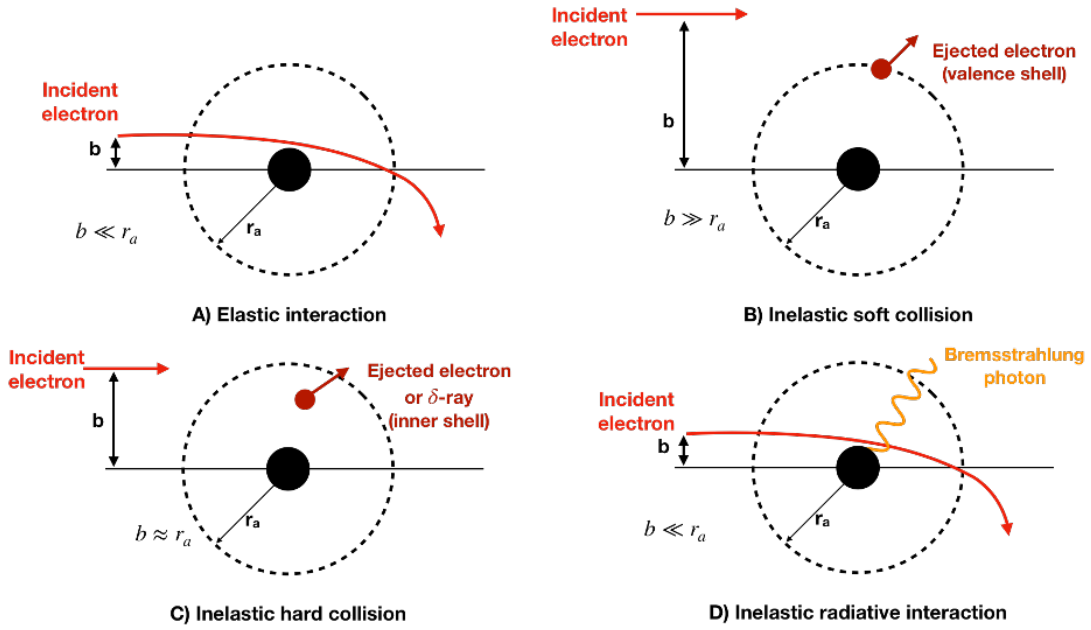

Figure 2.3 – Diagram the main types of interactions of charged particles with an atom, depending on the impact parameter, b, relative to the atomic radius, r_a. (a) elastic interaction, (b) inelastic soft collision, (c) Inelastic hard collision and (d) inelastic radiative interaction. Taken from reference [30].

Elastic collisions occur when $b \ll r_a$, the electron mainly interacts with the nucleus, and it is deflected by the nucleus electric field without losing energy (or rather losing a negligible amount of energy). Elastic collisions are the dominant mechanism of electron scattering, especially in high-Z media. The elastic scattering cross-section is proportional to Z^2 of the media [30].

Inelastic soft collisions occur if $b \gg r_a$, then a Coulomb interaction occurs between the electron and the atom. The electron transfers a small amount of energy ($\sim$ eV) to the atom, which becomes either excited or ionized. Inelastic soft collisions are the more probable and thus most common inelastic collision. Even if the energy transfer is minimal per interaction, globally, they account for half of the energy transferred to the medium [30].

Inelastic hard collisions, also known as knock-on collision, occur when $b \approx r_a$. The incident electron collides with an atomic electron, and the latter is ejected from the atomic shell, gaining a considerable amount of kinetic energy. The ejected electron, known as a δ ray or as a knock-on electron, usually follows a different trajectory than the primary electron, it is worth noting that the primary and secondary electron are indistinguishable. Inelastic hard collisions are less probable and less frequent than soft ones. However, the energy transferred in each hard collision is much larger; hence the energy lost by soft and hard inelastic collisions is comparable [30].

Radiative interactions

When the incident electron interacts with the external field of the nucleus, most of the interactions result in an elastic collision. However, 2-3% of the interactions result in an inelastic radiative process in which an x-ray is emitted. The incident electron slows down abruptly, giving up all or a fraction of its total kinetic energy. This phenomenon is called braking radiation or bremsstrahlung. This process is relevant for high Z materials and high energies ($>$ 10 MeV). The cross-section of this interaction is proportional to Z^2. Hence, for low Z materials and energies below 10 MeV, this interaction has a low probability. The emitted photon is energetic enough to travel several centimetres, probably escaping the medium of interest and depositing its energy elsewhere [30, 42].

Another radiative process is in-flight annihilation. This process can only occur when a positron is present, and it collides with an electron coming to rest creating two annihilation photons. The kinetic energy is distributed between the

annihilation photons [30, 42].

Stopping power

In each electron-matter interaction, only a minor fraction of the incident electron energy is transferred to the surrounding medium. The CSDA is a convenient way to account for the transferred energy in multiple interactions by considering a gradual energy loss [42]. The electronic stopping power is the average rate at which electrons lose energy along their path [43]. The mass electronic stopping power is defined as:

$$\frac{S_{\text{el}}}{\rho} = \frac{dE}{\rho dx} = \frac{Z}{A} N_A \int_{W_{\min}}^{W_{\max}} W \frac{d\sigma}{dW} dW, \tag{2.3}$$

where $(Z/A)N_A$ is the number of electrons per unit mass in the medium, W is the energy transferred to the medium and $d\sigma/dW$ is the cross-section, differential in this energy transfer, per atomic electron for inelastic collisions.

For electrons, the mass electronic stopping power is derived from the Bethe theory using the Møller cross section for hard collisions and it is given by [30, 43]:

$$\frac{1}{\rho} S_{\text{el}} = 2\pi r_e^2 m_e c^2 \frac{Z}{A} N_A \frac{1}{\beta^2} \left[\ln\left(\frac{E}{I}\right)^2 + ln(1+\tau/2) + F^-(\tau) - \delta(\beta) - 2\frac{C(\beta)}{Z} \right], \tag{2.4}$$

where r_e is the classical electron radius, c is the speed of light in vacuum, $\beta = v/c$ is electron speed in units of c, E is the kinetic energy of the electron, I is the mean excitation energy of a medium, known as I-value, $\tau = E/m_e c^2$ is the ratio of the kinetic energy to its rest energy, $\delta(\beta)$ is the density-effect correction factor, $C(\beta)/Z$ is the shell correction factor and F^- is defined as:

$$F^{-}(\tau) = (1-\beta^2)\left[1+\frac{\tau^2}{8}-(2\tau+1)\ln 2\right]. \tag{2.5}$$

The energy spent in collision interactions is transferred to the medium while energy spent in radiative interactions is usually carried away from the neighbourhood of the interaction by photons [43, 10, 30]. The mass stopping power can be divided according to the process of energy loss in collision stopping power and radiative stopping power, as shown in equation 2.6.

$$S = \frac{dE}{\rho dx} = \left(\frac{dE}{\rho dx}\right)_{col} + \left(\frac{dE}{\rho dx}\right)_{rad}. \tag{2.6}$$

If delta rays resulting from hard collisions are energetic enough to carry their energy away from the primary track, the electronic stopping power overestimates the local energy deposition, especially in small volumes. The restricted stopping power is the average energy loss per unit pathlength from interaction events in which the energy transferred to secondary electrons is smaller than a chosen cut-off value Δ [43], and is defined as:

$$S_{\mathrm{el}}(E,\Delta) = \frac{Z}{A}N_A\int_{W_{\min}}^{\Delta} W\frac{d\sigma}{dW}dW, \tag{2.7}$$

where the Δ value is chosen accordingly to the required spatial resolution.

2.1.2 Radiation transport equation

2.1.2.1 Definitions

Number of particles Considering a source of particles incident in a medium, the number of particles at the position $\vec{r}$, at time t, with momentum $\vec{p}$, is denoted by $N(\vec{r},\vec{p},t)$. The total number of particles at time t is given by:

$$N(t) = \int_{\mathbb{R}^3} d^3r \int_{4\pi} d\Omega \int_0^\infty p^2 n(\vec{r},\vec{p},t) dp, \tag{2.8}$$

where $n(\vec{r},\vec{p},t)$ is the particle number density defined as the number of particles of the same kind per unit volume, energy and solid angle.

Flux The flux or fluence rate, $\dot{f}$, is defined as the number of particles per area perpendicular to the particle direction per unit time. The mathematical definition is:

$$\dot{f}(\vec{r},\vec{p},t) = n(\vec{r},\vec{p},t) \times v \tag{2.9}$$

where v is the velocity. The flux units are $\mathrm{cm}^{-2}\ \mathrm{s}^{-1}\ \mathrm{sr}^{-1}\mathrm{MeV}^{-1}$

Fluence The fluence, f_i, is the number of particles type i at position $\vec{r}$ with momentum $\vec{p}$, per area perpendicular to the particle direction $\hat{\boldsymbol{u}}$, per unit energy, per unit solid angle $d\hat{\boldsymbol{u}} = sin\theta d\theta d\phi$. It has unit of $\mathrm{cm}^{-2}\mathrm{sr}^{-1}\mathrm{MeV}^{-1}$. It is illustrated in figure 2.4.

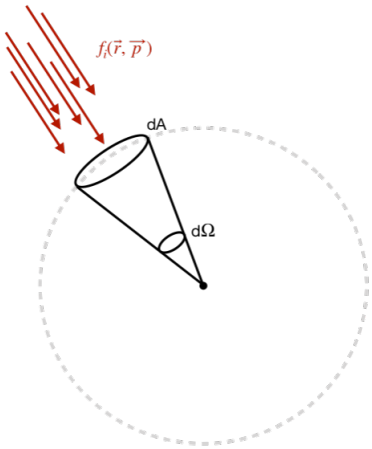

Figure 2.4 – Diagram illustrating the fluence, f_i, in the solid angle, $d\Omega$.

The fluence spectrum, F, considers the particles coming from all directions and is defined as:

$$F(\vec{r},\vec{p}) = \int_{4\pi} f(\vec{r},\vec{p}) d\Omega. \tag{2.10}$$

2.1.2.2 Radiation transport equation

The radiation transport equation or Boltzmann transport equation (BTE) describes the conservation of the number of particles in a volume by balancing the loss and gain of particles. Considering a volume, V, with a spatial particle distribution, $n(\vec{r},\vec{p},t)$, the transport of particles can be described by the continuity equation. If there are no external sources and no interactions, the continuity equation is written as:

$$\frac{dn(\vec{r},\vec{p},t)}{dt} = 0. \tag{2.11}$$

expanding the derivative of this equation:

$$\begin{aligned} \frac{dn}{dt} &= \frac{\partial n}{\partial t} + \frac{\partial n}{\partial x}\frac{dx}{dt} + \frac{\partial n}{\partial y}\frac{dy}{dt} + \frac{\partial n}{\partial z}\frac{dz}{dt} + \frac{\partial n}{\partial p_x}\frac{dp_x}{dt} + \frac{\partial n}{\partial p_y}\frac{dp_y}{dt} + \frac{\partial n}{\partial p_z}\frac{dp_z}{dt} \\ \frac{dn}{dt} &= \frac{\partial n}{\partial t} + \frac{d\vec{r}}{dt}\cdot\vec{\nabla}_r n + \frac{d\vec{p}}{dt}\cdot\vec{\nabla}_p n, \end{aligned} \tag{2.12}$$

since there are no external forces, then $d\vec{p}/dt = 0$. Using the equation 2.9, the left side of the continuity equation becomes:

$$\frac{dn}{dt} = \frac{\partial}{\partial t}\left(\frac{\dot{f}}{v}\right) + \vec{v}\cdot\vec{\nabla}_r\left(\frac{\dot{f}}{v}\right) \tag{2.13}$$

$$\frac{dn}{dt} = \frac{1}{v}\frac{\partial \dot{f}}{\partial t} + \hat{\boldsymbol{u}}\cdot\vec{\nabla}_r\dot{f} \tag{2.14}$$

with $\hat{\boldsymbol{u}}$ the unit vector in the direction of the particle momentum.

Considering a case with an external particle source, two terms must be added

to the continuity equation, one representing the primary particles coming from the source $\dot{S}(\vec{r},\vec{p},t)$, and an interaction term, $I\{\dot{f};\vec{r}\}$ representing the production of secondary particles in a medium with mass density ρ. Then, the continuity equation becomes:

$$\frac{dn}{dt} = \rho[\dot{S} + I\{\dot{f};\vec{r}\}]. \tag{2.15}$$

Combining equations 2.14 and 2.15, the radiation transport equation becomes:

$$\frac{1}{v}\frac{\partial \dot{f}}{\partial t} + \hat{\boldsymbol{u}} \cdot \vec{\nabla}_r \dot{f} = \rho[\dot{S} + I\{\dot{f};\vec{r}\}], \tag{2.16}$$

then integrating the Boltzmann radiation transport equation over time, gives:

$$\hat{\boldsymbol{u}} \cdot \vec{\nabla} f = \rho[S + I\{f;\vec{r}\}]. \tag{2.17}$$

In the following section, this equation is modified to account for the presence of an external force - the Lorentz force.

2.1.3 Radiation transport in the presence of an external magnetic field

The presence of an external magnetic field changes the transport of charged particles and their energy deposition. Charged particles are subjected to the Lorentz force, $\vec{F}_L$, if there is no electric field, it is given by

$$\vec{F}_L = q[\vec{v} \times \vec{B}], \tag{2.18}$$

with $q = -e$ for electrons and $q = +e$ for positrons, e the elementary electric charge ($1.602176634 \times 10^{-19}$ C), $\vec{v}$ the particle velocity and $\vec{B}$ the magnetic field. Note that the Lorentz force is determined only by the velocity component perpendicular to the magnetic field and it is zero if the vectors are parallels.

If an electron travels in vacuum, there is no energy loss, but there is a change in its direction [44]. Then, the electron spirals around the magnetic field lines

following a circular orbit with a gyration radius, r_g, as shown in figure 2.5.

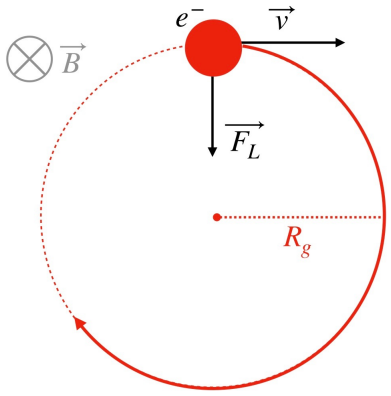

Figure 2.5 – In vacuum, the electron trajectory follows a circular trajectory due to the Lorentz force

Since the magnetic field acts like a centripetal force [44], defining α as the angle between the magnetic field and the electron velocity, and using $\beta = |\vec{v}|/c$, then the gyration radius is given by [26]

$$r_g = \frac{E_{\text{tot}}\ \beta\ \sin\alpha}{ec\ |\vec{B}|}, \tag{2.19}$$

where E_{tot} is the total energy of the electron and c the speed of light. When the electron moves completely perpendicular to the magnetic field, i.e., $\alpha = 90°$, the electron moves in a circular orbit as shown in figure 2.5 and the gyration radius is given by

$$r_g = \frac{E_{\text{tot}}\beta}{ec|\vec{B}|}. \tag{2.20}$$

Magnetic forces do no work, so they cannot speed or slow down the charged particles [44]. An electron travelling in a medium collides or interacts with atoms and electrons, losing energy according to the CSDA. As its energy decreases, the gyration radius becomes smaller and modifies the circular trajectory into a conical

spring, as illustrated in figure 2.6.

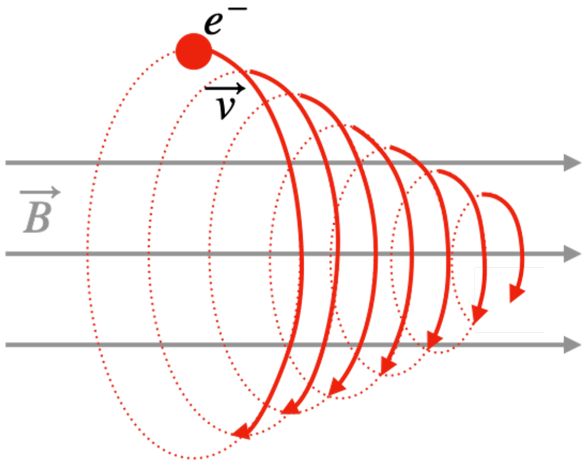

Figure 2.6 – In a medium, as the electron loses energy due to interaction with the medium, the electron path describes a spiral with decreasing radius due to the Lorentz force

The transport of charged particles is affected by the magnetic field. In section 2.1.2.2, the Boltzmann transport equation was derived assuming no external forces which is no longer valid due to the presence of the Lorentz force. Taking it into account and considering no electric field, the continuity equation (eq. 2.12) becomes:

$$\frac{dn}{dt} = \frac{\partial n}{\partial t} + \frac{\partial \vec{r}}{\partial t} \cdot \vec{\nabla}_r n + q[(\vec{v} \times \vec{B})] \cdot \vec{\nabla}_p n. \tag{2.21}$$

Using the relationship $n = \dot{f}/v$, the previous equation becomes:

$$\frac{dn}{dt} = \frac{\partial \dot{f}}{v \partial t} + \hat{\boldsymbol{u}} \cdot \vec{\nabla}_r \dot{f} + q(\hat{\boldsymbol{u}} \times \vec{B}) \cdot \vec{\nabla}_p \dot{f} \tag{2.22}$$

Considering an external particle source and combining equations 2.15 and 2.22, the time-dependent Boltzmann transport in the presence of a magnetic field is:

$$\rho[\dot{S} + \dot{I}\{f; \vec{r}\}] = \frac{\partial \dot{f}}{v \partial t} + \hat{\boldsymbol{u}} \cdot \vec{\nabla}_r \dot{f} + q(\hat{\boldsymbol{u}} \times \vec{B}) \cdot \vec{\nabla}_p \dot{f}. \tag{2.23}$$

For an external magnetic field $\vec{B}$ constant over time, the time-independent Boltzmann transport equation, i.e. equation 2.17, can be written as [45]:

$$\hat{\boldsymbol{u}} \cdot \vec{\nabla}_r f = \rho[S + I\{f; \vec{r}\}] + q(\hat{\boldsymbol{u}} \times \vec{B}) \cdot \vec{\nabla}_p f, \tag{2.24}$$

Noting that, just as for equation 2.17, the term $\partial \dot{f}/v\partial t$ vanishes as its initial and final value is zero, i.e. at the beginning and end of the irradiation. Equation 2.24 has no analytical solution, and Monte Carlo methods *can* be used to solve it.

2.2 Monte Carlo method for radiation transport

The Monte Carlo method is a statistical approach to solve integro-differential equations [46]. A physical problem is modelled in a system of equations for a quantity of interest. Then, this quantity is expressed as a parameter (an expectation value, usually the mean) of a distribution [47]. A sampling algorithm generates a random sample from the probability distribution and random numbers. Next, estimators for the parameter and its uncertainty are derived. Finally, the parameter of interest and its uncertainty are determined from the random sample distribution [47]. The uncertainty or confidence interval corresponds to the width of the sample distribution. The level of statistical uncertainty depends on the sample size; the larger the sample, the smaller is the uncertainty [47, 30]. In medical physics, there are several applications of Monte Carlo techniques, for instance, radiation transport, treatment planning, and detector dose-response characterization.

2.2.1 Simulation of radiation transport

In Monte Carlo simulations, particles are generated by a source; they travel through the medium and interact with it according to a probability distribution given by the total interaction cross-section [48]. As they interact, they produce secondary particles that are also transported. Particle transport finishes when most of their energy is absorbed by the medium or until the particle escapes the geometry of interest [48]. Each primary particle corresponds to a case or "history".

The number of histories determines the statistical uncertainty of the quantity of interest [48].

Particles are transported via two techniques: analog transport and condensed history (CH). In the first, every interaction event is explicitly simulated, primarily used for photon transport. For electrons, it is computationally inefficient to simulate every single event due to the high number of interactions [49]. For instance, an electron of 1 MeV typically will undergo $\approx 10^5$ interactions before losing its kinetic energy [42]. Hence, the transport simulation of one electron would require an extremely long calculation time. To avoid this, Berger [50] introduced the CH method, where a large number of events are grouped into a single step. This is feasible because most electron-matter interactions are either elastic (no energy loss) or inelastic, in which only a tiny amount of energy is lost and transferred to the medium. Furthermore, the changes in electron direction and scattering angles are generally small [51].

The step size of the particle pathlength is carefully chosen by minimizing the step number while maintaining a step size small enough to be adequate in the volume boundaries and to minimize angular deflection and energy loss [50]. There are two types of schemes: class I, where the collisions are grouped using a specific pathlength or energy loss, and class II, where collisions with small energy losses and deflections are grouped, and occasional catastrophic collisions with considerable loss of energy are treated separately by conventional random sampling according to single-scattering cross-sections [50]. Class II is the most common since it allows catastrophic processes above an energy threshold such as bremsstrahlung production or hard inelastic collisions, where energy is deposited far away from the primary track, and avoids dose overestimation especially in smaller volumes [48].

2.2.2 Radiation transport in magnetic fields

Among the Monte Carlo codes allowing charged particle transport in magnetic fields are PENELOPE, MCNP5, GEANT4 and EGSnrc. In particular, in EGSnrc [48], this transport is performed following the approach of Bielajew [52]. To explain

this approach, first, the equation of motion of a charged particle in vacuum in the presence of an external magnetic field is derived in section 2.2.2.1, and then its implementation into the Monte Carlo algorithm is described in section 2.2.2.2.

2.2.2.1 Equations of motion in vacuum in magnetic fields

In the case of relativistic motion, using $\vec{p} = m\gamma\vec{v}$, $\vec{v} = \vec{\beta}c$ and $\gamma = (1-\beta)^{-1/2}$, the force can be written as

$$\begin{aligned}
\vec{F} =& \frac{d\vec{p}}{dt} \\
=& mc\frac{d(\gamma\vec{\beta})}{dt} \\
=& mc\left[\frac{d\gamma}{dt}\vec{\beta} + \gamma\frac{d\vec{\beta}}{dt}\right] \\
=& mc\left[\gamma^3\beta\frac{d\beta}{dt}\vec{\beta} + \gamma\frac{d\vec{\beta}}{dt}\right]
\end{aligned} \tag{2.25}$$

making $\vec{\beta} = \beta\hat{\boldsymbol{u}}$, where $\hat{\boldsymbol{u}}$ is the direction unit vector, and making the inner product $\vec{F}\cdot\beta\hat{\boldsymbol{u}}$, then

$$\begin{aligned}
\vec{F}\cdot\beta\hat{\boldsymbol{u}} =& mc\left[\gamma^3\beta\frac{d\beta}{dt}\beta\hat{\boldsymbol{u}}\cdot\beta\hat{\boldsymbol{u}} + \gamma\frac{d\beta\hat{\boldsymbol{u}}}{dt}\cdot\beta\hat{\boldsymbol{u}}\right] \\
=& mc\left[\gamma^3\beta^3\frac{d\beta}{dt} + \gamma\beta\frac{d(\beta\hat{\boldsymbol{u}})}{dt}\cdot\hat{\boldsymbol{u}}\right] \\
=& mc\left[\gamma^3\beta^3\frac{d\beta}{dt} + \gamma\beta\left(\frac{d\beta}{dt}\hat{\boldsymbol{u}} + \frac{d\hat{\boldsymbol{u}}}{dt}\beta\right)\cdot\hat{\boldsymbol{u}}\right] \\
=& mc\gamma\beta\frac{d\beta}{dt}\left(\gamma^2\beta^2 + 1\right) \\
=& mc\gamma^3\beta\frac{d\beta}{dt},
\end{aligned} \tag{2.26}$$

taking $d\beta/dt$ from equation 2.26 and inserting it in equation 2.25

$$\begin{aligned}\vec{F} =& mc\left[\gamma^3\beta\frac{\vec{F}\cdot\hat{\boldsymbol{u}}}{mc\gamma^3}\beta\hat{\boldsymbol{u}}+\gamma\frac{d\vec{\beta}}{dt}\right]\\ \frac{\vec{F}}{mc} =& \beta^2\hat{\boldsymbol{u}}\frac{\vec{F}\cdot\hat{\boldsymbol{u}}}{mc}+\gamma\frac{d\vec{\beta}}{dt}\\ \frac{d\vec{\beta}}{dt} =& \frac{1}{\gamma mc}\left[\vec{F}-\beta^2\hat{\boldsymbol{u}}\left(\vec{F}\cdot\hat{\boldsymbol{u}}\right)\right],\end{aligned} \tag{2.27}$$

using the relation $ds = (ds/dt)dt = (c\beta)dt$, where ds is the differential pathlength associated to time dt, then

$$\frac{d\vec{\beta}}{ds} = \frac{1}{m\gamma\beta c^2}\left[\vec{F}-\beta^2\hat{\boldsymbol{u}}\left(\vec{F}\cdot\hat{\boldsymbol{u}}\right)\right], \tag{2.28}$$

changing $\vec{\beta} = \beta\hat{\boldsymbol{u}}$ and taking the inner product with $\hat{\boldsymbol{u}}$

$$\begin{aligned}\frac{d\vec{\beta}}{ds}\cdot\hat{\boldsymbol{u}} = \left(\beta\frac{d\hat{\boldsymbol{u}}}{ds}+\hat{\boldsymbol{u}}\frac{d\beta}{ds}\right)\cdot\hat{\boldsymbol{u}} =& \frac{1}{m\gamma\beta c^2}\left[\vec{F}-\beta^2\hat{\boldsymbol{u}}\left(\vec{F}\cdot\hat{\boldsymbol{u}}\right)\right]\cdot\hat{\boldsymbol{u}}\\ \frac{d\beta}{ds} =& \frac{1}{m\gamma\beta c^2}\left[\vec{F}\cdot\hat{\boldsymbol{u}}-\beta^2\left(\vec{F}\cdot\hat{\boldsymbol{u}}\right)\right],\end{aligned} \tag{2.29}$$

replacing equation 2.29 on equation 2.28

$$\frac{d\vec{\beta}}{ds} = \beta\frac{d\hat{\boldsymbol{u}}}{ds}+\hat{\boldsymbol{u}}\left\{\frac{1}{m\gamma\beta c^2}\left[\vec{F}\cdot\hat{\boldsymbol{u}}-\beta^2\left(\vec{F}\cdot\hat{\boldsymbol{u}}\right)\right]\right\} = \frac{1}{m\gamma\beta c^2}\left[\vec{F}-\beta^2\hat{\boldsymbol{u}}\left(\vec{F}\cdot\hat{\boldsymbol{u}}\right)\right], \tag{2.30}$$

then $d\hat{\boldsymbol{u}}/ds$ can be obtained

$$\begin{aligned}\frac{d\hat{\boldsymbol{u}}}{ds} =& \frac{1}{m\gamma\beta^2c^2}\left\{\left[\vec{F}-\beta^2\hat{\boldsymbol{u}}\left(\vec{F}\cdot\hat{\boldsymbol{u}}\right)\right]-\hat{\boldsymbol{u}}\left[\vec{F}\cdot\hat{\boldsymbol{u}}-\beta^2\left(\vec{F}\cdot\hat{\boldsymbol{u}}\right)\right]\right\}\\ \frac{d\hat{\boldsymbol{u}}}{ds} =& \frac{1}{m\gamma\beta^2c^2}\left[\vec{F}-\hat{\boldsymbol{u}}\left(\vec{F}\cdot\hat{\boldsymbol{u}}\right)\right],\end{aligned} \tag{2.31}$$

therefore, the equation of motion of a charged particle subjected to the Lorentz force is given by

$$\begin{aligned}\frac{d\hat{\boldsymbol{u}}}{ds} =& \frac{1}{m\gamma\beta^2c^2}\left[q(\vec{E}+c\beta\hat{\boldsymbol{u}}\times\vec{B})-\hat{\boldsymbol{u}}\left(q(\vec{E}+c\beta\hat{\boldsymbol{u}}\times\vec{B})\cdot\hat{\boldsymbol{u}}\right)\right]\\ \frac{d\hat{\boldsymbol{u}}}{ds} =& \frac{q}{m\gamma\beta^2c^2}\left[\vec{E}+c\beta\hat{\boldsymbol{u}}\times\vec{B}-\hat{\boldsymbol{u}}\left(\vec{E}\cdot\hat{\boldsymbol{u}}\right)\right],\end{aligned} \tag{2.32}$$

for the case of no electric field, the equation of motion in vacuum is

$$\frac{d\hat{\boldsymbol{u}}}{ds} = \frac{q}{m\gamma\beta^2c^2}\left[c\beta\hat{\boldsymbol{u}}\times\vec{B}\right]. \tag{2.33}$$

2.2.2.2 Implementation of an external magnetic field in Monte Carlo codes

Since there is no analytical solution of the Boltzmann transport equation in the presence of an external magnetic field, Bielajew proposed the superimposition of the transport in the magnetic field to the field-free case in the context of CH, as illustrated in figure 2.7. This imposes restrictions in the charged particle step, it must be short enough so that there is small energy loss and minimal change in the step direction [53]. In the Monte Carlo code, EGSnrc [48], the new direction of motion is given by

$$\Delta\vec{u} = \Delta\vec{u}_{\text{med}} + \Delta\vec{u}_{\text{em}}, \tag{2.34}$$

where $\Delta\vec{u}_{\text{med}}$ is the angular deflection due to elastic and inelastic scattering (in the field-free case) and $\Delta\vec{u}_{\text{em}}$ is the angular deflection due to the electromagnetic field. When there is no electric field, from equation 2.33, $\Delta\vec{u}_{\text{em}}$ is defined as

$$\Delta\vec{u}_{\text{em}} = \frac{q \cdot s}{m\gamma c^2 \beta_0^2}[c\beta_0 \vec{u}_0 \times \vec{B}], \tag{2.35}$$

with s the step path length and $\vec{u}_0$ the initial direction of motion. The final particle position is

$$\vec{r}_{f,\ em} = \vec{r}_0 + \vec{u}_0 s + \frac{s}{2}(\Delta\vec{u}_{\text{med}} + \Delta\vec{u}_{\text{em}}), \tag{2.36}$$

where $\vec{r}_0$ is the initial particle position.

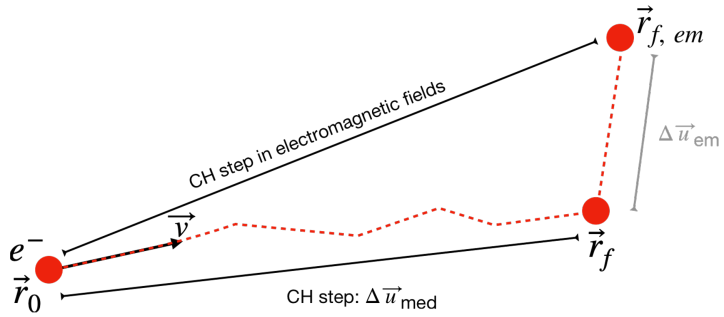

Figure 2.7 – Illustration of the CH step in EGSnrc.

The Monte Carlo simulations of particle transport in an electromagnetic field are slower than the field-free case. This limitation was overcome by Malkov and Rogers [54] by implementing an adaptive integration method in the transport algorithm method, where a one-point integration method (1-PI) is combined with a three-point integration method (3-PI). The 1-PI technique is used in the original EGSnrc algorithm under three assumptions complying with Bielajew approach: 1) small energy loss, 2) constant magnetic field, and 3) minimal change in the step direction. The 3-PI is used to account for energy loss and scattering, i.e., weakening assumptions 1 and 3 per step. This method is computationally slower, but it is more accurate than the 1-PI technique. The choice of the integration method depends on the step size: for the smaller step sizes, i.e. $|\Delta\vec{u}_{\text{em}} = 0.05|$, the 1-PI is chosen, and for larger step sizes, $|\Delta\vec{u}_{\text{em}} = 0.2|$, the 3-PI. This method is

implemented in the enhanced electromagnetic field macro in EGSnrc used in the simulations of this thesis.

2.2.3 Fano test

The Fano theorem [55] states that if a uniform source of uncharged particles irradiates an infinite medium with uniform atomic properties, then the secondary charged particle fluence is also uniform and independent of the density of the medium, as well as of the density variations from point to point [30]. In mathematical terms, since the fluence is constant, i.e. $\vec{\nabla}_r f = 0$, the left hand of the Boltzmann radiation transport equation (eq. 2.17), becomes

$$0 = \rho[S + I\{f; \vec{r}\}], \tag{2.37}$$

this equation is independent of the mass density.

Smyth et al [56] were the first to propose the reproduction of Fano conditions in Monte Carlo simulations to validate against a known theoretical value, to test the self-consistency of the radiation transport algorithm. In a Fano test, charged particle equilibrium (CPE) is created in an artificial experiment consisting of a cavity inside a phantom; the cavity material has the same atomic properties (i.e., cross-sections) as the phantom material but with different densities. The degree of agreement between the Fano test simulations and the analytical value is often referred to as the accuracy of the code [30, 57]. Historically, a 0.1% level of accuracy has been reached for cobalt and electrons beams with EGSnrc [58, 59, 60], and with PENELOPE [61].

2.2.3.1 Fano test in the presence of magnetic fields

Bouchard and Bielajew [45] demonstrated that in presence of a magnetic field, Fano's theorem is no longer valid. Under CPE conditions, $\vec{\nabla}_r f = 0$, then the

transport equation in magnetic fields (eq. 2.24) becomes

$$0 = \rho[S + I\{f;\vec{r}\}] + q(\hat{\boldsymbol{u}} \times \vec{B}) \cdot \vec{\nabla}_p f, \tag{2.38}$$

which is dependent of the density. In subsequent articles, Bouchard et al [57] and de Pooter et al [62] identified two special conditions where Fano's theorem is applicable in the presence of any magnetic field:

1. If the source is isotropic and spatially uniform. In this case, there are no restrictions on the magnetic field since it was proven that $q(\hat{\boldsymbol{u}} \times \vec{B}) \cdot \vec{\nabla}_p f = 0$ for any field, resulting in the conventional transport equation.
2. If the source is spatially uniform sources and the magnetic field scales with the mass density, i.e. $\vec{B} = \rho \vec{B}_m$. In this case, the transport equation becomes

$$0 = S + I\{f;\vec{r}\} + q(\hat{\boldsymbol{u}} \times \vec{B}_m) \cdot \vec{\nabla}_p f, \tag{2.39}$$

   which is independent of density.

These special conditions can be applied to benchmark the Monte Carlo simulations in the presence of magnetic fields.

2.3 Radiation dosimetry

2.3.1 Radiation detectors

A radiation detector or dosimeter provides a reading M that is, ideally, proportional to the absorbed dose in the detector sensitive volume, D_{det}. However, most detectors exhibit a degree of non-linearity between M and D_{det} over a dose range [30, 63]. Among the desired properties of a dosimeter in RT are [30, 63]:

1. Signal (light, charge, temperature rise, among others) proportional to the absorbed dose.
2. High spatial resolution - the smaller the sensitive volume, the higher is the spatial resolution.

3. Reproducibility or precision, i.e. small standard deviation in a set of measurements.
4. Stability with time, some detectors deteriorate with time because of storage conditions (temperature changes, humidity, light, etc.).
5. Portability to facilitate the regular measurements required for the linac quality assurance and calibration procedures.

The choice of detectors depends on the conditions of measurements. In RT, ionization chambers are by far the most widely used because of their repeatability, stability, linearity and portability [30]. Solid-states detectors are also commonly used for small photon beams dosimetry that are usually between 4×4 cm^2 and 0.3×0.3 cm^2 [64, 65].

2.3.1.1 Ionization chambers

An ionization chamber is a gas-filled detector, usually air, designed to collect the ion-pairs created by the interaction of the radiation with the air cavity [30, 63]. There are several types of ionization chambers, such as the free-air chambers used in primary standard laboratories to measure air kinetic energy released per unit mass (kerma), parallel-plate chambers used at lower photon energy and in electron beams, and cavity chambers used widely in reference dosimetry [30, 63]. In this thesis, only cavity chambers types are used.

A cavity chamber and its essential components are illustrated in figure 2.8. When a chamber is irradiated with a photon beam, the secondary electrons ionize the air in the cavity, creating a number of electron-ion pairs proportional to the energy deposited. The electrons are accelerated towards the anode and the ions to the cathode by an electric potential - typically between 200 V to 400 V - applied to the chamber wall or to the collector, depending on the model [30, 63]. These charges are collected by the central electrode connected to an electrometer. The measured current is proportional to the sensitive volume and to the radiation dose [30, 63]. Ionization chambers should be calibrated regularly in a standard laboratory and

submitted to quality control test to ensure their optimal operation [30, 63].

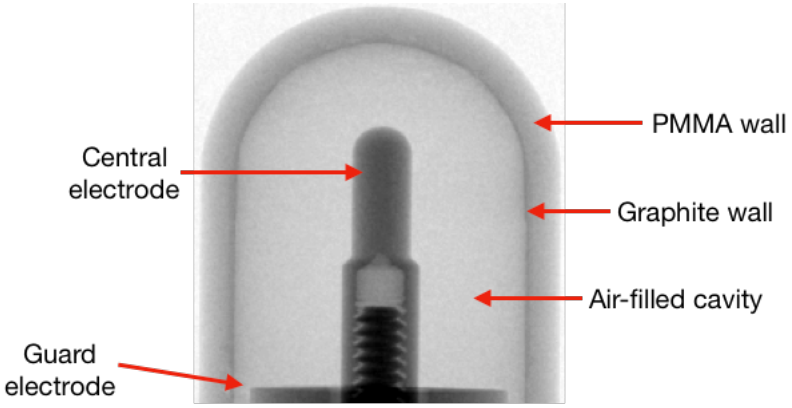

Figure 2.8 – Example of a cavity ionization chamber: micro-CT image of semiflex PTW31010. The main components are indicated: central and guard electrodes, air-filled cavity, graphite and PMMA wall.

Among the cavity chambers, there are different types, models, and sizes. For instance, there are three types of wall shapes: spherical, cylindrical and thimble. They have axial symmetry with respect to the rotation of the central electrode. Although, there can be an intra-type variation due to manufacturing imperfections and mechanical tolerances, leading to chamber response sensitive to orientation.

2.3.1.2 Solid-state detectors

There is a wide variety of solid-state detectors: thermoluminescence dosimeters, scintillators, semiconductor diodes, diamond detectors, among others [30]. In this work, the two detectors of interest are a silicon diode and a diamond detector. In the following, their operation is briefly explained.

The silicon diode consists of an n-type (excess of electrons) silicon layer and a p-type (excess of holes) silicon layer. These layers create a depletion region since electrons diffuse to the p-type layer and holes to the n-type layer, as shown in figure 2.9. The incident radiation generates electron-hole pairs in the depletion layer, electrons moving towards the p-type region generates a current proportional to the incident radiation that is measured by an electrometer [30].

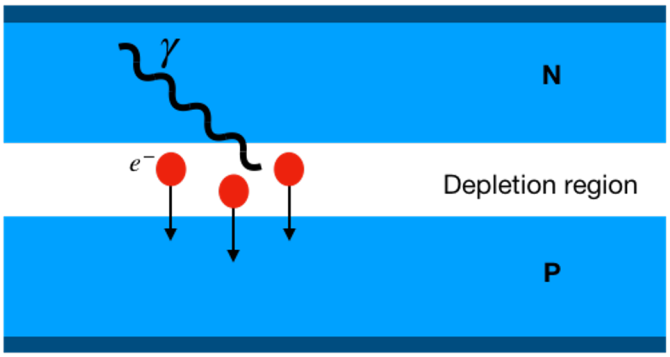

Figure 2.9 – Schematic of a p-n junction in a diode. Electrons generated by the radiation in the depletion region move towards the positive region, creating a current proportional to the incident radiation.

Silicon diodes have a small sensitive volume (< 0.2 mm^3), making them ideal for small field dosimetry. However, silicon diodes present some limitations: they show a degree of angular dependence due to their design and materials, they over-respond to low-energy photons, and they have a limited lifetime [30].

The diamond detector has a similar detection principle as the silicon diode. Diamonds are natural semiconductors; their intrinsic impurities (boron, nitrogen, aluminum, and others) make them natural p-type or n-type diodes. The incident radiation creates electron-hole pairs that move towards their corresponding region, and the generated proportional current is measured by an electrometer [30].

Diamond detector sensitive volumes can be very small (~ 0.004 mm^3) and since they are also composed of low-Z materials, they are attractive detectors for small field dosimetry. They have high sensitivity and their response is quasi-independent of energy, direction, and temperature [30].

2.3.1.3 Cavity theory

The ionization chamber signal is proportional to the mean absorbed dose in the detector sensitive volume, D_{det}. In radiation dosimetry, the detector can be considered a cavity of a certain material, usually air for the ionization chambers, inside a uniform medium of interest, usually water. The presence of the detector perturbs the mean absorbed dose to medium because it has different atomic com-

position and density than the medium. Cavity theory provides a link between D_{det} and the unperturbed absorbed dose to medium D_{med}, by determining the factor $f_{\text{med, det, Q}}$ defined as

$$f_{\text{med, det, Q}} = \left(\frac{D_{\text{med}}}{D_{\text{det}}}\right)_Q, \tag{2.40}$$

where Q is the beam quality. In general, there is no analytical method to calculate D_{det} or D_{med} hence Monte Carlo calculations are used to determine $f_{\text{med, det, Q}}$.

Under CPE, the absorbed dose to medium is related to charged particle fluence in the medium f_e

$$D_{\text{med}} \overset{\text{CPE}}{=} \int_0^{E_{max}} f_e(E) \left[\frac{S_{\text{el}}(E)}{\rho}\right]_{\text{med}} dE, \tag{2.41}$$

where $\left[\frac{S_{\text{el}}(E)}{\rho}\right]_{\text{med}}$ is the unrestricted mass electronic stopping power for the medium and $f_e(E)$ is the differential electron fluence in the medium.

Bragg-Gray cavity theory

Considering a homogeneous medium containing a cavity of low-density material and irradiated by a photon beam, the Bragg-Gray cavity theory imposes two conditions:

1. The cavity must be small relative to the electron ranges, in such a way that the electron fluence is not perturbed.
2. The absorbed dose in the cavity is deposited entirely by the charged particles crossing it and not created from a photon interaction inside the cavity.

Then, inserting equation 2.41 in the relationship 2.40 under Bragg-Gray conditions, that is $[f_e(E)]_{\text{det}} = [f_e(E)]_{\text{med}}$, gives

$$f_{\text{med, det, Q}} = \frac{D_{\text{med}}}{D_{\text{det}}} = \frac{\int_0^{E_{max}} [f_e(E)]_{\text{med}} \left[\frac{S_{el}(E)}{\rho}\right]_{\text{med}} dE}{\int_0^{E_{max}} [f_e(E)]_{\text{med}} \left[\frac{S_{el}(E)}{\rho}\right]_{\text{det}} dE} \tag{2.42}$$

The Bragg-Gray theory is limited as it assumes a local energy deposition of all electrons and does not consider the energy loss by the delta rays [30].

Spencer-Attix cavity theory

Spencer and Attix [66] improved the Bragg-Gray cavity theory by considering the total electron fluence incident on the cavity (and not only the primary as before) and by using the restricted stopping power with cut-off energy, Δ, related to the cavity size. In RT, $\Delta \approx 10 - 15$ keV is enough energy for electrons to cross the air cavities of standard ionization chambers [30].

An additional term was added later on by Nahum [67] to account for the energy deposition as the electron energy drops from Δ to 0 - the so-called track end term. The full expression of the Spencer-Attix cavity theory for the dose to a detector is

$$D_{\text{det}} = \int_{\Delta}^{E_{max}} [f_e^{\text{tot}}(E)]_{\text{med}} \left[\frac{L_{\Delta}(E)}{\rho}\right]_{\text{det}} dE + [f_e^{\text{tot}}(\Delta)]_{\text{med}} \left[\frac{S_{el}(\Delta)}{\rho}\right]_{\text{det}} \Delta \tag{2.43}$$

where $\left[\frac{L_{\Delta}(E)}{\rho}\right]_{\text{det}}$ is the mass electronic stopping power restricted to losses smaller than Δ. In the Spencer-Attix theory the factor f_Q given by equation 2.40 becomes

$$f_{\text{med, det, Q}} = \frac{\int_{\Delta}^{E_{max}} [f_e^{\text{tot}}(E)]_{\text{med}} \left[\frac{L_{\Delta}(E)}{\rho}\right]_{\text{med}} dE + [f_e^{\text{tot}}(\Delta)]_{\text{med}} \left[\frac{S_{el}(\Delta)}{\rho}\right]_{\text{med}} \Delta}{\int_{\Delta}^{E_{max}} [f_e^{\text{tot}}(E)]_{\text{med}} \left[\frac{L_{\Delta}(E)}{\rho}\right]_{\text{det}} dE + [f_e^{\text{tot}}(\Delta)]_{\text{med}} \left[\frac{S_{el}(\Delta)}{\rho}\right]_{\text{det}} \Delta}. \tag{2.44}$$

2.3.2 Reference dosimetry protocols

2.3.2.1 Standard reference dosimetry protocols

Dosimetry protocols and code of practice provide uniform procedures for beam calibration to ensure the accurate delivery of the prescribed dose. They follow a general formalism, first for the calibration of the ionization chamber and the beam calibration after. The AAPM has established standard protocols for beam calibration since the early 1960s. In 1983, task group 21 (TG-21) published an absorbed dose protocol [68] using an ionization chamber calibrated with air kerma calibration factor in a ^{60}Co beam considering the perturbation factors introduced by the detector.

Another standard protocol from AAPM was published in 1999, the TG-51 [31]. It is based on an absorbed dose to water calibration factor for the ionization chamber. This allows an easier user implementation by avoiding the calculation of theoretical dosimetry factors to convert to absorbed dose to water and a significant improvement in uncertainty reduction [10]. In the following, this protocol for megavoltage photon beams is described.

Ionization chambers are calibrated in terms of absorbed dose to water in a reference ^{60}Co beam in a primary standards laboratory or in a secondary standards dosimetry laboratory. At the standards laboratory, a calibration coefficient $N_{D,w}^{^{60}Co}$ is determined in reference conditions by comparing the chamber reading, M, to the known value of the absorbed dose of the reference beam. The calibration coefficient is defined as

$$N_{D,w}^{^{60}Co} = \frac{D_w^{^{60}Co}}{M}, \tag{2.45}$$

where $N_{D,w}^{^{60}Co}$ has units of Gy/C, M is the electrometer reading in Coulombs, corrected for pressure, temperature, humidity, ion recombination, polarity, and electrometer calibration effects. According to the reference conditions of the TG-51,

the detector is placed at 10 cm depth, with a source-to-surface distance (SSD) of 100 cm and an irradiation field of 10 × 10 cm^2 at the surface, as shown in figure 2.10.

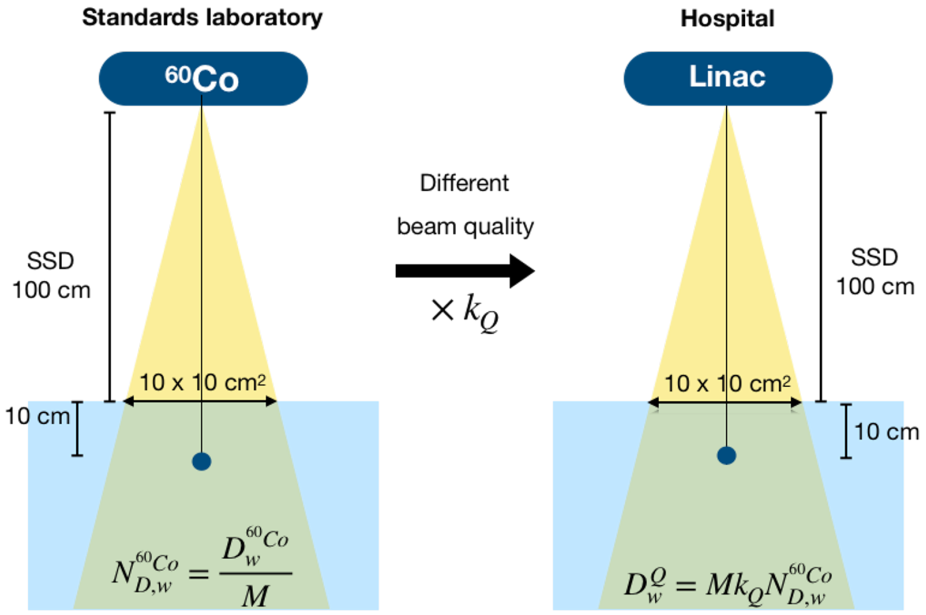

Figure 2.10 – Schematic of general formalism for reference dosimetry. On the left, the calibration of an ionization chamber in a standards laboratory, where the calibration coefficient is determined. On the right, the calibration of a clinical beam with a different beam quality. Both absorbed dose to water measurements are performed under the same reference conditions, using the SSD set up in this case.

In the clinical linacs, the beam quality is usually different than that of the standards laboratory. In the TG-51, the beam quality is specified by the photon beam percentage depth dose (PDD) at 10 cm depth, or $\%dd(10)_x$, in a 10 × 10 cm^2 field at the surface with SSD=100 cm, the experimental setup is shown in figure 2.10. It is worth noting that $\%dd(10)_x$ only corresponds to the photon component, i.e., the effects of electron contamination in the beam are excluded. This is particularly important for photon beams with higher energies (>10 MeV) where the electron contamination must be reduced using a 1 mm lead foil placed about 50 cm from the surface phantom while measuring the $\%dd(10)_x$. For the smaller beam ener-

gies, the lead foil is not necessary and the $\%dd(10)_x$ measurements are performed in the open beam. The $\%dd(10)_x$ is related to the beam quality correction factor, k_Q, accounting for the variation of absorbed-dose to water between the calibration beam and the beam of interest. The absorbed dose to water is defined as:

$$D_w^Q = M k_Q N_{D,w}^{^{60}Co}, \tag{2.46}$$

with M the fully corrected charge reading defined as

$$M = P_{\text{ion}} P_{\text{TP}} P_{\text{elec}} P_{\text{pol}} M_{\text{raw}}, \tag{2.47}$$

with M_{raw} the raw measurement of the charge [C] and correction factors defined below:

- P_{TP} is the temperature-pressure correction factor which accounts for variation of air mass inside the chamber due to environmental, i.e., temperature and pressure conditions with respect to the standards laboratory conditions. It is defined as

  $$P_{\text{TP}} = \frac{273.2+T}{273.2+22.0}\frac{101.3}{P}, \tag{2.48}$$

  with P the room pressure and T the water temperature - the chamber should be in thermal equilibrium with the water
- P_{ion} corrects for incomplete ion collection because of opposite charges recombination or due to saturation of the chamber [5]. For pulsed beams, where the linear form of the saturation curve is valid (i.e. P_{ion} <1.05), the factor is approximated by

  $$P_{\text{ion}}(V_H) = \frac{1 - V_H/V_L}{M_{\text{raw}}^H/M_{\text{raw}}^L - V_H/V_L}, \tag{2.49}$$

with V_H the normal operating voltage, V_L the reduced voltage (usually, $V_H/2$), and $M_{\text{raw}}^{H/L}$ the corresponding raw charge measurements.

- P_{elec} is the electrometer calibration factor. $P_{\text{elec}} = 1.00$ if the chamber and electrometer are calibrated together.
- P_{pol} corrects for polarity effects, i.e. under identical irradiation conditions the ionization chamber could give different readings for potentials of opposite polarity. This can be caused by distortions of the electric field inside the sensitive volume or by differences in mobility between positive and negative ions, or by Compton currents which are the radiation induced currents in the chamber structural components [5]. The mathematical definition is

$$P_{\text{pol}} = \frac{M_{\text{raw}}^{+} - M_{\text{raw}}^{-}}{2M_{\text{raw}}}, \tag{2.50}$$

with $M_{\text{raw}}^{\pm}$ the raw charge measurement when $\pm$ charge is collected.

2.3.2.2 Nonstandard reference dosimetry protocols

In some new RT techniques, beams are referred to as nonstandard because they do not fulfill the reference conditions of the standard absorbed dose protocols. In these beams, dosimetry errors can be considerably larger than in conventional beams [69]. In 2008, the IAEA, in collaboration with AAPM, proposed a new formalism [69] for the dosimetry of nonstandard beams, which includes a new correction factor. The protocol considers two routes traceable to a broad beam:

1. For small static-field dosimetry in which the conventional reference conditions cannot be established, an intermediate reference field known as *machine-specfic reference* (msr) field is introduced.
2. In composite-field dosimetry, i.e. combination of small fields forming an overall field with an extended area or volume or 4D delivery sequence [30], an intermediate reference field known as *plan-class specific reference* (pcsr) field is introduced. The pcsr field must be closer to patient-specific field, and provide a uniform dose over a region large enough to cover a reference

detector.

In the first route, illustrated on the left side of figure 2.11, the absorbed dose to water at the reference depth in a beam of quality Q_{msr} is given by

$$D_{w,Q_{msr}}^{f_{msr}} = M_{Q_{msr}}^{f_{msr}} N_{D,w,Q_0} k_{Q,Q_0} k_{Q_{msr},Q}^{f_{msr},f_{ref}}, \tag{2.51}$$

where $M_{Q_{msr}}^{f_{msr}}$ is the charge reading in the msr field corrected for the influence quantities as in the protocol TG-51, N_{D,w,Q_0} is the calibration coefficient in terms of absorbed dose to water for an ionization chamber at a reference beam quality Q_0, usually measured in a in a 10×10 cm^2 field, k_{Q,Q_0} is the beam quality correction factor for the differences between the reference beam quality at the standards laboratory and the beam quality Q of the conventional reference field, and $k_{Q_{msr},Q}^{f_{msr},f_{ref}}$ is the correction factor for the difference between the conditions of field size, geometry, phantom material compared to beam quality of the conventional reference field and the machine-specific reference field [69].

The factor $k_{Q_{msr},Q}^{f_{msr},f_{ref}}$ accounts for the difference between the responses of an ionization chamber in the fields f_{ref} and f_{msr} and is given by

$$k_{Q_{msr},Q}^{f_{msr},f_{ref}} = \frac{D_{w,Q_{msr}}^{f_{msr}} / M_{Q_{msr}}^{f_{msr}}}{D_{w,Q}^{f_{ref}} / M_{Q}^{f_{ref}}}. \tag{2.52}$$

In the second route, illustrated on the right side of figure 2.11, a pcsr field is used. The absorbed dose to water $D_{w,Q_{pcsr}}^{f_{pcsr}}$ at the reference depth in a beam of quality Q_{pcsr} and reference field f_{pcsr} is given by

$$D_{w,Q_{pcsr}}^{f_{pcsr}} = M_{Q_{pcsr}}^{f_{pcsr}} N_{D,w,Q_0} k_{Q,Q_0} k_{Q_{pcsr},Q}^{f_{pcsr},f_{ref}}, \tag{2.53}$$

the factor $k_{Q_{pcsr},Q}$ is defined as in equation 2.52 but with a pcsr field instead of a mrs field.

Currently, there are no dosimetry protocols or CoP available for reference

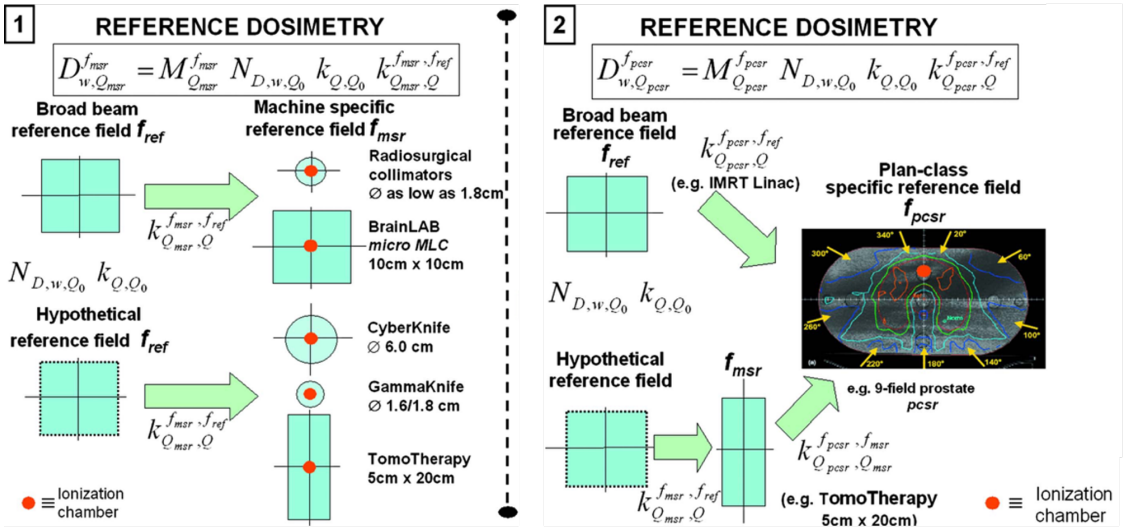

Figure 2.11 – Schematic overview of the dosimetry of 1) small static field with reference to a msr field on the left, and 2) nonstandard composite fields with reference to a plan-class specific reference field. Modified from reference [69].

dosimetry in the presence of a magnetic field. It has been suggested that ideally, these protocols could be developed as an add-on to the existing dosimetry protocols or CoP for conventional linacs [26]. A review of reference dosimetry in the presence of magnetic fields is described in the following section.

2.3.3 Towards reference dosimetry in the presence of magnetic fields

Before stating the general formalism for reference dosimetry in magnetic fields, different aspects of the magnetic field effect on dose measurements are described.

2.3.3.1 MRI-Linac design

Reference conditions, typically a 10 × 10 cm^2 at the isocenter or at the surface and an SSD setup between 90 and 110 cm [31], cannot be achieved in the commercially available MRI-Linacs. In the Elekta Unity® MRI-linac, the bore is 70 cm wide, and the source-to-isocenter distance (SID) is 143.5 cm. Similarly, in the ViewRay MRIdian® device, the width of the bore is 70 cm, and the SID is 105 cm for the linac version and 90 cm for the ^{60}Co version[26].

2.3.3.2 Effect of the magnetic field on the irradiation beam

The impact of the magnetic field on the irradiation beam depends on the configuration between them, as shown in figure 2.12. There is a more significant impact when the magnetic field is perpendicular to the photon beam than when they are parallel [35]. In the calibrations of the MRI-linac, the beam is perpendicular to the magnetic field.

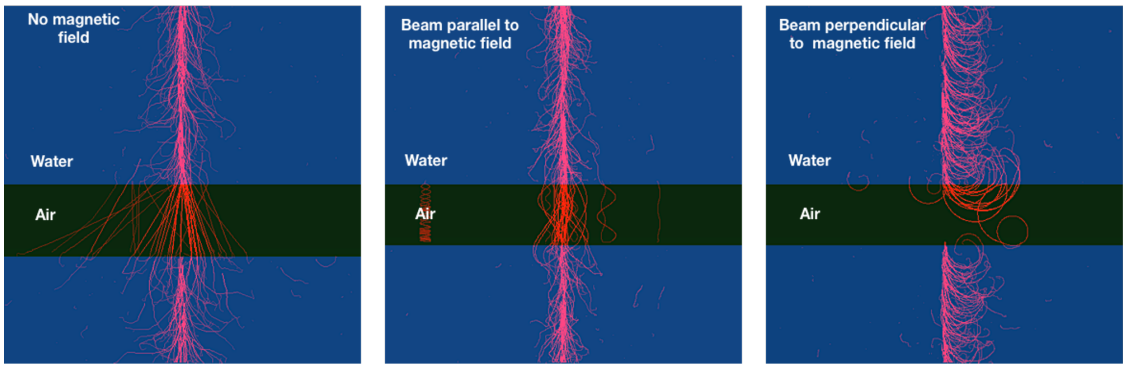

Figure 2.12 – Illustration of the impact of the magnetic field orientation on the secondary electrons, using a pencil 6 MeV photon beam. On the left, no magnetic field is present. In the middle, the magnetic field is parallel to the irradiation beam. On the right, the magnetic field is perpendicular to the irradiation beam.

In the right side of figure 2.12, secondary electrons are travelling through water and encounter an air slab. They return to the water region because of the Lorentz force and the change in density. This is the so-called electron return effect, first described by Raaijmakers et al [13]. In a low-density medium, such as air, the electron mean free path is long compared to the gyration radius, so the electrons can curl more without interacting than in a high-density medium where the mean free path is smaller [13]. Due to ERE, an extra dose deposition occurs near the high and low-density interfaces. On the contrary, dose deposition behind the low-density region decreases because fewer electrons cross it [13]. The impact on dose distribution depends on the magnetic field strength, electron energies, field size, the obliquity of the interface, and gap size [24]. Although the ERE is not relevant in reference dosimetry because the point of measurement is far from the phantom

boundaries. ERE can occur in the interfaces between the detector and the phantom.

Other characteristics changing in a reference field, 10×10 cm^2, due to the magnetic field are [26]:

1. A reduction in thickness of the build-up region since electrons deposit their energy closer to the photon interaction point. Also, there are fewer contamination electrons (created by interactions in other parts of the MR-Linac) arriving at the surface [1] because they are likely to curl back following the Lorentz force [70, 71, 72, 73].
2. Higher dose area at the beam exit because of ERE in the exit region [13, 74, 71, 72]
3. Lateral asymmetry in dose profiles in the direction of the Lorentz force [70].
4. The depth dose distributions changes since electrons deposit their energy closer to the photon interaction point resulting in a reduction of absorbed dose in magnetic fields [75, 76].

the magnitude of the four listed changes depends on the magnetic field strength.

2.3.3.3 Effect of the magnetic field on detector response

The presence of the magnetic field modifies the detector response. The characterization of different types of detectors for reference dosimetry measurements in MRI-linacs has been under investigation by several groups [35, 77, 75, 78, 40, 79, 39, 80, 81, 41]. However, the magnetic field effect has not been fully understood and described [26].

The orientation of the detector with respect to the magnetic field significantly impacts the detector response. In conventional reference dosimetry, the detector is placed perpendicular to the irradiation beam. However, in an MRI-linac, the detector can be placed in four ways with respect to the magnetic field and remaining

1. This is an aspect where the in-line MRI-linacs differ significantly from the orthogonal systems. The magnetic field actually channels contaminant electrons onto the patient, increasing the surface dose.

perpendicular to the photon beam, although for symmetry, there are only three different orientations, as shown in figure 2.13. In these, the electrons, on average, are deflected towards different components, impacting the detector response differently.

Meijsing et al [35] were the first to evaluate the impact of the magnetic field on the response of an ionization chamber Farmer NE2571. In their setup, the magnetic field is perpendicular to the radiation beam, and two orientations of the ionization chamber were studied: 1) the chamber axis is perpendicular to the magnetic field and to the radiation beam and 2) the chamber axis is parallel to the radiation beam and perpendicular to the magnetic field. The chamber response was measured as a function of the magnetic field strength, between 0 and 2 T. In configuration 1, the chamber response initially increased up to 8% and beyond 1 T, it slowly decreased. The opposite occurred in the second configuration: the response initially decreased and increased after the 1 T; the most significant variation was 11%.

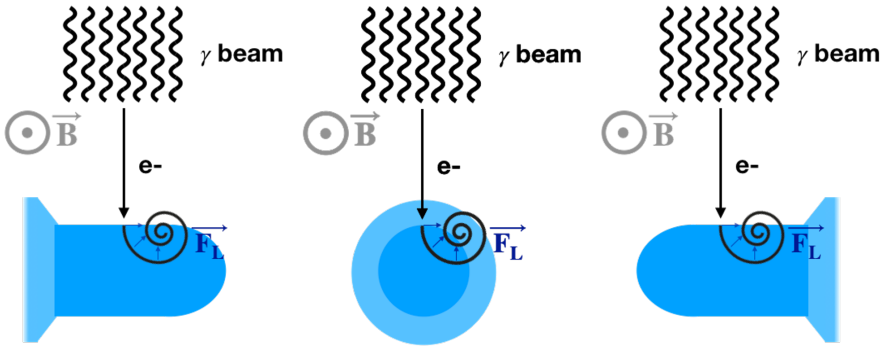

Figure 2.13 – Detector orientations in reference dosimetry where the beam is always perpendicular to the magnetic field. On the left, the detector axis is perpendicular to the beam with the Lorentz force pointing towards the tip. In the middle, the detector axis is parallel to the magnetic field. On the right, the detector axis is perpendicular to the beam with the Lorentz force pointing towards the stem.

The magnetic field enhances the sensitivity of detector response to design details that appear insignificant in conventional conditions. This is especially important in Monte Carlo calculations of quality correction factors. The MC model must be as accurate as possible, and in particular, the presence of dead volumes inside the

sensitive volume must be accounted for [40, 79, 39, 41].

Another relevant issue is the potential presence of air gaps surrounding the detector partially or totally, as shown in figure 2.14. The air gaps can occur between a non-waterproof chamber and its water-proof sleeve or between a chamber and a solid water phantom. Several groups [36, 54, 38, 37] have shown that these air gaps can strongly affect the chamber response in an external magnetic field, contrary to conventional reference dosimetry where the effect of the air gaps is negligible.

(a) Symmetrical air gap. **(b)** Asymmetrical air gap.

Figure 2.14 – Illustration of the modeled air gaps surrounding the chamber.

The formation of air gaps is random; their location, distribution and size are usually unknown. Hackett et al [36] were the first to point out variations of 0.7%-1.2% on detector response due to the presence of air gaps of 0.1 mm and 0.2 mm between the chamber and its water sleeve. Malkov et al [54] showed a variation of up to 1% on chamber response due to air gaps (0.5 mm and 1.0 mm) for multiple magnetic field strengths. Agnew et al [38] studied the effect of air gap position around the chamber; for the Farmer-type chamber, a variation of 3.8% on chamber response was found for asymmetrical air gaps of 0.3 mm thickness. Finally, O'Brien et al [37] investigated the effect of air gap shape, either symmetrical or asymmetrical, showing variations within 0.5% on chamber response for symmetrical air gaps with thicknesses: 0.2, 0.6, 1.0 and 1.4 mm and variations of up to 1.6% for asymmetric air gaps.

2.3.3.4 Generalized formalism

Some efforts have been attempted to adapt the standard, and nonstandard dosimetry protocols for reference dosimetry in a magnetic field [82, 75, 76]. Smit et al [82] proposed the adaptation of standard dosimetry protocols [31, 33] by correcting the effect of the magnetic field on the chamber reading. However, this approach is problematic since it neglects the influence of the magnetic field on local dose distribution and on detector response [76, 57].

The beams of MRI-linacs can be considered as nonstandard beam since CPE cannot exist in heterogeneous geometries in the presence of a magnetic field [45]. The formalism proposed by Alfonso et al [69] could be adapted to perform dosimetry in MRI-linacs. To consider the magnetic field effect, O'Brien et al [75] proposed to add a correction factor, $k_{Q_{msr}}^{B,f_{msr}}$, in the original equation (eq. 2.51) of Alfonso formalism. In the presence of a magnetic field, the absorbed dose to water $D_{w,Q_{msr}}^{B,f_{msr}}$ for the field f_{msr} with beam quality Q_{msr} is given by:

$$D_{w,Q_{msr}}^{B,f_{msr}} = M_{Q_{msr}}^{f_{msr}} N_{D,w,Q_0} k_{Q_{msr}}^{B,f_{msr}}, \tag{2.54}$$

where $k_{Q_{msr}}^{B,fmsr}$ is a correction factor for both beam quality and magnetic field, it is defined as:

$$k_{Q_{msr}}^{B,fmsr} = k_{Q,Q_0} k_{Q_{msr},Q}^{f_{msr},f_{ref}} k_B^{Q_{msr}}. \tag{2.55}$$

$k_B^{Q_{msr}}$ is the correction factor accounting for the magnetic field effect in the ionization chamber dose response, it is defined as:

$$k_B^{Q_{msr}} = \frac{D_{w,Q_{msr}}^{B,f_{msr}} / M_{Q_{msr}}^{B,f_{msr}}}{D_{w,Q_{msr}}^{f_{msr}} / M_{Q_{msr}}^{f_{msr}}}. \tag{2.56}$$

The correction factor $k_{Q_{msr}}^{B,f_{msr}}$ can be determined via Monte Carlo calculations,

assuming that W/e is constant with B and Q. O'Brien et al [75] did the calculation for six commercial Farmer type ionization chambers using the software GEANT4. The chambers were positioned at a depth of 10 cm in a 30 x 30 x 30 cm^3 water phantom at the isocenter of the Elekta MRI-linac. The absorbed dose in each chamber was calculated with and without the magnetic field of 1.5 T, to determine $k_{Q_{msr}}^{B,f_{msr}}$ according to equation 2.56. In the same study, four chamber orientations were considered: the chamber parallel to the field lines pointing in both directions and the chamber perpendicular to the field lines pointing in both possible directions.

Their results showed a clear dependence on the orientation; the parallel orientation presented the smallest corrections (<1%). In fact, two chambers - NE2571 without the waterproof sleeve and PTW30011 - did not require correction in this orientation. On the contrary, correction in the clockwise perpendicular orientation averaged 3.9% with a standard deviation of 0.2%. The counter-clockwise perpendicular orientation averaged 3.0% with a greater standard deviation of 0.7%; the increased variation is probably due to the design since the secondary electrons produced in the chamber stem deposit their energy in the sensitive volume [75].

The next chapter correspond to the introduction of the first article where quality correction factors accounting for the effect of the magnetic field are calculated for four small-cavity ionization chamber in two different configuration.

CHAPTER 3

INTRODUCTION TO ARTICLE 1

3.1 Context

With the advent of MRI-linacs, definitive dosimetric machine calibration and other dosimetric measurements relevant for machine commissioning must be performed in the presence of magnetic fields. Since 2009, several groups have investigated the magnetic field impact on ionization chamber dose-response via experimental measurements, and Monte Carlo simulations [35, 82, 77, 75, 54, 40, 39]. Most of the investigations focus on Farmer-type chambers, commonly used in reference dosimetry measurements. This investigation focuses on the magnetic field effects in small-cavity ionization chambers used for small field dosimetry measurements. As RT treatments with MRI-linac evolve, treatments using small fields will become routinely used in the clinic.

Monte Carlo calculations are crucial to determine quality correction factors for reference dosimetry, i.e. definitive machine calibration. For this reason, it is necessary to have accurate Monte Carlo models of ionization chambers. The charge collection efficiency in ionization chambers depends on the configuration of the electric field in the sensitive volume of the chamber. Therefore, the collection is not uniform. In fact, in chambers commonly used in reference dosimetry, there is a region near the guard electrode without charge collection, i.e. a dead volume. In recent years, it has been found that accurate modelling of the effective collecting volume, i.e., removing the dead volume, is essential to have good agreement between experimental measurements and Monte Carlo calculations of detector dose-response in the presence of magnetic fields [40, 83, 39].

Several approaches have been used to define the dead volume. For instance, cylindrical volumes of different thicknesses (Malkov and Rogers [79]) or different radius (Spindeldreier et al [40]) near the guard electrode were removed from the

sensitive volume to account for the dead volume.

A more exact approach was provided by Ross [84], who proposed to simulate the electric field inside the mechanical volume and to exclude the volume where the electric field lines go from the guard electrode to the cavity wall. Pojtinger et al [39] apply this methodology to define the dead volume inside the Farmer chamber PTW30013. The shape of the dead volume is a torus rather than a cylinder. Monte Carlo simulations of quality correction factors, k_{Q_B} were performed with and without the dead volume. The exclusion of the dead volume improved the agreement between measured k_{Q_B} and simulated k_{Q_B} from 1.44% to 0.1%.

The study presented herein uses the same methodology to determine the dead volume inside the small-cavity ionization chambers. The objectives of this work are:

1. To characterize small-cavity detector response in the presence of magnetic fields using four commercial ionization chambers in two experimental configurations.
2. To determine the effective sensitive volume in the chamber.
3. To calculate quality correction factors, $k_{Q_B,Q}^{f_B,f}$.
4. To provide a detailed uncertainty budget for $k_{Q_B,Q}^{f_B,f}$.

3.2 Uncertainty budget

In the article, an uncertainty budget is proposed. In this section, the definition of the terms is provided in more detail. In particular, the mathematical derivations of the experimental setup uncertainty, σ_{setup}, and of the uncertainty associated to the Fano test σ_{Fano} are given.

3.2.1 Definitions

The experimental absorbed dose is

$$D_{\text{exp}}(B) = \langle D_{\text{exp}}(B) \rangle + \delta_{\text{rep}}(B) + \delta_{\text{setup}}(B), \tag{3.1}$$

and the MC simulated absorbed dose is

$$D_{\text{num}}(B) = \langle D_{\text{num}}(B)\rangle + \delta_{\text{stat}}(B) + \delta_{\text{Fano}}(B) + \delta_{\text{data}} + \delta_{\text{geom}}(B) \tag{3.2}$$

with δ all random variables from the different sources of uncertainties:

1. $\delta_{\text{rep}}(B)$: error associated with measurement repeatability, assumed dependent of the set value of magnetic field B.
2. $\delta_{\text{setup}}(B)$: error associated with measurement setup error, one portion independent of B and the other symmetric with respect to the sign of B.
3. $\delta_{\text{stat}}(B)$: statistical uncertainty from MC simulation, assumed dependent of the set value of magnetic field B
4. $\delta_{\text{Fano}}(B)$: algorithmic error from MC simulation, assumed dependent of B.
5. δ_{data}: error caused by data, such as stopping-power and other cross-sections.
6. $\delta_{\text{geom}}(B)$: error cause by difference between blueprints and actual chamber design, as well as the error on the determined dead volume assumed dependent of the set value of magnetic field B.

3.2.2 Absorbed dose ratio relative to dose in the absence of magnetic fields

The following is an approximation, but probably good enough considering the estimates involved. Since the cross-terms are uncorrelated they are zero, then the ratio of numerical absorbed dose with and without magnetic fields is

$$\begin{aligned} r_{\text{num}}(B) =& \frac{\langle D_{\text{num}}(B)\rangle + \delta_{\text{stat}}(B) + \delta_{\text{Fano}}(B) + \delta_{\text{data}}(B) + \delta_{\text{geom}}(B)}{\langle D_{\text{num}}(0)\rangle + \delta_{\text{stat}}(0) + \delta_{\text{Fano}}(0) + \delta_{\text{data}}(0) + \delta_{\text{geom}}(0)} \\ \approx& \langle r_{\text{num}}(B)\rangle + \epsilon_{\text{stat}}(B) + \epsilon_{\text{Fano}}(B) + \epsilon_{\text{data}}(B) + \epsilon_{\text{geom}}(B), \end{aligned} \tag{3.3}$$

and the ratio of experimental absorbed dose with and without magnetic fields is

$$\begin{aligned} r_{\mathrm{exp}}(B) =& \frac{\langle D_{\mathrm{exp}}(B)\rangle + \delta_{\mathrm{rep}}(B) + \delta_{\mathrm{setup}}(B)}{\langle D_{\mathrm{exp}}(0)\rangle + \delta_{\mathrm{rep}}(0) + \delta_{\mathrm{setup}}(0)} \\ \approx& \langle r_{\mathrm{exp}}(B)\rangle + \epsilon_{\mathrm{rep}}(B) + \epsilon_{\mathrm{setup}}(B) \end{aligned} \tag{3.4}$$

with ϵ all random variables from the different sources of uncertainties (the same as above). Considering the following simplifications on the dependence of the errors ϵ on the strength of the magnetic field B:

1. ϵ_{stat}: statistical error from simulation.
2. ϵ_{Fano}: algorithmic error from simulation, assumed independent of B.
3. ϵ_{data}: error caused by physical data used in the radiation transport algorithm, such as stopping-power and other cross-sections.
4. ϵ_{geom}: error caused by difference between blueprints and actual chamber design, comprising the effect of the dead volume.
5. ϵ_{rep}: error associated with measurement repeatability.
6. $\epsilon_{\mathrm{setup}}$: error associated with measurement setup error. The portion independent of B is assumed to cancel with the ratio. The other portion, symmetric with respect to the sign of B, is to be characterized.

3.2.3 Mathematical derivations

Setup uncertainty

Two sources of experimental uncertainty are considered: one is defined as the repeatability uncertainty evaluated by calculating the standard deviation of N measurements, and the other one, named setup uncertainty, accounts for the difference in the detector response with the same magnetic field magnitude but with opposite direction.

In the parallel orientation, the chamber response is supposed to be symmetrical with the magnetic field; since the setup and the chamber are symmetrical, the

impact of the magnetic field is assumed to be the same in the negative and positive magnetic field direction. Mathematically, this is $\langle r_{\mathrm{exp}}(B)\rangle = \langle r_{\mathrm{exp}}(-B)\rangle$, defining the experimental error as

$$\epsilon_{\mathrm{exp}} = r_{\mathrm{exp}}(B) - r_{\mathrm{exp}}(-B) \approx \langle r_{\mathrm{exp}}(B)\rangle + \epsilon_{\mathrm{rep,+}} + \epsilon_{\mathrm{setup,+}} - \langle r_{\mathrm{exp}}(-B)\rangle - \epsilon_{\mathrm{rep,-}} - \epsilon_{\mathrm{setup,-}}$$

$$\epsilon_{\mathrm{exp}} \approx \epsilon_{\mathrm{rep,+}} + \epsilon_{\mathrm{setup,+}} - \epsilon_{\mathrm{rep,-}} - \epsilon_{\mathrm{setup,-}} \tag{3.5}$$

the average of $\bar{\epsilon}_{\mathrm{exp}}$ is given by:

$$\bar{\epsilon}_{\mathrm{exp}} \approx \frac{1}{N}\sum_{j=1}^{N} \epsilon_{\mathrm{exp},j} = \frac{1}{N}\sum_{j=1}^{N} \left(\epsilon_{\mathrm{rep,+,j}} + \epsilon_{\mathrm{setup,+,j}} - \epsilon_{\mathrm{rep,-,j}} - \epsilon_{\mathrm{setup,-,j}}\right). \tag{3.6}$$

for the N pairs of magnetic field and calculating the estimator :

$$\begin{aligned} \frac{1}{N}\sum_{i=1}^{N}\langle\left(\epsilon_{\mathrm{exp,i}} - \bar{\epsilon}_{\mathrm{exp,i}}\right)^2\rangle &= \frac{1}{N}\sum_{i=1}^{N}\langle\epsilon_{\mathrm{exp,i}}^2 - 2\epsilon_{\mathrm{exp,i}}\bar{\epsilon}_{\mathrm{exp,i}} + \bar{\epsilon}_{\mathrm{exp,i}}^2\rangle \\ &= \frac{1}{N}\sum_{i=1}^{N}\langle\epsilon_{\mathrm{exp,i}}^2\rangle - \frac{2}{N}\sum_{i=1}^{N}\langle\epsilon_{\mathrm{exp,i}}\bar{\epsilon}_{\mathrm{exp,i}}\rangle + \frac{1}{N}\sum_{i=1}^{N}\langle\bar{\epsilon}_{\mathrm{exp,i}}^2\rangle \end{aligned} \tag{3.7}$$

using the definition of the mean (eq. 3.6):

$$\begin{aligned}
\frac{1}{N}\sum_{i=1}^{N}\left\langle\left(\epsilon_{\mathrm{exp,i}}-\overline{\epsilon}_{\mathrm{exp,i}}\right)^2\right\rangle &= \frac{1}{N}\sum_{i=1}^{N}\left\langle\epsilon_{\mathrm{exp,i}}^2\right\rangle - \frac{2}{N}\sum_{i=1}^{N}\left\langle\epsilon_{\mathrm{exp,i}}\frac{1}{N}\sum_{j=1}^{N}\epsilon_{\mathrm{exp},j}\right\rangle + \frac{1}{N}\sum_{i=1}^{N}\left\langle\frac{1}{N}\sum_{i=1}^{N}\epsilon_{\mathrm{exp},i}\frac{1}{N}\sum_{j=1}^{N}\epsilon_{\mathrm{exp},j}\right\rangle \\
&= \frac{1}{N}\sum_{i=1}^{N}\left\langle\epsilon_{\mathrm{exp,i}}^2\right\rangle - \frac{2}{N^2}\sum_{i=1}^{N}\sum_{j=1}^{N}\left\langle\epsilon_{\mathrm{exp,i}}\epsilon_{\mathrm{exp},j}\right\rangle + \frac{1}{N^2}\sum_{i=1}^{N}\sum_{j=1}^{N}\left\langle\epsilon_{\mathrm{exp},i}\epsilon_{\mathrm{exp},j}\right\rangle \\
&= \frac{1}{N}\sum_{i=1}^{N}\left\langle\epsilon_{\mathrm{exp,i}}^2\right\rangle - \frac{1}{N^2}\sum_{i=1}^{N}\sum_{j=1}^{N}\left\langle\epsilon_{\mathrm{exp},i}\epsilon_{\mathrm{exp},j}\right\rangle \\
&= \frac{1}{N}\sum_{i=1}^{N}\left\langle\epsilon_{\mathrm{exp,i}}^2\right\rangle - \frac{1}{N^2}\sum_{i=1}^{N}\left\langle\epsilon_{\mathrm{exp},i}\epsilon_{\mathrm{exp},i}\right\rangle - \frac{1}{N^2}\sum_{i=1}^{N}\sum_{j=1,j\neq i}^{N}\left\langle\epsilon_{\mathrm{exp},i}\epsilon_{\mathrm{exp},j}\right\rangle \\
&= \frac{1}{N}\sum_{i=1}^{N}\left\langle\epsilon_{\mathrm{exp,i}}^2\right\rangle - \frac{1}{N^2}\sum_{i=1}^{N}\left\langle\epsilon_{\mathrm{exp},i}^2\right\rangle - \frac{1}{N^2}\sum_{i=1}^{N}\sum_{j=1,j\neq i}^{N}\left\langle\epsilon_{\mathrm{exp},i}\epsilon_{\mathrm{exp},j}\right\rangle \\
&= \frac{N-1}{N^2}\sum_{i=1}^{N}\left\langle\epsilon_{\mathrm{exp,i}}^2\right\rangle - \frac{1}{N^2}\sum_{i=1}^{N}\sum_{j=1,j\neq i}^{N}\left\langle\epsilon_{\mathrm{exp},i}\epsilon_{\mathrm{exp},j}\right\rangle
\end{aligned} \tag{3.8}$$

using the definition of ϵ_{exp}, the equation becomes:

$$\begin{aligned}
\frac{1}{N}\sum_{i=1}^{N}\left\langle\left(\epsilon_{\mathrm{exp,i}}-\overline{\epsilon}_{\mathrm{exp,i}}\right)^2\right\rangle \approx{}& \frac{N-1}{N^2}\sum_{i=1}^{N}\left\langle\left(\epsilon_{\mathrm{rep,+,i}}+\epsilon_{\mathrm{setup,+,i}}+\epsilon_{\mathrm{rep,-,i}}+\epsilon_{\mathrm{setup,-,i}}\right)^2\right\rangle \\
&- \frac{1}{N^2}\sum_{i=1}^{N}\sum_{j=1,j\neq i}^{N}\left\langle\left(\epsilon_{\mathrm{rep,+,i}}+\epsilon_{\mathrm{setup,+,i}}-\epsilon_{\mathrm{rep,-,i}}-\epsilon_{\mathrm{setup,-,i}}\right)\right. \\
&\left.\left(\epsilon_{\mathrm{rep,+,j}}+\epsilon_{\mathrm{setup,+,j}}-\epsilon_{\mathrm{rep,-,j}}-\epsilon_{\mathrm{setup,-,j}}\right)\right\rangle
\end{aligned}$$

the right-hand side of the equation can be expanded as

$$
\begin{aligned}
&\approx \frac{N-1}{N^2}\sum_{i=1}^{N}\Big[\langle\epsilon^2_{\text{rep,+,i}}\rangle + \langle\epsilon^2_{\text{setup,+,i}}\rangle + \langle\epsilon^2_{\text{rep,-,i}}\rangle + \langle\epsilon^2_{\text{setup,-,i}}\rangle \\
&+ 2\big(\langle\epsilon_{\text{rep,+,i}}\epsilon_{\text{setup,+,i}}\rangle - \langle\epsilon_{\text{rep,+,i}}\epsilon_{\text{rep,-,i}}\rangle - \langle\epsilon_{\text{rep,+,i}}\epsilon_{\text{setup,-,i}}\rangle \\
&- \langle\epsilon_{\text{setup,+,i}}\epsilon_{\text{rep,-,i}}\rangle - \langle\epsilon_{\text{setup,+,i}}\epsilon_{\text{setup,-,i}}\rangle + \langle\epsilon_{\text{rep,-,i}}\epsilon_{\text{setup,-,i}}\rangle\big)\Big] \\
&- \frac{1}{N^2}\sum_{i=1}^{N}\sum_{j=1,j\neq i}^{N}\big(\langle\epsilon_{\text{rep,+,i}}\epsilon_{\text{rep,+,j}}\rangle + \langle\epsilon_{\text{rep,+,i}}\epsilon_{\text{setup,+,j}}\rangle - \langle\epsilon_{\text{rep,+,i}}\epsilon_{\text{rep,-,j}}\rangle - \langle\epsilon_{\text{rep,+,i}}\epsilon_{\text{setup,-,j}}\rangle \\
&+ \langle\epsilon_{\text{setup,+,i}}\epsilon_{\text{rep,+,j}}\rangle + \langle\epsilon_{\text{setup,+,i}}\epsilon_{\text{setup,+,j}}\rangle - \langle\epsilon_{\text{setup,+,i}}\epsilon_{\text{rep,-,j}}\rangle - \langle\epsilon_{\text{setup,+,i}}\epsilon_{\text{setup,-,j}}\rangle \\
&- \langle\epsilon_{\text{rep,-,i}}\epsilon_{\text{rep,+,j}}\rangle - \langle\epsilon_{\text{rep,-,i}}\epsilon_{\text{setup,+,j}}\rangle + \langle\epsilon_{\text{rep,-,i}}\epsilon_{\text{rep,-,j}}\rangle + \langle\epsilon_{\text{rep,-,i}}\epsilon_{\text{setup,-,j}}\rangle \\
&- \langle\epsilon_{\text{setup,-,i}}\epsilon_{\text{rep,+,j}}\rangle - \langle\epsilon_{\text{setup,-,i}}\epsilon_{\text{setup,+,j}}\rangle + \langle\epsilon_{\text{setup,-,i}}\epsilon_{\text{rep,-,j}}\rangle + \langle\epsilon_{\text{setup,-,i}}\epsilon_{\text{setup,-,j}}\rangle\big)
\end{aligned}
$$

since there are no statistical correlations between repeatability and setup errors and neither amongst themselves, then

$$
\begin{aligned}
&\approx \frac{N-1}{N^2}\sum_{i=1}^{N}\Big[\langle\epsilon^2_{\text{rep,+,i}}\rangle + \langle\epsilon^2_{\text{setup,+,i}}\rangle + \langle\epsilon^2_{\text{rep,-,i}}\rangle + \langle\epsilon^2_{\text{setup,-,i}}\rangle \\
&+ 2\big(\langle\epsilon_{\text{rep,+,i}}\rangle\langle\epsilon_{\text{setup,+,i}}\rangle - \langle\epsilon_{\text{rep,+,i}}\rangle\langle\epsilon_{\text{rep,-,i}}\rangle - \langle\epsilon_{\text{rep,+,i}}\rangle\langle\epsilon_{\text{setup,-,i}}\rangle \\
&- \langle\epsilon_{\text{setup,+,i}}\rangle\langle\epsilon_{\text{rep,-,i}}\rangle - \langle\epsilon_{\text{setup,+,i}}\rangle\langle\epsilon_{\text{setup,-,i}}\rangle + \langle\epsilon_{\text{rep,-,i}}\rangle\langle\epsilon_{\text{setup,-,i}}\rangle\big)\Big] \\
&- \frac{1}{N^2}\sum_{i=1}^{N}\sum_{j=1,j\neq i}^{N}\big(\langle\epsilon_{\text{rep,+,i}}\rangle\langle\epsilon_{\text{rep,+,j}}\rangle + \langle\epsilon_{\text{rep,+,i}}\rangle\langle\epsilon_{\text{setup,+,j}}\rangle - \langle\epsilon_{\text{rep,+,i}}\rangle\langle\epsilon_{\text{rep,-,j}}\rangle - \langle\epsilon_{\text{rep,+,i}}\rangle\langle\epsilon_{\text{setup,-,j}}\rangle \\
&+ \langle\epsilon_{\text{setup,+,i}}\rangle\langle\epsilon_{\text{rep,+,j}}\rangle + \langle\epsilon_{\text{setup,+,i}}\rangle\langle\epsilon_{\text{setup,+,j}}\rangle - \langle\epsilon_{\text{setup,+,i}}\rangle\langle\epsilon_{\text{rep,-,j}}\rangle - \langle\epsilon_{\text{setup,+,i}}\rangle\langle\epsilon_{\text{setup,-,j}}\rangle \\
&- \langle\epsilon_{\text{rep,-,i}}\rangle\langle\epsilon_{\text{rep,+,j}}\rangle - \langle\epsilon_{\text{rep,-,i}}\rangle\langle\epsilon_{\text{setup,+,j}}\rangle + \langle\epsilon_{\text{rep,-,i}}\rangle\langle\epsilon_{\text{rep,-,j}}\rangle + \langle\epsilon_{\text{rep,-,i}}\rangle\langle\epsilon_{\text{setup,-,j}}\rangle \\
&- \langle\epsilon_{\text{setup,-,i}}\rangle\langle\epsilon_{\text{rep,+,j}}\rangle - \langle\epsilon_{\text{setup,-,i}}\rangle\langle\epsilon_{\text{setup,+,j}}\rangle + \langle\epsilon_{\text{setup,-,i}}\rangle\langle\epsilon_{\text{rep,-,j}}\rangle + \langle\epsilon_{\text{setup,-,i}}\rangle\langle\epsilon_{\text{setup,-,j}}\rangle\big)
\end{aligned}
$$

assuming that $\langle \epsilon_{\text{rep,+,i}} \rangle = \langle \epsilon_{\text{rep,-,i}} \rangle = \langle \epsilon_{\text{rep,i}} \rangle$, then

$$\begin{aligned}
&\approx \frac{N-1}{N^2} \sum_{i=1}^{N} \left[\langle \epsilon^2_{\text{rep,+,i}} \rangle + \langle \epsilon^2_{\text{setup,+,i}} \rangle + \langle \epsilon^2_{\text{rep,-,i}} \rangle + \langle \epsilon^2_{\text{setup,-,i}} \rangle - 2\langle \epsilon_{\text{rep,i}} \rangle^2 - 2\langle \epsilon_{\text{setup,+,i}} \rangle \langle \epsilon_{\text{setup,-,i}} \rangle \right] \\
&- \frac{1}{N^2} \sum_{i=1}^{N} \sum_{j=1, j\neq i}^{N} \left(\langle \epsilon_{\text{setup,+,i}} \rangle \langle \epsilon_{\text{setup,+,j}} \rangle - \langle \epsilon_{\text{setup,+,i}} \rangle \langle \epsilon_{\text{setup,-,j}} \rangle \right. \\
&\left. - \langle \epsilon_{\text{setup,-,i}} \rangle \langle \epsilon_{\text{setup,+,j}} \rangle + \langle \epsilon_{\text{setup,-,i}} \rangle \langle \epsilon_{\text{setup,-,j}} \rangle \right),
\end{aligned}$$

replacing $\sigma^2_{\text{rep},\pm,i} = \langle \epsilon^2_{\text{rep},\pm,i} \rangle - \langle \epsilon_{\text{rep,i}} \rangle^2$, and assuming the same mean and variance for the setup error, i.e., VAR($\epsilon_{\text{setup,+,i}}$)=VAR($\epsilon_{\text{setup,-,i}}$) and $\langle \epsilon_{\text{setup,-,i}} \rangle = \langle \epsilon_{\text{setup,+,i}} \rangle$, then

$$\frac{1}{N} \sum_{i=1}^{N} \langle (\epsilon_{\text{exp,i}} - \bar{\epsilon}_{\text{exp,i}})^2 \rangle \approx \frac{N-1}{N^2} \sum_{i=1}^{N} \left(\sigma^2_{\text{rep,+,i}} + \sigma^2_{\text{rep,-,i}} + 2\sigma^2_{\text{setup}} \right)$$

and

$$\frac{1}{N} \sum_{i=1}^{N} \left\langle \left(r_{\exp}(B_i) - r_{\exp}(-B_i) \right)^2 \right\rangle \approx \frac{N-1}{N^2} \sum_{i=1}^{N} \sigma^2_{\text{rep,+,i}} + \frac{N-1}{N^2} \sum_{i=1}^{N} \sigma^2_{\text{rep,-,i}} + \frac{2(N-1)}{N} \sigma^2_{\text{setup}}$$

therefore,

$$\sigma^2_{\text{setup}} \approx \frac{1}{2(N-1)} \sum_{i=1}^{N} \left\langle \left(r_{\exp}(B_i) - r_{\exp}(-B_i) \right)^2 \right\rangle - \frac{1}{N} \sum_{i=1}^{N} \left(\frac{\sigma^2_{\text{rep,+,i}} + \sigma^2_{\text{rep,-,i}}}{2} \right)$$

Fano uncertainty

In the Fano test a theoretical value is compared to a simulated value, these values are supposed to be the same, i.e. $D_{\text{theory}} = \langle D_{\text{num}}(B) \rangle$, the error of the simulation is given the difference between those two values

$$\begin{aligned}
\delta = D_{\text{num}}(B) - D_{\text{theory}}(B) &\approx \langle D_{\text{num}}(B) \rangle + \delta_{\text{stat}}(B) + \delta_{\text{Fano}}(B) - D_{\text{theory}} \\
&\approx \delta_{\text{stat}}(B) + \delta_{\text{Fano}}(B)
\end{aligned} \tag{3.9}$$

for the M ionization chambers, calculating the following estimator (using the previous derivation of 3.8),

$$\frac{1}{M}\sum_{j=1}^{M}\left\langle\left(\delta_j-\overline{\delta_j}\right)^2\right\rangle \approx \frac{M-1}{M^2}\sum_{j=1}^{M}\left\langle\delta_j^2\right\rangle - \frac{1}{M^2}\sum_{j=1}^{M}\sum_{k=1,k\neq j}^{M}\langle\delta_j\delta_k\rangle$$

the right-side of the previous equation can be expanded as

$$\begin{aligned}
&\approx \frac{M-1}{M^2}\sum_{j=1}^{M}\left\langle\left(\delta_{\text{stat},j}+\delta_{\text{Fano},j}\right)^2\right\rangle - \frac{1}{M^2}\sum_{j=1}^{M}\sum_{k=1,k\neq j}^{M}\left\langle\left(\delta_{\text{stat},j}+\delta_{\text{Fano},j}\right)\left(\delta_{\text{stat},k}+\delta_{\text{Fano},k}\right)\right\rangle\\
&\approx \frac{M-1}{M^2}\sum_{j=1}^{M}\left\langle\delta_{\text{stat},j}^2+\delta_{\text{Fano},j}^2+2\delta_{\text{stat},j}\delta_{\text{Fano},j}\right\rangle\\
&-\frac{1}{M^2}\sum_{j=1}^{M}\sum_{k=1,k\neq j}^{M}\left\langle\delta_{\text{stat},j}\delta_{\text{stat},k}+\delta_{\text{stat},j}\delta_{\text{Fano},k}+\delta_{\text{Fano},j}\delta_{\text{stat},k}+\delta_{\text{Fano},j}\delta_{\text{Fano},k}\right\rangle\\
&\approx \frac{M-1}{M^2}\sum_{j=1}^{M}\left(\left\langle\delta_{\text{stat},j}^2\right\rangle+\left\langle\delta_{\text{Fano},j}^2\right\rangle+2\left\langle\delta_{\text{stat},j}\delta_{\text{Fano},j}\right\rangle\right)\\
&-\frac{1}{M^2}\sum_{j=1}^{M}\sum_{k=1,k\neq j}^{M}\left(\left\langle\delta_{\text{stat},j}\delta_{\text{stat},k}\right\rangle+\left\langle\delta_{\text{stat},j}\delta_{\text{Fano},k}\right\rangle+\left\langle\delta_{\text{Fano},j}\delta_{\text{stat},k}\right\rangle+\left\langle\delta_{\text{Fano},j}\delta_{\text{Fano},k}\right\rangle\right)
\end{aligned}$$

assuming the variables are uncorrelated, then

$$\begin{aligned}
\frac{1}{M}\sum_{j=1}^{M}\left\langle\left(\delta_j-\overline{\delta_j}\right)^2\right\rangle \approx \frac{M-1}{M^2}\sum_{j=1}^{M}&\left(\left\langle\delta_{\text{stat},j}^2\right\rangle+\left\langle\delta_{\text{Fano},j}^2\right\rangle+2\left\langle\delta_{\text{stat},j}\right\rangle\left\langle\delta_{\text{Fano},j}\right\rangle\right)\\
&-\frac{1}{M^2}\sum_{j=1}^{M}\sum_{k=1,k\neq j}^{M}\left(\left\langle\delta_{\text{stat},j}\right\rangle\left\langle\delta_{\text{stat},k}\right\rangle+\left\langle\delta_{\text{stat},j}\right\rangle\left\langle\delta_{\text{Fano},k}\right\rangle\right.\\
&\left.+\left\langle\delta_{\text{Fano},j}\right\rangle\left\langle\delta_{\text{stat},k}\right\rangle+\left\langle\delta_{\text{Fano},j}\right\rangle\left\langle\delta_{\text{Fano},k}\right\rangle\right)
\end{aligned}$$

defining the mean value of δ_{stat} and δ_{Fano}, μ_{stat} and μ_{Fano} respectively,

$$\begin{aligned}\frac{1}{M}\sum_{j=1}^{M}\left\langle\left(\delta_j-\overline{\delta_j}\right)^2\right\rangle &\approx \frac{M-1}{M^2}\sum_{j=1}^{M}\left(\left\langle\delta_{\text{stat},j}^2\right\rangle+\left\langle\delta_{\text{Fano},j}^2\right\rangle\right)+\frac{M-1}{M}\left(2\mu_{\text{stat}}\mu_{\text{Fano}}\right)\\ &\quad-\frac{M-1}{M}\left(\mu_{\text{stat}}^2+\mu_{\text{stat}}\mu_{\text{Fano}}+\mu_{\text{Fano}}\mu_{\text{stat}}+\mu_{\text{Fano}}^2\right)\\ &\approx \frac{M-1}{M^2}\sum_{j=1}^{M}\left(\left\langle\delta_{\text{stat},j}^2\right\rangle+\left\langle\delta_{\text{Fano},j}^2\right\rangle\right)-\frac{M-1}{M}\left(\mu_{\text{stat}}^2+\mu_{\text{Fano}}^2\right)\end{aligned}$$

using $\left\langle\delta_{\text{stat, j}}^2\right\rangle=\sigma_{\text{stat, j}}^2+\left\langle\delta_{\text{stat, j}}\right\rangle^2$ and assuming the same Fano variance for all of the chambers, then $\left\langle\delta_{\text{Fano, j}}^2\right\rangle=\sigma_{\text{Fano}}^2+\left\langle\delta_{\text{Fano, j}}\right\rangle^2$. Hence, the right-side of the equation is

$$\begin{aligned}&\approx \frac{M-1}{M^2}\sum_{j=1}^{M}\left(\sigma_{\text{stat, j}}^2+\left\langle\delta_{\text{stat, j}}\right\rangle^2+\sigma_{\text{Fano}}^2+\left\langle\delta_{\text{Fano, j}}\right\rangle^2\right)-\frac{M-1}{M}\left(\mu_{\text{stat}}^2+\mu_{\text{Fano}}^2\right)\\ &\approx \frac{M-1}{M^2}\sum_{j=1}^{M}\sigma_{\text{stat, j}}^2+\frac{M-1}{M^2}\sum_{j=1}^{M}\left\langle\delta_{\text{stat, j}}\right\rangle^2+\frac{M-1}{M}\sigma_{\text{Fano}}^2\\ &+\frac{M-1}{M^2}\sum_{j=1}^{M}\left\langle\delta_{\text{Fano, j}}\right\rangle^2\frac{M-1}{M}\mu_{\text{stat}}^2-\frac{M-1}{M}\mu_{\text{Fano}}^2\\ &\approx \frac{M-1}{M^2}\sum_{j=1}^{M}\sigma_{\text{stat, j}}^2+\frac{M-1}{M}\sigma_{\text{Fano}}^2+\frac{M-1}{M}\mu_{\text{stat}}^2+\frac{M-1}{M}\mu_{\text{Fano}}^2-\frac{M-1}{M}\mu_{\text{stat}}^2-\frac{M-1}{M}\mu_{\text{Fano}}^2\\ &\approx \frac{M-1}{M^2}\sum_{j=1}^{M}\sigma_{\text{stat, j}}^2+\frac{M-1}{M}\sigma_{\text{Fano}}^2\end{aligned}$$

therefore,

$$\frac{1}{M}\sum_{j=1}^{M}\left\langle\left(D_{\text{num}}(B)-D_{\text{theory}}(B)\right)^2\right\rangle\approx\frac{M-1}{M^2}\sum_{j=1}^{M}\sigma_{\text{stat, j}}^2+\frac{M-1}{M}\sigma_{\text{Fano}}^2$$

and

$$\sigma_{\text{Fano}}^2\approx\frac{1}{M-1}\sum_{j=1}^{M}\left\langle\left(D_{\text{num}}(B)-D_{\text{theory}}(B)\right)^2\right\rangle-\frac{1}{M}\sum_{j=1}^{M}\sigma_{\text{stat, j}}^2,$$

with the restriction that the first term in the right side must be bigger than the second term, i.e.

$$\frac{1}{M-1}\sum_{j=1}^{M}\left\langle\left(D_{\text{num}}(B)-D_{\text{theory}}(B)\right)^2\right\rangle > \frac{1}{M}\sum_{j=1}^{M}\sigma^2_{\text{stat, j}}.$$

Geometrical uncertainty

The geometrical uncertainty is defined by equation 4.10, where one part corresponds to the uncertainty coming from the discrepancies between the blueprints and the chamber geometry and the other one from the presence of the dead volume. The dead volume uncertainty is the product of a sensitivity coefficient evaluating the effect of the presence and absence of the dead volume in the detector response and the uncertainty of the dead volume itself σ_{DV}. The value of σ_{DV} was arbitrary set to 1% since the mechanical tolerances of the blueprints are not available, and it is not possible to evaluate the propagation of this uncertainty in the Monte Carlo model and the Comsol model. Additionally, the σ_{DV} =1% value also accounts for the uncertainty introduced from the determination of the dead volume in the Comsol model.

3.3 Complementary information to materials and methods

3.3.1 Experimental setup

This section aims to provide more detail into some technical aspects of the materials and methods section of the article. The surface-to-source distance (SSD) is 306 cm; this extended SSD is used, so the electromagnet (GMW 3474-140) and its magnetic field do not impact the head linac components.

The electromagnet is calibrated, i.e., the magnetic field strength correspond to specific and known current values. In the gap, the magnetic field is uniform in an area of 5 $\times$ 5 cm^2 along the centre of the two magnetic poles was found to be 99.9%.

3.3.2 Intrinsic response

The intrinsic response, defined by equation 4.5, is equal to the ratio of the effective cavity mass over the energy necessary to create an ion pair (W/e). The latter is assumed to be independent of field size, beam quality [85, 86, 87] and magnetic field strength. No known mechanism could affect the energy necessary to create an ion pair (W/e), the effective mass or the dead volume by the presence of the magnetic field. Thus, the intrinsic response with and without magnetic field are assumed equal.

3.4 Results and impact

Four commercial small-cavity chamber responses to megavoltage photon beams in the presence of magnetic fields were characterized via experimental measurements and MC simulations. The magnetic field effect on the chamber relative response depends on the orientation setup. The magnetic field is always perpendicular to the irradiation beam and to the chamber axis. Two chamber-axis orientations are studied: parallel and perpendicular to the photon beam. In the parallel and perpendicular orientations, the chamber response is affected by as much as 4.1% and 4.5%, respectively.

The sensitive volume was reduced to account for the collection inefficiency adjacent to the guard electrode (i.e., dead volume) based on COMSOL simulations of electric field lines. The dead volume represents a large fraction (15%-23%) of the sensitive volume of the small-cavity chambers (models: PTW31010, PTW31016, PTW31021 and PTW31022)

In the parallel orientation, the maximal percentage difference in relative response was reduced from 4.37%, 6.06% and 2.81% to 0.60% for PTW31010, PTW31021, PTW31016 and PTW30122 and from 1.91% to 1.57% for PTW31016 when the dead volume was excluded. In the perpendicular orientation, for $B > 0T$, the maximal difference was reduced from 2.10%, 3.57%, 2.24% and 1.73% to 0.31%, 0.67%, 2.15% and 0.70% for PTW31010, PTW31021, PTW31016 and PTW30122,

respectively.

Our results pointed out the importance of having an accurate chamber model, including its dead volume, to calculate chamber dose-response in the presence of magnetic fields. The magnetic field exacerbates any discrepancy between the actual and the modelled detector geometry. Therefore, Monte Carlo simulation of detector dose-response must be (if possible) validated with experimental data.

To accurately model detector dose response in the presence of magnetic fields, it is recommended to follow a series of steps. First of all, the characterization of the dead volume is crucial. In the small cavity chambers, the dead volume corresponds to approximately 20% of the volume (depending on the model), and its exclusion from the mechanical volume is required to obtain good agreement between simulation and measured values.

Secondly, the blueprints of detector geometry should be as close to the detector as possible. It is often assumed that chambers of the same model and manufacturer are identical, but this is not always the case. There are chamber-to-chamber variations that are generally not significant in conventional reference dosimetry. However, they could be relevant when a magnetic field is present. To avoid any discrepancy, an x-ray of the detector can be taken to validate the details of the blueprints and confirm that there are no hidden details, such as air layers.

Finally, all the sources of uncertainty must be accounted for in an uncertainty budget. For the numerical simulations, this means that the Monte Carlo code should be benchmarked with a Fano test in the presence of magnetic fields.

3.5 Contributions

The experimental measurements of this work were performed at the National Physical Laboratory (NPL).

1. Yunuen Cervantes Espinosa
   - Development of original idea
   - Experimental measurements

- Analysis of experimental measurements
- Numerical simulations of dead volume
- Monte Carlo simulations of experimental measurements and Fano test
- Analysis of results
- Writing of the article

2. Ilias Billas
   - Development of original idea
   - Experimental measurements
   - Analysis of experimental measurements
   - Scientific support
   - Revision of the article
3. David Shipley
   - Support with Monte Carlo simulations and Fano test
   - Revision of the article
4. Simon Duane
   - Development of original idea
   - Experimental measurements
   - Scientific support
   - Revision of the article
5. Hugo Bouchard
   - Project direction
   - Result analysis
   - Mathematical formalism
   - Scientific support
   - Revision of the article

CHAPTER 4

SMALL-CAVITY CHAMBER DOSE RESPONSE IN MEGAVOLTAGE PHOTON BEAMS COUPLED TO MAGNETIC FIELDS

This article was published in the journal Physics and Medicine and Biology, volume 65, number 24 [41]. The results were presented in an oral presentation at the International Conference on the Use of Computers in Radiation Therapy and the International Conference on Monte Carlo Techniques for Medical Applications (ICCR-MCMA) in June 2019 and in the annual congress of the AQPMC in November 2019. Also, as a poster at the annual ESTRO Congress in 2020 [88].

Small-cavity chamber dose response in megavoltage photon beams coupled to magnetic fields

Yunuen Cervantes [1,2],Ilias Billas[3,4], David Shipley[3], Simon Duane[3], and Hugo Bouchard[1,2,5]

[1] *Département de physique, Université de Montréal, Complexe des sciences, 1375 Avenue Thérèse-Lavoie-Roux, Montréal, Québec H2V 0B3, Canada.*

[2] *Centre de recherche du Centre hospitalier de l'Université de Montréal, 900 Rue Saint-Denis, Montréal, Québec, H2X 0A9, Canada*

[3] *National Physical Laboratory, Chemical, Medical and Environmental Science Department, Teddington, United Kingdom*

[4] *Joint Department of Physics, The Institute of Cancer Research and The Royal Marsden NHS Foundation Trust, London, United Kingdom*

[5] *Département de radio-oncologie, Centre hospitalier de l'Université de Montréal (CHUM), 900 Rue Saint-Denis, Montréal, Québec, H2X 0A9, Canada*

Abstract

In MRgRT, dosimetry measurements are performed in the presence of magnetic fields. For high-resolution measurements, small-cavity ionization chambers are required. While Monte Carlo simulations are essential to determine dosimetry correction factors, models of small-chambers require careful validation with experimental measurements. The aim of this study is to characterize small-cavity chamber response coupled to magnetic fields. Small-cavity chambers (PTW31010, PTW31016, PTW31021 and PTW3022) are irradiated by a 6 MV photon beam for 9 magnetic field strengths between -1.5T and +1.5T. The chamber axis is orientated either parallel or perpendicular to the irradiation beam, with the magnetic field always perpendicular to the beam. MC simulations are performed in EGSnrc. The sensitive volume of the chambers is reduced to account for the inefficiency adjacent to the guard electrode (dead volume) based on COMSOL calculations of electric potentials. The magnetic field affects the chamber response by up to 4.1%

and 4.5% in the parallel and perpendicular orientations, respectively, compared to no magnetic field. The maximal difference in dose response between experiments and simulations is up to 6.1% and 4.5% for parallel and perpendicular orientation, respectively. When the dead volume is removed, which accounts for the 15%-23% of the nominal volume, the difference, in most cases, is within the stated uncertainties. Nevertheless, for a particular chamber, the reduced nominal volume barely improved the agreement between the experimental and calculated relative response (4.53% to 4.13%). This disagreement may be due to the imperfect chamber geometry model, as was found from microCT images. A detailed uncertainty analysis is presented. The characterization of small-cavity ion chamber response coupled to magnetic fields is complex. Small differences between real and model chamber geometry that normally would be insignificant become an issue in the presence of magnetic fields. Accurate characterization of the nominal volume is essential for small-cavity ion chamber modelling.

Keywords: Magnetic fields, reference dosimetry, small-cavity ion chamber, Monte Carlo simulations

4.1 Introduction

Magnetic resonance guided radiation therapy (MRgRT) promises more precise radiation delivery than conventional techniques by allowing real-time visualization of internal structures before and during treatment. The anticipated benefits of this technique are a more focused radiation absorbed dose at the tumour and an increased sparing of healthy tissues. To achieve accurate absorbed dose delivery, treatment planning systems require accurate absorbed dose measurements. The magnetic field has a significant impact on dose deposition and on detector response due to the Lorentz force acting on charged particles and its interplay with charged particle equilibrium (CPE) [45, 57, 62]. It was shown that magnetic fields can have a strong impact on dose deposition, creating profile distortions, depth-dose shifts, and more importantly under- and over-dosage at tissue-air interfaces. One explanation for the latter is based on the so-called electron return effect (ERE) [13],

which states that electrons in air can re-enter the tissue, thus causing an increase in dose deposition in that region. The magnetic field effect on ionization chambers response has also been reported by several studies [35, 77, 82, 75, 40], most of these focusing on chamber response dedicated to reference dosimetry (i.e., regular-size chambers). In the context of radiation detectors, the ERE also exists and causes CPE violation. Formally, CPE cannot be achieved in external megavoltage (MV) photon beams [89]. But leaving photon attenuation effects aside, Fano's theorem governs the use of ionization chambers in broad MV photon beams by assuring the absence of electron perturbations between air-equivalent wall materials and the chamber cavity [55]. In such conditions, Bragg-Gray's principle [90] can be applied with small corrections for electron perturbation effects [91, 92]. However in the presence of external magnetic fields, Fano's conditions are violated due to the magnetic field not scaling proportionally with the mass density of the media [45]. As a consequence, radiation measurements in the presence of magnetic fields are done in conditions of electronic disequilibrium without fundamental principles governing the cavity-to-medium dose conversion. Thus, dosimetry measurements involving strong density heterogeneities are subject to significant ionization chamber perturbation effects in comparison to conventional beams. These effects were observed in previous studies and it was recommended that special attention should be paid to regions where air is present inside the chamber and to possible air gaps formed at the interface of chamber and water [36, 37, 38].

Several formalisms were proposed to quantify the change in detector-to-dose conversion due to magnetic field [82, 75, 76]. Based on the formalism for non-standard beams by Alfonso *et al* [69], O'Brien *et al* [75] proposed an additional quality correction factor accounting for the magnetic field effect on dose response. They calculated the magnetic field correction factor for 7 chambers in a 1.5 T magnetic field for three different chamber axis orientations with respect to the magnetic field and the irradiation beam. The quality correction factors strongly depended on chamber orientation. In all cases, the irradiation beam is perpendicular to the chamber axis. When the chamber axis was parallel to the magnetic field, the cor-

rection factors were found within 1% of unity. When the chamber axis was 90° clockwise perpendicular to the magnetic field, the correction factor was on average 0.961 ± 0.002 over all chamber models, and for the 90° counter-clockwise, the average correction factor was 0.970 ± 0.007 over all chamber models. In the latter case, the larger variation was attributed to differences in chamber design, such as electrode, stem materials or other geometry features which were highlighted in the perpendicular orientation.

Another important effect in chamber dose response in MRgRT beams is the existence of a dead volume near the junction of the wall and the guard electrode, which decreases the collection efficiency. Indeed, an electric field reduction has been spotted in high spatial resolution dosimetric response maps for several chambers by Butler *et al* [93]. The guard and central electrodes have the same potential, therefore there is a region in which the charges are more likely to be collected by the guard electrode rather than by the central electrode thus creating a dead volume. Spindeldreier *et al* [40] demonstrated that the agreement between measurements and Monte Carlo simulations in the presence of magnetic fields could be improved by excluding a cylindrical dead volume adjacent to the guard electrode from the sensitive volume. For different chamber models, other investigations [94, 39] reached the same conclusion by following a finite element method to calculate the dead volume.

With future developments in MRgRT, it is anticipated that small photon beams will be used routinely to deliver complex radiation therapy. Therefore, it is necessary to develop techniques supporting clinical measurements for the characterization of small fields in MRgRT. Despite of the existence of a code of practice for small photon fields [95], additional considerations are anticipated to provide clear guidelines for clinical physicists. Furthermore, due to the non-flatness of the commercial MRI-linacs, it is recommended to use a small-cavity chambers for reference dosimetry to avoid measuring absorbed dose in the presence of lateral gradients. Indeed, detector size becomes an issue for fields where the region of uniform fluence is limited or non-existent. Previous studies have established that volume averaging

effects as well as the interplay between the lack of electronic equilibrium and the detector density, govern ionization chamber quality correction factors in small photon beams [96, 97, 98, 99, 100]. Small cavity ion chambers with a sensitive volume of 0.01-0.3 cm^3 are among the suitable detectors to perform small field dosimetry down to a field of 2 cm $\times$ 2 cm [95]. The magnetic field impact on small cavity ion chamber dose response remains unknown, to our knowledge, as few studies approached this subject. Looe *et al* [94] explored the possibility of minimizing the magnetic field perturbations on dose profiles by reducing the chamber size. They found that the lateral dose response function was less asymmetrical for the smallest chamber. By comparing the change in simulated dose profiles and measured signal profiles at 1.5 T, they concluded that the output correction factor is closer to unity for the smallest chamber. Their study exhibits the advantages of using a small-size chamber in the presence of magnetic field, however it also highlights the complexity of the interplay between the magnetic field and detector size via its impact on detector dose response.

The goal of the present study is to characterize small cavity detector response in the presence of magnetic fields using four commercial ionization chambers and calculate the corresponding magnetic field correction factors. This study is structured as follows. In the next section is presented the material and methods describing the experimental measurements, the numerical simulations, the formalism and the uncertainty analysis. The third section presents the results and comparison between experimental measurements and numerical methods as well as quality correction factors. In the discussion, our results are compared to different studies, followed by recommendations and conclusion.

4.2 Materials and Methods

4.2.1 The IAEA-AAPM formalism

The IAEA-AAPM formalism describes the conversion of ionization chamber signal to dose to water and was proposed by Alfonso *et al* [69] in the context of

nonstandard photon beams. Using that notation, absorbed dose to water for a field size f and beam quality Q is obtained as from an ionization chamber reading as such

$$D^{f}_{\mathrm{w},Q} = N^{f}_{D,\mathrm{w},Q} M^{f}_{Q} \tag{4.1}$$

with $D^{f}_{\mathrm{w},Q}$ the absorbed dose to water (in Gy), M^{f}_{Q} the corrected chamber reading (in nC) and $N^{f}_{D,\mathrm{w},Q}$ the chamber calibration coefficient (in Gy/nC) specific for the field size f and the beam quality Q. It is worth mentioning that the field size f and the beam quality Q implicitly involves the setup in which measurements are achieved (i.e., source-to surface distance, phantom size, etc.). The IAEA-AAPM formalism, also referred to as the Alfonso *et al* formalism, defines a quality correction factor from field size f_1 to f_2 and beam quality Q_1 to Q_2 to convert calibration coefficients as follows:

$$k^{f_2,f_1}_{Q_2,Q_1} \equiv \frac{N^{f_2}_{D,\mathrm{w},Q_2}}{N^{f_1}_{D,\mathrm{w},Q_1}}. \tag{4.2}$$

The quality correction factor $k^{f_2,f_1}_{Q_2,Q_1}$ quantifies the interplay between the change in beam quality $Q_1 \rightarrow Q_2$ and the ionization chamber dose response. In the context of Monte Carlo simulations, separating the factor into two components:

$$k^{f_2,f_1}_{Q_2,Q_1} = \left[k^{f_2,f_1}_{Q_2,Q_1}\right]_{\mathrm{MC}} \frac{R^{f_1}_{Q_1}}{R^{f_2}_{Q_2}} \tag{4.3}$$

with the first right-hand side term defined as the quality correction factor determined with Monte Carlo:

$$\left[k^{f_2,f_1}_{Q_2,Q_1}\right]_{\mathrm{MC}} \equiv \frac{\left(\frac{D^{f_2}_{\mathrm{w},Q_2}}{D^{f_2}_{\mathrm{cav},Q_2}}\right)}{\left(\frac{D^{f_1}_{\mathrm{w},Q_1}}{D^{f_1}_{\mathrm{cav},Q_1}}\right)} \tag{4.4}$$

with $D^{f}_{\mathrm{cav},Q}$ is the calculated absorbed dose to air (in Gy) in the chamber cavity

for the field size f and the beam quality Q. The second term on the right-hand side of the equation is an intrinsic effect referred to as the ratio of the chamber *intrinsic response* in the field size f_2 and the beam quality Q_2 relative to the field size f_1 and the beam quality Q_1. The chamber intrinsic response (in nC/Gy) for the field size f and the beam quality Q is defined as such

$$R_Q^f \equiv \frac{M_Q^f}{D_{\text{cav},Q}^f}. \tag{4.5}$$

The definition *intrinsic response* refers to response in terms of cavity dose rather than the response in terms of dose to water, the latter being commonly used in literature and simple referred as *dose response* [101]. For air ionization chambers, the intrinsic response is equal to the ratio of the effective cavity mass over the energy necessary to create an ion pair in air and should be, in principle, independent of field size or beam quality [102, 103].

The context of MRgRT dosimetry involves a nonstandard experimental setup (i.e., the presence of a magnetic field B) resulting in a change in beam quality compared to the absence of magnetic field, where the field size and beam quality would be f and Q, respectively. This way, we note the new field size f_B to specify that the photon field of size f is in the presence of a magnetic field B, and we note the new beam quality Q_B. This way, the quality correction factor accounting for the effect of the magnetic field becomes

$$k_{Q_B,Q}^{f_B,f} \equiv \frac{N_{D,\text{w},Q_B}^{f_B}}{N_{D,\text{w},Q}^{f}} \tag{4.6}$$

such that the absorbed dose to water is determined using this relation:

$$D_{\text{w},Q_B}^{f_B} = N_{D,\text{w},Q}^{f} k_{Q_B,Q}^{f_B,f} M_{Q_B}^{f_B} \tag{4.7}$$

Note here that f_B should be read "a field size f coupled to a magnetic field B".

In our study, agreement between experimental and Monte Carlo results is estimated by direct comparison of relative chamber response with respect to the

response at 0 T, this way neglecting the intrinsic effect expressed on the right-hand side of equation 4.3. That is

$$\begin{aligned} \frac{R_{Q_B}^{f_B}}{R_Q^f} \approx 1 \Rightarrow & \frac{M_{Q_B}^{f_B}}{M_Q^f} \approx \frac{D_{\mathrm{cav},Q_B}^{f_B}}{D_{\mathrm{cav},Q}^f} \\ & \Rightarrow k_{Q_B,Q}^{f_B,f} \approx \left[k_{Q_B,Q}^{f_B,f}\right]_{\mathrm{MC}}. \end{aligned} \tag{4.8}$$

4.2.2 Experimental measurements

The 4 different small-cavity ion chambers are placed in a custom-made water phantom (PMMA walls, dimensions of $7 \times 21 \times 18.2$ cm^3) placed in the gap of an electromagnet (GMW 3474-140) and are irradiated by a conventional 6 MV Elekta linear accelerator photon beam. The ion chambers used are Semiflex PTW31010, Semiflex 3D PTW31021, Pinpoint 3D PTW31016 and Pinpoint 3D PTW30122, and the nominal sensitive volumes are respectively: 0.125 cm^3, 0.070 cm^3, 0.016 cm^3, 0.016 cm^3. The surface-to-source distance (SSD) is 306 cm, the field size is 1.9 cm $\times$ 4.4 cm at the isocenter and the response is measured at 5 cm depth. The magnetic field is set to be always perpendicular to the irradiation beam and the chamber axis. Two chamber axis orientations are used: parallel and perpendicular to the beam. The experimental setup for parallel and perpendicular orientations is shown in figure 4.1. The ionization chamber response is measured for 9 magnetic field strengths: 0 T, $\pm$0.35 T, $\pm$0.5 T, $\pm$1 T, $\pm$1.5 T, the sign representing the field's orientation with respect to the poles of the magnet, as shown on figure 4.1. Chamber readings are corrected for temperature, pressure, polarity and ion recombination.

To verify the geometrical integrity of the chambers, computed tomography (CT) images of the chambers PTW31010, PTW31016 and PTW31021 are acquired with a Nikon XT H 225 scanner. The radiological technique is 120kV/80μA for PTW31010 and 70kV/60μA for the rest of the chambers. The microCT-images are reconstructed with a resolution of 96 pixels per inch (i.e., $\sim$ 0.265 mm in each

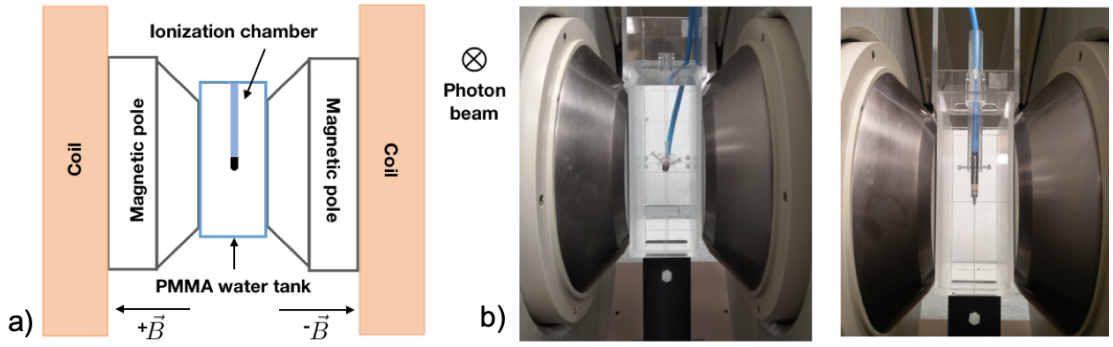

Figure 4.1 – a) Diagram of the experimental setup and b) chamber axis parallel and perpendicular to the irradiation beam (from left to right).

dimension).

4.2.3 Numerical methods

4.2.3.1 Monte Carlo simulations

A particle phase space of the Elekta Synergy linac is generated using BEAMnrc. The source model was previously validated via depth dose percentage and dose profiles measurements [81]. An additional validation of the 6 MV beam model in the presence of magnetic field is performed by comparing dose measurements performed with Gafchromic EBT3, which has been assessed by Billas *et al* [104] to be suitable detector for dosimetry in magnetic field, and Monte Carlo simulations at 0 T and 1.5 T. The film is placed in a Perspex® phantom, 5 cm width and 14 cm height that was designed to fit inside the 7 cm gap between the two poles of the magnet. The phantom consists of two symmetrical Perspex® plates, in where the film is enclosed with its edge orientated parallel to the radiation beam. The SSD is 305 cm and the field size is 1.9 cm × 4.4 cm at the isocenter. The measurements are meant to reproduce: 1) a percentage depth dose in homogeneous Perspex®, and 2) the dose distribution in Perspex® surrounded by air to reproduce the ERE.

Monte Carlo simulations of detector dose response are performed by modeling the experimental setup described in section 4.2.2. The experimental setup with each individual ion chamber is simulated using the Monte Carlo user code `egs_chamber`

from the EGSnrc [48]. The ion chambers models are built from the blueprints kindly provided by the manufacturer (PTW, Freiburg). To improve calculation efficiency, variance reduction techniques (VRTs) are used: photon cross-section enhancement (CSE), range-rejection-based Russian Roulette and intermediate phase-space storing [105]. A magnetic field is applied using the enhanced electromagnetic field macro by Malkov and Rogers [54]. Simulation parameters are set as follows. The maximum global energy loss in a step is set to the default value ESTEPE = 0.25, the additional parameter accounting for the changes in direction and energy loss caused by the magnetic field is set to EMESTEPE = 0.01, the energy production threshold is set to AE = 0.512 MeV for electrons and to AP = 0.001 MeV for photons. CSE is used with an enhancement factor set to 128, and ESAVE = 0.512 MeV. The Monte Carlo quality correction factor is calculated with equation 4.4 where $Q_2 = Q_B$ corresponds to the beam quality in the presence of magnetic fields and $Q_1 = Q$ is the beam quality without magnetic field. Absorbed dose to water is scored at the point of measurement in a water cylinder of 1 mm radius and 0.25 mm height.

To verify the self-consistency of the simulations using the set of simulation parameters described above, Fano cavity tests are performed to validate the consistency of the condensed history algorithm with and without magnetic field in the 4 chamber geometries of interest. Bouchard *et al* [57] and de Pooter *et al* [62] proposed two special cases where Fano test is valid in the presence of the magnetic fields: in the first one, the source must be isotropic and spatially uniform and in the second one, the source must be spatially uniform and the magnetic field must be scaled with the density. In this study, only the first case is implemented. The chamber is placed at the center of a $30 \times 30 \times 30$ cm^3 water phantom. To fulfil the Fano condition of a medium with uniform atomic properties, the atomic properties of all chamber materials are replaced by those of liquid water while maintaining the electron density of the original material. The irradiation is performed with a monoenergetic `egs++` Fano source which is isotropic, spatially uniform and density-scaled [48]. The Fano test is ran for two energies 0.1 MeV and 1.25 MeV at 0 T and

1.5 T. The simulations are performed in the user code `egs_chamber` using range rejection to reduce the simulation time, this with CSE switched off. The number of histories are such that simulations uncertainties are 0.1% for the chambers PTW 31010, PTW 31021 and PTW 31022 and 0.3-0.5% for the PTW31016. The chamber dose response is compared to an analytical value given by the ratio of energy and total mass.

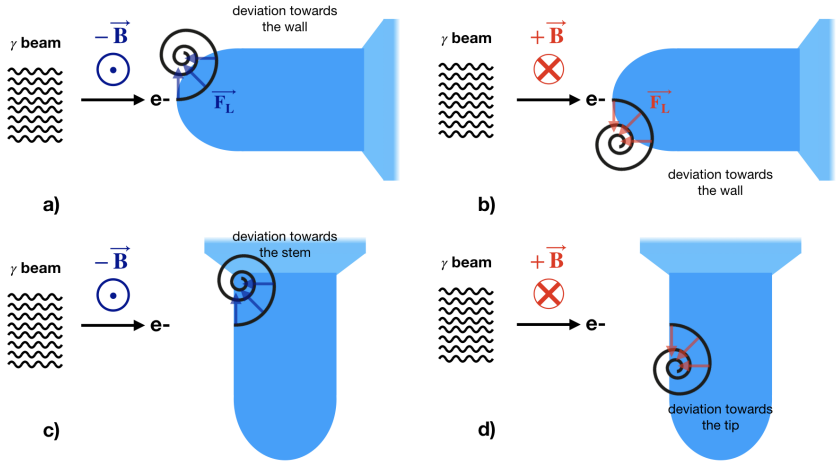

Figure 4.2 – Sketch of the chamber setup, the magnetic field is always perpendicular to the irradiation beam and to the chamber axis. a) chamber parallel to the beam at a negative magnetic field, b) chamber parallel to the beam at a positive magnetic field, c)chamber perpendicular to the beam at a negative magnetic field, and d) chamber perpendicular to the beam at a positive magnetic field. The electron trajectories are curved due to the Lorentz force and the curvature radius diminishes with decreasing energy, resulting in average trajectories forming a spiral (chamber dimensions and electron trajectories are not to scale).

4.2.3.2 Dead volume simulations

To account for accurate collection efficiency, an approach similar to previous studies is implemented [39, 94]. The electric field inside the ionization chambers is calculated using COMSOL Multiphysics software. Chamber models are built in COMSOL following the manufacturing blueprints. To calculate the electric field,

a 400 V is applied to the central and guard electrodes resulting in electric field lines coming either from the guard or central electrode towards the cavity wall. The dead volume is defined as the region where the electric field lines connect to the guard electrode. This volume is excluded from the sensitive one in the Monte Carlo simulation in order to define the cavity dose.

4.2.4 Uncertainty analysis

4.2.4.1 Experimental uncertainty

Experimental uncertainties are evaluated as type A and type B, i.e., using statistical and non-statistical means, respectively [106]. The combined type A uncertainties are evaluated by reproducing the measurements N times during each setup and calculating the standard deviation, noted σ_{rep}, being specific to a field strength and chamber model. The combined type B uncertainty contains other sources that cannot be evaluated easily without assumptions, e.g., the experimental setup and the discrepancies between the real and modelled chamber geometry. Because the data is expected to behave in a certain way, the discrepancy between expectation and observation is used to extract a sensible estimation of some of these type B sources. In the parallel orientation, the chamber signal should behave symmetrically between positive and negative magnetic field. Therefore, for each chamber, the uncertainty from the experimental asymmetry is estimated and added to the experimental uncertainty. This uncertainty can be determined by comparing the relative responses for the same magnetic field magnitude but opposite direction, i.e., $B_i = -B_{-i}$, using the following unbiased estimator:

$$\sigma^2_{\text{setup}} \approx \frac{1}{2(N-1)} \sum_{i=1}^{N} \left\langle \left(r_{\text{exp}}(B_i) - r_{\text{exp}}(-B_i) \right)^2 \right\rangle - \frac{1}{N} \sum_{i=1}^{N} \left(\frac{\sigma^2_{\text{rep,+,i}} + \sigma^2_{\text{rep,-,i}}}{2} \right) \quad (4.9)$$

where $N = 4$ is the number of magnetic field magnitudes (0.35 T, 0.5 T, 1 T and 1.5 T) and $r_{\text{exp}}(B_i)$ the relative response at magnetic field B_i relative to a field

strength of 0 T.

4.2.4.2 Numerical uncertainty

The statistical uncertainties of the Monte Carlo simulations are evaluated as type A, and they are denoted as σ_{stat}. The type B numerical uncertainties are defined by: 1) physical data used by the Monte Carlo algorithms, 2) inconsistencies between the real and blueprint detector geometry as well as the active volume definition, and 3) inconsistencies due to approximations in the transport algorithm.

Muir and Rogers [85] calculated the systematic uncertainties for Monte Carlo calculated beam quality correction factors for 32 ionization chamber models. These systematic uncertainties result from uncertainties in photon cross-sections, stopping powers, chamber dimensions, the use of a photon spectra instead of a linac model and potential fluctuations in the required energy to create an ion pair (W/e) with beam energy. In this study, W/e is assumed constant within the energy range of interest. Since photon cross sections uncertainties are correlated, the systematic uncertainty coming from photon cross section data is negligible [85], which is consistent with a study by Wulff et al [107]. Among the 32 studied models, the PTW 31010 and PTW 31016 are reported, the other two chambers (PTW31021 and PTW31022) are not in the study. However, because they share the similar materials (PMMA, graphite and aluminium) and dimensions, the same systematic uncertainty arising from the physical data is considered, $\sigma_{\text{data}} = 0.20\%$, coming mainly from the mean ionization value of graphite wall. This value is also consistent with the value found by Wulff et al [107] for 6 MV beams.

In the chamber geometry error, there are two sources of uncertainty: one coming from the discrepancies between blueprints and the real chamber, and the other one from the characterization of the dead volume. The geometry uncertainty, σ^2_{geom}, is defined as:

$$\sigma^2_{\text{geom}} = \sigma^2_{\text{print}} + \left(\frac{\partial r_{\text{num}}}{\partial V}\right)^2 \sigma^2_{\text{DV}} \tag{4.10}$$

with $\sigma_{\text{print}} = 0.1\%$, as established by Muir et al [85] where the impact of chamber dimensions variations on quality correction factors calculations was evaluated. The second part of equation 4.10 corresponds to the uncertainty due to the sensibility variations when the dead volume is removed. The sensitivity coefficient $|\partial r_{\text{num}}/\partial V|$ is calculated from dose response with and without consideration of the dead volume. The uncertainty σ_{DV} associated to our method to delineate the dead volume is set to an estimated value of 1%.

The last type B uncertainty comes from the algorithm consistency that can be assessed with a Fano cavity test. During this test, two source of uncertainty are present in the result, and the unbiased estimator of σ_{Fano} is found to be

$$\sigma^2_{\text{Fano}} \approx \frac{1}{M-1} \sum_{j=1}^{M} \left\langle \left(D_{\text{num},i}(B) - D_{\text{theory},i}(B) \right)^2 \right\rangle - \frac{1}{M} \sum_{j=1}^{M} \sigma^2_{\text{stat, j}} \tag{4.11}$$

where $M = 8$, the product of the number of chambers times the two energies investigated, $D_{\text{num},i}(B)$ is the calculated dose value compared to the theoretical value, $D_{\text{theory},i}(B)$, this during the Fano test for a given value of B. For the response at a field strength B relative to no magnetic field, one can show that the component of the algorithm error related to the magnetic field is dominant, compared to the remaining part, and therefore the algorithmic component of the uncertainty equals σ_{Fano} defined in equation 4.11.

In summary, the combined uncertainty is defined as :

$$\sigma^2_{\text{total}} = \sigma^2_{\text{rep}} + \sigma^2_{\text{setup}} + \sigma^2_{\text{geom}} + \sigma^2_{\text{stat}} + \sigma^2_{\text{data}} + \sigma^2_{\text{Fano}}. \tag{4.12}$$

4.3 Results

4.3.1 Numerical models

4.3.1.1 Validation of Monte Carlo methods

Additionally to previous validation of the beam model [81], experimental and simulated normalized dose response to maximum dose is shown in figure 4.3 for 0 T and 1.5 T, presenting good agreement in both cases which reassures the confidence in the beam model. The experimental uncertainty of film measurements is estimated at 2%, but unfortunately, this value is too conservative to extract an accurate estimate of the beam model uncertainty.

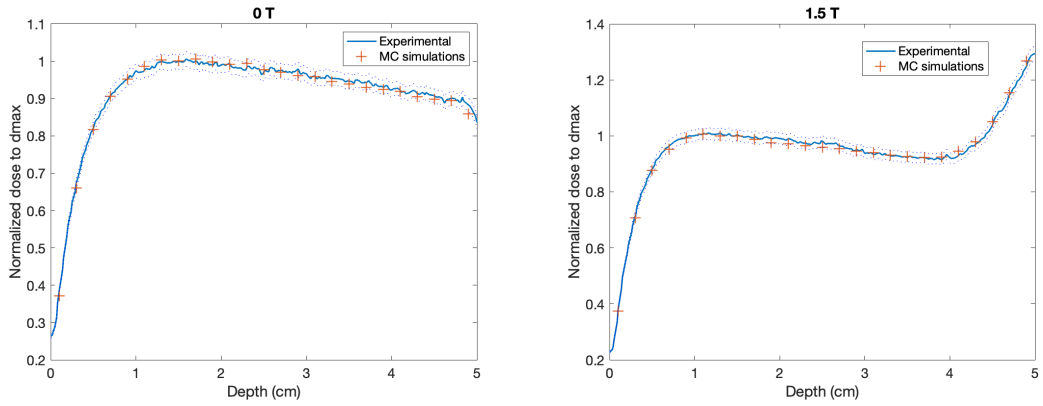

(a) **(b)**

Figure 4.3 – Validation of the beam model, normalized dose to $d_{\max}$ as a function of depth for a) 0 T and b) 1.5 T . An experimental uncertainty of 2% is assumed (dashed lines).

Fano tests are performed for the 4 ion chamber models as described in section 4.2.3.1. The transport parameters used in the simulations are verified with Fano tests. Using the method explained in section 4.2.4.2, the accuracy of the Fano test is better than 0.1% for the cases at 0 T and is 0.13% for 1.5 T. Hence, the algorithmic accuracy of chamber response in non-zero magnetic fields relative to no field is set equal to 0.13%.

4.3.1.2 Dead volume simulations

The calculated electric field lines for the chamber PTW31010 are shown in figure 4.4. The dashed lines define the volume where the lines go from the guard electrode towards the cavity wall, the charged particles inside this volume are not collected by the central electrode, thus this volume is removed from the collecting volume. For each chamber, the size of the removed dead volume is different. The percentage of the dead volumes are 15.62%, 19.31%, 23.00% and 18.45%, for PTW 31010, PTW 31016, PTW 31021 and PTW 31022, respectively. The dead volume is calculated using the dimensions provided in the blueprints. Unfortunately most of the mechanical tolerances are not provided so it is impossible to propagate this unknown. However an uncertainty is defined (in equation 4.10) to account for the impact of errors in the sensitive volume definition on the chamber response.

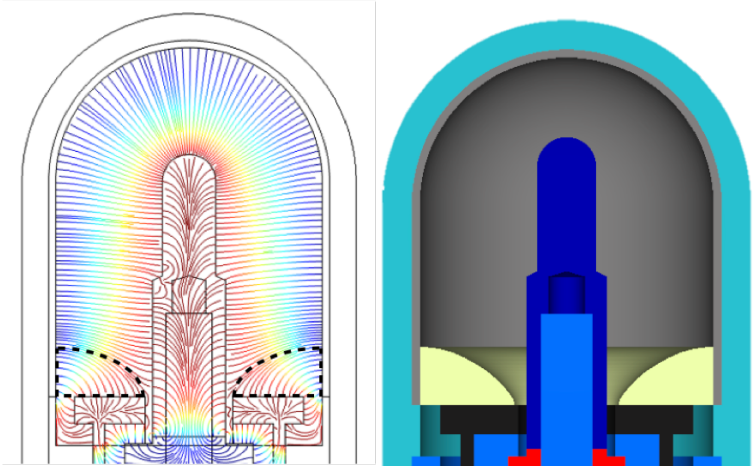

Figure 4.4 – a) Example of COMSOL simulation showing field lines for PTW 31010. The volume defined by the dashed black lines adjacent to the guard electrode is the removed dead volume. b) Dead volume in the Monte Carlo chamber model

4.3.2 Small-cavity ion chamber response in the presence of magnetic fields

4.3.2.1 Chamber axis parallel to the irradiation beam

The experimental measurements of the relative response (ratio of the chamber signal with and without magnetic fields) for the four ion chambers in the parallel orientation are presented in figure 4.5. The experimental type A uncertainty was below 0.23% in all cases. As a general trend, the relative response increases with magnetic field strength except for one of the smallest chambers (PTW 31022). Experimentally, the maximal magnetic field impact is distinctive for each chamber: 2.28%, 1.41%, 4.38% and 0.39% for PTW 31010, PTW 31021, PTW 31016 and PTW 31022, respectively. In the parallel orientation, relative dose responses are expected to be symmetrical with magnetic field strengths because the chamber geometry is symmetrical with respect to the beam and magnetic field directions. However, when experimental chamber readings are compared for same magnetic field strength but with opposite orientation ($B \rightarrow -B$), differences of up to 0.81 $\pm$ 0.19 % are revealed even for low magnetic fields, which could imply a variation coming from the experimental setup or from the chamber design itself. This effect is characterized into a type B uncertainty, the values for each chamber are calculated using equation 4.9 and are presented in table 4.III and 4.IV. This uncertainty must be accounted for the perpendicular orientation as well.

The experimental measurements are compared with the Monte Carlo simulations considering two sets of simulation: 1) using the full collective volume specified by the construction design; 2) removing the non-collecting volume from the manufacturing details based on COMSOL simulations. The ratio of the simulated relative response to experimental relative response for the parallel orientation is displayed as a function of magnetic field strength for each chamber model in figure 4.6. Considerable improvement between experimental and Monte Carlo simulation values is noticed when the collecting volume is reduced as shown in figure 4.6. The maximal variations of Monte Carlo simulations with respect to experiments are dis-

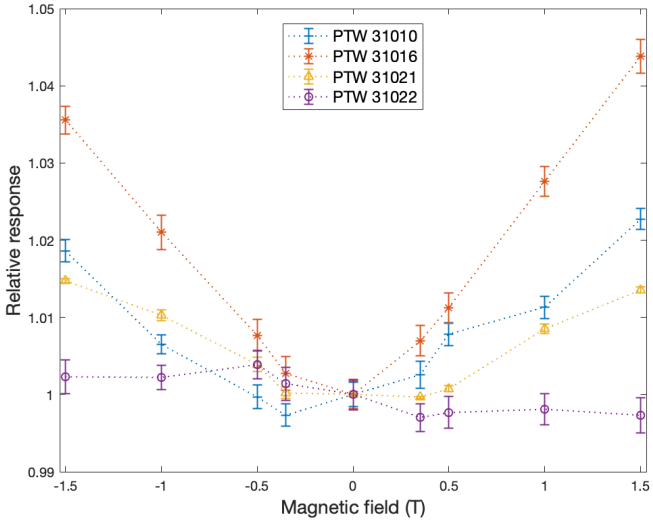

Figure 4.5 – Experimental relative response of PTW31010, PTW31016, PTW31021 and PTW31022 for parallel orientation. For each chamber, the experimental measurement at each magnetic is normalized by the experimental measurement at 0 T.

played in table 4.I. The agreement is always better than 0.6% for chambers PTW 31010, PTW 31021 and PTW 31022 and below 1.6% for PTW 31016. Considering a coverage factor of $k = 2$, when the dead volume is reduced, the results of the simulations for chambers PTW31010, PTW31021 and PTW31022 are within the uncertainty. For chamber PTW31016, for positive magnetic field, all points are with in the uncertainty when the dead volume is removed, however, in the negative side, the -1.5 T point is outside this region.

Chamber model	Full volume	Removed volume
PTW 31010	4.37 ± 0.20 %	0.60 ± 0.22 %
PTW 31016	1.91 ± 0.33 %	1.57 ± 0.32 %
PTW 31021	6.06 ± 0.20 %	0.60 ± 0.18 %
PTW 31022	2.81 ± 0.36 %	0.58 ± 0.32 %

Table 4.I – Maximal percentage difference in relative dose response between experiments and Monte Carlo simulations in the parallel orientation. The maximum values are taken over all magnetic fields strengths, i.e., $B = 0$ T, ± 0.3 T, ± 0.5 T, ± 1 T, ± 1.5 T.

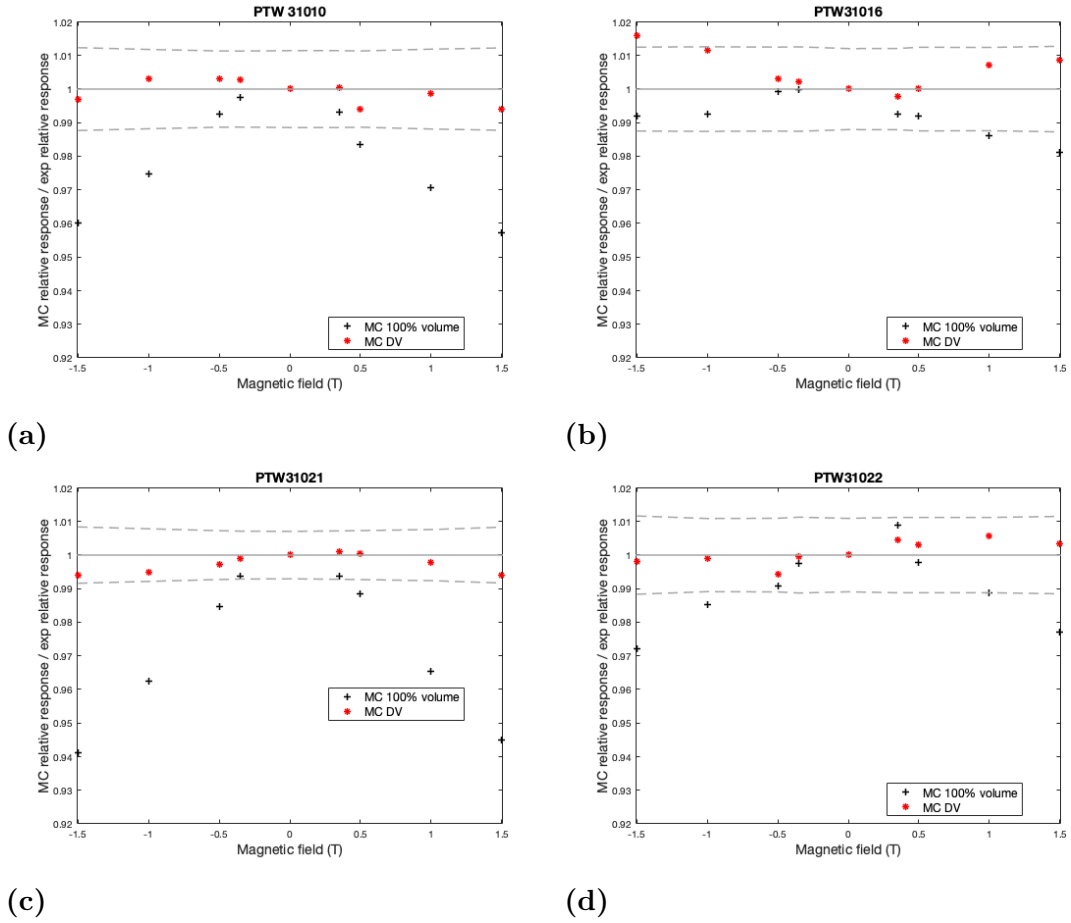

Figure 4.6 – Simulated relative response normalised to experimental relative response for the parallel orientation: (a) PTW 31010; (b) PTW 31016; (c) PTW 31021; (d) PTW 31022. The simulations for the full sensitive volume specified by the design (in black) and the sensitive volume after removing the dead volume(DV) characterized with COMSOL (in red) . The dashed line represents the total (type A and B) uncertainty($k = 2$).

4.3.2.2 Chamber axis perpendicular to the irradiation beam

The experimental measurements in the perpendicular orientation are presented in figure 4.7. The maximal type A experimental uncertainties range from 0.07% to 0.32% over the chamber models. In this orientation, relative dose response is more complex since the electrons are subjected to the ERE towards or outwards the dead volume. In the experimental setup for negative magnetic field, electrons

are deflected towards the stem which should result in a lower signal [40]. This behaviour is observed experimentally and the relative response is always less than unity for all chamber models. On the contrary, for positive magnetic field, electrons are deflected towards the tip. This should result in an increase of the relative signal with increasing magnetic field strength until a maximum is reached and the relative response then decreases [40]. Experimentally, this behaviour is observed in the ion chambers PTW 31010 and PTW 31016. In the case of chambers PTW 31021 and PTW 31022 a different trend is noticed, for $B > 0$ T it appears that the maximum is reached before 0.35 T and then the signal decreases as expected.

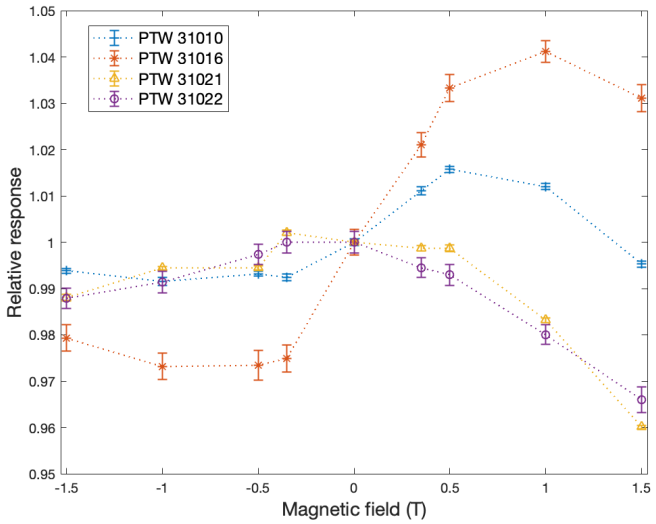

Figure 4.7 – Experimental relative response of PTW31010, PTW31016, PTW31021 and PTW31022 for perpendicular orientation.

To compare the simulation results to the experimental results, the ratio of simulated relative response to the experimental is presented in figure 4.8 for each chamber model. Removing the dead volume from the sensitive volume improves the agreement between experiments and simulations for all chambers. In general, the agreement is better for positive magnetic field strengths, although the degree of agreement is different for each chamber model. The dead volume is placed adjacent to the stem, so when electrons are deflected towards the stem, i.e. for $B < 0$ T,

the exclusion of the dead volume has a bigger impact. On the contrary, for $B > 0$ T, the dead volume removal is not as important since electron are mainly moving towards the tip of the chamber. The maximal percentage in difference of relative response between simulations and measurements is presented in table 4.II. For chambers PTW31010, PTW31021 and PTW31022, the agreement is always better than 0.7% for $B > 0$ T and better than 1.6% for $B < 0$ T. Removing the dead volume of chamber PTW31016 presents a minor improvement but not as good as the other models, with 4.13% for $B < 0$ and 2.15% for $B > 0$. The results of the models PTW31010, PTW31021 and PTW31022 for positive magnetic fields are within the uncertainty $k = 2$.

	B < 0 T		B > 0 T	
Chambel model	Full volume	Reduced volume	Full volume	Reduced volume
PTW 31010	3.25 ± 0.18 %	1.56 ± 0.19 %	2.10 ± 0.18 %	0.31 ± 0.19 %
PTW 31016	4.53 ± 0.42 %	4.13 ± 0.41 %	2.24 ± 0.43 %	2.15 ± 0.41 %
PTW 31021	3.65 ± 0.21 %	1.07 ± 0.19 %	3.57 ± 0.20 %	0.67 ± 0.20 %
PTW 31022	3.09 ± 0.37 %	1.50 ± 0.33 %	1.73 ± 0.37 %	0.70 ± 0.34 %

Table 4.II – Maximal percentage difference in relative dose response between experiments and Monte Carlo simulations in the perpendicular orientation. The maximum values are taken over all magnetic fields strengths, i.e., $B = 0$ T, ± 0.3 T, ± 0.5 T, ± 1 T, ± 1.5 T. When $B < 0$ the average trajectory of electrons is diverted towards the stem and when $B > 0$ the average trajectory of electrons is diverted towards the tip.

4.3.3 Verification of manufacturing details with micro-CT measurements

The agreement between experimental measurements and MC simulations is better for the parallel orientation than for the perpendicular configuration. In the latter, the chamber geometry plays a more important role, therefore an accurate chamber model is essential. The main factor identified as major source of uncertainty in MC results is the potential discrepancies between the manufacturing blueprints and the real geometry of the chamber, mostly due to its impact on the de-

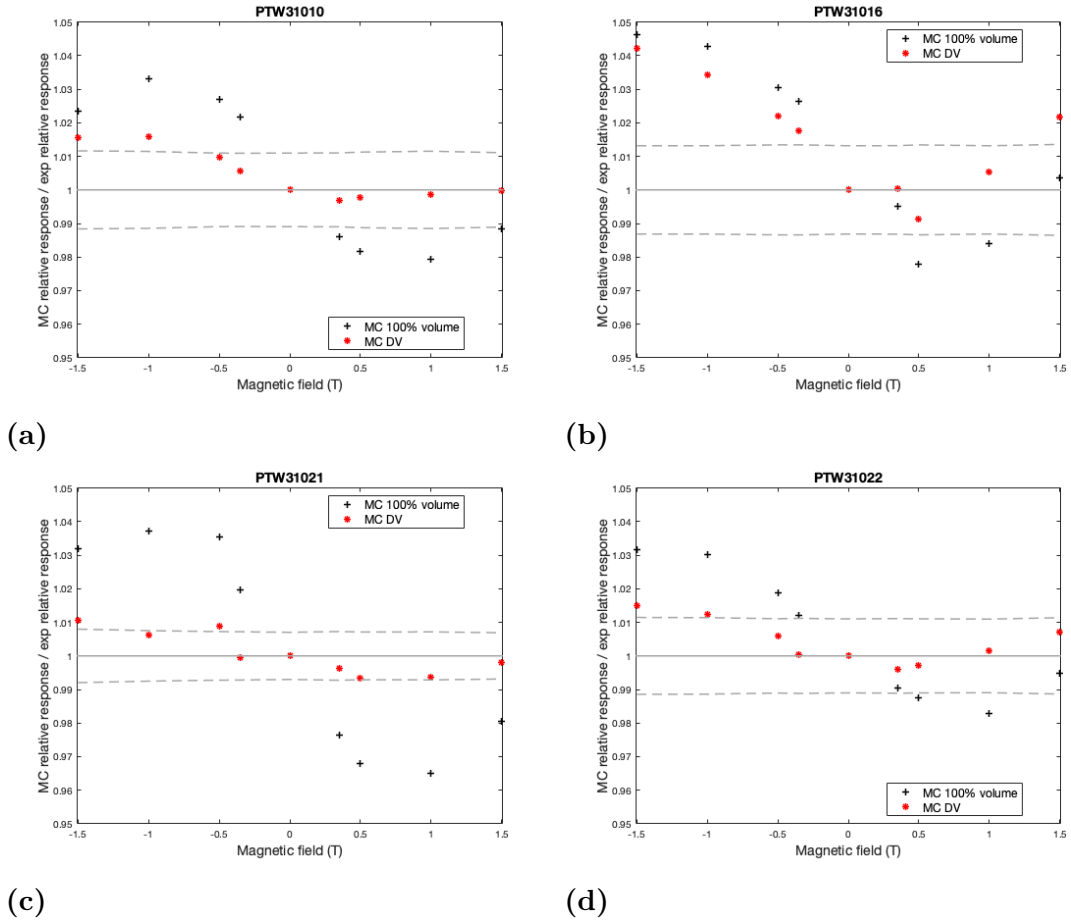

Figure 4.8 – Simulated relative response normalised to experimental relative response for the perpendicular orientation: (a) PTW 31010; (b) PTW 31016; (c) PTW 31021; (d) PTW 31022. The simulations for the full sensitive volume specified by the design (in black) and the sensitive volume after removing the dead volume(DV) characterized with COMSOL (in red) . The dashed line represents the total (type A and B) uncertainty($k = 2$).

termination of the dead volume and the potential presence of air gaps. To evaluate the accuracy of the blueprints and its translation into the MC model, micro-CT images of chambers PTW31010, PTW31016 and PTW31021 are acquired (Fig. 4.9). Unfortunately, it was not possible to acquire a micro-CT image for the PTW 31022. The micro-CT images reveal variations on the graphite wall thickness and on the air layer between the PMMA and the graphite wall for PTW31021 and PTW31016. For the PTW31010, there was not any visible air gap, as indicated

from the blueprints. Although it is difficult to accurately evaluate the dimensions of the chamber from the microCT, it is possible to have an idea or a reference of the size of the details missing in the blueprints. For the chamber PTW 31021, the air layer is actually bigger, by approximately 0.04 mm, that the one shown in the blueprints. For PTW 31016, in figure 4.9c, the air layer is not indicated in the manufacturing drawings. In magnetic fields, the presence of an air layer can have a significant effect on detector dose response because of ERE; for instance, when the air layer is included for the PTW31021 model, the maximal difference in the relative response is of 0.38% in the parallel orientation and of 0.25% in the perpendicular orientation. Another feature revealed from the microCT image of PTW31021 is that the thickness of the air layers is not uniform, as shown in figure 4.9b), this is very difficult to model without knowing the exact size of the layers. In general as the cavity size is smaller, it is more challenging to realistically model the air layer. Discrepancies between micro-CT and blueprints that one would normally dismiss for being too small to cause perturbation effects turn out to cause much bigger effects when there is a strong magnetic field. These discrepancies also impact the characterization of the dead volume since the calculated electric field lines depends on the chamber geometry. Additionally at the dead volume boundary, the behaviour of charged particles is more complex, specially in the presence of magnetic fields. Near the boundary, particles inside the dead volume might be collected and some outside the boundaries might not. Another assumption of the model is that once the dead volume is excluded, the collection efficiency is assumed to be uniform in the rest of the sensitive volume [108], the inhomogeneities of the sensitive volume is beyond the scope of this study and is left for future work.

4.3.4 Generated data with uncertainty budget

The model uncertainty is calculated for each orientation at 0.35 T and 1.5 T following the framework explained at section 4.2.4 and presented at table 4.III and 4.IV for the parallel and perpendicular orientation, respectively. The uncertainty arising from experimental repeatability, experimental setup, chamber geometry,

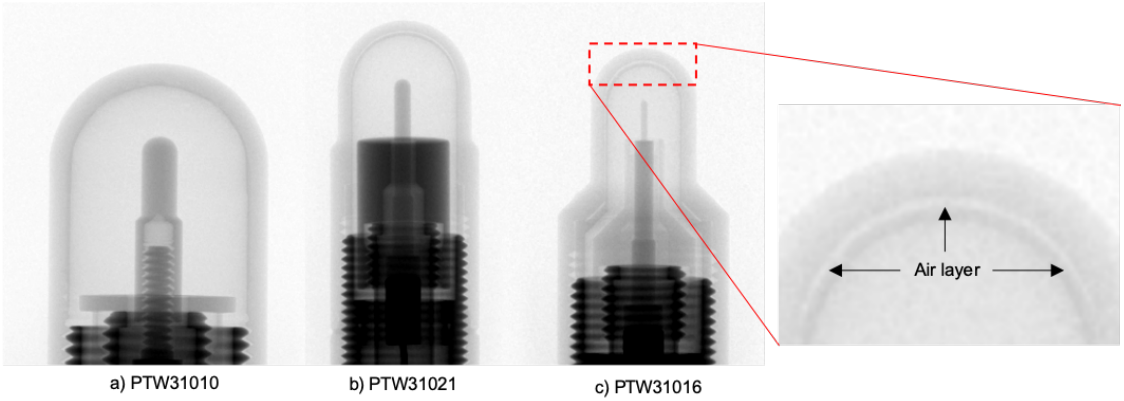

Figure 4.9 – Micro-CT image of a) PTW31010 where the microCT images appear in agreement with the blueprints, b) PTW31021 where the air layer is indicated in the blueprints but in the microCT image it appears to be at least 4 times bigger than expected and c) PTW31016 where the air layer is not indicated in the technical drawing.

Monte Carlo statistical uncertainty, the Fano test and the physical data, are shown at table 4.III and 4.IV. The combined uncertainty ranges from 0.36% to 0.61% in the parallel orientation and between 0.34% and 0.68% for the perpendicular orientation. For both orientations, the combined uncertainty increases with magnetic field. The contribution of each uncertainty sources varies for each chamber and each magnetic field. For instance, the largest contribution emerges from the experimental setup, in both orientations, for chamber PTW31010, PTW31016 and PTW31021, while for chamber PTW31021 at $B = 1.5$ T it comes from the geometry in the parallel orientation and from the physical data in the perpendicular orientation.

4.3.5 Quality correction factors

The calculated correction factors for both configurations are presented in table 4.V for 1.5 T and 0.35 T which are the magnetic field strengths used in commercially-available MR-Linacs units. The combined uncertainty of the correction factors considers the type A uncertainty from the Monte Carlo simulations of the absorbed dose to water and the uncertainties as referred on table 4.III.

			PTW 31010		PTW 31016		PTW 31021		PTW 31022	
	Source	Type	$\sigma_{0.35\ T}$	$\sigma_{1.5\ T}$	$\sigma_{0.35\ T}$	$\sigma_{1.5\ T}$	$\sigma_{0.35\ T}$	$\sigma_{1.5\ T}$	$\sigma_{0.35\ T}$	$\sigma_{1.5\ T}$
Experimental	Repeatability	A	0.17%	0.14%	0.20%	0.22%	0.01%	0.04%	0.18%	0.23%
	Irradiation setup	B	0.45%	0.45%	0.44%	0.44%	0.15%	0.15%	0.35%	0.35%
Numerical	MC statistics	A	0.17%	0.18%	0.25%	0.27%	0.20%	0.19%	0.30%	0.26%
	Detector geometry	B	0.11%	0.26%	0.10%	0.18%	0.10%	0.24%	0.10%	0.17%
	Physical data	B	0.20%	0.20%	0.20%	0.20%	0.20%	0.20%	0.20%	0.20%
	Algorithm consistency	B	0.13%	0.13%	0.13%	0.13%	0.13%	0.13%	0.13%	0.13%
	Combined		0.57%	0.61%	0.60%	0.64%	0.36%	0.42%	0.56%	0.58%

Table 4.III – Uncertainty budget of chamber relative response estimated from various sources of uncertainty for the parallel orientation. Type A and B uncertainties refer to values estimated with statistical methods and non-statistical methods, respectively.

			PTW 31010		PTW 31016		PTW 31021		PTW 31022	
	Source	Type	$\sigma_{0.35\ T}$	$\sigma_{1.5\ T}$	$\sigma_{0.35\ T}$	$\sigma_{1.5\ T}$	$\sigma_{0.35\ T}$	$\sigma_{1.5\ T}$	$\sigma_{0.35\ T}$	$\sigma_{1.5\ T}$
Experimental	Repeatability	A	0.09%	0.06%	0.26%	0.29%	0.05%	0.03%	0.21%	0.28%
	Irradiation setup	B	0.45%	0.45%	0.44%	0.44%	0.15%	0.15%	0.35%	0.35%
Numerical	MC statistics	A	0.15%	0.16%	0.30%	0.30%	0.20%	0.17%	0.25%	0.23%
	Detector geometry	B	0.13%	0.14%	0.15%	0.18%	0.10%	0.10%	0.13%	0.10%
	Physical data	B	0.20%	0.20%	0.20%	0.20%	0.20%	0.20%	0.20%	0.20%
	Algorithm consistency	B	0.13%	0.13%	0.13%	0.13%	0.13%	0.13%	0.13%	0.13%
	Combined		0.55%	0.55%	0.66%	0.68%	0.36%	0.34%	0.56%	0.57%

Table 4.IV – Uncertainty budget of chamber relative response estimated from various sources of uncertainty for the perpendicular orientation. Type A and B uncertainties refer to values estimated with statistical methods and non-statistical methods, respectively.

	Parallel orientation		Perpendicular orientation	
Chambel model	0.35 T	1.5 T	0.35 T	1.5 T
PTW 31010	0.9981 ± 0.0057	0.9802 ± 0.0060	0.9930 ± 0.0055	1.0015 ± 0.0055
PTW 31016	0.9961 ± 0.0060	0.9466 ± 0.0060	0.9802 ± 0.0065	0.9459 ± 0.0064
PTW 31021	1.0003 ± 0.0036	0.9891 ± 0.0041	1.0062 ± 0.0036	1.0399 ± 0.0036
PTW 31022	0.9997 ± 0.0056	0.9957 ± 0.0057	1.0107 ± 0.0056	1.0243 ± 0.0058

† Discrepancies between microCT and blueprint geometry.

Table 4.V – Estimated quality correction factors of four chamber models with two magnetic field strengths in each orientation. The uncertainty budget is detailed in table 4.III and 4.IV.

4.4 Discussion

4.4.1 Comparison with other studies

Chamber response in the presence of magnetic fields exhibits a complex behaviour due to the dependency on multiple factors such as magnetic field strength

and orientation, chamber size and chamber design/geometry. In general, excluding the dead volume from the sensitive volume improves significantly the agreement between the Monte Carlo simulations and the measurements for both orientations.

4.4.1.1 Chamber axis parallel to the irradiation beam

Looe *et al* [94] simulated the response of the chamber PTW 31021 and PTW 31010 for three magnetic field strengths: 0.35 T, 1 T and 1.42 T for a 6 MV photon beam for 3 possible orientations where the beam and the magnetic are always perpendicular: 1) chamber axis parallel to the beam, 2) chamber axis parallel to the magnetic field and 3) chamber axis perpendicular to both the beam and the magnetic field. The dead volume was also excluded by calculating the electric field. Experimental measurements were performed only for the first configuration. Their results comparing simulations and experiments are consistent with ours; the magnetic field effect is less than 2% for the first configuration and the exclusion of the dead volume reduces the disagreement between simulations and measurements from approximately 3% to less than 0.5%. The less than 2% magnetic field effect is also observed in the third orientation which corresponds to the perpendicular orientation of this study with negative magnetic field. However this is not the case when the magnetic field is pointed in the opposite direction, i.e., when electrons are generally going towards the tip, the effect is around 4%.

4.4.1.2 Chamber axis perpendicular to the irradiation beam

In this configuration, the chamber geometry details plays a key role in the response. For negative magnetic fields, i.e., when the Lorentz force acting on electrons points towards the stem, the experimental relative response is always less than unity. The reduction in the relative response could be explained by the higher fluence of electrons towards the region with the dead volume where charges are not effectively collected. Meijsing et al [35] explained that there is a reduction in the number of electrons entering the cavity and that the electron pathlength increases

for low magnetic fields up to a strength and then decreases depending on the electron energy. In small cavity ion chambers, the enlargement of the pathlength could have a minor impact since the air cavity is smaller. The reduction of the number of electrons entering the cavity and the variation of their pathlength could also account for the reduction in the relative response.

The importance of characterizing the effective collecting volume in the presence of magnetic fields has been demonstrated and studied by several groups [40, 79, 94, 39]. This was accomplished by using different models for determining the dead volume. Spindeldrier *et al* [40] used a cylindrical dead volume and simulated the response for different dead volume sizes. In the perpendicular orientation, for a positive magnetic field, the best agreement between experimental and MC simulations was for the biggest dead volume ($r = 0.15$ cm). On the contrary, for a negative magnetic field, the agreement was better for the smallest dead volume ($r = 0.07$ cm). Demonstrating that the same dead volume is unable to adequately reproduce the measurements for both magnetic field orientations. Additionally, the agreement is always better in the positive magnetic field, i.e., when electrons are diverted towards the tip. It is worth noting that the agreement between measurements and MC simulations decreases with increasing magnetic field which is also observed in our results.

For positive magnetic fields, i.e. when the Lorentz force acting on electrons points towards the tip, our results show that there is not a unique trend in the perpendicular orientation for small cavity ion chambers meaning that there is no simple explanation for this complex behaviour. For the chambers PTW 31010 and PTW 31016, the relative response rises up to a maximum and then it decreases. For the chambers PTW 31021 and PTW 31022, the response decreases with increasing magnetic field strength. In all cases the agreement is better when the dead volume is reduced which coincides with the results of Spindeldreier [40]. Our results show that switching the magnetic field orientation has a significant impact in the relative response in this configuration, the difference can be as big as 6% differing from the 1% of Spindeldreier.

4.4.1.3 Characterizing the dead volume

Malkov *et al* [79] studied the size of the sensitive volume by excluding the volume corresponding to 1 mm or 5 mm away from the guard electrode which correspond to 17.2% and 8.6% of the sensitive volume of the ion chamber PTW 31010. The maximal variation for 7 MV photon beam was 1.93 ± 0.06 % when excluding 17.2% for positive magnetic fields. In our results, for the same chamber model and configuration with an energy of 6 MV and removing 15.62% from the sensitive volume, the discrepancy is minimal. That indicates, that the knowledge of the shape and location of the dead volume is fundamental to achieve a good agreement.

The size of the dead volume in small cavity ion chamber corresponds to a higher fractional volume than in regular size chambers. For instance, for a Farmer ionization chamber PTW 30013, the dead volume correspond to 7% of the nominal volume [39]. In the same reference, the difference between experiment and Monte Carlo simulation when this dead volume is removed in the perpendicular orientation is between 0.02% and 0.31%. The agreement is quite good for both directions of the magnetic field. Implying that even if the effect of the magnetic field is more important in Farmer ion chambers, a better agreement can be achieved since the presence of the dead volume is not as significant as for small cavity ion chambers.

4.4.2 Impact of geometry discrepancies

The dosimetric characterization and calibration of MRgRT beams could require a change of practice, not only in the experimental techniques but also when it comes to detector dose response modelling with Monte Carlo methods. In conventional radiotherapy broad beams, small air gaps inside or around ionization chambers often have negligible impact on their dose response. This is governed by the principle that, in the first order, Fano's theorem is applicable; in the absence of magnetic fields and in an infinitely broad beam with homogeneous fluence irradiating a medium of homogeneous properties, the theorem predicts that charged particle

equilibrium exists and the electron fluence remains unchanged from variations in density. In the presence of a homogeneous magnetic field, Fano's theorem simply cannot hold with external photon beams, as shown in previous work [45, 57, 62]. The consequence is that equilibrium conditions are violated and therefore air gaps should be expected to perturb the electron fluence crossing the detector sensitive volume, hence leading to a modification of its dose response. Any geometrical detail near the cavity, especially changes in medium density (i.e., in terms of interaction site per unit volume - or electron density), should therefore be fully taken into account to accurately model the electron fluence perturbation and its effect on dose response. This brings us to the conclusion that, to model the response of small-cavity ion chambers in the presence of magnetic fields, it is essential to consider all the regions near the sensitive volume where air is present. The MicroCT images, shown in figure 4.9, indicate a difference in the size of the air layer for the chamber PTW31021 and the presence of the air layer in PTW31016 that is not indicated in the blueprints. An air layer is also modelled for the PTW31022 based on the blueprints. For bigger chambers, the size of the air layer is negligible when compared to the cavity size. However for small-cavity ion chamber, the air layer becomes more significant since the sensitive volume is smaller. The PTW31016 and the PTW31022 are the same size and are the smallest chambers investigated in this work. One difference between these two chambers is near the guard ring. For instance, the PTW31016 has a smaller guard ring and therefore there is a bigger air gap between the guard electrode and the graphite wall. The presence of a larger air region near the sensitive electrode would also naturally affect the characterization of the dead volume. This, combined with an inaccurate model of the air layer, could have a significant impact on the modelled detector dose response. This could explain why there is a larger disagreement between experiments and simulations for the PTW31016 chamber and also why the experiments show a higher response for this chamber compared to the other ones when there is a strong magnetic field.

In spite of the discrepancies encountered for the PTW31016, the models of the other three chambers, PTW31010, PTW31021 and PTW31022, are valid for

the parallel orientation and for the positive magnetic fields in the perpendicular orientation where electrons are deflected towards the tip of the chamber. Future work could incorporate tolerances on the dimensions of the chamber to evaluate the sensitivity of the response from blueprints, which could be included in a more complete uncertainty budget.

4.4.3 Recommendations for determination of quality correction factors

The magnetic field highlights the chamber geometry imperfections in simulations and in measurements and discrepancies between simulations and experiments increases with magnetic field strength. Our recommendation is to account for these discrepancies in a realistic uncertainty budget. The experimental setup of this study is different from the one used in the clinic in MR-Linac environments. In the perpendicular orientation, the physical phenomena are more important, providing a better understanding of the chamber response behaviour, and yields a larger quality correction factor as expected. Based on our results, it is strongly recommended that reference dosimetry measurements be performed with the chamber parallel to the irradiation beam and perpendicular to the magnetic field. This way, irradiations implicating an increase or decrease of electrons crossing the dead volume can be avoided. In the particular case of small cavity ion chambers measurements and for Monte Carlo simulations, PTW31010, PTW31021 and PTW31022 present better agreement between experimental and simulated values.

4.5 Conclusion

This study shows the complexity of characterizing small cavity ion chamber response in the presence of magnetic fields. Several factors that appear insignificant in conventional conditions, such as fine air layers and the exact position of the sensitive volume, become an issue in the presence of magnetic fields. For small cavity ion chambers, the dead volume represents a significant portion of the sensitive volume ($\approx 20\%$) and its removal is decisive to improve the accuracy of the

simulations. In the presence of magnetic fields, a higher level of details in manufacturing drawing compared to conventional conditions is essential to model the detector dead volume and the detector dose response. This work demonstrates that even small discrepancies in chamber modelling can be significant when modelling small cavity chamber response in the presence of magnetic fields.

Acknowledgements

This research was enabled in part by the support provided by Calcul Québec (www.calculquebec.ca) and Compute Canada (www.computecanada.ca). We acknowledge Frédéric Sirois and CMC Microsystems for providing the computational resources required to perform the numerical simulations. We also gratefully acknowledge financial support by the Consejo Nacional de Ciencia y Tecnología (CONACyT) and the Natural Sciences and Engineering Research Council of Canada (NSERC RGPIN/04178-2015). Finally, we are grateful to Dr. Christian Pychlau and Dr. Rafael Kranzer from PTW for kindly providing the engineering details of the detectors and precious feedback on this study.

CHAPTER 5

INTRODUCTION TO ARTICLE 2

5.1 Context

The measurement of absorbed dose at a point in water is fundamental for the calibration of radiotherapy beams. This measurement involves using a detector with a finite volume, i.e. not a point, manufactured with materials different from water, changing physical properties such as mass density, atomic number, and the mean ionization potential. Cavity theories describe the differences in detector dose response introduced by the detector but are limited to specific conditions. A more accurate approach to characterize detector response under general conditions is to decompose it into specific perturbation factors coming from detector presence.

The total perturbation factor, P, is a product of subfactors coming from the structural components of the detector such as the central electrode, the wall, and the stem, and from differences in density and atomic composition. Each perturbation sub-factor corresponds to a ratio between the geometry excluding and including the perturbing element. For instance, to evaluate the central electrode (CE) perturbation, the ratio is $D_{\text{detector without CE}}/D_{\text{detector with CE}}$.

In conventional reference dosimetry, these sub-factors differ from unity less than a few percent [45]. However, this is not true for non-conventional dosimetry; Scott et al [97] showed that density perturbation factors could differ from unity by as much as 60% in small beams. The same study demonstrated that besides the volume averaging factor, the perturbations on detector dose response in the solid-state detectors and ionization chambers mainly come from density differences rather than from atomic number differences.

Several approaches with different chains of perturbation subfactors have been proposed [105, 109, 110, 111, 97, 112, 113, 98]. In the article, the formalism by Bouchard et al [45, 113] was adapted to account for the effect of the magnetic

field on three perturbation factors. The first is the overall perturbation factor, P_{MC}, accounting for extracameral components, the atomic properties, and the density. The second is the density perturbation factor, P_{ρ}. The third is the volume averaging perturbation factor, P_{vol}. The subfactors are not independent of each other, i.e. they are correlated. Therefore, the overall perturbation factor is studied rather than the individual perturbations. Only the density perturbation factor is calculated individually due to its predominance in small fields. The impact of the 1.5 T magnetic field is calculated with the ratio of the perturbation factor with and without magnetic fields, i.e. $P_i(1.5\ \mathrm{T})/P_i(0\ \mathrm{T})$.

With the increasing use of MRI-linac treatments, small fields will become part of the regular clinical workflow. Therefore, it is necessary to understand the interplay between them and magnetic fields and to characterize detectors suitable for small field dosimetry. The magnetic field impact on detector response depends on its strength and direction and on the irradiation conditions.

The objectives of this work are

1. To provide physical insights on the effects of magnetic fields on three small-cavity chambers (PTW31010, PTW31021, PTW31022) and in two solid-state detectors (silicon diode PTW60012 and microDiamond PTW60019)
2. To calculate perturbation factors and quality correction factors of several detectors irradiated by beams of multiple field sizes in the presence of magnetic fields.
3. To determine the conditions that minimize perturbations on detector response.

5.2 Results and impact

Monte Carlo simulations of dose-responses in water are determined with Monte Carlo simulations (EGSnrc), using Elekta Unity 7 MV FFF phase-spaces of square field widths between 0.25 and 10 cm. The detectors are three ionization chambers (PTW31010, PTW31021, and PTW31022) validated previously [41] and two solid-

state detectors (PTW60012 and PTW60019). The four detector-axis orientations, shown in figure 6.2, are: 1) parallel to the photon and perpendicular to the 1.5 T field, 2) perpendicular to photon beam and to the 1.5 T field, with the Lorentz pointing towards the stem, 3) perpendicular to photon beam and to the 1.5 T field, with the Lorentz pointing towards the tip, and 4) perpendicular to photon beam and parallel to the 1.5 T field.

In the article, the magnetic field effect on small-cavity detector dose response to multiple irradiation field sizes is quantified by the perturbation factors: P_ρ, P_{MC}, and P_{vol} in different orientations. The ratio $P_i(1.5\ \mathrm{T})/P_i(0\ \mathrm{T})$ quantifying the magnetic field effect in each perturbation factor is shown in figures 6.3-6.8. In this section, the perturbation factors in the absence and presence of magnetic fields are explicitly presented in figures 5.1, 5.2 and 5.3.

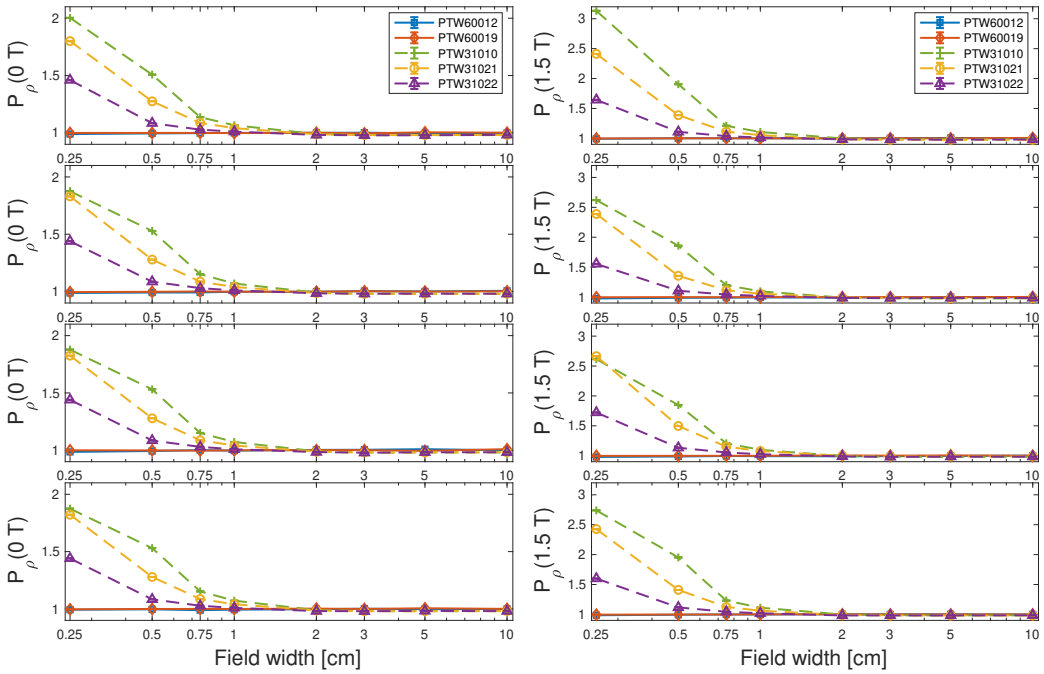

Figure 5.1 – On the left side, P_ρ, for solid detectors (PTW60012 and PTW60019) and ionization chambers (PTW31010, PTW31021 and PTW31022) for four orientations as function of the field sizes at 0 T. On the right side, P_ρ at 1.5 T.

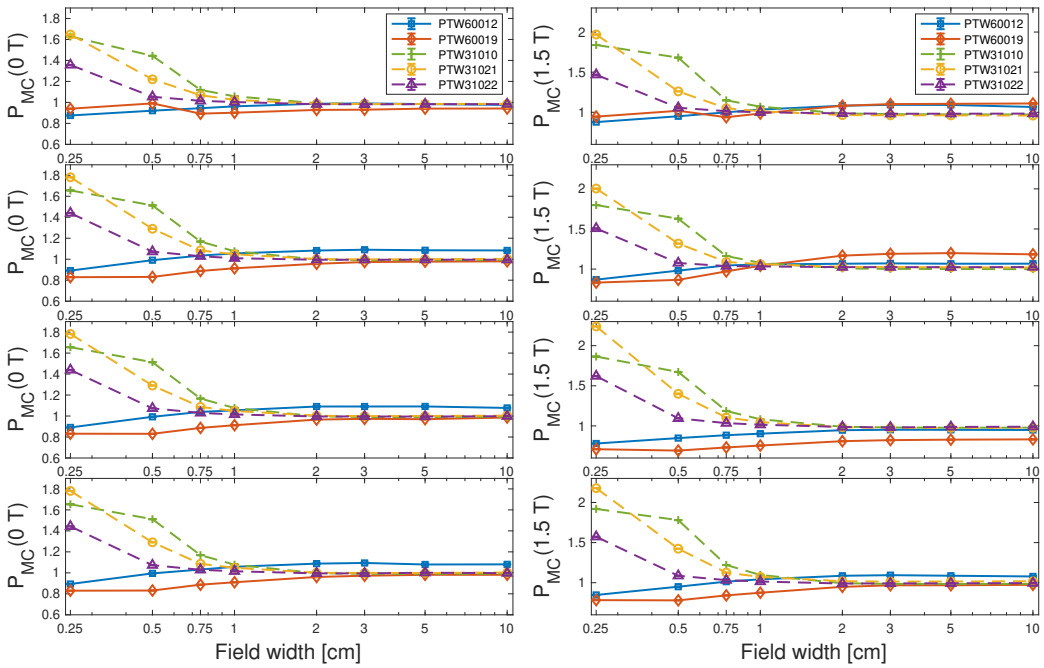

Figure 5.2 – On the left side, P_{MC}, for solid detectors (PTW60012 and PTW60019) and ionization chambers (PTW31010, PTW31021 and PTW31022) for four orientations as function of the field sizes at 0 T. On the right side, P_{MC} at 1.5 T.

Additionally, the percentage of maximal variations of each perturbation factor from unity, at 0 T and 1.5 T, are listed in the table 5.I for all detectors and in the four orientations.

These results show that for solid-state detectors, the magnetic field impact on P_{MC} is more significant than in the other two factors. P_{MC} exhibits different trends with orientation, indicating that the beam incident angle and geometry play a crucial role. The effect is more substantial at large fields, as observed on the right of figure 5.2. Perturbations coming from the extracameral components are more critical in the solid-state detectors than in ionization chambers.

On the contrary, for ionization chambers, the magnetic field effect is more important P_{ρ}. In most cases, the magnetic field doubles the perturbation factor, see table 5.I. The magnetic field impact is smaller in P_{MC}, probably because the

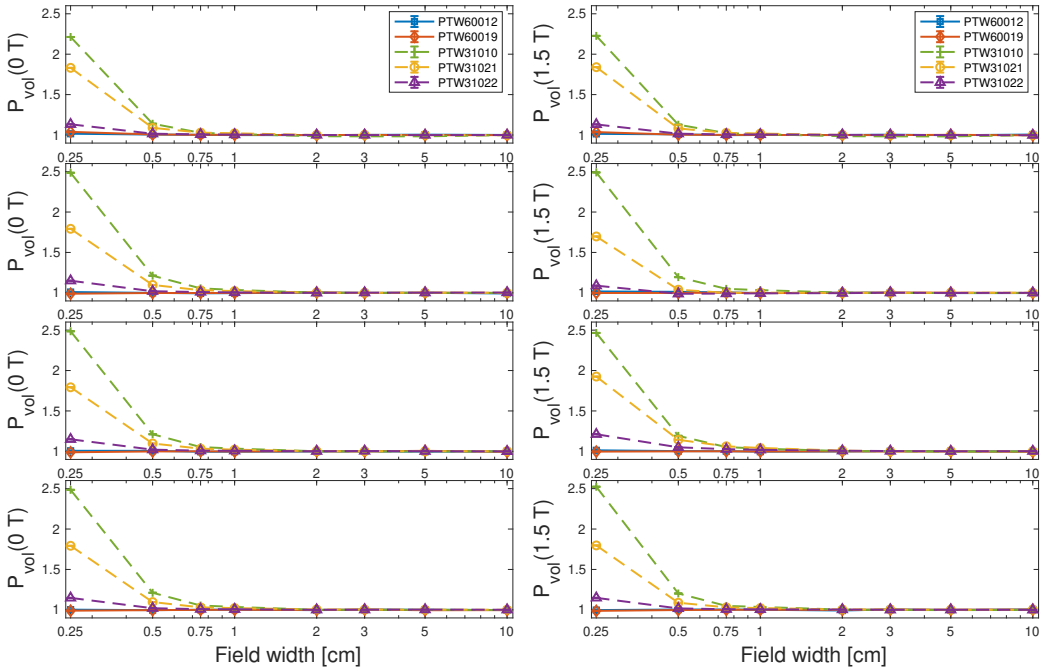

Figure 5.3 – On the left side, P_{vol}, for solid detectors (PTW60012 and PTW60019) and ionization chambers (PTW31010, PTW31021 and PTW31022) for four orientations as function of the field sizes at 0 T. On the right side, P_{vol} at 1.5 T.

extracameral perturbations act in the opposite direction of P_ρ and the overall perturbation is somewhat compensated. The magnetic field effect on P_{MC} is complex and varies with orientations because the incident beam encounters different geometries or structural components in each orientation.

P_{vol} remains the most significant perturbation in small fields, with and without magnetic fields. However, P_{vol} at 0 T and at 1.5 T remains of the same order in most cases, except for chambers PTW31021 and PTW31022 that over-respond and under-respond in orientations 2 and 3, respectively, at small fields. For solid-state detectors, the variation between P_{vol} in the absence and presence of magnetic fields is smaller than 1%.

Finally, k_{Q_B} factors account for the variation in beam quality due to the magnetic field and are presented in figure 5.4 and in the article in tables 6.I, 6.II 6.III

Orientation	Detector	P_{MC}		P_{ρ}		P_{vol}	
		0 T	1.5 T	0 T	1.5 T	0 T	1.5 T
1	PTW60012	12.46%	12.23%	1.04%	0.79%	1.55%	1.40%
	PTW60019	10.70%	10.98%	0.47%	0.76%	3.88%	3.61%
	PTW31010	62.82%	83.88%	100.32%	213.22%	121.30%	122.66%
	PTW31021	64.70%	96.97%	80.07%	141.18%	83.11%	83.94%
	PTW31022	35.69%	46.81%	46.06%	64.34%	13.25%	13.08%
2	PTW60012	10.85%	13.16%	1.26%	2.41%	0.99%	1.73%
	PTW60019	17.14%	19.92%	0.50%	0.38%	1.09%	0.37%
	PTW31010	65.58%	79.79%	87.55%	162.12%	148.57%	149.00%
	PTW31021	78.12%	100.38%	83.02%	138.81%	79.24%	69.77%
	PTW31022	43.96%	50.67%	43.94%	55.38%	15.01%	8.88%
3	PTW60012	10.88%	21.94%	1.45%	2.08%	0.68%	1.28%
	PTW60019	16.96%	30.77%	0.96%	0.46%	1.15%	0.50%
	PTW31010	65.63%	86.44%	87.78%	161.48%	148.62%	146.53%
	PTW31021	78.24%	123.98%	82.53%	166.48%	79.27%	92.53%
	PTW31022	43.94%	62.10%	43.99%	72.25%	14.92%	21.14%
4	PTW60012	10.64%	15.28%	1.10%	1.42%	0.37%	0.84%
	PTW60019	17.02%	21.99%	0.58%	0.40%	1.03%	1.26%
	PTW31010	65.37%	91.95%	87.47%	173.95%	148.51%	152.32%
	PTW31021	78.05%	117.85%	82.22%	142.63%	79.27%	79.72%
	PTW31022	44.27%	57.27%	44.07%	59.99%	14.80%	14.85%

Table 5.I – Percentage of maximal variation with respect to unity of the perturbation factors. The uncertainty is not presented here but in all cases it is smaller than 0.1%

6.IV, 6.V, for each detector and orientation. Solid-state detectors yield large k_{Q_B}, close to 1.2, in orientation 1 (recommended orientation), and chamber PTW31022 yields k_{Q_B} factors closer to unity in orientations 2 and 4.

This study quantifies and explains the magnetic field effect on small-cavity detector dose-responses to megavoltage photon beams of multiple sizes. These findings are crucial for the dosimetry in MR-Linac, where regular use of small photon beams is expected to be included to deliver complex radiation therapy. The magnetic field strongly impacts solid-state detector dose responses in the recommended measurement orientation, especially for large fields. They are not suitable for reference dosimetry measurements in magnetic fields. In general, ionization chambers yield a k_{Q_B} closer to unity, especially in orientations 2 and 4.

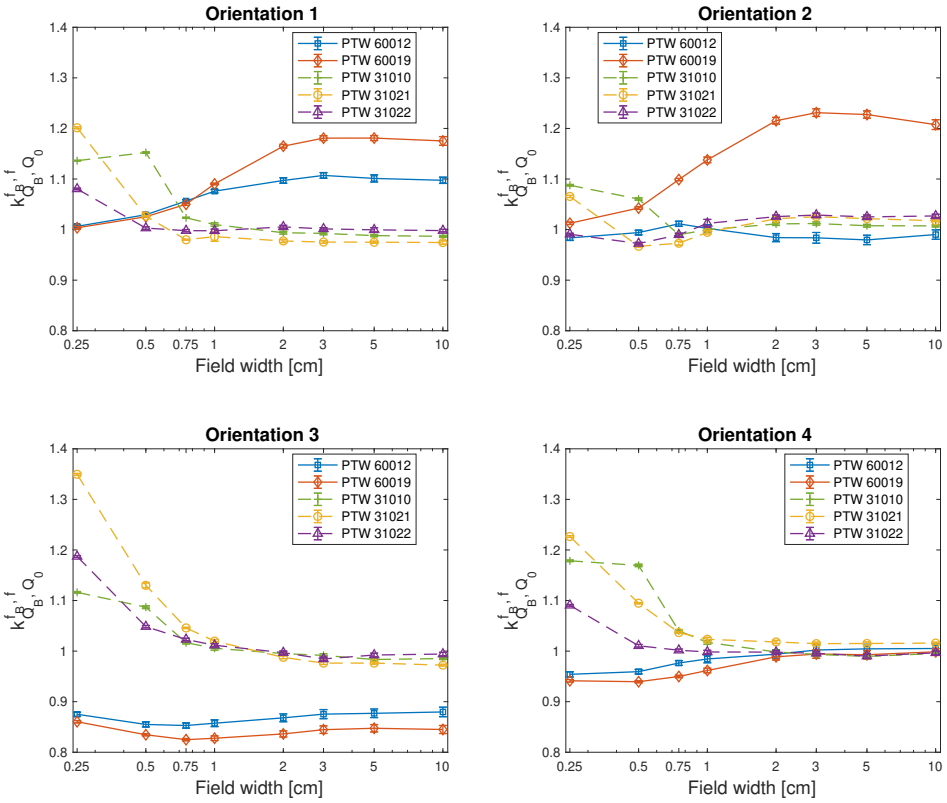

Figure 5.4 – Quality correction factors accounting for the magnetic field effect as a function of field size for four orientations.

5.3 Contributions

1. Yunuen Cervantes Espinosa
   - Development of original idea
   - Monte Carlo simulations
   - Result analysis
   - Writing of the article
2. Jasmine Duchaine
   - Solid-state detector models
   - Revision of the article
3. Ilias Billas

- Scientific support
- Revision of the article

4. Simon Duane
    - Scientific support
    - Revision of the article
5. Hugo Bouchard
    - Development of original idea
    - Result analysis
    - Scientific support
    - Revision of the article

CHAPTER 6

DETECTOR PERTURBATION AND QUALITY CORRECTION FACTORS IN MAGNETIC RESONANCE GUIDED RADIATION THERAPY SMALL PHOTON BEAMS

This article was published in the journal Physics and Medicine and Biology, volume 66, number 22 [114]. The results were presented in an oral presentation at the AAPM annual congress 2021. Preliminary results of this work were presented in a poster at the AAPM annual congress 2020.

Monte Carlo calculation of detector perturbation and quality correction factors in a 1.5 T magnetic resonance guided radiation therapy small photon beams

Yunuen Cervantes [1,2], Jasmine Duchaine[1,2], Ilias Billas[3,4], Simon Duane[3], and Hugo Bouchard[1,2,5]

[1] *Département de physique, Université de Montréal, Complexe des sciences, 1375 Avenue Thérèse-Lavoie-Roux, Montréal, Québec H2V 0B3, Canada.*

[2] *Centre de recherche du Centre hospitalier de l'Université de Montréal, 900 Rue Saint-Denis, Montréal, Québec, H2X 0A9, Canada*

[3] *National Physical Laboratory, Chemical, Medical and Environmental Science Department, Teddington, United Kingdom*

[4] *Joint Department of Physics, The Institute of Cancer Research and The Royal Marsden NHS Foundation Trust, London, United Kingdom*

[5] *Département de radio-oncologie, Centre hospitalier de l'Université de Montréal (CHUM), 900 Rue Saint-Denis, Montréal, Québec, H2X 0A9, Canada*

Abstract

With future advances in magnetic resonance imaging-guided radiation therapy, small photon beams are expected to be included regularly in clinical treatments. This study provides physical insights on detector dose-response to multiple megavoltage photon beam sizes coupled to magnetic fields and determines optimal orientations for measurements. Monte Carlo simulations determine small-cavity detector (solid-state: PTW60012 and PTW60019, ionization chambers: PTW31010, PTW31021, and PTW31022) dose-responses in water to an Elekta Unity 7 MV FFF photon beam. Investigations are performed for field widths between 0.25 cm and 10 cm in four detector axis orientations with respect to the 1.5 T magnetic field and the photon beam. The magnetic field effect on the overall perturbation factor (P_{MC}) accounting for the extracameral components,

atomic composition, and density is quantified in each orientation. The density (P_ρ) and volume averaging (P_{vol}) perturbation factors and quality correction factors ($k_{Q_B,Q}^{f_B,f}$) accounting for the magnetic field are also calculated in each orientation. Results show that P_{vol} remains the most significant perturbation both with and without magnetic fields. In most cases, the magnetic field effect on P_{vol} is 1% or less. The magnetic field effect on P_ρ is more significant on ionization chambers than on solid-state detectors. This effect increases up to 1.564±0.001 with decreasing field size for chambers. On the contrary, the magnetic field effect on the extracameral perturbation factor is higher on solid-state detectors than on ionization chambers. For chambers, the magnetic field effect on P_{MC} is only significant for field widths <1 cm, while, for solid-state detectors, this effect exhibits different trends with orientation, indicating that the beam incident angle and geometry play a crucial role. Solid-state detectors' dose-response is strongly affected by the magnetic field in all orientations. In general, ionization chambers yield $k_{Q_B,Q}^{f_B,f}$ closer to unity, especially in orientations where the chamber axis is parallel to the magnetic field.

Keywords: Magnetic fields, MRgRT, ionization chamber, solid-state detectors, Monte Carlo, quality correction factors, perturbation factors, small fields

6.1 Introduction

In magnetic resonance-guided radiation therapy (MRgRT), real-time imaging of the target volumes and organs at risk (OARs) allows online adaptive radiation therapy with no additional dose coming from the imaging system. Future advances in MRgRT are expected to include the regular use of small photon beams to deliver complex radiation therapy. Therefore, it is essential to investigate the effect of the magnetic field on small field dosimetry.

In small field dosimetry, the field size can critically compromise lateral charged particle equilibrium (LCPE). The interplay between the lack of LCPE and the detector density can cause significant perturbation effects [95, 109, 97, 112, 113, 98]. Additionally, if the detector size is comparable to the field size, the absorbed dose gradient over the detector sensitive volume can cause volume averaging perturba-

tions, which usually underestimates the absorbed dose at the point of measurement. Moreover, due to the small field collimation, a diminished number of scattered photons can reach the detector compared to broad beams, which affects the dose response by changing the mass energy-absorption coefficients and the mass stopping power ratios [65].

Several studies investigated and quantified the perturbation effects on detector dose response in different non-conventional beams such as in intensity-modulated radiation therapy (IMRT) [110, 111, 115], in small fields [109, 97, 112, 113, 98] and in the presence of magnetic fields [40, 83]. This approach uses Monte Carlo simulations to decompose the detector into separate components. Each component corresponds to a perturbation of the ideal conditions established in cavity theory. These perturbations are due to the detector's geometry, atomic composition, density, and cavity size. During calculation, each of these components is removed one by one, and the corresponding perturbation factor is calculated at each stage. In small fields, the two dominant perturbation factors are: 1) the volume averaging perturbation factor [109, 110, 97] and 2) the density perturbation factor [110, 97, 116]. Scott et al demonstrated a significant variation of the ratio of dose-to-water over dose-to-detector-in-water with field size for ion chambers, silicon diodes, and diamond detectors. In general, it was found that this variation was mainly due to the change in density with respect to the surrounding medium; high-density detectors tend to over-respond, and low-density detectors to under-respond [97]. It was also shown that density and volume averaging perturbation factors are constant for large field sizes and diverge for smaller field sizes, the specific field size at which the change occurs depends on detector size [97]. The same behaviour was found in Monte Carlo calculations of quality correction factors with respect to field size for ionization chambers and diodes irradiated with 6 MV beams [87].

Analogously to small photon beams, photon beams coupled to magnetic fields involve violation of charged particle equilibrium (CPE) with a much stronger degree than for broad beams for which transient CPE and full lateral CPE are achieved at some reference position. While small fields compromise lateral CPE, the pres-

ence of an external magnetic field violates CPE through the interplay between the detector density and the Lorentz force, and more specifically, the relation between the electron gyration radius and its energy. That is, even when neglecting photon attenuation and scatter, CPE cannot be assured in detectors unless the mass density of the detector scales with the magnetic field strength [57, 45, 62]; this is not the case in MRgRT in general as the detector is not water-equivalent. As Fano's theorem governs ionization chamber dosimetry of photon beams [55], one can anticipate the loss of CPE in small photon beams coupled to a magnetic field to introduce further electron fluence perturbations, especially at low-energies since the gyration radius increases with decreasing energy.

The dose response of some commercial ionization chambers in magnetic fields has been characterized in several studies considering different detector axis orientations with respect to the photon beam and the magnetic field [35, 77, 82, 75, 40]. In a previous study focused on the response of small-cavity ionization chambers [41], it was shown that for small-cavity ionization chambers, the effect of the magnetic field in dose deposition also varies with the geometry or size of the detector as well as with the orientation of the chamber with respect to the magnetic field and the irradiation beam. Moreover, it was confirmed that the effective sensitive volume must be modelled for small-cavity chambers by removing the dead volume adjacent to the guard electrode where there is ineffective charge collection [40, 41].

In addition to the complexity of chamber response modeling in the presence of magnetic fields, currently, there are no available codes of practice or guidelines for the reference dosimetry of MR-Linacs, neither for reference field size nor small fields [26, 117]. Thus, one objective of this study is to provide physical insights into the effects of magnetic fields on detector response by calculating perturbation factors for three commercial small-cavity ionization chambers and two solid-state detectors irradiated by beams of multiple sizes. Another objective is to determine experimental conditions under which perturbations are minimized. Finally, this study provides quality correction factor data for these commercial detectors using Elekta Unity phase space files and different field size settings.

6.2 Materials and Methods

6.2.1 Dosimetry formalism

In reference dosimetry, the quantity of interest is absorbed dose at a point in water. This quantity is determined via measurements using detectors with a finite cavity made of a specific material. The atomic composition and density of the cavity are usually different from that of water. There is also a wide variation in shape and dimension of detector cavities commercially available. The present study follows the approach of Bouchard et al [113] to determine the perturbation and quality correction factors of different detectors. The absorbed dose in water relative to the cavity is defined by a ratio $f(Q)$ depending on the atomic properties of the detection medium, the geometry of the detector, and the beam quality Q:

$$f(Q) = \frac{D_w}{D_{\text{det}}} = \left(\frac{\overline{Z}}{A}\right)^{w}_{det} P(Q) \tag{6.1}$$

where the D_w is the absorbed dose at the point of measurement in water, D_{det} is the averaged absorbed dose in the detector, Z is the atomic number, A is the atomic mass, $\left(\frac{\overline{Z}}{A}\right)^{w}_{det}$ is the ratio of water atomic properties to the detector medium, $P(Q)$ is the total perturbation factor and Q is the beam quality in its general meaning, i.e., it represents the particle phase space distribution surrounding the detector as a consequence of the irradiation conditions (field size, depth, magnetic field strength, etc.).

6.2.2 Decomposition of the perturbation factors

The detector in water perturbs the dose deposition because of the extracameral components, the differences in atomic composition and mass density of the detector materials (i.e., hence in atomic cross sections and density-effect corrections), and the finite size of the detecting cavity. The overall perturbation factor is defined as the product of perturbation subfactors associated with the detector's specific

components, i.e., stem, central electrode, wall cavity, atomic composition, and density of the sensitive material. The decomposition of subfactors is illustrated in figure 6.1. The perturbation factor and subfactors are determined with Monte Carlo simulations, and they are defined as:

$$P = P_{\mathrm{MC}} P_{\mathrm{vol}} = P_{\mathrm{ext}} P_{\mathrm{med}} P_{\rho} P_{\mathrm{vol}} \tag{6.2}$$

where P_{MC} is the overall perturbation factor. It is composed of the extracameral (stem, central electrode and cavity wall) perturbation factor, P_{ext}, of the medium perturbation factor, P_{med}, and of the density perturbation factor, P_{ρ}. P_{vol} is the volume averaging perturbation factor. These subfactors, P_i, are illustrated in figure 6.1 and are defined by Bouchard et al's formalism [113]:

$$P_i = \frac{D_{i+1}}{D_i} \frac{\left(\frac{\overline{Z}}{A}\right)_i}{\left(\frac{\overline{Z}}{A}\right)_{i+1}} \tag{6.3}$$

where D_{i+1}/D_i is the dose ratio in the geometry $i+1$ without the perturbing element relative to that of the geometry i including it and $\left(\frac{\overline{Z}}{A}\right)_i$ is the electron density (in mol^{-1}) of the cavity medium of geometry i. A calculation chain of perturbation factors is chosen arbitrarily, yet consistently, as follows. The first geometry ($i = 1$) corresponds to the full detector, as shown in figure 6.1. The second geometry ($i = 2$) corresponds to the bare cavity filled with air. The third geometry ($i = 3$) is a bare cavity filled with an artificial water vapor medium, noted w*, having the same atomic properties as water but with the electron density of air. The fourth geometry ($i = 4$) is the cavity filled with water. The last geometry ($i = 5$) is a sphere of 1 mm radius meant to represent a water point. The ratio $\left(\frac{\overline{Z}}{A}\right)_{i+1}^{i}$ is unity except for the case $i = 2$.

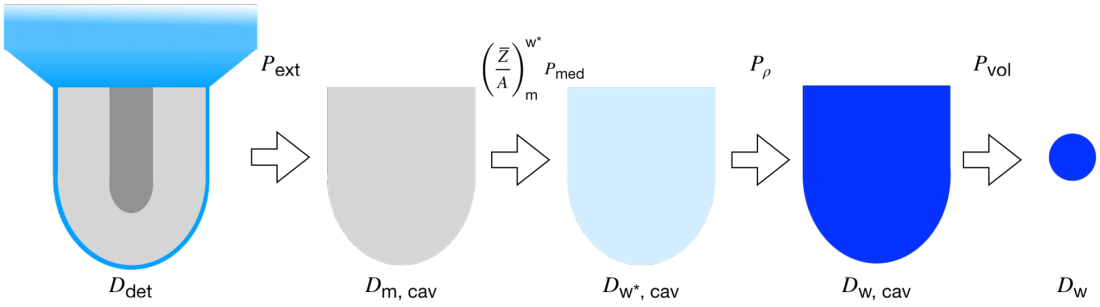

Figure 6.1 – Decomposition of perturbation factors using an arbitrary, yet consistent, route. The perturbation factors on top of the arrows corresponds to the ratio of each adjacent cavity dose.

6.2.3 Quality correction factors

Magnetic field correction factors accounting for the magnetic field have been defined by several authors [75, 76, 118, 41] using inconsistent notation, such as k_B or k_{Q_B}.This quality correction factor is usually the ratio of calibration coefficients with and without magnetic fields. Using the methodology proposed by Bouchard et al [112, 113], the quality correction factor $k^{f_B,f}_{Q_B,Q}$ (following IAEA-AAPM notation [69]) is calculated as follows:

$$k^{f_B,f}_{Q_B,Q} = \frac{P^{f_B}_{Q_B}}{P^{f}_{Q}} \tag{6.4}$$

where the subscripts Q and Q_B indicate the beam quality in the absence and presence of a magnetic field, respectively. The superscripts f and f_B represent the field sizes in the absence and presence of a magnetic field, respectively.

6.2.4 Monte Carlo simulations

The Monte Carlo calculations of absorbed dose-to-detector are performed with the EGSnrc user code `egs_chamber` [48]. The five detectors studied are three small-cavity ionization chambers models: PTW31010, PTW31021, and PTW31022 (PTW, Freiburg, Germany), the unshielded silicon diode PTW60012, and the microDiamond detector PTW60019. The ionization chamber models have been previ-

ously validated with an experimental setup and Monte Carlo simulations [41]. The chamber active sensitive volumes were defined with COMSOL Multiphysics 5.5 (COMSOL Inc., Burlington, MA, USA) calculations of the electric field accounting for the absence of ion collection near the guard electrode. The silicon diode model is based on a previously published model built from the manufacturer blueprints [111], and the microDiamond detector model is also built from blueprints but has not been used in previous work. The detector is placed inside a water tank phantom of $30 \times 30 \times 30$ cm^3 at 10 cm depth. The source-to-surface distance (SSD) is set to 133.5 cm, and the field widths are 10, 5, 3, 2, 1, 0.75, 0.5 and 0.25 cm at the isocenter. For field widths between 1 cm and 10 cm, 7 MV FFF photon beam phase spaces of the Elekta Unity MR-Linac, kindly provided by the manufacturer (Elekta Instrument AB Stockholm, Sweden), are used. These phase spaces consider the transport throughout the MR-linac components, as shown in reference [119], and they are scored at 129.5 cm from the source.

The smallest feasible field in the Elekta Unity MR-Linac is 1×1 cm^2. Smaller field sizes are also investigated, although they are not clinically relevant at the moment. They are academically interesting since they provide insights into the interplay between magnetic fields and small fields. To produce these smaller phase spaces, the `egs_collimated_source` library is used to generate a collimated square field at the isocenter using the spectral distribution extracted from the 1×1 cm^2 phase space.

Since the beam is perpendicular to the magnetic field, in principle, there can exist six orientations where the chamber axis forms either an orthogonal system with the other two axes or is parallel to one axis. However, because of the symmetry of cylindrical detectors and that the beam should never hit first the detector stem and cables, and by symmetry of two out of six orientations, only four chamber axis orientations are considered and are illustrated in figure 6.2: 1) chamber axis perpendicular to the magnetic field and parallel to the beam; 2) chamber axis perpendicular to the magnetic field and perpendicular to the beam with the Lorentz force pointing towards the stem, 3) chamber axis perpendicular to the magnetic field

and perpendicular to the beam with the Lorentz force pointing towards the tip and 4) chamber axis perpendicular to the beam and parallel to the magnetic field. The magnetic field is implemented with the enhanced electromagnetic field macro [54]. Calculation times are optimized by implementing variance reduction techniques such as cross-section enhancement (CSE), range-rejection-based Russian Roulette, intermediate phase-space scoring and correlated sampling [105]. The `egs_chamber` default parameters are used except for EM ESTEPE= 0.01, the threshold energy for electrons AE = 0.512 MeV and for photons AP = 0.001 MeV.

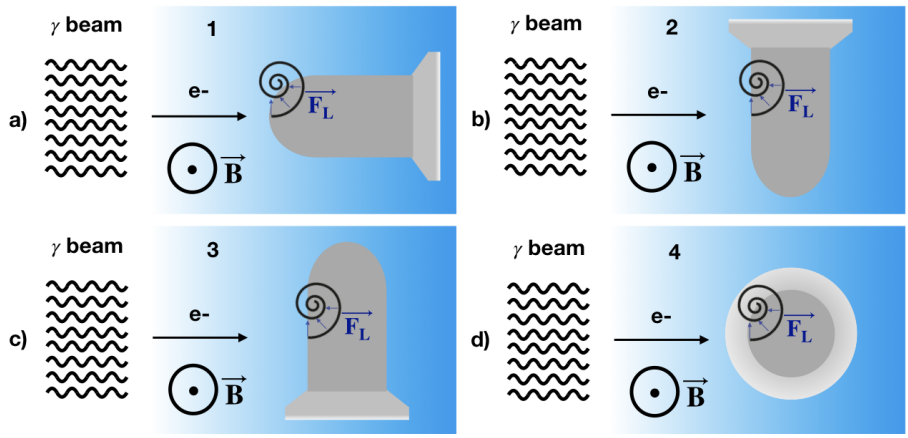

Figure 6.2 – Diagrams of the chamber setup: a) detector axis perpendicular to the magnetic field and parallel to the beam; b)detector axis perpendicular to the magnetic field and perpendicular to the beam with the Lorentz force pointing secondary electrons towards the stem on average; c)detector axis perpendicular to the magnetic field and perpendicular to the beam with the Lorentz force pointing secondary electrons towards the tip on average; d)detector axis parallel to the magnetic field and perpendicular to the beam.

6.2.5 Uncertainty analysis

As explained in our previous study [41], for the quality correction factors, the sources of uncertainty associated with Monte Carlo simulations of the five detectors dose response are: 1) the type A statistical uncertainty, σ_{stat}, 2) a type B due to the inconsistencies of the transport algorithm, set to be σ_{Fano}=0.13%, coming from the Fano test of the ionization chambers, 3) a type B emerging from the

uncertainty of the physical data used in the Monte Carlo code, $\sigma_{\text{data}} = 0.2\%$ [85, 107], applicable to all of the detector simulations, and 4) the type B detector geometry uncertainty accounting for the discrepancies between blueprints and the real chamber geometry and for the uncertainty in the characterization of the dead volume, the values of σ_{geom} are set to 0.1% for the silicon and microDiamond detectors (these detectors do not have a dead volume) and to 0.26%, 0.24% and 0.17% for PTW31010, PTW31021 and PTW31022, respectively, more details on the determination of these values can be found in reference [41]. Then the combined uncertainty of the quality correction factors is obtained by adding these values in quadrature. For the perturbation factor calculations, which are meant only to provide physical insights, only the type A statistical uncertainty is considered.

6.3 Results

The perturbation factors of five radiation detectors are evaluated with Monte Carlo simulations: three ionization chambers and two solid-state detectors. Calculations include eight squared field sizes, f, between 0.25×0.25 cm^2 and 10×10 cm^2 at 0 T and 1.5 T. Four detector orientations in an Elekta's Unity MR-Linac setup are studied. In section 6.3.1, results of the perturbation factors in the absence of magnetic fields are presented, and in section 6.3.2 the effect of the magnetic field on each perturbation factor is presented.

6.3.1 Perturbation factors in the absence of magnetic fields

6.3.1.1 Density perturbation factor, P_ρ

The density perturbation factor at 0 T is presented on the left side of figures 6.3 and 6.4 for solid-state detectors and ionization chamber, respectively. For the solid-state detectors, P_ρ is independent of field size and orientation, and it is close to unity by less than 1.5%. For ionization chambers, for $f > 1 \times 1$ cm^2, P_ρ is mostly constant and close to 1. However, for $f \leq 1 \times 1$ cm^2, P_ρ increases with decreasing field size. Over all chamber orientations, the maximal perturbation (2.003 ± 0.001)

occurs for the PTW31010 chamber.

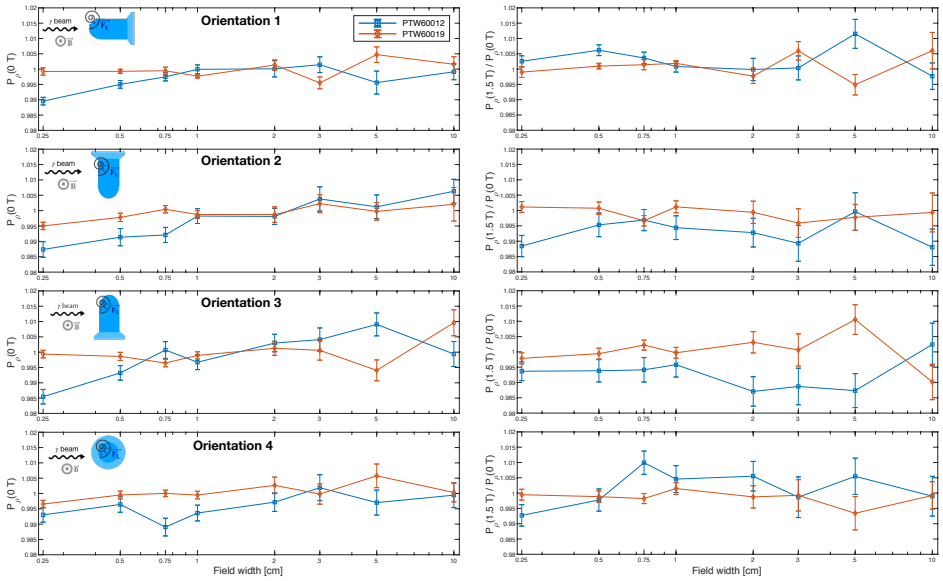

Figure 6.3 – On the left side, P_ρ of solid-state detectors for four orientations as function of the field sizes at 0 T. On the right side, the effect of the magnetic on P_ρ as a function of the field size.

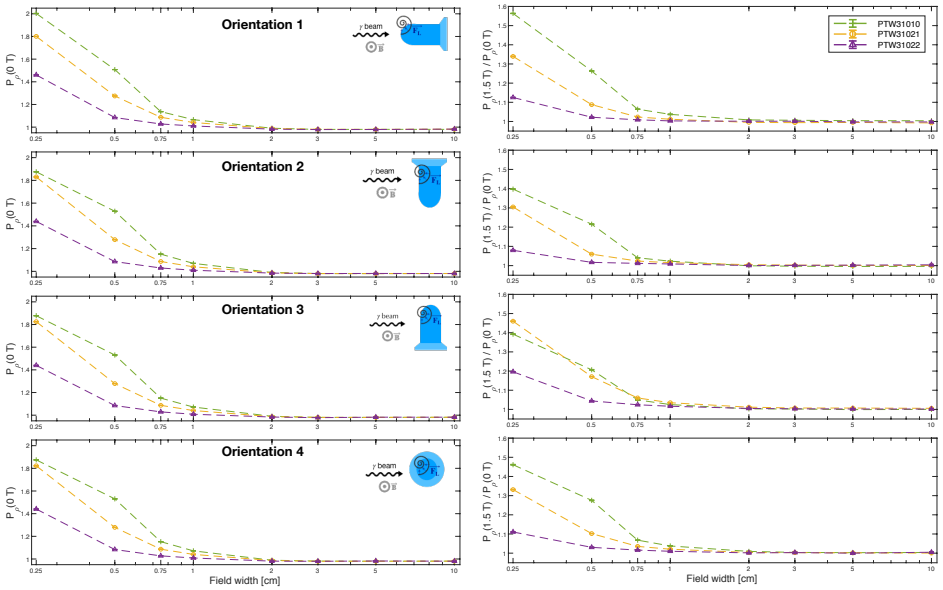

Figure 6.4 – On the left side,P_ρ of ionization chambers for four orientations as function of the field sizes at 0 T. On the right side, the effect of the magnetic on P_ρ as a function of the field size.

6.3.1.2 Overall perturbation factor, P_{MC}

The overall perturbation factor at 0 T for the five detectors is shown on the left side of figure 6.5 and 6.6 for each orientation. For the solid-state detectors, P_{MC} behaves similarly in the four orientations; P_{MC} remains mostly constant for $f > 1 \times 1$ cm^2 and decreases for the smaller fields. For the ionization chambers, in all orientations, P_{MC} is close to unity for $f > 1 \times 1$ cm^2. For $f \leq 1 \times 1$ cm^2, P_{MC} increases with decreasing field size. Note that the variation rate is different for each chamber model. The semiflex 3D (PTW31021) presents the maximal perturbation: $P_{MC} = 1.782 \pm 0.001$. It is noteworthy that at the 0.5 cm field width, the PTW31010 chamber falls out of the general trend. CPE is lost because the sensitive volume is larger than the field size. Indeed, this behaviour was confirmed with an alternate method by estimating the dose response behaviour with respect to field size using Monte Carlo dose response functions (defined in ref [111]).

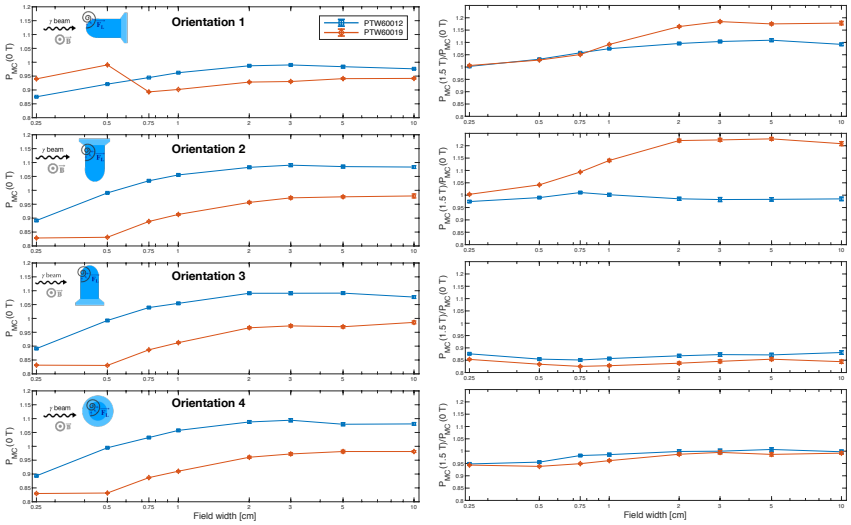

Figure 6.5 – On the left side, P_{MC} of solid-state detectors for four orientations as function of the field sizes at 0 T. On the right side, the effect of the magnetic on P_{MC} as a function of the field size.

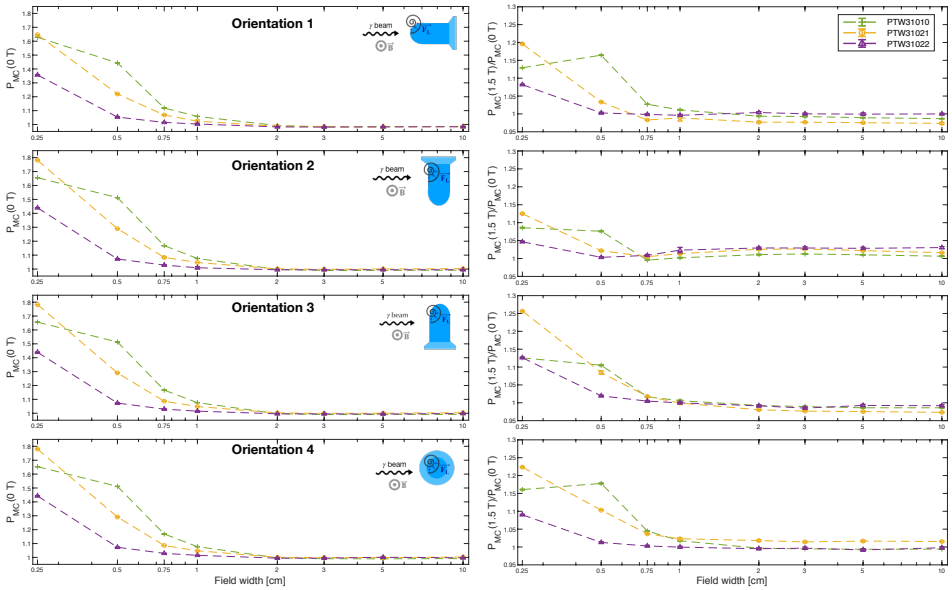

Figure 6.6 – On the left side, the overall perturbation factor of ionization chambers, for four orientations as function of the field sizes at 0 T. On the right side, the effect of the magnetic on P_{MC} as a function of the field size.

6.3.1.3 Volume averaging perturbation factor

The volume averaging perturbation factor at 0 T is presented as a function of the field size in each orientation, left side of figures 6.7 and 6.8. For solid-state detectors, the volume averaging perturbation is negligible for $f > 0.25 \times 0.25$ cm^2; P_{vol} is mostly constant and very close to unity. For the smallest field size, P_{vol} increases 1.5% from unity.

For ionization chambers, for $f > 1 \times 1$ cm^2, P_{vol} is independent of field size and very close to 1. For the smaller field sizes, P_{vol} increases as the field size decreases. The smallest chamber (PTW31022) presents the smallest P_{vol}, attaining a maximal value of 1.150 ± 0.001, in orientation 2. For the PTW31010 and PTW31021 chambers, P_{vol} rises rapidly in the smallest field sizes, reaching the maximal values of 2.486 ± 0.001 (orientation 1) and 1.831 ± 0.001 (orientations 2 and 3), respectively.

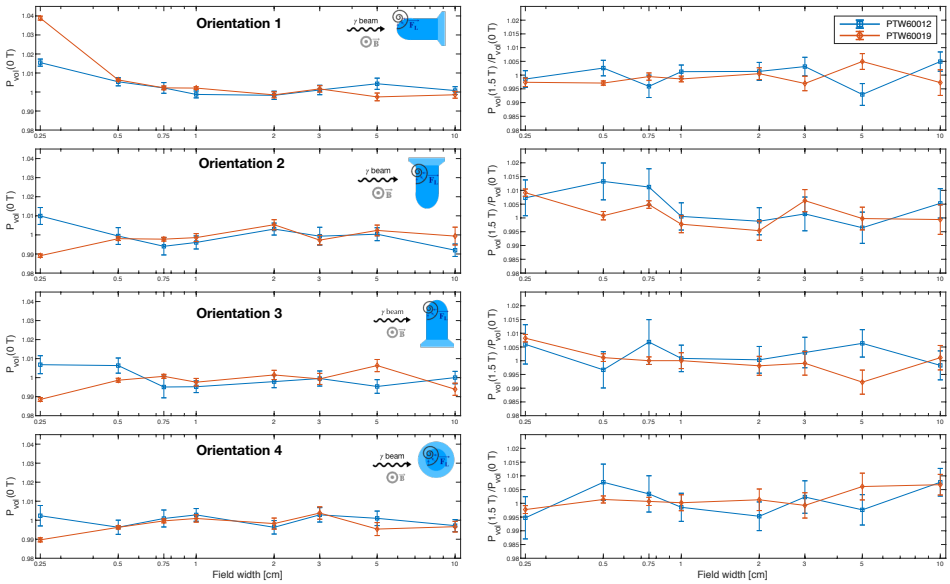

Figure 6.7 – On the left side, the volume averaging factor of solid-state detectors for four orientations as function of the field sizes at 0 T. On the right side, the effect of the magnetic on P_{vol} as a function of the field size.

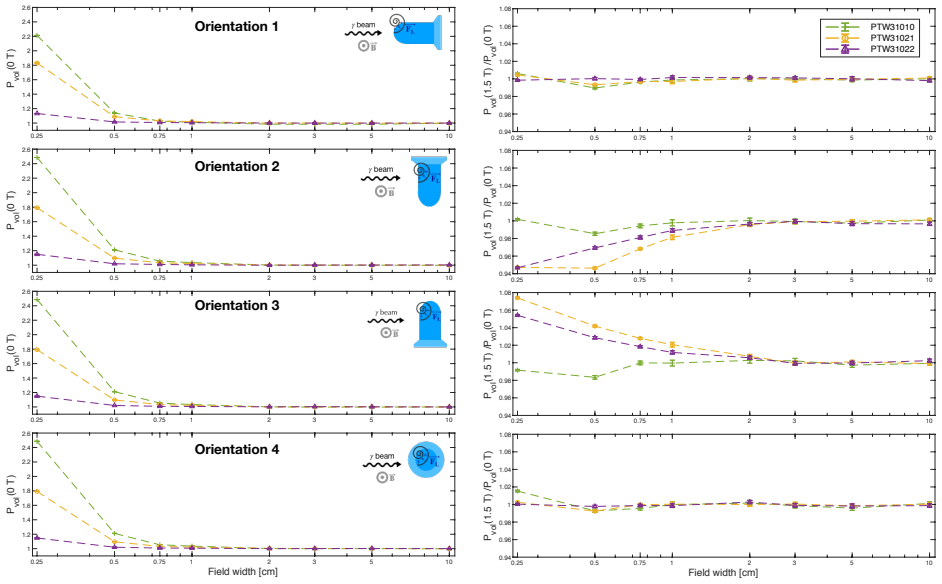

Figure 6.8 – On the left side, the volume averaging factor of ionization chambers for four orientations as function of the field sizes at 0 T. On the right side, the effect of the magnetic on P_{vol} as a function of the field size.

6.3.2 Effect of the magnetic field on the perturbation factors

6.3.2.1 Density perturbation factor, P_ρ

The magnetic field effect is quantified by the ratio of P_ρ(1.5 T) to P_ρ(0 T) in each orientation, on the right side of figures 6.3 and 6.4. For the solid-state detectors, the magnetic field effect on P_ρ is 1% or less from unity, over all field sizes and orientations. For the ionization chambers, for $f > 1 \times 1$ cm^2, the effect of the magnetic field is mostly constant and around 1%, the exact value depends on detector model and orientation. For $f \leq 1 \times 1$ cm^2, this effect increases abruptly, and it can reach as high as 1.564 ± 0.001 (PTW31010, orientation 1). Over all field sizes and orientations, the smallest density perturbation caused by the magnetic field is observed for the smallest chamber (PTW31022). In general, the magnetic field impact on P_ρ is lower in orientations 2 and 4. In orientation 4, the magnetic field's effect is smaller because it is parallel to the chamber axis. In orientation 2, electrons are deflected towards the stem and towards the dead volume, where the collection is inefficient. This results in a decrease of signal in magnetic fields, which could be why the magnetic field effect is smaller in P_ρ.

6.3.2.2 Overall perturbation factor, $P_{\mathbf{MC}}$

The magnetic field effect on P_{MC}, in each orientation, is presented on the right side of figures 6.5 and 6.6. For ionization chambers, in all orientations, for $f \geq 1 \times 1$ cm^2, the magnetic field effect is 3% or less from unity. As field size decreases, this effect increases to a maximal value that depends on the orientation. The largest impact considering all field sizes and orientations is 1.257 ± 0.001, occurring for the chamber PTW31021 in orientation 3.

For the solid-state detectors, P_{MC} behaves similarly in all orientations in the absence of a magnetic field. However, when the magnetic field is present, P_{MC} varies with orientation, shown in figure 6.5. Since the magnetic field effect on P_ρ is minor, then the increase on P_{MC} in magnetic fields mainly comes from the extracameral components perturbations. This is why there are large variations in

the magnetic field effect among the orientations; in each one, the beam encounters different geometrical components.

6.3.2.3 Volume averaging perturbation factor

The magnetic field effect on P_{vol} in each orientation is presented on the right side of figures 6.7 and 6.8. For solid-state detectors, the magnetic field effect on P_{vol} is 1% or less from unity. For ionization chambers, the magnetic field affects P_{vol} in different ways depending on chamber orientation. In orientations 1 and 4, the magnetic field effect is mostly independent of field size, and the variations are around 1% or less from unity. In contrast, the magnetic field has a noticeable impact on chambers PTW31021 and PTW31022; these over-respond and under-respond, in orientations 2 and 3, respectively, for the smaller fields.

6.3.3 Quality correction factors

The quality corrections factors for detectors: PTW60012, PTW60019, PTW31010, PTW31021 and PTW31022 are presented in tables 6.I, 6.II, 6.III, 6.IV and 6.V, respectively. Over all the detectors, chamber PTW31022 has the $k_{Q_B,Q}^{f_B,f}$ closer to unity. In particular, in orientations 1 and 4, for $f > 0.25 \times 0.25$ cm^2, $k_{Q_B,Q}^{f_B,f}$ corrections are smaller than 1.5%. Orientations 2 and 3 present larger $k_{Q_B,Q}^{f_B,f}$ over all field sizes.

Field size [cm^2]	Orientation 1	Orientation 2	Orientation 3	Orientation 4
10×10	1.097± 0.006	0.990± 0.009	0.880± 0.010	1.005± 0.009
5×5	1.101± 0.007	0.980± 0.009	0.877± 0.009	1.004± 0.009
3×3	1.107± 0.006	0.984± 0.011	0.875± 0.009	1.002± 0.011
2×2	1.097± 0.006	0.984± 0.008	0.868± 0.008	0.994± 0.009
1×1	1.076± 0.004	1.002± 0.008	0.857± 0.007	0.984± 0.008
0.75 × 0.75	1.056± 0.003	1.011± 0.005	0.853± 0.005	0.976± 0.005
0.5 ×0.5	1.029± 0.003	0.994± 0.005	0.855± 0.005	0.959± 0.005
0.25 × 0.25	1.006± 0.003	0.984± 0.005	0.875± 0.004	0.954± 0.005

Table 6.I – Calculated quality correction factors for the PTW60012 in a 1.5 T magnetic field, in four orientations, for multiple square field sizes. Uncertainties are estimated using the method described in section 6.2.5.

Field size [cm^2]	Orientation 1	Orientation 2	Orientation 3	Orientation 4
10×10	1.175± 0.009	1.208± 0.010	0.845± 0.008	0.999± 0.007
5×5	1.181± 0.005	1.227± 0.007	0.847± 0.007	0.993± 0.008
3×3	1.181± 0.005	1.231± 0.008	0.845± 0.008	0.994± 0.008
2×2	1.165± 0.004	1.215± 0.007	0.836± 0.006	0.989± 0.007
1×1	1.090± 0.002	1.138± 0.006	0.828± 0.005	0.962± 0.005
0.75 × 0.75	1.050± 0.003	1.099± 0.003	0.825± 0.003	0.950± 0.003
0.5 ×0.5	1.025± 0.002	1.043± 0.003	0.835± 0.003	0.939± 0.003
0.25 × 0.25	1.004± 0.003	1.013± 0.003	0.860± 0.003	0.941± 0.003

Table 6.II – Calculated quality correction factors for the PTW60019 in a 1.5 T magnetic field, in four orientations, for multiple square field sizes. Uncertainties are estimated using the method described in section 6.2.5.

6.4 Discussion

6.4.1 Perturbation factors in the absence of magnetic fields

6.4.1.1 Density perturbation factor, P_ρ

Scott et al [97] investigated the effect of density and atomic composition on the dose response of several detectors, including an unshielded silicon detector, a diamond detector, and a 3D pinpoint chamber PTW31016 (previous model to PTW31022) in small photon fields, in the absence of a magnetic field. For the silicon diode, Scott et al reported a P_ρ value around 0.95, while our results for

Field size [cm^2]	Orientation 1	Orientation 2	Orientation 3	Orientation 4
10×10	0.987± 0.004	1.007± 0.004	0.985± 0.004	0.995± 0.004
5×5	0.988± 0.004	1.008± 0.004	0.983± 0.004	0.990± 0.004
3×3	0.993± 0.005	1.012± 0.005	0.992± 0.005	0.993± 0.005
2×2	0.994± 0.005	1.011± 0.005	0.995± 0.005	0.998± 0.005
1×1	1.010± 0.005	1.000± 0.005	1.006± 0.005	1.017± 0.005
0.75 × 0.75	1.023± 0.004	0.990± 0.004	1.017± 0.004	1.040± 0.004
0.5 ×0.5	1.152± 0.004	1.060± 0.004	1.087± 0.004	1.169± 0.004
0.25 × 0.25	1.136± 0.004	1.088± 0.004	1.116± 0.004	1.179± 0.004

Table 6.III – Calculated quality correction factors for the PTW31010 in a 1.5 T magnetic field, in four orientations, for multiple square field sizes. Uncertainties are estimated using the method described in section 6.2.5.

Field size [cm^2]	Orientation 1	Orientation 2	Orientation 3	Orientation 4
10×10	0.974± 0.005	1.017± 0.004	0.972± 0.004	1.016± 0.004
5×5	0.975± 0.004	1.022± 0.004	0.976± 0.004	1.015± 0.004
3×3	0.975± 0.004	1.025± 0.004	0.976± 0.004	1.015± 0.005
2×2	0.978± 0.005	1.022± 0.005	0.988± 0.004	1.018± 0.005
1×1	0.986± 0.010	0.995± 0.005	1.020± 0.005	1.023± 0.005
0.75 × 0.75	0.980± 0.004	0.973± 0.005	1.046± 0.004	1.037± 0.004
0.5 ×0.5	1.026± 0.004	0.967± 0.004	1.130± 0.006	1.095± 0.004
0.25 × 0.25	1.201± 0.004	1.066± 0.004	1.350± 0.004	1.227± 0.004

Table 6.IV – Calculated quality correction factors for the PTW31021 in a 1.5 T magnetic field, in four orientations, for multiple square field sizes. Uncertainties are estimated using the method described in section 6.2.5.

the PTW60012 diode model are found between 0.986 ± 0.002 and 0.993 ± 0.002 depending on the orientation. For the microDiamond detector, in both studies, the values decrease below unity. However, here P_ρ remains very close to unity (0.995 ± 0.001 to 0.999 ± 0.001) in all orientations, whereas in their study, it decreases to approximately 0.85. The differences may be attributed to variations in the model geometry: their detectors are simply modelled by a pixel of 2.26 mm of diameter and thickness of 0.26 mm for the diamond and thickness of 0.06 mm for the silicon diode, while in the present study, the solid-state detectors are much smaller, as they are based on the manufacturer blueprints.

Field size [cm^2]	Orientation 1	Orientation 2	Orientation 3	Orientation 4
10×10	0.998± 0.004	1.027± 0.005	0.994± 0.004	0.997± 0.004
5×5	0.999± 0.005	1.025± 0.005	0.992± 0.005	0.990± 0.005
3×3	1.001± 0.004	1.029± 0.005	0.985± 0.005	0.996± 0.005
2×2	1.005± 0.004	1.026± 0.004	0.997± 0.004	0.998± 0.004
1×1	0.998± 0.004	1.012± 0.008	1.012± 0.004	0.998± 0.004
0.75 × 0.75	0.998± 0.004	0.990± 0.004	1.023± 0.004	1.002± 0.004
0.5 ×0.5	1.003± 0.004	0.972± 0.004	1.048± 0.004	1.011± 0.004
0.25 × 0.25	1.080± 0.003	0.991± 0.003	1.187± 0.003	1.091± 0.003

Table 6.V – Calculated quality correction factors for the PTW31022 in a 1.5 T magnetic field, in four orientations, for multiple square field sizes. Uncertainties are estimated using the method described in section 6.2.5.

For ionization chambers, the behaviour of P_ρ found by Scott et al follows the same trend as the one observed in the three chambers studied here. It is constant for $f >$ 1 cm × 1 cm, and it increases as the field size decreases. In their study, P_ρ was approximately 1.5 at 0.25 cm × 0.25 cm for the 3D pinpoint chamber. This is close to our results for the same field size where P_ρ of PTW31022 varies between 1.439 ± 0.001 and 1.461 ± 0.001 depending on the orientations, see the left side of figure 6.3.

6.4.1.2 Overall perturbation factor, $P_{\mathbf{MC}}$

The overall perturbation factor is the product of the perturbations coming from extracameral components and the variations in the detector's atomic properties and density with respect to the medium. Volume average effects aside, the perturbations of dose response in small fields are dominated by the effect of density and the presence of extracameral components, rather than by the atomic composition [97, 109, 112, 113]. Crop et al [109] reported perturbations of up to 1% from unity coming from the central electrode and the wall cavity for two pinpoint ionization chambers in small fields. Bouchard et al [113] showed that the extracameral perturbations could be significant and comparable to density perturbation factors in small photon beams for detectors with higher mass density than water, which is

the case for the solid-state detectors.

6.4.1.3 Volume averaging perturbation factor

For solid-state detectors, Scott et al also performed simulations of P_{vol} for two pixel sizes (1.33 mm and 2.26 mm of diameter and 0.26 mm thick), representing the volume of small field detectors [97]. Their results showed a similar behaviour of P_{vol} at large fields. However, for the smallest field, the increase of P_{vol} is significant, approximately 10%, which is larger than the variation observed in this study. This is expected as the sensitive volumes are submillimetric: 0.25 mm^3 and 0.004 mm^3 for the PTW60012 and PTW60019, respectively. On the other hand, the ionization chamber results of this work are consistent with the findings of Scott et al [97] for all fields.

6.4.2 Effect of the magnetic field on the perturbation factors

6.4.2.1 Density perturbation factor, P_ρ

For each detector, P_ρ behaves similarly in the four orientations with and without magnetic fields, as seen in figures 6.3 and 6.4. The behaviour of P_ρ is related to the charged particle fluence in the cavity and, thus, to the cavity size. For ionization chambers, the cavity density is three orders of magnitude smaller than water density. In such low-density materials, the production of secondary electrons diminishes; hence the electron fluence inside the cavity is smaller than in a cavity filled with the surrounding medium. Additionally, as field size decreases, there is a further reduction of the electron fluence in the cavity, explaining the rise on P_ρ. In contrast, for the solid-state detectors, the cavity and medium densities are of the same order of magnitude (silicon 2.33 g/cm^3 and diamond 3.53 g/cm^3); thus, the density perturbation is small and quasi-independent of field size in the absence and presence of a magnetic field.

In the presence of a magnetic field, when the beam enters the artificial water vapor cavity (i.e., water atomic composition with air electron density), the electron

mean free path increases, and electrons become more susceptible to the Lorentz force. In particular, the low-energy electrons would be more likely to get trapped in air cavities and deposit their energy locally. In contrast, the high-energy electrons would be more likely to escape from the cavity. However, since the main contribution to dose comes from low-energy electrons, a dose increase would be expected in the presence of a magnetic field.

6.4.2.2 Overall perturbation factor, P_{MC}

For the ionization chambers, P_ρ is the dominant factor within P_{MC}. Therefore, P_{MC} follows the general trend of P_ρ in all orientations. However, there are small variations in the magnetic field effect among the orientations. These differences might come from variations in the geometry depending on the incidence of the beam. For instance, in orientation 1, the central electrode is aligned with the photon beam, and since it has a mass density remarkably higher than air (i.e., approximately 2.34 g/cm^3), the central electrode produces more electrons which increases the electron fluence in the cavity. Orientations 2 and 3 are similar but with opposite magnetic field directions. In orientation 3, there is a slight underresponse of the chambers compared to orientation 2. This could be explained because electrons are, on average, either deflected towards or away from the stem, for orientations 2 and 3, respectively. In orientation 4, the magnetic field is parallel to the chamber, and the geometry plays a less critical role because of the symmetry in the experimental setup and in the chamber.

For solid-state detectors, in orientation 1, the magnetic field effect on P_{MC} increases with field size until a plateau is reached for $f > 1 \times 1$ cm^2. At larger fields, scattering increases the fluence of low-energy electrons towards the solid-state detectors. However, it seems that these low-energy electrons are not reaching the sensitive volume since $P_{\mathrm{MC}}(1.5\ \mathrm{T})$ is actually increasing. Even if low-energy electrons are more susceptible to the magnetic field, the electron path also depends on the medium density; thus, components with high density surrounding the active volume could be responsible for the decrease in electron fluence. To support these

physical insights, figure 6.9 illustrates the interplay between medium density and the magnetic field with two dose maps of a cavity with different density in a 10 $\times$ 10 $\times$ 10 cm^3 water phantom irradiated with a 2 cm $\times$ 2 cm field at 1.5 T. In figure 6.9a, where the cavity material is air, there is an extra dose deposition at the water-air upstream interface because of the electron return effect (ERE), as explained by Raaijmakers et al [13], and the dose deposition decreases at the air-water downstream interface (on the air side). In figure 6.9b, the opposite effect is observed if the cavity has a higher density than water, diamond in this case, and dose deposition diminishes at the water-diamond upstream interface and increases at the diamond-water downstream interface.

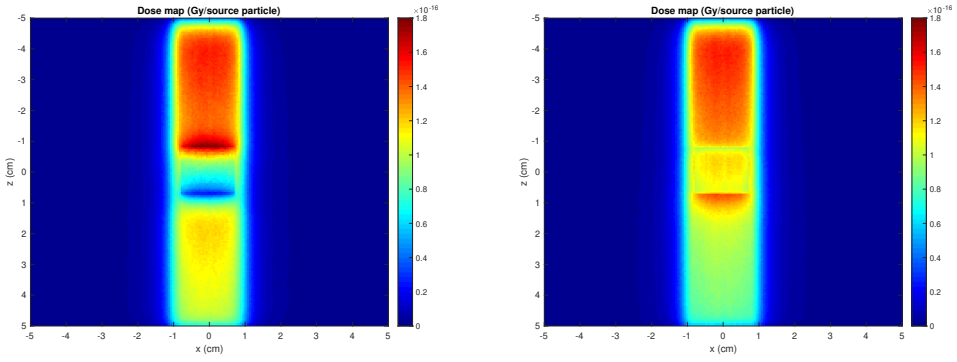

(a) Air cavity **(b)** Diamond cavity

Figure 6.9 – Illustration of ERE using a dose map of a 2 $\times$ 2 cm^2 field irradiating a 10 $\times$ 10 $\times$ 10 cm^3 water phantom with a rectangular cavity in the center made of a) air and b) diamond at 1.5 T.

Inside the solid-state detector, the materials have a higher density than water. In fact, for the microDiamond, there are materials with a density as high as 8.44 g/cm^3, and just beside the sensitive volume, there is a large (compared to the sensitive volume) layer of diamond with a density of 3.53 g/cm^3. The high-density materials surrounding the sensitive volume are likely to be absorbing the majority of the scattered electrons, which would reduce the electron fluence in the cavity and increase the perturbations of P_{MC}. Also, it has been experimentally observed that, for large fields, the angular sensitivity of the microDiamond detector is intensified

in the presence of magnetic fields, and this detector is not suitable for profile characterization nor for determination of large-field beam parameters [120].

For orientations 2 and 3, the silicon diode exhibits a relatively small dependence on the field size, while this is not the case for the microDiamond detector, suggesting the role of the extracameral components on electron fluence variations. In orientation 2, the magnetic field is perpendicular to the chamber axis, and the Lorentz force main direction is towards the stem. The stem of the microDiamond is more heterogeneous and with more high-density materials, while the stem of the silicon diode is mostly air. This could explain the different behaviour between the solid-state detectors in orientation 2. In orientation 3, electrons are, on average, deflected towards the tip where the geometry is more homogeneous, which justifies a similar behaviour of the magnetic field effect on both solid-state detectors. In orientation 4, the magnetic field effect remains relatively constant with field size.

6.4.2.3 Volume averaging perturbation factor

The notable effect of the magnetic field in the over-response and under-response in chambers PTW31021 and PTW31022, in orientations 2 and 3, respectively at the smaller fields could be attributed to the spherical symmetry of the chambers. The point of measurement is equidistant to the tip and to the stem. Also, the dead volumes adjacent to the guard electrodes correspond to 23.00% (PTW31021) and 18.45% (PTW31022) of their sensitive volume [41]. The presence and size of the dead volumes could explain the over-response and under-response since electrons are mainly deflected towards and away from the dead volume, in orientations 2 and 3, respectively. The chamber PTW31010 has the largest sensitive volume, and hence the largest volume averaging perturbation which is significant even without the magnetic field, so the magnetic field effect on P_{vol} appears insignificant.

6.4.2.4 Quality correction factors

In a review by de Pooter et al [26], the authors recompiled the published quality correction factors, $k_{Q_B,Q}^{f_B,f}$, for two regular-size chambers: PTW30013 and IBA FC65-G from several studies. They applied a criterion to select the chamber types and $k_{Q_B,Q}^{f_B,f}$ values to be suitable for comparison. For IBA FC65-G, considering a 1.5 T magnetic field, for a 10 × 10 cm^2 field, the mean values of $k_{Q_B,Q}^{f_B,f}$ are 0.9540 ± 0.0029 and 0.9977 ± 0.0048, in the perpendicular orientation (orientation 3 in this study) and in the parallel orientations (orientation 4 here), respectively [78, 76, 118, 80, 121]. For the PTW30013, the mean $k_{Q_B,Q}^{f_B,f}$ values are 0.9594 ± 0.0025 (orientation 2), 0.9620 ± 0.0047 (orientation 3) and 0.9928 ±0.0046 (orientation 4) [40, 39, 118, 76, 80, 121, 122]. Comparing the magnitude of quality correction factors between the regular-size chamber (reviewed by de Pooter et al [26]) and the small-cavity chambers (present study), in a reference field between, in the parallel orientation (orientation 4), the variation of $k_{Q_B,Q}^{f_B,f}$ from unity is below 1.6% for both groups of chambers. However, in the perpendicular orientations (orientations 2 and 3), $k_{Q_B,Q}^{f_B,f}$ values tend to be closer to unity for the small-cavity chambers.

Tekin et al [123] calculated $k_{Q_B,Q}^{f_B,f}$ factors for the microDiamond PTW 60019 detector, they found a value around 1.1 for a 4.6 × 4.6 cm^2, at 1.4 T while the value in this work is 1.181 ± 0.005 in the same configuration (orientation 1 of this study). The differences can be attributed to the differences in the experimental setup: the measurements in Tekin et al are performed at 5 cm depth, in a water phantom with dimensions 7 × 20 × 20 cm^3, using a 6 MV photon beam at a SSD of 110 cm, in this work the calculations are performed at 10 cm depth, in a water phantom with dimensions 30 × 30 × 30 cm^3, using a 7 MV FFF photon beam at a SSD of 133.5 cm. Further work should include experimental measurements to validate Monte Carlo calculations of quality correction factors under clinical conditions, for instance using a traceability route with alanine detectors as shown by Billas et al [124].

6.5 Suitability for clinical environment

Detector dose response to small photon beams in the presence of magnetic fields is complex. Several perturbation factors are present and compete with each other. In some cases, the perturbations act in opposite directions, so they mitigate each other, while in other cases, they increase the global perturbation factor. This is reflected in the quality correction factors, presented in tables 6.I, 6.II, 6.III, 6.IV and 6.V. According to our results, the two solid-state detectors exhibit large extracameral perturbations in magnetic fields. Thus, these detectors might not be suitable for dosimetry in magnetic fields. Both detectors, especially the microDiamond, present large perturbation factors at larger fields in the recommended measurement setup (orientation 1). Moreover, an experimental study demonstrated that the microDiamond presents a strongly asymmetric response to large radiation fields [120].

Since the integration of MR-Linac, several studies have investigated the characteristics and response of ionization chambers for dosimetry measurements in the presence of magnetic fields. The recommended orientation for cylindrical chambers is parallel to the magnetic field (orientation 4 in the present work) [26]; this is consistent with our findings since $k_{Q_B,Q}^{f_B,f}$ are closer to unity in orientations 1 and 4 for the ionization chambers. However, the clinical setup of orientation 1 might be more challenging and not feasible in all MR-Linac environments. Since few chamber MC models have been adequately characterized (i.e., dead volume must be removed from the sensitive volume) and validated with experimental measurements, there is limited reliable data of $k_{Q_B,Q}^{f_B,f}$ values. In most cases, these values only exist for a reference field size, as discussed in the previous section. In this investigation, the $k_{Q_B,Q}^{f_B,f}$ values of three small cylindrical chambers are determined in multiple field sizes. The three ionization chambers present similar $k_{Q_B,Q}^{f_B,f}$ values which tend to be closer to unity in orientation 4. When the smaller beam field sizes are used, the recommendation is to use the chamber with the smallest sensitive volume.

6.6 Conclusion

The magnetic field effect on small-cavity detector dose response to multiple irradiation field sizes is quantified by isolating different perturbation factors in different orientations. Solid-state detectors' dose response is strongly affected by the magnetic field in all orientations. The extracameral perturbations are amplified in magnetic fields, especially for large fields, while the effect on the density and volume averaging perturbations is lower (1% or less from unity). On the other hand, for ionization chambers, the magnetic field effect is more significant on the density perturbation factor. Volume averaging is the largest perturbation with and without magnetic fields. Orientations where the chamber axis is aligned with the magnetic field yield $k_{Q_B,Q}^{f_B,f}$ factors closer to unity. The orientation where electrons deflect towards the stem should be avoided. This study also shows that $k_{Q_B,Q}^{f_B,f}$ factors close to unity can be obtained for commercial small-cavity chambers in small MRgRT beams.

Quality correction factors are often calculated with Monte Carlo methods. This study reveals the source of dose response perturbations for different detectors in magnetic fields and emphasizes the importance of detailed characterization of the detector geometry in Monte Carlo models accounting for them. Further investigations should focus on particle fluence simulations to provide insights into the interplay between cavity geometry, density, and magnetic field.

Acknowledgements

This research was enabled in part by the support provided by Calcul Québec (www.calculquebec.ca) and Compute Canada (www.computecanada.ca). We gratefully acknowledge PTW for providing the detectors blueprints and Elekta for sharing the Unity phases-spaces. We also acknowledge financial support by the Consejo Nacional de Ciencia y Tecnología (CONACyT) and the Natural Sciences and Engineering Research Council of Canada (NSERC RGPIN/04178-2015).

The work was supported by the UK government's Department for Business,

Energy and Industrial Strategy and the EMPIR programme, grant 19NRM01, co-financed by the Participating States and from the European Union's Horizon 2020 research and innovation programme.

CHAPTER 7

INTRODUCTION TO ARTICLE 3

7.1 Context

In the previous article, the magnetic field effect on perturbation factors was characterized for several detectors in different irradiation conditions. The magnetic field emphasizes perturbations coming from density on ionization chambers and from extracameral components on the solid-state detectors.

Detector correction factors due to the presence of the magnetic field are related to differences in electron fluence perturbations in the absence and presence of magnetic fields. These differences vary with detector type and are expected to increase for detectors whose materials differ drastically from water in atomic composition and density.

Irradiation field size also affects the detector correction factors. Multiple publications [125, 97, 126, 127] have concluded that the stopping power ratio can be considered independent of field size. Thus, in small field dosimetry, the correction factors are only related to variations in particle fluence between reference and small fields [128].

In the present article, electron fluence spectra in six commercial detectors in the absence and presence of magnetic fields are calculated to provide a more detailed understanding of detector response in magnetic fields. The objectives are:

1. To study the behaviour of electron spectra and restrictions of Fano's theorem in the presence of magnetic fields
2. To characterize and explain the variations in electron spectral fluence in a Farmer ionization chamber and in small-cavity detectors in narrow and broad beams coupled to magnetic fields, in different configurations.
3. To evaluate the effect of air gaps surrounding the ionization chambers in the electron fluence spectra.

7.2 Supplementary theory

In the article, conditions to benchmark Monte Carlo calculations of electron fluence spectra are established, using the Fano conditions in magnetic fields [45, 62]. Additionally, the Monte Carlo calculations of electron fluence spectra are compared to a theoretical approximation established by Kawrakov [59]. In this section, more detail on this theoretical approximation is provided.

Kawrakow [59] defined the dose spectrum, n as :

$$n(E) = S(E) f_e(E) \tag{7.1}$$

where $S(E)$ is the unrestricted stopping power and f_e is the electron fluence spectra differential in energy and the analytical expression of the dose spectrum is given by:

$$n(E) = C_{\text{inc}} F_0^{(\text{tot})} \left[2\frac{(\kappa+1)^2}{\kappa^2(2\kappa+1)} + \frac{2\kappa+1}{\kappa^3} - \frac{2\kappa}{(2\kappa+1)^2} + \frac{2\kappa^2-2\kappa-2}{\kappa^3} \right.$$
$$\left. \ln\left(\frac{(2\kappa+1)(\kappa-\tau)}{\kappa}\right) - \frac{2\tau(\kappa^3-\tau)+\kappa^2(2+4\tau-3\tau^2)+\kappa\tau(2-4\tau+\tau^2)}{2\kappa^4(\kappa-\tau)} \right]$$

where $C_{\text{inc}} = 2\pi r_e^2 \rho_e$ are the constant factors in the Klein-Nishina cross section times electron density of the medium with units of $[\text{cm}]^{-1}$, F_0^{tot} is the incident photon energy fluence with units of $[\text{cm}^{-2}]$, $\kappa = k_0/m$ and $\tau = E/m$, with m=0.511 MeV, k_0 is the initial photon energy and E the electron energy.

Combining equations 7.1 and 7.2, the analytical expression of the electron fluence spectra is [59]

$$f_e(E) = \frac{C_{\text{inc}} F_0^{(\text{tot})}}{S(E)} \left[2\frac{(\kappa+1)^2}{\kappa^2(2\kappa+1)} + \frac{2\kappa+1}{\kappa^3} - \frac{2\kappa}{(2\kappa+1)^2} + \frac{2\kappa^2-2\kappa-2}{\kappa^3} \right.$$
$$\left. \ln\left(\frac{(2\kappa+1)(\kappa-\tau)}{\kappa}\right) - \frac{2\tau(\kappa^3-\tau)+\kappa^2(2+4\tau-3\tau^2)+\kappa\tau(2-4\tau+\tau^2)}{2\kappa^4(\kappa-\tau)} \right] \quad (7.2)$$

7.3 Results and impact

Electron fluence spectra have been calculated for six detectors - one Farmer chamber, three small-cavity ionization chambers, two solid-state detectors - in a small and a reference field, in different orientations, and in the absence and presence of a magnetic field. Additional calculations of the electron fluence were performed in two modified detector geometries: the bare sensitive volume filled with artificial water having the same electronic density as the original material, w^*, and filled with water. Three chamber axis orientations are investigated: parallel or perpendicular (two possibilities: $\mathbf{F}_{\text{L}}$ towards the stem or the tip) to the magnetic field and always perpendicular to the photon beam. One orientation for the solid-state detector is studied: parallel to the photon beam and perpendicular to the magnetic field.

The variations of the total electron fluence due to the magnetic field in all detectors are summarized in table 7.I.

		Parallel to B-field [%]	Perpendicular to B-field ($\mathbf{F}_L \rightarrow$ stem) [%]	Perpendicular to B-field ($\mathbf{F}_L \rightarrow$ tip) [%]	Parallel to beam [%]
PTW30013	10×10 cm^2	-0.08 ± 0.00	4.42 ± 0.00	5.12 ± 0.00	
	3×3 cm^2	-1.24 ± 0.00	4.75 ± 0.00	2.35 ± 0.00	
PTW31010	10×10 cm^2	0.14 ± 0.00	-2.56 ± 0.00	-0.24 ± 0.00	
	1×1 cm^2	-11.60 ± 0.03	-10.62 ± 0.03	-11.39 ± 0.03	
PTW31021	10×10 cm^2	-0.19 ± 0.00	-6.08 ± 0.01	-1.27 ± 0.00	
	1×1 cm^2	-10.56 ± 0.03	-11.85 ± 0.03	-14.50 ± 0.04	
PTW31022	10×10 cm^2	-0.18± 0.00	-4.58 ± 0.01	-0.90 ± 0.00	
	1×1 cm^2	-9.96 ± 0.04	-11.08 ± 0.04	-12.34 ± 0.04	
PTW60012	10×10 cm^2				-9.84 ± 0.07
	1×1 cm^2				-15.06 ± 0.09
PTW60019	10×10 cm^2				-14.97 ± 0.08
	1×1 cm^2				-16.00 ± 0.07

Table 7.I – Percentage of total electron fluence variation due to the magnetic field in the detectors.

7.3.1 Farmer chamber

The magnetic field effect in the electron fluence in each detector type was different. In the Farmer chamber (PTW30013) case, the magnetic field impact is smaller in the parallel orientation than in the perpendicular orientation. The interplay between the gyration radius and the cavity size (the cavity length is 3.77 times larger than the cavity diameter) dramatically affects the electron fluence in the perpendicular orientation.

7.3.2 Small-cavity chambers

For the small-cavity chambers (PTW31010, PTW31021 and PTW31022), in the reference field, the magnetic field impact on total electron fluence drastically increases when the Lorentz force points towards the chamber stem than in the other two orientations. Contrary to the Farmer chamber, the cavity length is comparable to the cavity diameter in these chambers, explaining the similar behaviour among these two orientations. A significant impact of the small field size is observed in the small-cavity chambers in all orientations; the total electron fluence at 1.5 T

decreases between 9.96% to 14.50 % depending on the orientation, compared to the 0 T case.

7.3.3 Solid-state detectors

The magnetic field strongly impacted the solid-state detectors in both field sizes, probably due to the high-density extracameral components. The maximal reductions of total electron fluence are 15.06 ± 0.09% (silicon) and 16.00 ± 0.07% (microDiamond).

The electron fluence spectra calculations of this article are consistent with the results of the second article [114]. In solid-state detectors, the extracameral component perturbations increase in the presence of a magnetic field. In ionization chambers, the density variations increase the electron fluence perturbations in the presence of magnetic fields. Additionally, it was observed that perturbations from the extracameral components are in the opposite direction of the density perturbations in ionization chambers. However, there was only a slight compensation in the overall perturbation since the density perturbation remains the most significant.

7.3.4 Air gaps

Simulations of symmetrical and asymmetrical air gaps surrounding the chambers in the parallel orientation are performed. Results show a significant impact of the magnetic field on the electron fluence spectra for asymmetrical air gaps, as seen in the dose ratio of the air gap case relative to the no air gap in tables 7.II and 7.III. This impact is present all along the energy spectrum, and it increases at low-energies. Asymmetrical air gaps have a more significant impact in the small-cavity chamber than in the Farmer chamber.

7.3.5 Impact

This article provides physical insights into the response of different detectors when irradiated with megavoltage photon beams coupled to an external magnetic

Air gap	Symmetrical		Asymmetrical	
thickness [mm]	0 T	1.5 T	0 T	1.5 T
0.2	1.0007 ± 0.0015	1.0015 ± 0.0015	0.9922 ± 0.0013	0.9888 ± 0.0012
0.5	0.9991 ± 0.0016	1.0014 ± 0.0016	0.9818 ± 0.0013	0.9673 ± 0.0012
1.0	1.0004 ± 0.0015	1.0009 ± 0.0014	0.9730 ± 0.0012	0.9456 ± 0.0011
1.5	1.0003 ± 0.0015	1.0038 ± 0.0014	0.9705 ± 0.0012	0.9374 ± 0.0011

Table 7.II – Ratio of dose in the PTW30013 cavity with different air gap thickness relative to that with no air gap.

Air gap	Symmetrical		Asymmetrical	
thickness [mm]	0 T	1.5 T	0 T	1.5 T
0.2	0.9989 0.0014	0.9987 ± 0.0015	0.9950 ± 0.0015	0.9893 ± 0.0016
0.5	1.0013 0.0014	1.0002 ± 0.0015	0.9933 ± 0.0014	0.9725 ± 0.0016
1.0	1.0003 0.0015	1.0009 ± 0.0016	0.9871 ± 0.0014	0.9464 ± 0.0018
1.5	1.0019 0.0015	1.0013 ± 0.0015	0.9846 ± 0.0014	0.9245 ± 0.0015

Table 7.III – Ratio of dose in the PTW31010 cavity with different air gap thickness relative to that with no air gap.

field. The electron fluence differential in energy in the detector cavity can be severely modified in magnetic fields. Low-energy electron trajectories are more susceptible to change in magnetic fields, and generally, they are associated with detector response perturbation. Detectors with high-density extracameral components exhibit more significant perturbations in the presence of a magnetic field, regardless of field size. The electron fluence simulations presented in this study illustrate the interplay between several factors that can make perturbation effects unpredictable in photon beams coupled to magnetic fields: 1) chamber and B-field orientation, 2) cavity size and shape, 3) extracameral components, 4) air gaps and their asymmetry, 5) electron energy.

The performance of detectors dedicated to dosimetry in the presence of a magnetic field improves by avoiding high-density materials surrounding the sensitive volume, non-uniform internal air layers and situations where air bubbles or gaps surrounding the detector can occur.

7.4 Supplementary results

In the article, the results for the small-cavity chambers are explained and illustrated with the results only of chamber PTW31010. Due to lack of space, the results for chamber semiflex 3D and pinpoint 3D are not presented. In this section, the electron fluence spectral differences due to the magnetic field of chambers PTW31021 and PTW31022 are presented on figures 7.1 and 7.2, respectively. The behaviour of the spectral differences are explained in section 8.3.3.2. In particular, the inflexion point, vertical dashed line in figures 7.1 and 7.2, associated to the cavity diameter and the gyration radius is explained in detail in section 8.3.4.

7.5 Contributions

1. Yunuen Cervantes Espinosa
   - Development of original idea
   - Mathematical formalism
   - Monte Carlo simulations of electron fluence spectra
   - Analysis of results
   - Writing of the article
2. Simon Duane
   - Scientific support
   - Revision of the article
3. Hugo Bouchard
   - Development of original idea
   - Project direction
   - Mathematical formalism
   - Scientific support
   - Revision of the article

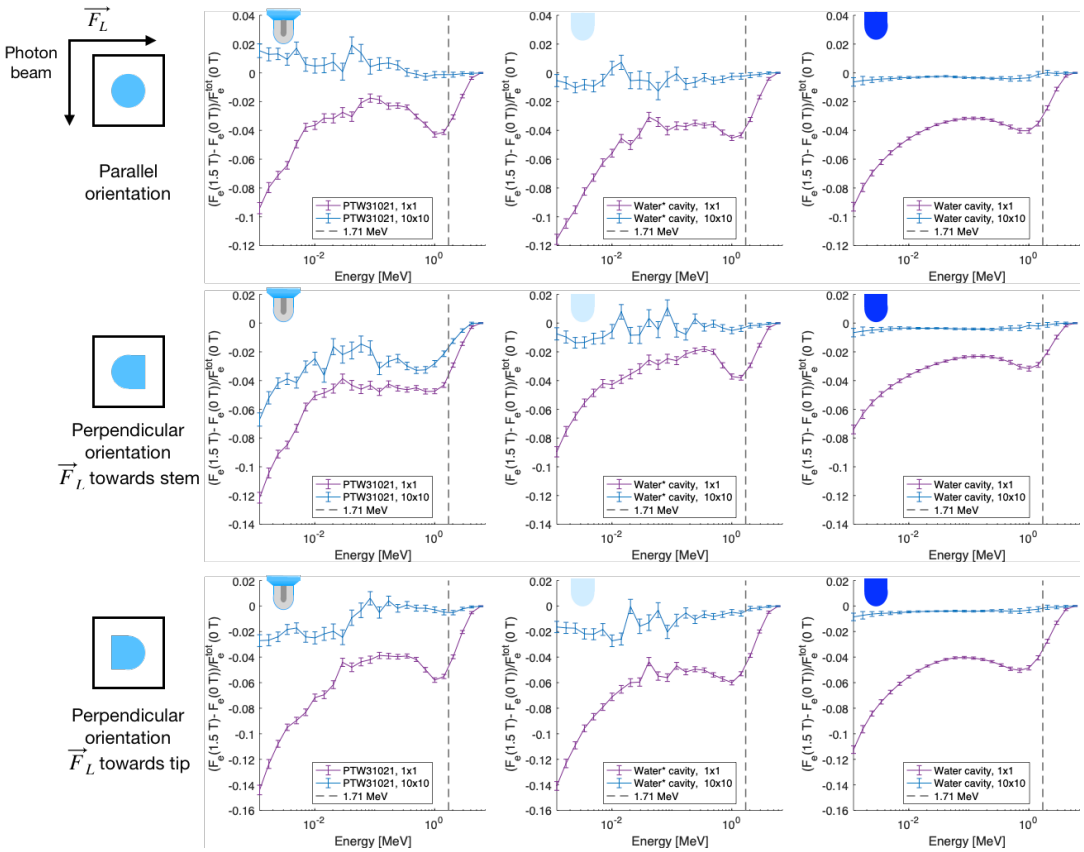

Figure 7.1 – The electron fluence spectral differences due to the magnetic field in each semiflex 3D PTW31021 chamber geometry considered in the parallel orientation on the top row and perpendicular orientations with $\mathbf{F}_\mathrm{L}$ pointing towards the stem on the middle row and $\mathbf{F}_\mathrm{L}$ pointing towards the tip on the bottom row. The geometries are: chamber (left), the bare cavity with artificial water (middle) and the bare cavity filled with water (right) at 0 T and 1.5 T for fields of 10×10 cm ^{2} and 1×1 cm^2. The vertical dashed line is at the energy at which the gyration radius equals the cavity thickness. On the left, an illustration of the sensitive volume in the smallest field size in each orientation.

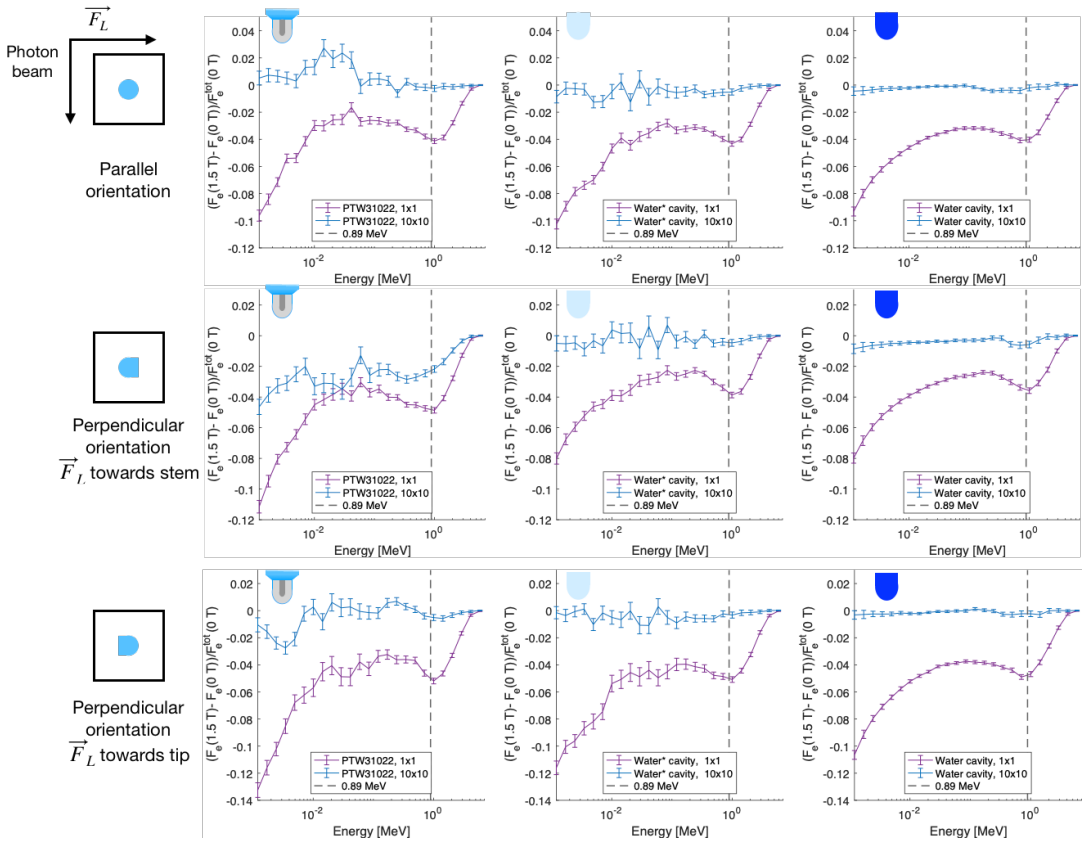

Figure 7.2 – The electron fluence spectral differences due to the magnetic field in each pinpoint 3D PTW31022 chamber geometry considered in the parallel orientation on the top row and perpendicular orientations with $\mathbf{F}_\mathrm{L}$ pointing towards the stem on the middle row and $\mathbf{F}_\mathrm{L}$ pointing towards the tip on the bottom row. The geometries are: chamber (left), the bare cavity with artificial water (middle) and the bare cavity filled with water (right) at 0 T and 1.5 T for fields of 10×10 cm ^{2} and 1×1 cm^2. The vertical dashed line is at the energy at which the gyration radius equals the cavity thickness. On the left, an illustration of the sensitive volume in the smallest field size in each orientation.

CHAPTER 8

MONTE CARLO INVESTIGATION OF ELECTRON FLUENCE PERTURBATION IN MR-GUIDED RADIOTHERAPY BEAMS USING SIX COMMERCIAL RADIATION DETECTORS

This article has been submitted to the journal Physics and Medicine and Biology [129].

Electron fluence spectral distribution in detector response to megavoltage photon beams in the presence of an external magnetic field

Yunuen Cervantes [1,2] Simon Duane[3], and Hugo Bouchard[1,2,5]

[1] *Département de physique, Université de Montréal, Complexe des sciences, 1375 Avenue Thérèse-Lavoie-Roux, Montréal, Québec H2V 0B3, Canada.*

[2] *Centre de recherche du Centre hospitalier de l'Université de Montréal, 900 Rue Saint-Denis, Montréal, Québec, H2X 0A9, Canada*

[3] *National Physical Laboratory, Chemical, Medical and Environmental Science Department, Teddington, United Kingdom*

[5] *Département de radio-oncologie, Centre hospitalier de l'Université de Montréal (CHUM), 900 Rue Saint-Denis, Montréal, Québec, H2X 0A9, Canada*

Abstract

With the integration of treatments with MRI-linacs to the clinical workflow, the understanding and characterization of detector response in reference dosimetry in magnetic fields are required. The external magnetic field perturbs the electron fluence. The degree of perturbation depends on the irradiation conditions and on the detector type. The purpose of this study is to evaluate the magnetic field impact on the electron fluence spectra in several detectors to provide a deeper understanding of detector response in these conditions. Monte Carlo calculations of the electron fluence are performed in six detectors (solid-state: PTW60012 and PTW60019, ionization chambers: PTW30013, PTW31010, PTW31021, and PTW31022) in water and irradiated by a 7 MV FFF photon beam with a small and a reference field, at 0 T and 1.5 T. Three chamber axis orientations are investigated: parallel or perpendicular (either the Lorentz force pointing towards the stem or the tip) to the magnetic field and always perpendicular to the photon beam. One orientation for the solid-state detector is studied: parallel to the photon beam and perpendicular

to the magnetic field. Additionally, electron fluence spectra are calculated in modified detector geometries to identify the underlying physical mechanisms behind the fluence perturbations. The total electron fluence in the Farmer chamber varies up to 1.24% and 5.12% at 1.5 T, in the parallel and perpendicular orientation, respectively. The interplay between the gyration radius and the Farmer chamber cavity length significantly affects the electron fluence in the perpendicular orientation. For the small-cavity chambers, the maximal variation in total electron fluence is 0.19%, for the reference field, in the parallel orientation. Significant small-field effects occur in these chambers; the magnetic field reduces the total electron fluence (with respect to the no field case) between 9.86% to 14.50% depending on the orientation. The magnetic field strongly impacted the solid-state detectors in both field sizes, probably due to the high-Z components and cavity density. The maximal reductions of total electron fluence are 15.06 ± 0.09% (silicon) and 16.00 ± 0.07% (microDiamond). This work provides insights into detector response in magnetic fields by illustrating the interplay between several factors causing dosimetric perturbation effects: 1) chamber and magnetic field orientation, 2) cavity size and shape, 3) extracameral components, 4) air gaps and their asymmetry, 5) electron energy. Low-energy electron trajectories are more susceptible to change in magnetic fields, and they are associated with detector response perturbation. Detectors with higher density and high-Z extracameral components exhibit more significant perturbations in the presence of a magnetic field, regardless of field size.

Keywords: Magnetic fields, MRgRT, reference dosimetry, ion chamber, solid-state detectors, Monte Carlo, cavity size, small fields, electron fluence

8.1 Introduction

With the integration of magnetic resonance imaging with clinical linear accelerators (MRI-linacs), the characterization of different types of detectors for reference dosimetry measurements in MRI-linacs has been under investigation [35, 77, 75, 78, 40, 79, 39, 80, 81, 41]. The majority of these studies focus on the character-

ization of ionization chamber responses and the calculation of correction factors in the presence of magnetic fields, either by experimental measurements, Monte Carlo calculations or both. Detector response depends on the detector geometry, magnetic field strength and orientation, beam quality, field size, and the potential presence of air gaps around the chamber [26]. Nevertheless, the behaviour of detector response in the presence of a strong magnetic field is still not fully understood and remains a question of interest.

The presence of any detector perturbs the particle fluence at the point of measurement compared to that in the absence of the detector. The degree of the perturbation depends on the detector design and materials and on the irradiation conditions, i.e. magnetic field strength and direction, beam quality, and field size. Particle fluence perturbations are more pronounced for detectors with materials differing drastically from water in terms of atomic composition and density. For small field dosimetry, when the field size is comparable to the detector size, the particle fluence perturbations increase, mainly due to volume averaging perturbations, and in the case of ionization chambers, also due to density perturbations [97].

The underlying physics behind the magnetic field effect on detector response, along with the effect of the irradiation field size, were investigated in a previous work [114]. Perturbations coming from extracameral components (stem, cavity wall, central electrode), atomic composition, density and volume of the detector were studied. The results showed that for small-cavity ionization chambers, the impact of the magnetic field was stronger in the density perturbation factor irradiated by fields smaller than 1×1 cm^2. On the contrary, for solid-state detectors (silicon diode and microDiamond detector), the magnetic field strongly increases the perturbations from extracameral components in fields larger than 1×1 cm^2. Even though this work provided an overview on dose perturbation factors, the interplay between cavity geometry, density and magnetic field was not fully described.

The objectives of this work are to detail the following effects due to the presence of a magnetic field: 1) fluence perturbations enhanced by high-Z components

and cavity density, 1) the sensitivity of low energy electrons to fluence perturbations, 3) various geometrical effects related to cavity dimensions and orientation with respect to electron energy and field strength, and 4) fluence perturbations due to the presence air gaps of different shapes. Firstly, to demonstrate the first objective, the theoretical basis demonstrating the link between electron fluence perturbations and low-energy electrons with small gyration radii is presented in section 8.2.1, along with restrictions of Fano's theorem in the presence of magnetic fields. Secondly, to provide insights into the drastic effects of density and high-Z components, the variations in electron spectral fluence in six different detectors (one Farmer ionization chamber, three small-cavity chambers and two solid-state detectors) are characterized in narrow and broad beams coupled to magnetic fields, using different configurations. Thirdly to describe the impact of detector geometry on electron fluence in the presence of magnetic fields, in section 8.3.4, a simple detector model is presented where the variation of electron pathlength due to the magnetic field explains the shape of the electron fluence spectra. Finally, the electron fluence perturbations due symmetrical and asymmetrical air gaps surrounding different ionizations chambers are evaluated.

8.2 Materials and Methods

8.2.1 Theory

This section demonstrates that density fluctuations and small curvature radii have significant anticipated effects on fluence perturbations. Additionally, a particular condition applicable to the external beam setup is proposed to fulfil the special conditions to validate the Fano theorem in the presence of magnetic fields [45] and perform special Fano cavity test in the Monte Carlo simulations of radiation transport.

8.2.1.1 Definitions

Considering the following variables in the laboratory frame:

— $\vec{r}$: the vector corresponding to the particle position in space

— $\vec{p}$: the vector corresponding to the particle momentum

— $\hat{\boldsymbol{u}}$: the unit vector in the direction of the particle momentum

— β: speed in units of c

— Σ : mass macroscopic cross section (in $\mathrm{cm}^2\ \mathrm{g}^{-1}$)

— $f_i(\vec{r},\vec{p})$: the particle type i fluence differential in energy and direction corresponding to the number particles at $\vec{r}$ with momentum $\vec{p}$ per unit energy, per unit area perpendicular to $\hat{\boldsymbol{u}}$ and per unit solid angle $d\hat{\boldsymbol{u}} = sin\theta d\theta d\phi$

— $F_i(\vec{r},p)$: the spectral distribution of a given $f_i(\vec{r},\vec{p})$ integrated over all directions, defined as

$$F_i(\vec{r},p) \equiv \int_{4\pi} f_i(\vec{r},\vec{p}) d\Omega. \tag{8.1}$$

— The spherical coordinates convention for representing $\vec{p} = p\hat{\boldsymbol{u}}$ are

$$\begin{aligned}
\hat{\boldsymbol{u}} =& \sin\theta\cos\phi\hat{\boldsymbol{x}} + \sin\theta\sin\phi\hat{\boldsymbol{y}} + \cos\theta\hat{\boldsymbol{z}} \\
\hat{\boldsymbol{\theta}} =& \cos\theta\cos\phi\hat{\boldsymbol{x}} + \cos\theta\sin\phi\hat{\boldsymbol{y}} - \sin\theta\hat{\boldsymbol{z}} \\
\hat{\boldsymbol{\phi}} =& -\sin\phi\hat{\boldsymbol{x}} + \cos\phi\hat{\boldsymbol{y}} \\
\vec{\nabla}_p =& \hat{\boldsymbol{u}}\frac{\partial}{\partial p} + \hat{\boldsymbol{\theta}}\frac{1}{p}\frac{\partial}{\partial\theta} + \hat{\boldsymbol{\phi}}\frac{1}{p\sin\theta}\frac{\partial}{\partial\phi} \\
\mathrm{d}\hat{\boldsymbol{u}} =& \mathrm{d}\cos\theta\mathrm{d}\phi
\end{aligned}$$

— $S \equiv S(\vec{r},\vec{p})$: the primary source term representing the number of particles of momentum $\vec{p}$ generated at $\vec{r}$ by an external source per unit mass, energy and direction (in $\mathrm{g}^{-1}\mathrm{MeV}^{-1}\mathrm{sr}^{-1}$).

— $\mathcal{I}\{f;\vec{r}\}$: the interaction term is an operator representing the production of secondary particles (in $\mathrm{g}^{-1}\mathrm{MeV}^{-1}\mathrm{sr}^{-1}$).

— R: the gyration radius of charged particles subjected to a magnetic field of strength B.

8.2.1.2 Radiation transport equation in the presence of magnetic fields

The Boltzmann radiation transport equation predicts the charged particle fluence rate by balancing the number of particles entering, created in and leaving the point of interest. It has been adapted to account for the presence of external electromagnetic fields by adding a term describing the effect of the Lorentz force on particle fluence in references [45, 57]. Considering the case free of an electric field, the radiation transport equation for charged particle fluence in the presence of an external magnetic field, $\vec{B}$ is

$$\hat{\boldsymbol{u}} \cdot \vec{\nabla}_r f = \rho \left[S + \mathcal{I}\{f; \vec{r}\} \right] - q\, \hat{\boldsymbol{u}} \times \vec{B} \cdot \vec{\nabla}_p f. \tag{8.2}$$

For choice of coordinates such that $\vec{B} = B\hat{\boldsymbol{z}}$, and using the equation 8.15 derived in the appendix 8.A for the Lorentz force term, then the transport equation becomes

$$\hat{\boldsymbol{u}} \cdot \vec{\nabla}_r f = \rho \left[S + \mathcal{I}\{f; \vec{r}\} - \frac{1}{R\rho} \frac{\partial f}{\partial \phi} \right]. \tag{8.3}$$

Note that the energy-dependent gyration radius and the mass density are in the denominator of the last term on the right-hand side of the equation. Therefore, the impact of the magnetic field on electron fluence are expected to increase with small gyration radius and low-density materials. The electron gyration radius increases with increasing kinetic energy and decreasing magnetic field strength. Hence, in a constant magnetic field, low-energy electrons have small gyration radii.

8.2.1.3 Special Fano conditions

Under classical Fano conditions [55], the following is fulfilled: 1) the atomic properties of the medium are homogeneous, hence $\mathcal{I}\{f; \vec{r}\} = \mathcal{I}\{f\}$, and 2) the source produces equilibrium, i.e., S_{eq} is such that $\vec{\nabla} S_{\text{eq}} = \vec{0}$. Then, equation 8.3 becomes

$$\begin{aligned}\hat{\boldsymbol{u}}\cdot\vec{\nabla}_r f =&\rho\left[S_{\mathrm{eq}}+\mathcal{I}\{f\}-\frac{1}{R\rho}\frac{\partial f}{\partial\phi}\right],\\ 0 =&S_{\mathrm{eq}}+\mathcal{I}\{f\}-\frac{1}{R\rho}\frac{\partial f}{\partial\phi},\end{aligned}\tag{8.4}$$

and since the density is present in the last term, the secondary fluence is no longer independent of the density in the presence of an external electromagnetic field, hence Fano's theorem is no longer valid [45]. Bouchard et al [57] and de Pooter et al [62] identified two special conditions to obtain equilibrium in this case. Fano's theorem is applicable in magnetic fields with the fulfilment of one of the following conditions:

1. The magnetic field strength is proportional to the mass density spatial distribution, such that $\vec{\nabla}(R\rho)=\vec{0}$.
2. The source is isotropic, i.e., $\frac{\partial S_{\mathrm{eq}}}{\partial\theta}=\frac{\partial S_{\mathrm{eq}}}{\partial\phi}=0$, which causes f_{eq} to be also isotropic, hence $q\left(\hat{\boldsymbol{u}}\times\vec{B}\right)\cdot\vec{\nabla}_p f_{\mathrm{eq}}=0$.

Since condition 1 imposes a restriction on the magnetic field and not on the source (as condition 2 does), then it is more representative of an external beam geometry. Thus, the transport equation is

$$\begin{aligned}\hat{\boldsymbol{u}}\cdot\vec{\nabla}_r f_{\mathrm{eq}} =&\rho\left[S_{\mathrm{eq}}+\mathcal{I}\{f_{\mathrm{eq}}\}-\frac{1}{R_{\mathrm{eq}}}\frac{\partial f_{\mathrm{eq}}}{\partial\phi}\right],\\ 0 =&S_{\mathrm{eq}}+\mathcal{I}\{f_{\mathrm{eq}}\}-\frac{1}{R_{\mathrm{eq}}}\frac{\partial f_{\mathrm{eq}}}{\partial\phi},\end{aligned}\tag{8.5}$$

with $R_{\mathrm{eq}}=R\rho=\frac{p}{qB}$. To fulfil the magnetic field proportionality to mass density in condition 1, the calculations of particle fluence can be performed in water, then the solution corresponds to the CPE spectrum prescribed by Fano's conditions, which is the same as in the absence of a magnetic field.

8.2.1.4 Electron fluence spectra

To benchmark the electron fluence spectra calculations in the presence of magnetic fields, in this section it is shown that the electron fluence spectrum is the same in the absence and presence of magnetic fields when the first special Fano condition is fulfilled. For this, the transport equation (eq 8.5) is integrated over all directions

$$0 = \int_{4\pi} S_{\mathrm{eq}} d\Omega + \int_{4\pi} \mathcal{I}\left\{f_{\mathrm{eq}}\right\} d\Omega - \int_{4\pi} \frac{1}{R_{\mathrm{eq}}} \frac{\partial f_{\mathrm{eq}}}{\partial \phi} d\Omega, \tag{8.6}$$

defining a spectral source S_Q as

$$S_Q \equiv \int_{4\pi} s_Q\left(\vec{r},\vec{p}\right) \mathrm{d}\Omega, \tag{8.7}$$

and the integration of the interaction term given by

$$\begin{aligned} \int_{4\pi} \mathcal{I}\left\{f\left(\vec{r},\vec{p}\right)\right\} \mathrm{d}\Omega &= -\Sigma\left(p\right) F\left(\vec{x},p\right) + \int_p^{\infty} \Sigma\left(p' \rightarrow p\right) F\left(\vec{x},p'\right) \mathrm{d}p' \\ &\equiv I\left\{F\left(\vec{r},p\right)\right\}, \end{aligned} \tag{8.8}$$

with F the spectral distribution of f, defined in equation 8.1. The complete integration of the interaction term is presented in appendix 8.B. Finally, the last term to integrate is

$$\int_{4\pi} \frac{1}{R_B \rho} \frac{\partial f}{\partial \phi} \mathrm{d}\Omega = \frac{1}{R_B \rho} \int_0^{\pi} \sin\theta \mathrm{d}\theta \int_0^{2\pi} \frac{\partial f}{\partial \phi} \mathrm{d}\phi = 0. \tag{8.9}$$

Then, the direction-integrated transport equation is

$$0 = S_Q + I\left\{F\left(\vec{r},p\right)\right\}. \tag{8.10}$$

The solution to this equation is independent of magnetic fields. Hence, the electron fluence spectrum is the same in the absence and presence of magnetic fields when the first special Fano condition is fulfilled.

8.2.2 Monte Carlo calculations

8.2.2.1 Validation of Monte Carlo calculations of electron fluence spectra in the presence of magnetic fields

As shown in the theory (section 8.2.1.4), under the first special Fano condition, the Monte Carlo calculations of electron spectra in magnetic fields can be benchmarked with calculations in the absence of magnetic fields. Furthermore, an additional comparison can be made with the analytical approximation of the electron fluence spectra established by Kawrakow [59]. For this, the electron fluence is scored in a water voxel of 1 mm^3 at 10 cm depth inside a $30 \times 30 \times 30$ cm^3 water phantom irradiated by a monoenergetic 1.25 MeV beam at 0 T and 1.5 T, using the user code `cavity` from EGSnrc [48].

8.2.2.2 Electron fluence in detectors

Monte Carlo calculations of the electron fluence differential in energy (or electron fluence, as it is referred throughout the article) in six detectors are performed in the user code `cavity` from EGSnrc [48]. In this code, the electron fluence differential in energy is normalized by the total incident photon fluence, ${F_0}^{\mathrm{tot}}$. The six detectors studied are a Farmer-type ionization chamber PTW30013 (PTW, Freiburg, Germany), three small-cavity ionization chamber models PTW31010, PTW31021, and PTW31022, the unshielded silicon diode PTW60012, and the microDiamond detector PTW60019. Detector size specifications are listed in table

8.I. The ionization chamber's active sensitive volumes were previously defined in references [41] and [122] for the small-cavity chambers, and for the Farmer-type chamber, respectively. The detector is positioned at 10 cm depth in a water tank phantom of 30 × 30 × 30 cm^3. The 7 MV FFF photon beam phase spaces of the Elekta Unity MR-Linac (Elekta Instrument AB Stockholm, Sweden), kindly provided by the manufacturer, are used. The source-to-surface distance (SSD) is set to 133.5 cm. The reference field size is 10 × 10 cm^2 and the small field is set to 1 × 1 cm^2 at the isocenter for all detectors except for the Farmer type chamber, for which a small field of 3 × 3 cm^2 is used to cover the full sensitive volume. The 1.5 T magnetic field is perpendicular to the irradiation beam, consistently with the Elekta Unity MR-Linac.

	PTW60012	PTW60019	PTW31022	PTW31021	PTW31010	PTW30013
Type of detector	Silicon diode	microDiamond	Pinpoint 3D	Semiflex 3D	Semiflex	Farmer
Sensitive volume diameter [mm]	1.0	2.2	2.9	4.8	5.5	6.1
Sensitive volume length [mm]	0.03	0.001	2.9	4.8	6.5	23.0
Nominal sensitive volume [mm^3]	0.25	0.004	16	70	125	600

Table 8.I – Detector specifications, taken from the manufacturer catalogue.

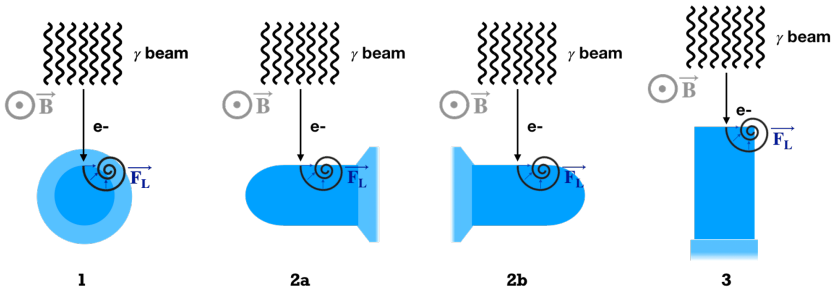

Figure 8.1 – Diagram of three orientations for ionization chambers and one orientation for the solid-state detectors. 1) The chamber axis is parallel to the magnetic field, 2a) the chamber axis is perpendicular to the magnetic field and the Lorentz force ($\mathbf{F}_L$) points towards the stem, 2b) the chamber axis is perpendicular to the magnetic field with $\mathbf{F}_L$ pointing towards the tip and 3) the solid-state detector axis is perpendicular to the magnetic field and parallel to the beam.

For the ionization chambers, three detector orientations with respect to the photon beam and the magnetic field are studied. The chamber axis always remains perpendicular to the photon beam and three orientations with respect to

the magnetic field are considered: 1) parallel, 2a) perpendicular with the Lorentz force pointing towards the stem, and 2b) perpendicular with the Lorentz force pointing towards the tip, as illustrated in figure 8.1. For the solid-state detectors, one orientation is studied: 3) the detector axis is parallel to the photon beam and perpendicular to the magnetic field, as shown on the right of figure 8.1. Only the recommended measurement orientation is considered for the solid-state detectors since the purpose is to evaluate the impact of high-Z components and density for these detectors. In a previous study [114], detector dose perturbations in different orientations in these detectors has been investigated.

The magnetic field is implemented with the enhanced electromagnetic field macro [54] with the recommended step value of EM ESTEPE=0.2. The default parameters are used except for the threshold energy for electrons AE = 0.512 MeV and for photons AP = 0.001 MeV. No variance reduction techniques are applied for the electron fluence spectra calculations accordingly to the EGSnrc code recommendations.

For each detector, the electron spectra simulations are performed in three different geometries, as shown in figure 8.2: 1) the entire detector, 2) the bare cavity with the medium replaced by artificial water, i.e., an artificial medium, denoted w^*, having the same atomic properties as water including stopping-power density corrections but with the electron density of the original sensitive volume material (i.e., silicon for PTW60012, diamond for PTW60019 and air for the ionization chambers), and 3) the bare cavity filled with water.

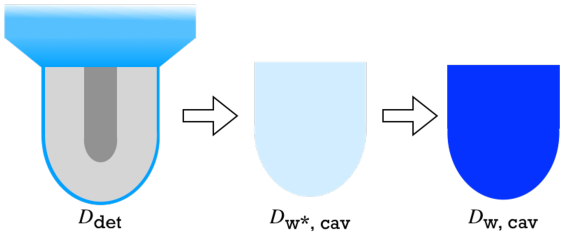

Figure 8.2 – Scheme of the three detector geometries where the electron fluence is calculated. On the left, the full detector, on the middle the bare cavity with artificial water w^*, having the same atomic properties as water with the electron density of the original sensitive volume material, and on the right, the bare cavity filled with water.

To quantify the effect of the magnetic field, the difference between the differential electron fluence at 1.5 T and at 0 T is normalized by the total electron fluence at 0 T:

$$\Delta_B = \frac{F_e(1.5\text{ T}) - F_e(0\text{ T})}{F_e{}^{\text{tot}}(0\text{ T})}. \tag{8.11}$$

For the uncertainty of the electron fluence only the statistical uncertainty from the Monte Carlo simulations is considered.

8.2.2.3 Presence of air gaps around ionization chambers

In reference dosimetry measurements, air gaps surrounding the detector partially or totally can occur, for instance, between a non-waterproof chamber and its water sleeve or between a chamber and a solid water phantom. In the absence of magnetic fields, the effect of the air gaps has negligible perturbation effects. However, several groups [36, 54, 38, 37] have shown that these air gaps can strongly affect the chamber response in the presence of an external magnetic field.

Due to the nature of the air gap formation, the location, distribution and size are usually unknown. Diverse situations have been explored, Agnew et al [38] investigated the effect of the location of the air gap around the chamber, Malkov et al [54] studied the variation of chamber response due to air gaps for multiple magnetic field strengths, and O'Brien et al [37] investigated the effect of the shape

of the air gap, either symmetrical (i.e. with uniform thickness around the chamber) or asymmetrical (i.e. uniform thickness but only in one side of the chamber). Most of the studies were performed for Farmer-type chambers. In this study, the effect of symmetrical and asymmetrical air gaps on chamber response in a Farmer-type chamber and in a smaller chamber, the semiflex PTW31010 is evaluated via the calculation of electron fluence spectra.

The influence of air gaps surrounding the detectors is evaluated in the same experimental setup described previously. The Monte Carlo calculations are performed in two chambers (PTW30013 and PTW31010) for a reference field, at 0 T and 1.5 T, in the parallel orientation. Considering two types of air gaps: 1) symmetrical air gaps are modelled as air layers with uniform thickness (0.2 mm, 0.5 mm, 1.0 mm and 1.5 mm) surrounding the chamber, and 2) asymmetrical air gaps are modelled as air layers with uniform thickness (0.2 mm, 0.5 mm, 1.0 mm and 1.5 mm) placed only in the upper part of the chamber, as shown in the figure 8.3. The air gap effect with or without magnetic fields is evaluated with the electron fluence spectral difference:

$$\Delta_{\text{air gap}}(B_i) = \frac{F_{e,\text{ air gap}}(B_i) - F_{e,\text{ no air gap}}(B_i)}{F^{\text{tot}}_{e,\text{ no air gap}}(B_i)}, \tag{8.12}$$

with B_i either 0 T or 1.5 T and $F^{\text{tot}}_{e,\text{ no air gap}}$ the total electron fluence when there is no air gap.

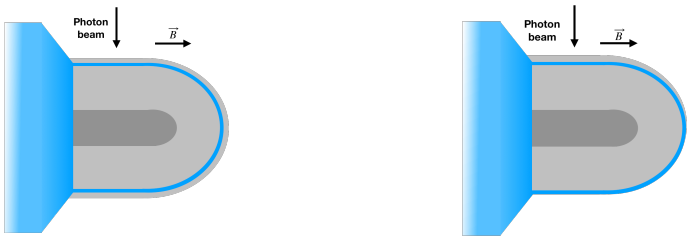

(a) Symmetrical air gap. **(b)** Asymmetrical air gap.

Figure 8.3 – Illustration of the modeled air gaps surrounding the chamber in the parallel orientation.

8.3 Results and discussion

8.3.1 Validation of Monte Carlo calculations of electron fluence in the presence of magnetic fields

If Fano conditions are fulfilled, electron fluence spectra in the presence of a magentic field is identical to the electron fluence spectra in the absence of magnetic fields. Therefore, the Monte Carlo calculations of electron fluence spectra at 1.5 T can be validated against the electron fluence spectra at 0 T. For this, a geometry fulfilling the first special Fano condition is simulated, the comparison between Monte Carlo simulations of electron fluence in the absence and presence of an external magnetic field is shown in figure 8.4. The agreement is good and consistent with the statistical uncertainty of the simulations (<0.1%). The percentage difference fluctuates around zero for most of the energies except for the higher energies, in which the difference increases because F_e/F_0^{tot} at 0 T and 1.5 T tend to zero, thus small differences become more significant. An additional comparison with Kawrakov's analytical approximation [59] is presented.

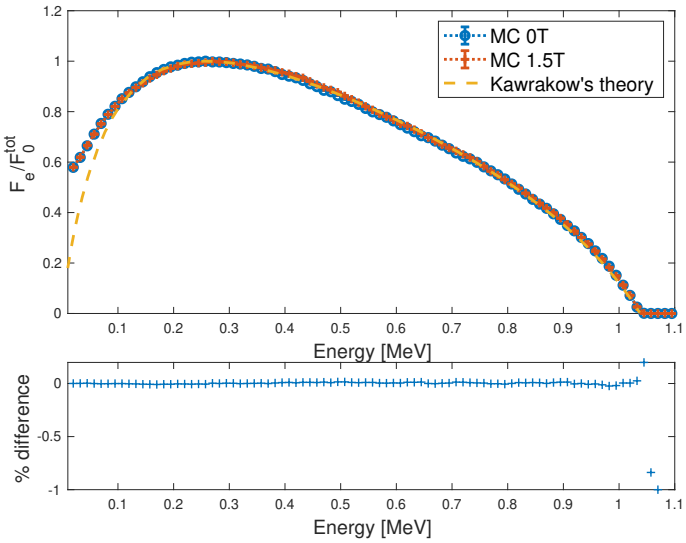

Figure 8.4 – Normalized electron fluence simulated with `cavity` (EGSnrc) in a water voxel of 1 mm^3 at 0 T and 1.5 T and the theoretical prediction from reference [59]. The percentage difference between the Monte Carlo simulations at 0 T and 1.5 T are presented in the bottom.

8.3.2 Electron fluence in ionization chambers

Electron fluence spectra normalized by the total incident photon fluence are scored in each ionization chamber for a reference and a small field, at 0 T and 1.5 T, in the parallel and in the two perpendicular orientations, results are shown in the top row of figures 8.5, 8.6 and 8.7. The spectral differences due to the magnetic field (eq. 8.11) are presented in the bottom row of each figure. Additionally, the variation in the total electron fluence due to the magnetic field is presented in table 8.II. In the three orientations, the magnetic field impact is more significant in small fields than in the reference field in all chambers, but it is especially relevant in the small-cavity chambers.

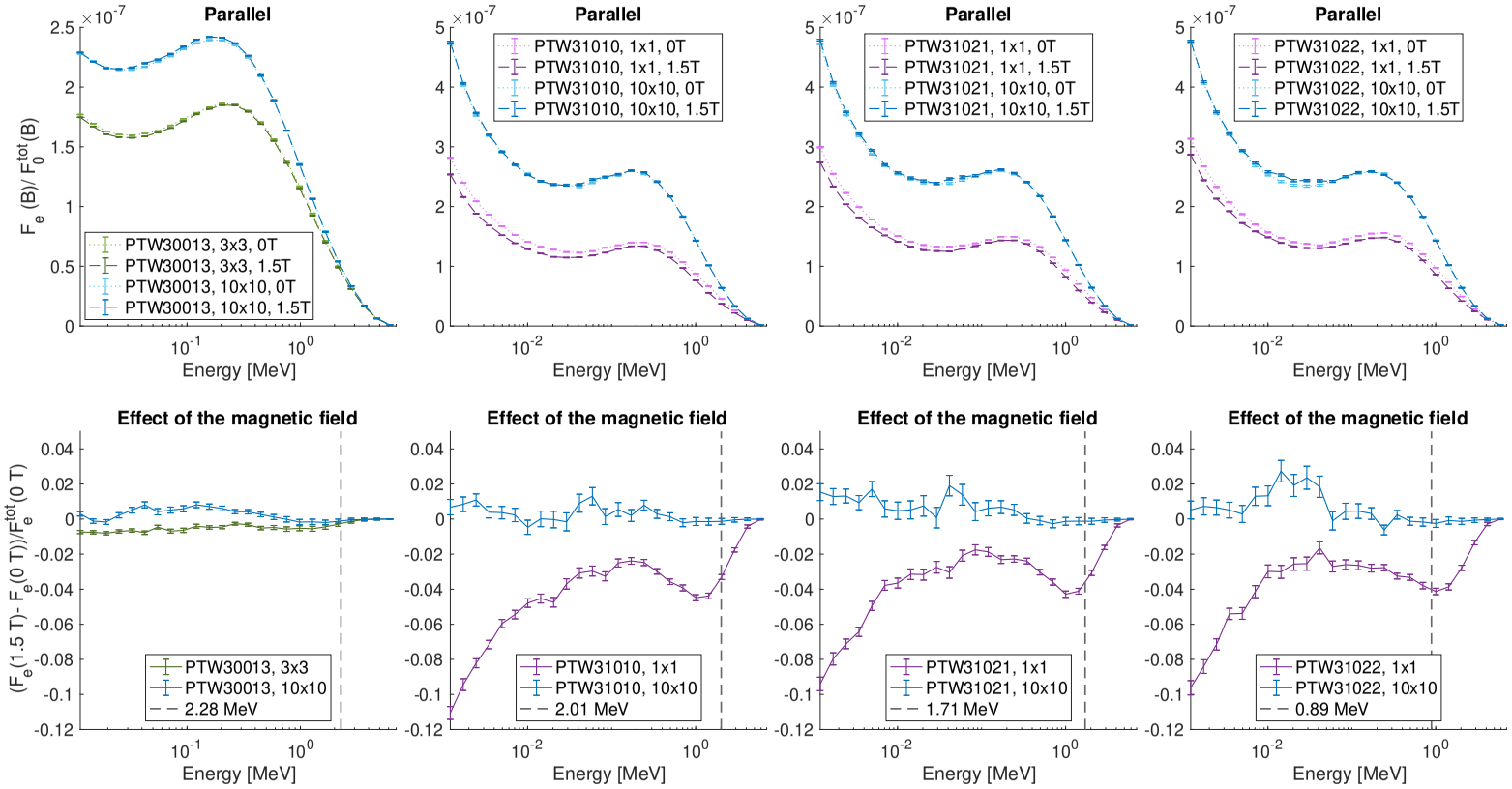

Figure 8.5 – In the top row, Monte Carlo calculated electron fluence spectra per total incident photon fluence, at 0 T and 1.5 T, in each ionization chamber (from left to right: PTW30013, PTW31010, PTW31021 and PTW31022), in the parallel orientation. In the bottom row, the corresponding electron fluence differences due to the presence of the magnetic field in each field size and chamber model. The vertical dashed line is at the energy at which the gyration radius equals the cavity diameter, explained in section 8.3.4.

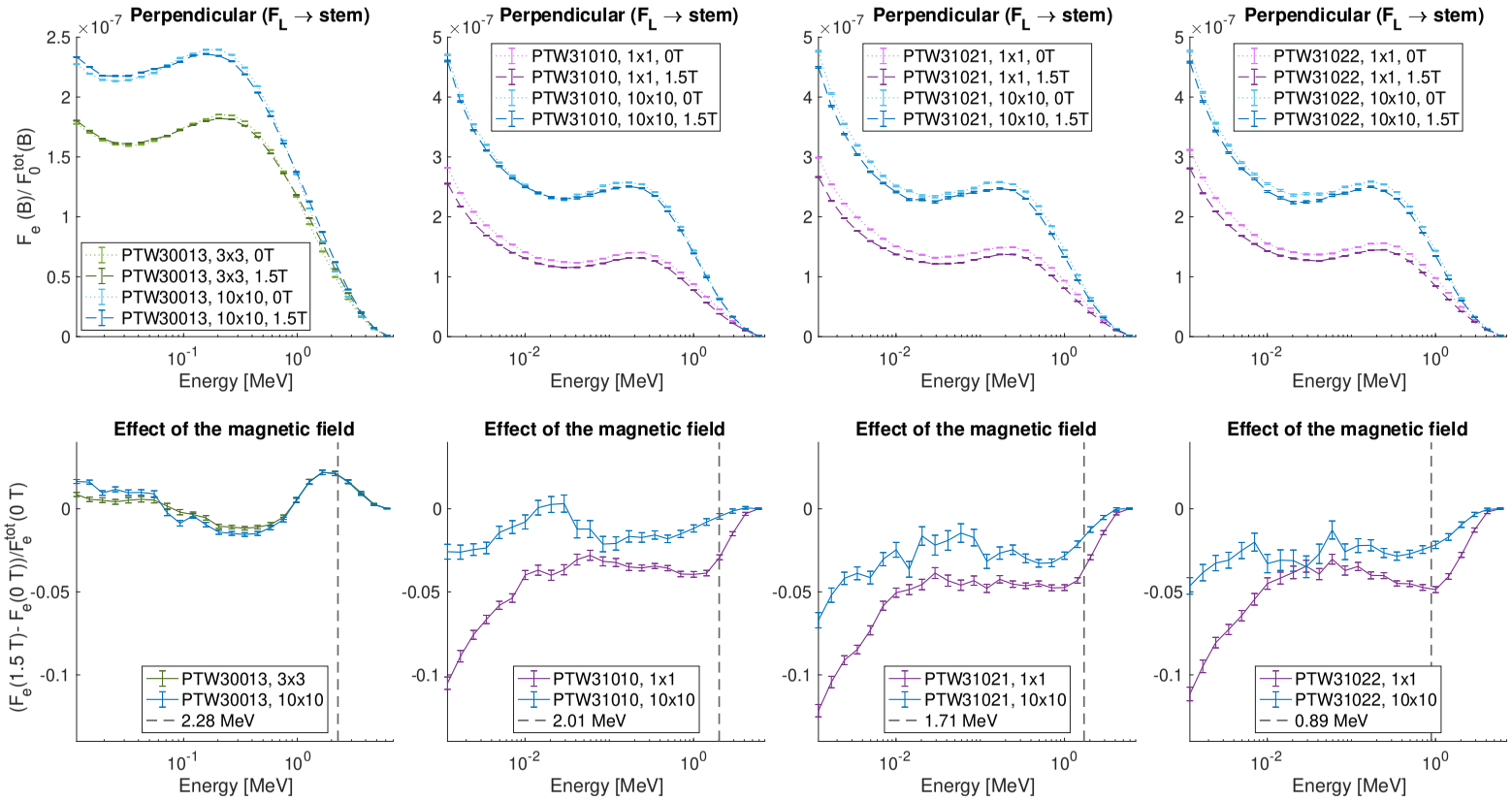

Figure 8.6 – In the top row, Monte Carlo calculated electron fluence spectra per total incident photon fluence, at 0 T and 1.5 T, in each ionization chamber (from left to right: PTW30013, PTW31010, PTW31021 and PTW31022), in the perpendicular orientation 2a ($\mathbf{F}_L \rightarrow$ stem). In the bottom row, the corresponding electron fluence differences due to the presence of the magnetic field in each field size and chamber model. The vertical dashed line is at the energy at which the gyration radius equals the cavity diameter, explained in section 8.3.4.

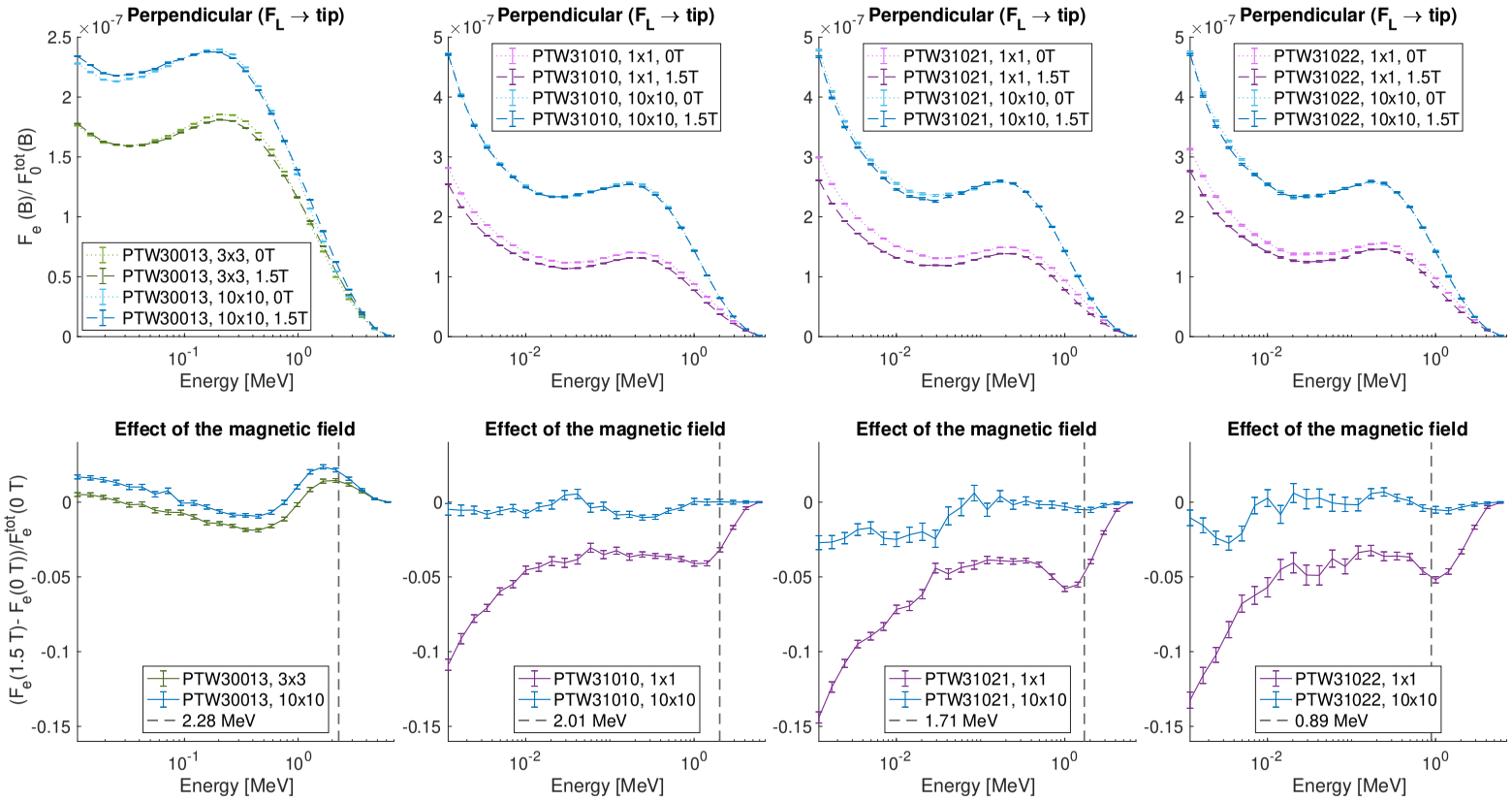

Figure 8.7 – In the top row, Monte Carlo calculated electron fluence spectra per total incident photon fluence, at 0 T and 1.5 T, in each ionization chamber (from left to right: PTW30013, PTW31010, PTW31021 and PTW31022), in the perpendicular orientation 2b ($\mathbf{F}_L \rightarrow$ tip). In the bottom row, the corresponding electron fluence differences due to the presence of the magnetic field in each field size and chamber model. The vertical dashed line is at the energy at which the gyration radius equals the cavity diameter, explained in section 8.3.4.

In small fields, the electron fluence decreases at 1.5 T compared to the 0 T case. In particular, in the small-cavity chambers, the electron fluence decreases with decreasing energy. This is in agreement with the reduction in absorbed dose previously observed in the presence of a magnetic field [75, 76] because electrons deposit their energy closer to the point where they are created due to the Lorentz force [26].

The electron fluence spectra vary with orientation; the magnetic field influence is more significant in the perpendicular orientations because there are larger perturbations coming from the extracameral components than in the parallel orientation. In orientation 2a, electrons, on average, are deflected towards the stem, while in orientation 2b, they are deflected towards the tip. In magnetic fields, the total fluence is reduced up to 11.6% in the parallel orientation and up to 14.50% in the perpendicular orientations.

Another effect of the extracameral components can be observed in chamber PTW31021; there is a reduction in the low-energy electrons for both field sizes. This is due to the presence of an inner air layer between the graphite and the PMMA wall, as pointed out previously in reference [41].

The magnetic field effect on electron spectra follows a similar trend in the small-cavity chambers in all orientations. On the contrary, there is a different trend between the parallel and the perpendicular orientations for the Farmer-type chamber. The magnetic field effect is more or less constant in the parallel orientations, while in the perpendicular orientation, the variations with energy are more important. This is mainly due to the cavity length and is discussed in detail in the following sections.

		Parallel	Perpendicular ($\mathbf{F}_L \rightarrow$ stem)	Perpendicular ($\mathbf{F}_L \rightarrow$ tip)
PTW30013	10×10 cm^2	-0.08 ± 0.00%	4.42 ± 0.00%	5.12 ± 0.00%
	3×3 cm^2	-1.24 ± 0.00%	4.75 ± 0.00%	2.35 ± 0.00%
PTW31010	10×10 cm^2	0.14 ± 0.00%	-2.56 ± 0.00%	-0.24 ± 0.00%
	1×1 cm^2	-11.60 ± 0.03%	-10.62 ± 0.03%	-11.39 ± 0.03%
PTW31021	10×10 cm^2	-0.19 ± 0.00%	-6.08 ± 0.01%	-1.27 ± 0.00%
	1×1 cm^2	-10.56 ± 0.03 %	-11.85 ± 0.03%	-14.50 ± 0.04%
PTW31022	10×10 cm^2	-0.18± 0.00%	-4.58 ± 0.01%	-0.90 ± 0.00%
	1×1 cm^2	-9.96 ± 0.04%	-11.08 ± 0.04%	-12.34 ± 0.04%

Table 8.II – Percentage of total electron fluence variation due to the magnetic field in the ionization chambers.

8.3.3 Effect of detector geometry and density

8.3.3.1 Farmer-type chamber

Electron fluence spectral differences due to the presence of an external magnetic field for two irradiation fields (10×10 cm^2 and 3×3 cm^2) in the Farmer-type chamber geometries, in all orientations, are presented in figure 8.8. The three different geometries are the cavity of the full detector (left), the bare cavity filled with artificial water w^* (middle) and the bare cavity filled with water (right).

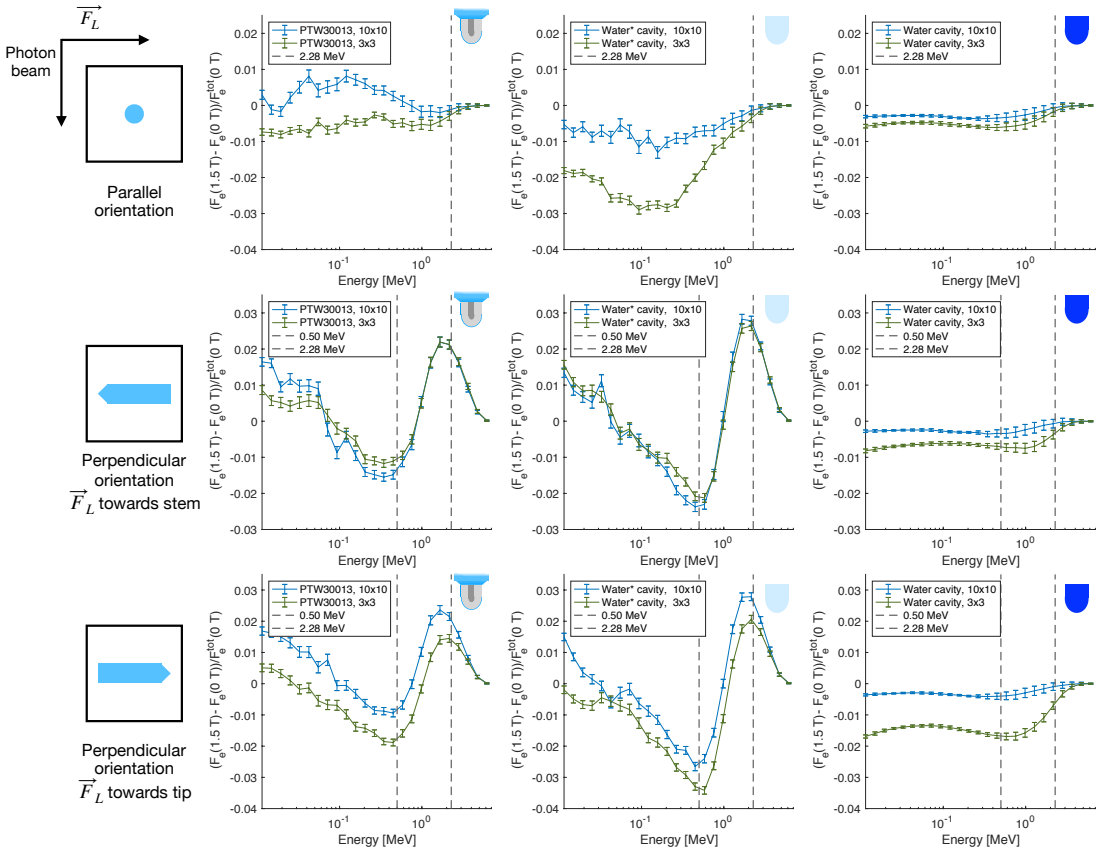

Figure 8.8 – The electron fluence spectral differences due to the magnetic field in each Farmer-type chamber geometry considered in the parallel orientation on the top row and perpendicular orientations with $\mathbf{F}_\mathrm{L}$ pointing towards the stem on the middle row and $\mathbf{F}_\mathrm{L}$ pointing towards the tip on the bottom row. The geometries are: the Farmer type chamber (left), the bare cavity with artificial water (middle) and the bare cavity filled with water (right) at 0 T and 1.5 T for fields of 10×10 cm ^{2} and 3×3 cm^2. The first vertical dashed line (at 0.50 MeV) is at the energy at which $\Delta = 0$, , explained in section 8.3.4.
The vertical dashed line (at 2.28 MeV) is at the energy at which the gyration radius equals the cavity diameter. On the left, an illustration of the sensitive volume in the smallest field size in each orientation.

In the parallel orientation, shown in the top row of figure 8.8, the magnetic field has a stronger impact in the small field than in the reference field in the three chamber geometries. The largest fluctuations occur for the second geometry (middle), i.e. when the only difference between the cavity and the medium is the density, especially for the small field. These results confirm that the density is one

of the main causes for the small-field effects as previously seen in the absence of magnetic fields [97] and in the presence of magnetic fields [114]. The perturbations mainly come from low-energy electrons since in a constant magnetic field, the lower the energy, the smaller is the gyration radius which results in an increase in the magnetic field term in the radiation transport equation (equation 8.3). Note that the perturbations in the full chamber geometry (left) are smaller than in the w^* geometry; this indicates that the extracameral components perturbations are in the opposite direction, i.e. they increase the electron fluence which compensates the density perturbations.

In the perpendicular orientations, shown in the middle and bottom rows of figure 8.8, there are no significant variations for the water cavity. For the other two geometries, the magnetic field effect varies considerably with energy, and it does not vary significantly with field size. In this case, the cavity is so large that low-energy electrons deposit their energy locally, and perturbations from lateral electrons are less significant, which explains the lack of small-field effects.

The general trend of the magnetic field effect comes mainly from the density differences, as can be seen in the middle column of figure 8.8. The trend variations are due to the cavity dimensions, and the explanation is in section 8.3.4. As in the parallel orientation, perturbations are smaller for the full chamber (left) because the extracameral components are compensating the electron loss, especially at low energies.

The variations on electron fluence are smaller in the parallel orientation than in the perpendicular orientations because the extracameral components play a more critical role in the perpendicular orientations, which the Farmer chamber length emphasizes.

8.3.3.2 Small-cavity chambers

The differences in electron fluence due to the magnetic field are similar in the three small-cavity chambers in all orientations. They are shown in figure 8.9 only for the chamber PTW31010 and its corresponding geometries. The magnetic field

impact depends strongly on chamber geometry, the Farmer-type chamber and the small-cavity chambers are impacted differently. There are two main geometrical differences between these types of chambers: the length of the cavity (see table 8.I) and the shape of the tip, which is semi-spherical for the small-cavity chamber and conical pointed for the Farmer chamber.

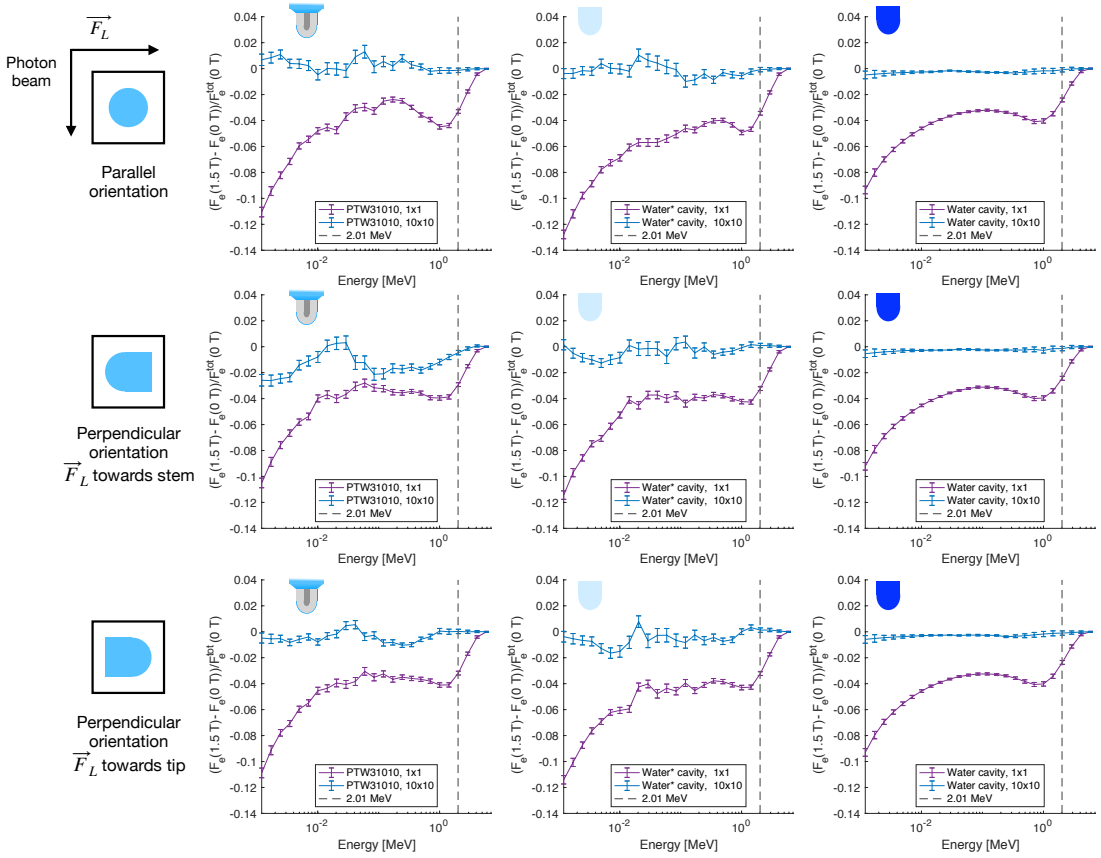

Figure 8.9 – The electron fluence spectral differences due to the magnetic field in each semiflex chamber geometry considered in the parallel orientation on the top row and perpendicular orientations with $\mathbf{F}_\mathrm{L}$ pointing towards the stem on the middle row and $\mathbf{F}_\mathrm{L}$ pointing towards the tip on the bottom row. The geometries are: chamber (left), the bare cavity with artificial water (middle) and the bare cavity filled with water (right) at 0 T and 1.5 T for fields of 10 × 10 cm ^{2} and 1 × 1 cm^2. The vertical dashed line is at the energy at which the gyration radius equals the cavity thickness, explained in section 8.3.4. On the left, an illustration of the sensitive volume in the smallest field size in each orientation.

For the reference field, the magnetic field effect fluctuates around zero with

spectral differences within 1.5% in all orientations except in orientation 2a for the full chamber geometry (left). The reason being that the stem perturbations increase in this orientation; electrons are, on average, deflected towards the stem reducing the electron fluence, especially the low-energy electrons.

When the chamber is irradiated with the reference field, there is charged particle equilibrium (CPE), and if the sensitive volume is filled with water, then the first special Fano condition is fulfilled. Hence, the electron fluence remains the same in the absence and presence of a magnetic field, as shown in the right of figure 8.9. In contrast, when the irradiation field size decreases, the electron fluence decreases significantly with decreasing energy in the presence of magnetic fields. The fluence reduction is due to the loss of lateral CPE in small fields, which is amplified by the asymmetry introduced by the Lorentz force.

When the cavity electron density equates that of air (middle), the magnetic field effect follows the same trend as in the water sensitive volume, but the electron fluence is further reduced in this case. Density perturbations increase in the presence of magnetic fields [114], in low-density materials, fewer secondary electrons are produced, and the electron mean free path generally increases, thus becoming susceptible to the Lorentz force.

When the full chamber (left) is simulated, the magnetic field impact also follows the same trend as in the other two geometries for small fields. However, there are slight variations associated with the influence of extracameral components that changes with orientation. In general, the perturbations are smaller, as the extracameral components seem to compensate the electron fluence reduction.

8.3.4 Effect of the cavity size

The cavity size is relevant for small fields dosimetry in the absence and presence of magnetic fields. The relation between the cavity size and the magnetic field can be approached by considering an electron travelling in vacuum through an infinite slab with the same thickness as the cavity, as shown in figure 8.10. Depending on its energy, an electron can either traverse the cavity (left of figure 8.10) or it can

fully return to the incident wall (right of figure 8.10). The behaviour change occurs when the gyration radius is equal to the cavity thickness at a certain energy, named E_{ERE}. This ERE energy is presented as a dashed line for each detector in figures 8.5-8.16b. In these figures, for the magnetic field effect at small fields, the ERE energy is near the convex region at high energies where there is a local minimum. Note that the ERE energy is only an approximation, and the true scenario is much more complex: electrons enter the cavity in different positions, electrons interact with the medium and lose energy, there is lateral gain and loss of electrons, the thickness cavity is not uniform, and the fluence varies with detector orientation.

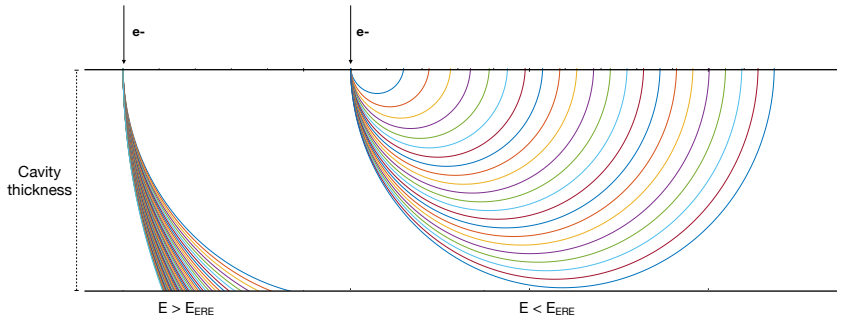

Figure 8.10 – Electrons entering an infinite slab at the same position in a vacuum in the presence of an external 1.5 T magnetic field. E_{ERE} is the energy at which the gyration radius equals the cavity thickness. On the left, electrons with enough energy to fully traverse the slab. On the right, electrons with energy to return to the incident wall.

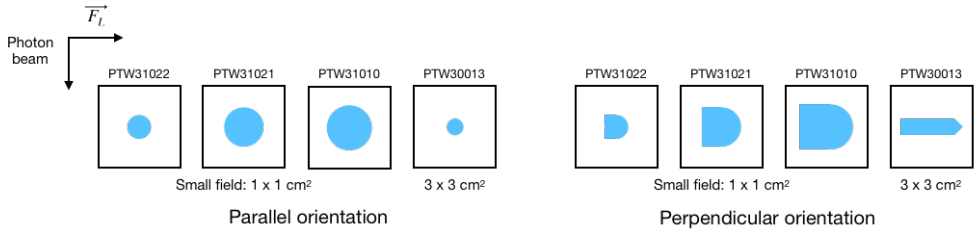

Figure 8.11 – Illustration of each chamber sensitive volume inside the smallest field. The dimensions of the sensitive volume and the field are to scale.

In the parallel orientation, electrons coming in the main direction encounter a plane with approximately the same thickness and length (i.e. sensitive diameter of

table 8.I), as illustrated on the left figure of 8.11. Whereas, in the perpendicular orientation, the encountered plane has a thickness equal to the sensitive volume diameter and the length of the sensitive volume, as illustrated on the right of figure 8.11. For the pinpoint 3D (PTW31022) and the semiflex 3D (PTW31021), the diameter and length of the sensitive volume are equal, the semiflex (PTW31010) is slightly longer than wider, and the Farmer chamber is almost four times longer than wider. The latter case approaches the infinite slab geometry in the perpendicular orientation and explains the remarkable trend change of the Farmer between the parallel and perpendicular orientation.

To explain the magnetic field effect trend in the Farmer chamber in the perpendicular orientation, see figure 8.8, the cavity can be approximated to an infinite slab where only the effect of the magnetic field is considered. Then a pathlength correction, Δl, due to the magnetic field can be defined as

$$\Delta l = \pi * R - d \tag{8.13}$$

where $\pi * R$ is the electron pathlength in magnetic fields, and d is the electron pathlength in the absence of magnetic fields which is equal to the cavity thickness. For energies below E_{ERE}, three cases can occur

1. If $\Delta l < 0$, then the electron pathlength is smaller in magnetic fields than without it.
2. If $\Delta l = 0$, then the electron pathlength is the same with and without magnetic fields.
3. If $\Delta l > 0$, then the electron pathlength is bigger in magnetic fields than without it.

The variation of Δl explains the trend of magnetic field effect, the minimum of the curves in the middle and bottom row of figure 8.8 occurs close to the energy at which $\Delta l = 0$. For the chamber PTW30013 dimensions, this energy is 0.50 MeV, which is the first vertical dashed line in figure 8.8. Even though these cases depict a

simplistic scenario, they provide a good enough approximation of the full radiation transport scenario.

It is worth noting that such a simplistic scenario cannot fully explain the perturbation effects of any radiation detector. While evaluating pathlength differences with an infinite slab might be valuable in large air cavities, for small cavities, it cannot suffice since the geometry is more complex with a central electrode and a wall tip in the vicinity, which produces additional electrons entering the cavity for which the trajectory cannot be addressed analytically. For solid detectors, the situation is even more complex. In such cases, one needs to fully consider what transport equation implicates and how the electron fluence is perturbed compared to ideal conditions, such as in Fano conditions. Unfortunately, in the presence of homogeneous magnetic fields, Fano's theorem cannot hold, and therefore conventional simplifications cannot be used. Monte Carlo remains the only valid method to approach this problem.

8.3.5 Air gap effect on electron fluence spectrum

8.3.5.1 Symmetrical air gaps

The influence of the symmetrical air gaps on electron fluence is presented in figure 8.12 for the Farmer chamber and the semiflex chamber. In general, there are no significant differences among the thicknesses considered, and the air gap effect on electron fluence is 1% or less with respect to the no air gap case for all thicknesses for both chambers.

8.3.5.2 Asymmetrical air gaps

The electron fluence spectra normalized by the total incident photon fluence at 0 T and 1.5 T for chamber PTW30013 surrounded by an asymmetrical gap are shown in figure 8.13. Even in the absence of magnetic fields, there is an air gap effect, and the fluence perturbations increase with air gap thickness.In the presence of an external magnetic field, illustrated on the right of figure 8.13, there is a further

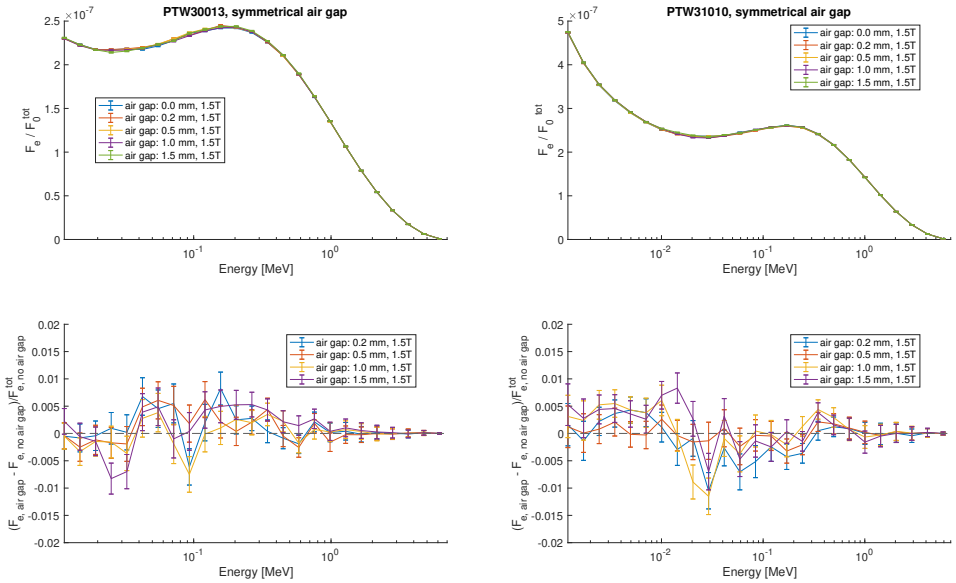

Figure 8.12 – Symmetrical air gaps around chambers PTW30013 (left) and PTW31010 (right) at 1.5 T. In the top row, the electron fluence spectra per total incident photon fluence in the chamber for air gaps of different thickness. In the bottom row, the effect of the air gap is evaluated with respect to no air gap in the electron fluence in the presence of magnetic fields.

reduction of low-energy electrons; the reduction becomes more pronounced with increasing air gap thickness.

The results for the asymmetrical air gap surrounding the small-cavity chamber are presented in figure 8.14. In this case, the electron fluence perturbations are 2.52% or less at 0 T and they decrease as much as 8.63% at 1.5 T. The influence of the magnetic field is present along all the energy spectrum, but it increases, once again, at low-energies. The presence of asymmetrical air gaps has a bigger impact in chambers with smaller cavity sizes in the presence of an external magnetic field.

8.3.5.3 Chamber dose response

In the case of symmetrical air gaps, the 1% variation in electron fluence due to the magnetic field corresponds to a variation of the chamber dose responses within 0.5% as shown in figure 8.15. These results are consistent with reference [37], where results showed that symmetrical air gaps around the chambers have a

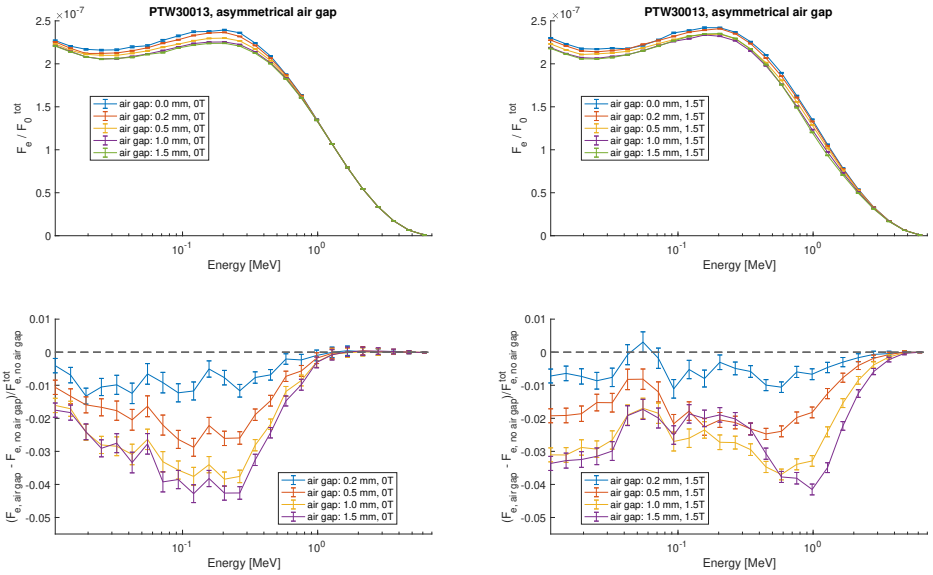

Figure 8.13 – Asymmetrical air gaps around the Farmer-type chamber at 0 T (left) and at 1.5 T (right). In the top row, the electron fluence spectra per total incident photon fluence in the chamber for air gaps of different thickness. In the bottom row, the effect of the air gap is evaluated with respect to no air gap.

minimal effect.

For the case of asymmetrical air gaps, the variation in electron fluence in the Farmer chamber corresponds to a maximal dose reduction of 2.95% and of 6.26%, at 0 T and 1.5 T, respectively, as observed in figure 8.15. For the small-cavity chamber, the dose is further reduced, by as much as 7.55% in the presence of magnetic field, as shown in figure 8.15.

The total fluence variation due to the presence of the magnetic field in all the air gap cases are presented in table 8.III.

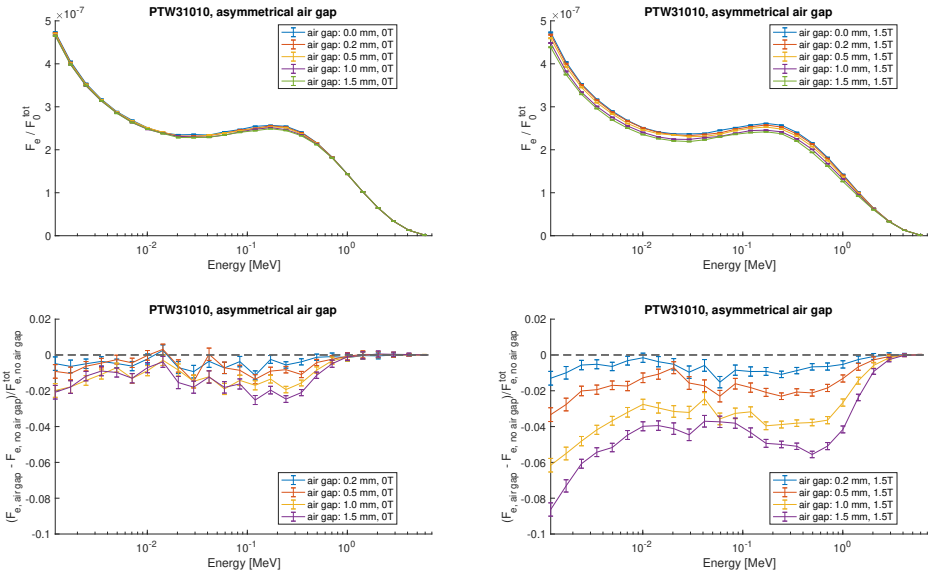

Figure 8.14 – Asymmetrical air gaps around the PTW31010 chamber at 0 T (left) and at 1.5 T (right). In the top row, the electron fluence spectra per total incident photon fluence in the chamber for air gaps of different thickness. In the bottom row, the effect of the air gap is evaluated with respect to no air gap.

Air gap thickness [mm]	PTW30013 symmetrical [%]	PTW30013 asymmetrical [%]	PTW31010 symmetrical [%]	PTW31010 asymmetrical [%]
0.2	0.04	-0.75	-0.31	-0.83
0.5	0.02	-2.25	-0.19	-2.44
1.0	-0.04	-4.08	-0.25	-4.73
1.5	0.08	-5.13	-0.45	-7.04

Table 8.III – Percentage of total electron fluence variation due to the magnetic field in the ionization chambers surrounded by an air gap. The uncertainty is below 0.01% in all cases.

8.3.6 Solid-state detectors

The electron fluence spectra normalized by the total incident photon fluence in the solid-state detectors are only calculated in orientation 3, in which the detector axis is aligned with the photon beam, and it is perpendicular to the magnetic field. These spectra are calculated in three detector geometries (shown in figure 8.2) in

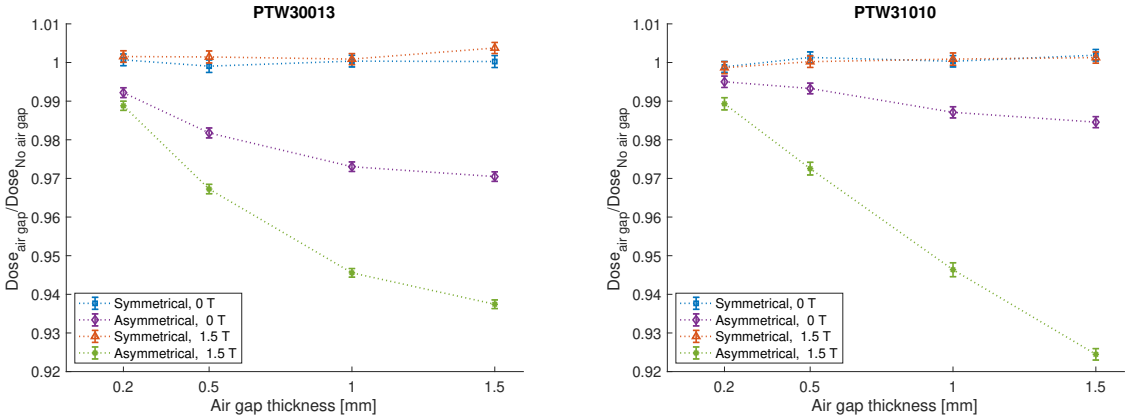

Figure 8.15 – Ratio of dose in the cavity with an air gap relative to that with no air gap at 0 T and 1.5 T for chambers PTW30013 (left) and PTW31010 (right)

two square fields 10 × 10 cm^2 and 1 × 1 cm^2 for 0 T and 1.5 T, the results are presented in the top rows of figures 8.16a and 8.16b for the silicon diode and the microDiamond detector, respectively. The corresponding spectral differences due to the magnetic field are presented in the bottom row of each figure.

The electron fluence decreases in both solid-state detectors in the presence of magnetic fields, as shown on the left columns of figures 8.16a and 8.16b. The effect is very similar in both field sizes for the silicon diode and almost identical for the microDiamond detector, indicating the strong magnetic field impact even in large field sizes, as previously seen in reference [114]. The magnetic field effect is more pronounced for the low-energy electrons.

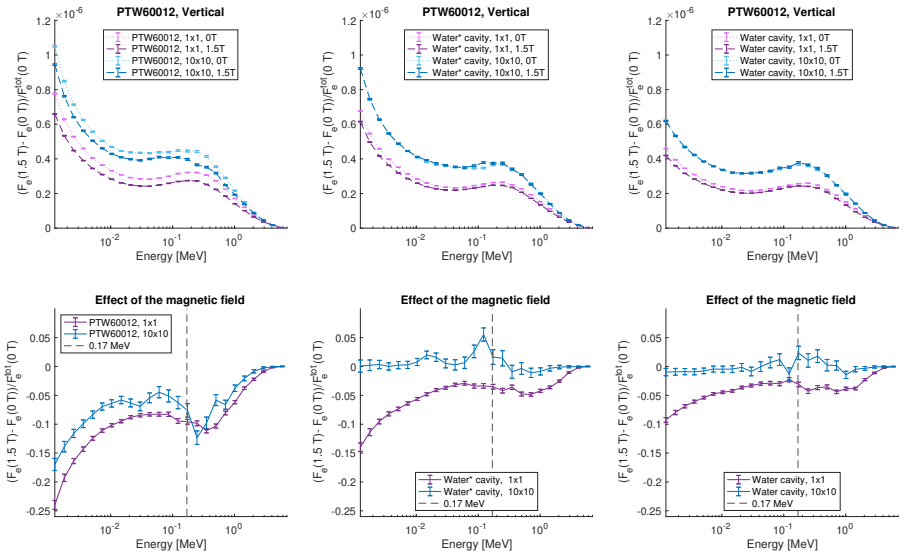

(a) Silicon detector, PTW60012

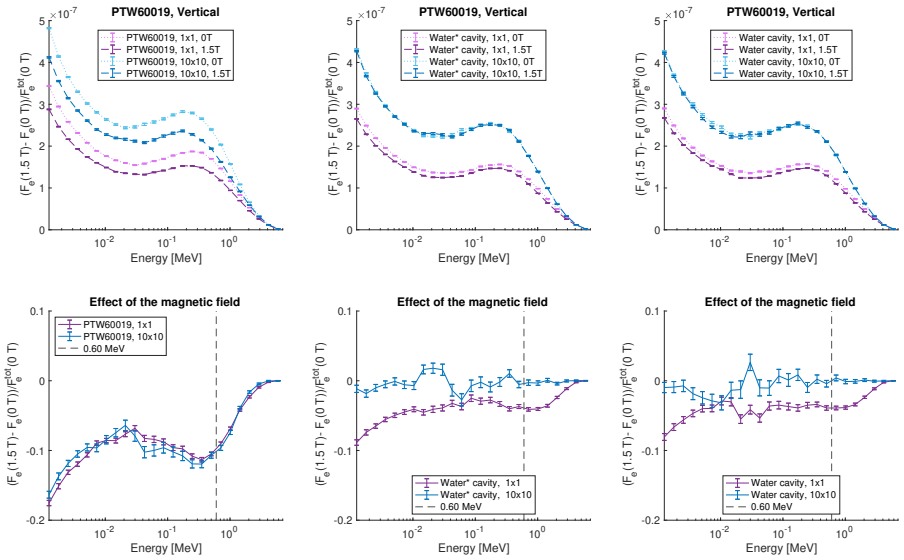

(b) MicroDiamond detector, PTW60019

Figure 8.16 – In the top row, the electron fluence per incident photon fluence for the full solid-state detector (top left), for the bare cavity with artificial water (top middle) and for the bare cavity filled with water (top right) at 0 T and 1.5 T for square irradiation beams of 10×10 cm^2 and 1×1 cm^2. In the bottom row, the relative difference between the electron fluence at 0 T and 1.5 T for each field size and each geometry considered. The vertical dashed line is at the energy at which the gyration radius equals the cavity thickness, explained in section 8.3.4.

When comparing the effect of the magnetic field in the full geometry to the one in the water$*$ cavity, the behaviour is different, particularly in the reference field. Perturbations seem to be strongly amplified by the extracameral components. The density effect can be evaluated by comparing the spectra in the second and third geometry (middle and right columns of figures 8.16a and 8.16b). The trends are very similar for each field size, agreeing with previous results [114] where it was shown that the magnetic field effect on the density perturbation factors is not significant, 1% or less in the dose response. Differences in behaviour between the two field sizes come from the lack of lateral CPE in small fields that is amplified by the asymmetry introduced by the Lorentz force.

8.4 Discussion

Electron fluence spectra have been calculated for six detectors in a reference field and in a small field, in different orientations, in the absence and presence of a magnetic field. The magnetic field effect in the electron fluence in each detector was different. To identify the underlying mechanism behind the magnetic field impact, additional calculations of the electron fluence were performed in two modified detector geometries: the bare sensitive volume filled with artificial water having the same electronic density as the original material, w^*, and filled with water. In solid-state detectors, the extracameral component perturbations increase in the presence of a magnetic field. In ionization chambers, the density variations increase the electron fluence perturbations in the presence of magnetic fields, as previously observed in reference [114].

Three chamber orientations are investigated, the variation in total electron fluence due to the magnetic field is presented in table 8.II. In the Farmer chamber case, the magnetic field impacts less in the parallel orientation than in the perpendicular orientation. In the latter, the interplay between the gyration radius and the cavity size (the cavity length is 3.77 times larger than the cavity diameter) dramatically affects the electron fluence, as explained in section 8.3.4.

For the small-cavity chambers, in the reference field, the magnetic field impact on total electron fluence drastically increases when the Lorentz force points towards the chamber stem. A smaller effect appears in the other two orientations. Contrary to the Farmer chamber, the cavity length is comparable to the cavity diameter in these chambers, explaining the similar behaviour among these two orientations. A significant impact of the small field size is observed in the small-cavity chambers (note that the narrow field used in the Farmer-type chamber is not that small) for all orientations; the magnetic field reduces the total electron fluence between 9.96% to 14.50 % depending on the orientation.

The cases of symmetrical and asymmetrical air gaps (thicknesses between 0.2 mm and 1.5 mm) surrounding a Farmer chamber and a small-cavity chamber are also investigated. The variation in the total electron fluence due to the magnetic field in these cases are presented in table 8.III. For all the symmetrical air gaps, the variation is equal or below 0.08% for the Farmer chamber and below 0.5% for the semiflex. In the case of the asymmetrical air gaps, the magnetic field effect in total fluence increases with the gap thickness up to -5.13% and 7.04% for the Farmer chamber and semiflex chamber, respectively.

The magnetic field strongly impacted the solid-state detectors in both field sizes. The total fluence is reduced by as much as -15.06 $\pm$ 0.09 % and -16.00 $\pm$ 0.07 % for the silicon diode and the microDiamond, respectively. The high-density extracameral components seem to be responsible for the strong effect of the magnetic field.

8.5 Conclusion

This investigation provides physical insights on the response of different detectors - one Farmer chamber, three small-cavity chambers and two solid-state detectors - when irradiated with megavoltage photon beams coupled to an external magnetic field. The electron fluence differential in energy in the detector cavity can be severely modified in magnetic fields, and fluence perturbations are gener-

ally more apparent for low-energy electrons. The electron fluence simulations presented in this study illustrate the interplay between several factors that can make perturbation effects unpredictable in photon beams coupled to magnetic fields: 1) chamber and magnetic field orientation, 2) cavity size and shape, 3) extracameral components, 4) air gaps and their asymmetry, 5) electron energy, and 6) field size.

For reference fields, perturbations in electron fluence in ionization chambers due to the magnetic field are small or even negligible in some cases. However, for small fields, i.e. 1×1 cm^2, the presence of a magnetic field leads to significant perturbations on electron fluence, especially in the low-energy region. Therefore, the determination of quality correction factors for small-cavity ionization chambers is crucial for small fields. Further investigations and corroboration of these factors from independent research groups is still needed.

The magnetic field strongly modifies the electron fluence in solid-state detectors for reference and small fields; hence they should be avoided in the clinic. Similarly, situations where asymmetrical air gaps could occur should be avoided, especially for the small-cavity chambers. The performance of detectors dedicated to dosimetry in the presence of a magnetic field can be improved by avoiding high-density materials surrounding the sensitive volume and non-uniform internal air layers.

Acknowledgements

We gratefully acknowledge Ilias Billas and David Shipley for sharing the Monte Carlo model of the chamber PTW30013, and Jasmine Duchaine for the solid-state detector models. We also acknowledge PTW for providing the detectors blueprints and Elekta for sharing the Unity phases-spaces. We also acknowledge financial support by the Consejo Nacional de Ciencia y Tecnología (CONACyT) and the Natural Sciences and Engineering Research Council of Canada (NSERC RGPIN/04178-2015). This research was enabled in part by the support provided by Calcul Québec (www.calculquebec.ca) and Compute Canada (www.computecanada.ca).

APPENDIX

8.A Magnetic-field term in the radiation transport equation

The term due to the presence of the magnetic field in equation 8.2 can be developed as follows

$$\begin{aligned} q\left(\hat{\boldsymbol{u}}\times\vec{B}\right)\cdot\vec{\nabla}_p f =& q\vec{\nabla}_p f\cdot\left(\hat{\boldsymbol{u}}\times\vec{B}\right) \\ =& q\vec{B}\cdot\left[\vec{\nabla}_p f\times\hat{\boldsymbol{u}}\right] \\ =& q\vec{B}\cdot\left[\frac{1}{p}\left[\frac{\partial f}{\partial\theta}\hat{\boldsymbol{\theta}}+\frac{1}{\sin\theta}\frac{\partial f}{\partial\phi}\hat{\boldsymbol{\phi}}\right]\times\hat{\boldsymbol{u}}\right] \\ =& \frac{q}{p}\vec{B}\cdot\left[\frac{\partial f}{\partial\theta}\hat{\boldsymbol{\theta}}\times\hat{\boldsymbol{u}}+\frac{1}{\sin\theta}\frac{\partial f}{\partial\phi}\hat{\boldsymbol{\phi}}\times\hat{\boldsymbol{u}}\right], \end{aligned} \tag{8.14}$$

choosing the coordinates such that $\vec{B}=B\hat{\boldsymbol{z}}$ and recalling that the gyration radius is defined as $R=\frac{p}{|q|B}$. Then for electrons, $q=-|q|$ and therefore

$$\begin{aligned} q\left(\vec{u}\times\vec{B}\right)\cdot\vec{\nabla}_p f =& -\frac{1}{R}\hat{\boldsymbol{z}}\cdot\left[\frac{\partial f}{\partial\theta}\hat{\boldsymbol{\theta}}\times\vec{u}+\frac{1}{\sin\theta}\frac{\partial f}{\partial\phi}\hat{\boldsymbol{\phi}}\times\vec{u}\right] \\ =& -\frac{1}{R}\hat{\boldsymbol{z}}\cdot\left[\frac{\partial f}{\partial\theta}\left[\sin\phi\hat{\boldsymbol{x}}-\cos\phi\hat{\boldsymbol{y}}\right]+\frac{1}{\sin\theta}\frac{\partial f}{\partial\phi}\left[\cos\theta\cos\phi\hat{\boldsymbol{x}}+\cos\theta\sin\phi\hat{\boldsymbol{y}}-\sin\theta\hat{\boldsymbol{z}}\right]\right] \\ =& -\frac{1}{R}\hat{\boldsymbol{z}}\cdot\left[\left(\sin\phi\frac{\partial f}{\partial\theta}+\cot\theta\cos\phi\frac{\partial f}{\partial\phi}\right)\hat{\boldsymbol{x}}\right. \\ & \left.+\left(-\cos\phi\frac{\partial f}{\partial\theta}+\cot\theta\sin\phi\frac{\partial f}{\partial\phi}\right)\hat{\boldsymbol{y}}+\left(-\frac{\partial f}{\partial\phi}\right)\hat{\boldsymbol{z}}\right] \\ =& \frac{1}{R}\frac{\partial f}{\partial\phi}. \end{aligned} \tag{8.15}$$

8.B Radiation transport equation for the electron fluence spectrum

Considering a geometry in which the medium atomic properties are homogeneous , i.e. the first classical Fano condition is fulfilled, but with an arbitrary mass

density distribution given by $\rho = \rho(\vec{r})$ and defining a particle source as $s_Q = s_Q(\vec{r},\vec{p})$ and an homogeneous magnetic field $\vec{B} = B\hat{\boldsymbol{z}}$. The transport equation is given by

$$\hat{\boldsymbol{u}} \cdot \vec{\nabla}_r f = \rho \left[S_Q + \mathcal{I}\{f\} - \frac{1}{R_{B\rho}} \frac{\partial f}{\partial \phi} \right], \tag{8.16}$$

the solution of this equation is unique and defined by Q, B and ρ, noting the solution as $f = f^{\rho}_{Q_B}$. To integrate the transport equation of f over all directions, each term is integrated separately. First, the integration of the left term in equation 8.16 is

$$\begin{aligned}
\int_{4\pi} \vec{u} \cdot \vec{\nabla}_r f \,\mathrm{d}\Omega =& \int_{4\pi} \frac{\partial}{\partial x} \left[\sin\theta \cos\phi f\left(\vec{x},\vec{p}\right) \right] \mathrm{d}\Omega + \int_{4\pi} \frac{\partial}{\partial y} \left[\sin\theta \sin\phi f\left(\vec{x},\vec{p}\right) \right] \mathrm{d}\Omega \\
&+ \int_{4\pi} \frac{\partial}{\partial z} \left[\cos\theta f\left(\vec{x},\vec{p}\right) \right] \mathrm{d}\Omega \\
=& \frac{\partial}{\partial x} \left[\int_{4\pi} \sin\theta \cos\phi f\left(\vec{x},\vec{p}\right) \mathrm{d}\Omega \right] + \frac{\partial}{\partial y} \left[\int_{4\pi} \sin\theta \sin\phi f\left(\vec{x},\vec{p}\right) \mathrm{d}\Omega \right] \\
&+ \frac{\partial}{\partial z} \left[\int_{4\pi} \cos\theta f\left(\vec{x},\vec{p}\right) \mathrm{d}\Omega \right] \\
=& \frac{\partial}{\partial x} \left[\frac{\int_{4\pi} \sin\theta \cos\phi f\left(\vec{x},\vec{p}\right) \mathrm{d}\Omega}{\int_{4\pi} f\left(\vec{x},\vec{p}\right) \mathrm{d}\Omega} F\left(\vec{x},p\right) \right] + \frac{\partial}{\partial y} \left[\frac{\int_{4\pi} \sin\theta \sin\phi f\left(\vec{x},\vec{p}\right) \mathrm{d}\Omega}{\int_{4\pi} f\left(\vec{x},\vec{p}\right) \mathrm{d}\Omega} F\left(\vec{x},p\right) \right] \\
&+ \frac{\partial}{\partial z} \left[\frac{\int_{4\pi} \cos\theta f\left(\vec{x},\vec{p}\right) \mathrm{d}\Omega}{\int_{4\pi} f\left(\vec{x},\vec{p}\right) \mathrm{d}\Omega} F\left(\vec{x},p\right) \right]
\end{aligned}$$

defining position-dependent and momentum-dependent functions

$$\begin{aligned}
\langle \sin\theta\cos\phi \rangle^{\rho}_{Q_B} \equiv \langle \sin\theta\cos\phi \rangle^{\rho}_{Q_B}\left(\vec{x},p\right) &= \frac{\int_{4\pi} \sin\theta\cos\phi f^{\rho}_{Q_B}\left(\vec{x},\vec{p}\right) \mathrm{d}\Omega}{\int_{4\pi} f^{\rho}_{Q_B}\left(\vec{x},\vec{p}\right) \mathrm{d}\Omega} \\
\langle \sin\theta\sin\phi \rangle^{\rho}_{Q_B} \equiv \langle \sin\theta\sin\phi \rangle^{\rho}_{Q_B}\left(\vec{x},p\right) &= \frac{\int_{4\pi} \sin\theta\sin\phi f^{\rho}_{Q_B}\left(\vec{x},\vec{p}\right) \mathrm{d}\Omega}{\int_{4\pi} f^{\rho}_{Q_B}\left(\vec{x},\vec{p}\right) \mathrm{d}\Omega} \\
\langle \cos\theta \rangle^{\rho}_{Q_B} \equiv \langle \cos\theta \rangle^{\rho}_{Q_B}\left(\vec{x},p\right) &= \frac{\int_{4\pi} \cos\theta f^{\rho}_{Q_B}\left(\vec{x},\vec{p}\right) \mathrm{d}\Omega}{\int_{4\pi} f^{\rho}_{Q_B}\left(\vec{x},\vec{p}\right) \mathrm{d}\Omega}
\end{aligned} \tag{8.17}$$

$\Rightarrow$

$$\int_{4\pi} \hat{\boldsymbol{u}} \cdot \vec{\nabla}_r f^{\rho}_{Q_B} \mathrm{d}\Omega = \frac{\partial}{\partial x}\left[\langle \sin\theta\cos\phi\rangle^{\rho}_{Q_B} F^{\rho}_{Q_B}(\vec{x},p)\right] + \frac{\partial}{\partial y}\left[\langle \sin\theta\sin\phi\rangle^{\rho}_{Q_B} F^{\rho}_{Q_B}(\vec{x},p)\right] + \frac{\partial}{\partial z}\left[\langle \cos\theta\rangle^{\rho}_{Q_B} F^{\rho}_{Q_B}\right. \tag{8.18}$$

note that $f^{\rho}_{Q_B}$ as well as the functions in equation 8.17 are entirely defined by Q, B and ρ. Thus, their explicit dependence on f can be omitted and be reported in terms of Q, B and ρ.

Defining the spectral source S_Q as

$$S_Q \equiv \int_{4\pi} s_Q(\vec{x},\vec{p})\,\mathrm{d}\Omega. \tag{8.19}$$

Recalling that the interaction term is given by

$$\mathcal{I}\{f(\vec{x},\vec{p})\} = -\Sigma(p) f(\vec{x},\vec{p}) + \int_p^{\infty} \mathrm{d}p' \int_{4\pi} f\left(\vec{x},\vec{p}'\right) \sigma\left(\vec{p}' \rightarrow \vec{p}\right) \mathrm{d}\Omega' \tag{8.20}$$

with the mass macroscopic cross section differential in momentum only defined as

$$\Sigma\left(p \rightarrow p'\right) = \int_{4\pi} \sigma\left(\vec{p} \rightarrow \vec{p}'\right) \mathrm{d}\Omega' \tag{8.21}$$

and the mass macroscopic cross section defined as

$$\Sigma(p) = \int_0^{p} \Sigma\left(p \rightarrow p'\right) \mathrm{d}p' \tag{8.22}$$

then, the integration of the interaction term over all directions is

$$\begin{aligned}
\int_{4\pi}\mathcal{I}\left\{f\left(\vec{x},\vec{p}\right)\right\}\mathrm{d}\Omega =& -\int_{4\pi}\Sigma\left(p\right)f\left(\vec{x},\vec{p}\right)\mathrm{d}\Omega+\int_{4\pi}\mathrm{d}\Omega\int_{p}^{\infty}\mathrm{d}p'\int_{4\pi}f\left(\vec{x},\vec{p}'\right)\sigma\left(\vec{p}'\rightarrow\vec{p}\right)\mathrm{d}\Omega' \\
=& -\Sigma\left(p\right)\int_{4\pi}f\left(\vec{x},\vec{p}\right)\mathrm{d}\Omega+\int_{p}^{\infty}\mathrm{d}p'\int_{4\pi}f\left(\vec{x},\vec{p}'\right)\left[\int_{4\pi}\sigma\left(\vec{p}'\rightarrow\vec{p}\right)\mathrm{d}\Omega\right]\mathrm{d}\Omega' \\
=& -\Sigma\left(p\right)F\left(\vec{x},p\right)+\int_{p}^{\infty}\mathrm{d}p'\int_{4\pi}f\left(\vec{x},\vec{p}'\right)\Sigma\left(p'\rightarrow p\right)\mathrm{d}\Omega' \\
=& -\Sigma\left(p\right)F\left(\vec{x},p\right)+\int_{p}^{\infty}\Sigma\left(p'\rightarrow p\right)\left[\int_{4\pi}f\left(\vec{x},\vec{p}'\right)\mathrm{d}\Omega'\right]\mathrm{d}p' \\
=& -\Sigma\left(p\right)F\left(\vec{x},p\right)+\int_{p}^{\infty}\Sigma\left(p'\rightarrow p\right)F\left(\vec{x},p'\right)\mathrm{d}p' \\
\equiv& I\left\{F\left(\vec{x},p\right)\right\}.
\end{aligned} \tag{8.23}$$

Finally, the last term to integrate is

$$\begin{aligned}
\int_{4\pi}\frac{1}{R_B\rho}\frac{\partial f}{\partial\phi}\mathrm{d}\Omega =& \frac{1}{R_B\rho}\int_{0}^{\pi}\sin\theta\mathrm{d}\theta\int_{0}^{2\pi}\frac{\partial f}{\partial\phi}\mathrm{d}\phi \\
=& 0.
\end{aligned} \tag{8.24}$$

From these results, the direction-integrated transport equation is

$$\frac{\partial}{\partial x}\left[\left\langle\sin\theta\cos\phi\right\rangle_{Q_B}^{\rho}F\right]+\frac{\partial}{\partial y}\left[\left\langle\sin\theta\sin\phi\right\rangle_{Q_B}^{\rho}F\right]+\frac{\partial}{\partial z}\left[\left\langle\cos\theta\right\rangle_{Q_B}^{\rho}F\right]=\rho\left[S_Q+I\left\{F\right\}\right] \tag{8.25}$$

with the solution expressed as $F=F_{Q_B}^{\rho}\left(\vec{x},p\right)$ being unique and entirely defined by Q, B and ρ.

CHAPTER 9

CONCLUSION

With the advent of MRI-linacs to the clinic, reference dosimetry must be performed in the presence of external magnetic fields. This thesis studied the effect of the magnetic field detector dose response and its perturbations under multiple configurations. Several small-cavity detector dose response were characterized, and quality correction factors, $k_{Q_B,Q}^{f_B,f}$, accounting for the impact of the magnetic field were calculated.

In the first part, four small cavity ion chamber responses in several magnetic fields were characterized in two configurations, using experimental measurements and Monte Carlo simulations. In the design of these ionization chambers, there is a region where the charge collection is inefficient; thus, detailed Monte Carlo simulations accounting for these dead volumes were performed. Additionally, quality correction factors accounting for the magnetic field (table 4.V) and its uncertainty budget uncertainty (tables 4.III and 4.IV) were presented for different configurations.

Results showed that several factors that appear insignificant in conventional conditions, such as fine air layers, minor geometrical discrepancies, and the sensitive volume's exact position, are relevant in magnetic fields. To know the geometry of each chamber, we recommend acquiring an image of the detectors to ensure that the blueprints correspond to the real geometry and that there are no hidden features. Additionally, it is important to perform experimental measurements to validate Monte Carlo models. For small cavity ion chambers, the dead volume represents a significant fraction of the sensitive volume ($\approx 20\%$), and its modelling is crucial to improve the simulation accuracy. Therefore, a higher level of detail in manufacturing drawing is essential to accurately model the detector dose response in magnetic fields.

The second part provided physical insights on the magnetic field impact on

five detectors - including three small-cavity ionization chambers and two solid-state detectors - in different irradiation field sizes. For this, perturbation factors corresponding to the extracameral components, differences in density and atomic composition and volume averaging were isolated.

On the one hand, solid-state detector dose responses are strongly affected by the magnetic field in all orientations. The extracameral perturbations are amplified in magnetic fields, especially for large fields, while the effect on the density and volume averaging perturbations is lower (1% or less from unity). Therefore, the current designs of solid-state detectors (PTW60012 and PTW60019) should be avoided for reference dosimetry in the presence of magnetic fields.

On the other hand, the magnetic field effect for ionization chambers is more significant on the density perturbation factor. Volume averaging is the largest perturbation with and without magnetic fields. Orientations where the chamber axis is aligned with the magnetic field yield $k_{Q_B,Q}^{f_B,f}$ factors closer to unity. The orientation where electrons deflect towards the stem should be avoided. Considering that the smallest possible field in the Elekta Unity is 1×1 cm^2, the three studied ionization chambers (PTW31010, PTW31021 and PTW31022) are suitable for that or larger field sizes in the parallel orientation.

Quality correction factors were calculated for five detectors, in four orientations and for multiple field sizes, shown in tables 6.I-6.V. Future clinical development of MRgRT will require these factors for reference dosimetry measurements and beam calibration.

The third part focused on particle fluence simulations to explain the interplay between the magnetic field and detector geometry, density, size, and orientation. Electron fluence differential in energy spectra was calculated in six detectors - one Farmer chamber, three small-cavity chambers and two solid-state detectors - irradiated with reference and small megavoltage photon beams coupled to a 1.5 T magnetic field.

Results showed that the magnetic field impact on the electron fluence in the detector cavity could be severely modified in magnetic fields, and fluence perturba-

tions are generally more evident for low-energy electrons. The impact also strongly depends on the irradiation conditions, and it is more prominent for small fields. Another important consideration is the configuration between the detector and the magnetic field; electron fluence perturbations are minimized in the parallel orientation.

The electron fluence simulations presented in this study illustrate the interplay between several factors that can make perturbation effects unpredictable in photon beams coupled to magnetic fields:

1. detector and magnetic field orientation
2. cavity size and shape
3. extracameral components
4. air gaps
5. electron energy.

This work provides a deeper understanding of how the dose is deposited in magnetic fields by calculating the electron fluence spectra. Detectors with high-density materials surrounding the sensitive volume and non-uniform internal air layers should not be used in reference dosimetry in the presence of a magnetic field. Additionally, the effect of air gaps surrounding ionization chambers was evaluated; situations where asymmetrical air gaps could occur must be avoided, especially for the small-cavity chambers where the dose can decrease as much as 8.6% with respect to the no air gap case.

These three articles show the complexity of reference dosimetry in the presence of an external magnetic field. In conventional reference dosimetry, CPE can be approximated, and cavity theory (governed by Fano's theorem) is applied with perturbation factors of a small order of magnitude. In contrast, in MRgRT dosimetry, Fano's conditions are violated, and Bragg-Grays' principle can no longer be applied. Thus, it becomes a complex and challenging problem with irradiation conditions in which detector response is extremely sensitive to the features mentioned above, and significant perturbation effects can occur. Consequently, we need reli-

able Monte Carlo simulations to characterize these effects and special attention to ensure that experiments (especially in small fields) match the MC predictions.

The thesis studies the response of two types of commercial radiation detectors in the context of MRgRT radiation dosimetry. While it is concluded that current designs of solid-state detectors should be avoided, we recommend a series of steps to validate Monte Carlo models of ionization chambers in the presence of magnetic fields:

1. Characterization of the dead volume and remove it from the sensitive volume.
2. Confirm that the technical drawings are accurate if possible acquire a high-resolution image of the internal structure.
3. Perform a Fano test and including the discrepancies in the uncertainty budget.
4. Validate the simulations with experimental measurements.
5. Compute an extensive uncertainty budget.

Reference dosimetry is established in dosimetry protocols or CoP that require vetted reference data sets for different detectors. The currently available data for quality correction factors accounting for the effect of the magnetic field is limited. There is a consistent data set of $k_{Q_B,Q}^{f_B,f}$ factors for some Farmer-type ionization chambers with an uncertainty of 0.2% [26] but not for small-cavity chambers. For large fields, this thesis shows that the studied small-cavity chambers (PTW31010, PTW31021, and PTW31022) are reliable and can provide robust measurements in magnetic fields since their quality correction factors are small in the optimal orientations.

In the small field dosimetry case, $k_{Q_B,Q}^{f_B,f}$ data set is scarce, but there is a global effort to overcome this. Recently, Delfs et al [130] showed good agreement with our values of $k_{Q_B,Q}^{f_B,f}$ for chambers PTW31021 and PTW31022 measured in the experimental setup of article 1. However, this setup does not consider the most recommended orientation in the MR-linac (chamber parallel to the magnetic field).

There is still much research to be done for small field dosimetry, $k_{Q_B,Q}^{f_B,f}$ values must be determined by different groups to establish a robust data set. Other types of MR-compatible detectors in terms of perturbation (e.g. plastic scintillator, film, etc.) should also be actively researched.

BIBLIOGRAPHY

[1] H Sung, J Ferlay, R L Siegel, M Laversanne, I Soerjomataram, A Jemal, and F Bray. Global cancer statistics 2020: Globocan estimates of incidence and mortality worldwide for 36 cancers in 185 countries. *CA: a cancer journal for clinicians*, 71(3):209–249, 2021.

[2] D R Brenner, H K Weir, A A Demers, L F Ellison, C Louzado, A Shaw, D Turner, R R Woods, and L M Smith. Projected estimates of cancer in canada in 2020. *Cmaj*, 192(9):E199–E205, 2020.

[3] R Baskar, K Ann Lee, R Yeo, and KW Yeoh. Cancer and radiation therapy: current advances and future directions. *International journal of medical sciences*, 9(3):193, 2012.

[4] M Maqbool. *An introduction to medical physics*. Springer, 2017.

[5] EB Podgorsak. *Radiation oncology physics*. IAEA Vienna, 2005.

[6] W C Röntgen. Uber eine neue art von strahlen. *Sitzungsber Phys Med Ges Wurtzburg*, 9:132–141, 1895.

[7] H Becquerel. Sur les radiations émises par phosphorescent. *Comptes Rendus*, 122:420–421, 1896.

[8] J M Slater. From x-rays to ion beams: A short history of radiation therapy. In *Ion Beam Therapy*, pages 3–16. Springer, 2012.

[9] D I Thwaites and John B Tuohy. Back to the future: the history and development of the clinical linear accelerator. *Physics in Medicine and Biology*, 51(13):R343, 2006.

[10] F M Khan and J P Gibbons. *Khan's the physics of radiation therapy*. Lippincott Williams & Wilkins, 2014.

[11] C Garibaldi, B Al Jereczek-Fossa, G Marvaso, S Dicuonzo, D P Rojas, F Cattani, A Starzyńska, D Ciardo, A Surgo, M C Leonardi, et al. Recent advances in radiation oncology. *Ecancermedicalscience*, 11, 2017.

[12] D A Jaffray. Image-guided radiotherapy: from current concept to future perspectives. *Nature Reviews Clinical Oncology*, 9(12):688, 2012.

[13] A J E Raaijmakers, B W Raaymakers, and J J W Lagendijk. Integrating a MRI scanner with a 6 MV radiotherapy accelerator: dose increase at tissue–air interfaces in a lateral magnetic field due to returning electrons. *Physics in Medicine and Biology*, 50(7):1363–1376, 2005.

[14] BW Raaymakers, IM Jürgenliemk-Schulz, GH Bol, M Glitzner, ANTJ Kotte, B Van Asselen, JCJ De Boer, JJ Bluemink, SL Hackett, MA Moerland, et al. First patients treated with a 1.5 t mri-linac: clinical proof of concept of a high-precision, high-field mri guided radiotherapy treatment. *Physics in Medicine and Biology*, 62(23):L41, 2017.

[15] S Mutic and J F Dempsey. The viewray system: magnetic resonance–guided and controlled radiotherapy. In *Seminars in radiation oncology*, volume 24, pages 196–199. Elsevier, 2014.

[16] S Acharya, B W Fischer-Valuck, R Kashani, P Parikh, D Yang, T Zhao, O Green, O Wooten, H H Li, Y Hu, et al. Online magnetic resonance image guided adaptive radiation therapy: first clinical applications. *International Journal of Radiation Oncology Biology Physics*, 94(2):394–403, 2016.

[17] P J Keall, M Barton, S Crozier, et al. The australian magnetic resonance imaging–linac program. In *Seminars in radiation oncology*, volume 24, pages 203–206. Elsevier, 2014.

[18] B G Fallone. The rotating biplanar linac–magnetic resonance imaging system. In *Seminars in radiation oncology*, volume 24, pages 200–202. Elsevier, 2014.

[19] B Whelan, B Oborn, G Liney, and P Keall. Mri linac systems. In *MRI for Radiotherapy*, pages 155–168. Springer, 2019.

[20] Gary P Liney, B Whelan, B Oborn, Michael Barton, and P Keall. Mri-linear accelerator radiotherapy systems. *Clinical Oncology*, 30(11):686–691, 2018.

[21] S Klüter. Technical design and concept of a 0.35 t mr-linac. *Clinical and translational radiation oncology*, 18:98–101, 2019.

[22] B W Raaymakers, A J E Raaijmakers, A N T J Kotte, D Jette, and J J W Lagendijk. Integrating a MRI scanner with a 6 MV radiotherapy accelerator: dose deposition in a transverse magnetic field. *Physics in Medicine and Biology*, 49(17):4109–4118, 2004.

[23] Elekta. First patient treated with ce-marked elekta unity at university medical center utrecht. url = https://www.elekta.com/pressreleases/4D12CB723E319A4F/first-patient-treated-with-ce-marked-elekta-unity-at-university-medical-center-utrecht/, 2018. Last accessed 28 June 2021.

[24] JJW Lagendijk, BW Raaymakers, AJE Raaijmakers, J Overweg, KJ Brown, EM Kerkhof, RW van der Put, B Hårdemark, M van Vulpen, and UA van der H. MRI/linac integration. *Radiotherapy and Oncology*, 86(1):25–29, 2008.

[25] JJW Lagendijk, M Van Vulpen, and BW Raaymakers. The development of the mri linac system for online mri-guided radiotherapy: a clinical update. *Journal of internal medicine*, 280(2):203–208, 2016.

[26] J de Pooter, I Billas, L de Prez, S Duane, RP Kapsch, C P Karger, B van Asselen, and J Wolthaus. Reference dosimetry in mri-linacs: evaluation of available protocols and data to establish a code of practice. *Physics in Medicine and Biology*, 66(5):05TR02, 2021.

[27] KJ Brown, J Goldwein, and L de Vries. Elekta unity for magnetic resonance radiation therapy.

[28] International Commission on Radiation Units and Measurements. *Determination of Absorbed Dose in a Patient Irradiated by Beams of X Or Gamma Rays in Radiotherapy Procedures; Reprint*. International Commission on Radiation Units and Measurements, 1976.

[29] D van der Merwe, J Van Dyk, E Healy, Band Zubizarreta, J Izewska, B Mijnheer, and A Meghzifene. Accuracy requirements and uncertainties in radiotherapy: a report of the international atomic energy agency. *Acta oncologica*, 56(1):1–6, 2017.

[30] P Andreo, DT Burns, AE Nahum, J Seuntjens, and FH Attix. *Fundamentals of ionizing radiation dosimetry*. John Wiley & Sons, 2017.

[31] P R Almond, P J Biggs, B M Coursey, W F Hanson, M S Huq, R Nath, and D W O Rogers. AAPM's TG-51 protocol for clinical reference dosimetry of high-energy photon and electron beams. *Medical Physics*, 26(9):1847–1870, 1999.

[32] M McEwen, L DeWerd, G Ibbott, D Followill, D W O Rogers, S Seltzer, and J Seuntjens. Addendum to the aapm's tg-51 protocol for clinical reference dosimetry of high-energy photon beams. *Medical physics*, 41(4):041501, 2014.

[33] P Andreo, M S Huq, M Westermark, H Song, A Tilikidis, L DeWerd, and K Shortt. Protocols for the dosimetry of high-energy photon and electron beams: a comparison of the iaea trs-398 and previous international codes of practice. *Physics in Medicine and Biology*, 47(17):3033, 2002.

[34] H Szymanowski, WY Baek, R Neungang-Nganwa, H Nettelbeck, and H Rabus. Po-0850: Mri-linac: Effect of the magnetic field on the interaction cross sections. *Radiotherapy and Oncology*, 115:S431, 2015.

[35] I Meijsing, B W Raaymakers, A J E Raaijmakers, J G M Kok, L Hogeweg, B Liu, and J J W Lagendijk. Dosimetry for the MRI accelerator: the impact

of a magnetic field on the response of a Farmer NE2571 ionization chamber. *Physics in Medicine and Biology*, 54(10):2993–3002, 2009.

[36] S L Hackett, B van Asselen, J W H Wolthaus, J G M Kok, S J Woodings, J J W Lagendijk, and B W Raaymakers. Consequences of air around an ionization chamber: Are existing solid phantoms suitable for reference dosimetry on an MR-linac? *Medical physics*, 43(7):3961, 2016.

[37] D J O'Brien and G O Sawakuchi. Monte Carlo study of the chamber-phantom air gap effect in a magnetic field. *Medical Physics*, 44(7):3830–3838, 2017.

[38] J Agnew, F O'Grady, R Young, S Duane, and G J Budgell. Quantification of static magnetic field effects on radiotherapy ionization chambers. *Physics in Medicine and Biology*, 62(5):1731–1743, 2017.

[39] S Pojtinger, RP Kapsch, OS Dohm, and D Thorwarth. A finite element method for the determination of the relative response of ionization chambers in MR-linacs: simulation and experimental validation up to 1.5 T. *Physics in Medicine & Biology*, 64(13):135011, 2019.

[40] C K Spindeldreier, O Schrenk, A Bakenecker, I Kawrakow, L Burigo, C P Karger, S Greilich, and A Pfaffenberger. Radiation dosimetry in magnetic fields with Farmer-type ionization chambers: determination of magnetic field correction factors for different magnetic field strengths and field orientations. *Physics in Medicine & Biology*, 62(16):6708–6728, 2017.

[41] Y Cervantes, I Billas, D R Shipley, S Duane, and H Bouchard. Small-cavity chamber dose response in megavoltage photon beams coupled to magnetic fields. *Physics in Medicine and Biology*, 2020.

[42] F H Attix. *Introduction to radiological physics and radiation dosimetry*. John Wiley & Sons, 1986.

[43] MJ Berger, M Inokuti, HH Anderson, H Bichsel, JA Dennis, D Powers, SM Seltzer, and JE Turner. Report 37. *Journal of the International Commission on Radiation Units and Measurements*, (2):NP–NP, 1984.

[44] D J Griffiths. *Introduction to electrodynamics*. Cambridge Univeristy Press, fourth edition, 2017.

[45] H Bouchard and A Bielajew. Lorentz force correction to the Boltzmann radiation transport equation and its implications for Monte Carlo algorithms. *Physics in Medicine and Biology*, 60(13):4963–4971, 2015.

[46] N Metropolis and S Ulam. The monte carlo method. *Journal of the American statistical association*, 44(247):335–341, 1949.

[47] Oleg N Vassiliev. Monte carlo methods for radiation transport. *Fundamentals and Advanced Topics*, 2017.

[48] I Kawrakow, E Mainegra-Hing, D W O Rogers, F Tessier, and B R B Walters. *The EGSnrc code system, Monte Carlo simulation of electron and photon transport*. 2001.

[49] AF Bielajew. Fundamentals of the monte carlo method for neutral and charged particle transport. *The University of Michigan*, 1, 2001.

[50] MJ Berger. Monte carlo calculation of the penetration and diffusion of fast charged particles. *Methods in Computational Physics.*, 135, 1963.

[51] J Seco and F Verhaegen. *Monte Carlo techniques in radiation therapy*. CRC/Taylor & Francis, 2013.

[52] A F Bielajew. Electron transport in $\vec{E}$ and $\vec{B}$ fields. In *Monte Carlo transport of electrons and photons*, pages 421–434. Springer, 1988.

[53] A Bielajew. Ionisation cavity theory: A formal derivation of perturbation factors for thick-walled ion chambers in photon beams. *Physics in Medicine and Biology*, 31(2):161–170, 1986.

[54] V. N. Malkov and D. W. O. Rogers. Charged particle transport in magnetic fields in EGSnrc. *Medical Physics*, 43(7):4447–4458, 2016.

[55] U Fano. Note on the bragg-gray cavity principle for measuring energy dissipation. *Radiation Research*, 1(3):237–240, 1954.

[56] VG Smyth, AC McEwan, AF Bielajew, and D WO Rogers. Interface artefacts in monte carlo calculations; and reply. *Phys. Med. Biol.;(United Kingdom)*, 31(3), 1986.

[57] H Bouchard, J de Pooter, A Bielajew, and S Duane. Reference dosimetry in the presence of magnetic fields: conditions to validate Monte Carlo simulations. *Physics in Medicine and Biology*, 60(17):6639–6654, 2015.

[58] I Kawrakow. Accurate condensed history Monte Carlo simulation of electron transport. I. EGS nrc, the new EGS4 version. *Medical Physics*, 27(3):485–498, 2000.

[59] I Kawrakow. Accurate condensed history Monte Carlo simulation of electron transport. II. Application to ion chamber response simulations. *Medical Physics*, 27(3):499–513, 2000.

[60] JP Seuntjens, I Kawrakow, J Borg, F Hobeila, and DWO Rogers. Calculated and measured air-kerma response of ionization chambers in low and medium energy photon beams. In *Recent Developments in Accurate Radiation Dosimetry: Proc. Int. Workshop*, pages 69–84, 2002.

[61] J Sempau and P Andreo. Configuration of the electron transport algorithm of PENELOPE to simulate ion chambers. *Physics in Medicine and Biology*, 51(14):3533–3548, 2006.

[62] J A de Pooter, L A de Prez, and H Bouchard. Application of an adapted Fano cavity test for Monte Carlo simulations in the presence of B-fields. *Physics in Medicine and Biology*, 60(24):9313–9327, 2015.

[63] G F Knoll. *Radiation detection and measurement*. John Wiley, 2010.

[64] I Das. We-d-201-01. *Medical Physics*, 44(6), 2017.

[65] H Palmans, P Andreo, M S Huq, J Seuntjens, K E Christaki, and A Meghzifene. Dosimetry of small static fields used in external photon beam radiotherapy: Summary of trs-483, the iaea–aapm international code of practice for reference and relative dose determination. *Medical physics*, 45(11):e1123–e1145, 2018.

[66] LV Spencer and F H Attix. A theory of cavity ionization. *Radiation research*, 3(3):239–254, 1955.

[67] AE Nahum. Water/air mass stopping power ratios for megavoltage photon and electron beams. *Physics in Medicine and Biology*, 23(1):24, 1978.

[68] R J Schulz, PE Almond, JR Cunningham, JG Holt, R Loevinger, N Suntharalingam, K A Wrigth, and G Lempert. AAPM Protocol: Task Group 21: A protocol for the determination of absorbed dose from high-energy photon and electron beams. *Medical Physics*, 10(6):741–771, 1983.

[69] R Alfonso, P Andreo, R Capote, M Saiful Huq, W Kilby, P Kjäll, T R Mackie, H Palmans, K Rosser, J Seuntjens, W Ullrich, and S Vatnitsky. A new formalism for reference dosimetry of small and nonstandard fields. *Medical Physics*, 35(11):5179–5186, 2008.

[70] S J Woodings, JJ Bluemink, JHW De Vries, Y Niatsetski, B van Veelen, J Schillings, J G M Kok, JWH Wolthaus, S L Hackett, B van Asselen, et al. Beam characterisation of the 1.5 t mri-linac. *Physics in Medicine and Biology*, 63(8):085015, 2018.

[71] BM Oborn, PE Metcalfe, MJ Butson, and AB Rosenfeld. High resolution entry and exit monte carlo dose calculations from a linear accelerator 6 mv beam under the influence of transverse magnetic fields. *Medical physics*, 36(8):3549–3559, 2009.

[72] BM Oborn, PE Metcalfe, MJ Butson, and AB Rosenfeld. Monte carlo characterization of skin doses in 6 mv transverse field mri-linac systems: effect of field size, surface orientation, magnetic field strength, and exit bolus. *Medical physics*, 37(10):5208–5217, 2010.

[73] S L Hackett, B van Asselen, J WH Wolthaus, JJ Bluemink, K Ishakoglu, J Kok, J JW Lagendijk, and B W Raaymakers. Spiraling contaminant electrons increase doses to surfaces outside the photon beam of an mri-linac with a perpendicular magnetic field. *Physics in Medicine and Biology*, 63(9):095001, 2018.

[74] AJE Raaijmakers, BW Raaymakers, and JJW Lagendijk. Magnetic-field-induced dose effects in mr-guided radiotherapy systems: dependence on the magnetic field strength. *Physics in Medicine and Biology*, 53(4):909, 2008.

[75] D. J. O'Brien, D. A. Roberts, G. S. Ibbott, and G. O. Sawakuchi. Reference dosimetry in magnetic fields: formalism and ionization chamber correction factors. *Medical Physics*, 43:4915–4927, 2016.

[76] B van Asselen, S J Woodings, S L Hackett, T L van Soest, J G M Kok, B W Raaymakers, and J W H Wolthaus. A formalism for reference dosimetry in photon beams in the presence of a magnetic field. *Physics in Medicine & Biology*, 63(12):125008, 2018.

[77] M. Reynolds, B. G. Fallone, and S. Rathee. Dose response of selected ion chambers in applied homogeneous transverse and longitudinal magnetic fields. *Medical Physics*, 40(4):042102, 2013.

[78] J Wolthaus, B Van Asselen, S Woodings, T Van Soest, J Kok, L de Prez, B Jansen, J de Pooter, and B Raaymakers. Th-cd-bra-03: Direct measurement of magnetic field correction factors, kqb, for application in future codes of practice for reference dosimetry. *Medical physics*, 43(6Part45):3873–3873, 2016.

[79] VN Malkov and DWO Rogers. Sensitive volume effects on Monte Carlo calculated ion chamber response in magnetic fields. *Medical Physics*, 44(9):4854–4858, 2017.

[80] L de Prez, S Woodings, J de Pooter, B van Asselen, J Wolthaus, B Jansen, and B Raaymakers. Direct measurement of ion chamber correction factors, k q and k b, in a 7 mv mri-linac. *Physics in Medicine and Biology*, 64(10):105025, 2019.

[81] I Billas, H Bouchard, U Oelfke, D Shipley, C Gouldstone, and S Duane. Alanine dosimetry in strong magnetic fields: use as a transfer standard in mri-guided radiotherapy. *Physics in Medicine and Biology*, 65(11):115001, 2020.

[82] K Smit, B van Asselen, J G M Kok, A H L Aalbers, J J W Lagendijk, and B W Raaymakers. Towards reference dosimetry for the MR-linac: magnetic field correction of the ionization chamber reading. *Physics in Medicine and Biology*, 58(17):5945–5957, 2013.

[83] H K Looe, B Delfs, D Poppinga, D Harder, and B Poppe. Magnetic field influences on the lateral dose response functions of photon-beam detectors: Mc study of wall-less water-filled detectors with various densities. *Physics in Medicine and Biology*, 62(12):5131, 2017.

[84] CK Ross. Comments on 'ionization chamber volume determination and quality assurance using micro-ct imaging'. *Physics in Medicine and Biology*, 54(6):L23, 2009.

[85] BR Muir and DWO Rogers. Monte carlo calculations of k_q, the beam quality conversion factor. *Medical physics*, 37(11):5939–5950, 2010.

[86] BR Muir, MR McEwen, and DWO Rogers. Measured and monte carlo calculated kq factors: Accuracy and comparison. *Medical physics*, 38(8):4600–4609, 2011.

[87] P. Francescon, S. Cora, and N. Satariano. Calculation of $k_{Qclin,Qmsr}^{fclin,fmsr}$ for several small detectors and for two linear accelerators using Monte Carlo simulations. *Medical Physics*, 38(12):6513–6527, 2011.

[88] Y Cervantes, I Billas, D Shipley, S Duane, and H Bouchard. Small-cavity chamber dose response to megavoltage photon beams in the presence of magnetic fields. In *Radiotherapy and Oncology*, volume 152, pages S16–S16. Elsevoer Ireland LTD Elsevier House, Brookvale Plaza, East Park Shannon, CO, 2020.

[89] H Bouchard, J Seuntjens, and H Palmans. On charged particle equilibrium violation in external photon fields. *Medical physics*, 39(3):1473–1480, 2012.

[90] L H Gray. An ionization method for the absolute measurement of γ-ray energy. *Proceedings of the Royal Society of London. Series A-Mathematical and Physical Sciences*, 156(889):578–596, 1936.

[91] Task Group 21 Radiation Therapy Committee (AAPM). A Protocol for the Determination of Absorbed Dose from High-Energy Photon and Electron Beams. *Med. Phys.*, 10(6):741–771, 1983.

[92] International Atomic Energy Agency. Absorbed Dose Determination in Photon and Electron Beams: An International Code of Practice. Technical Report TRS-277, International Atomic Energy Agency, Vienna (Austria), 1987.

[93] D J Butler, A W Stevenson, T E Wright, P D Harty, J Lehmann, J Livingstone, and J C Crosbie. High spatial resolution dosimetric response maps for radiotherapy ionization chambers measured using kilovoltage synchrotron radiation. *Physics in Medicine and Biology*, 60(22):8625–8641, 2015.

[94] H K Looe, B Delfs, D Poppinga, D Harder, and B Poppe. 2D convolution kernels of ionization chambers used for photon-beam dosimetry in magnetic fields: the advantage of small over large chamber dimensions. *Physics in Medicine & Biology*, 63(7):075013, 2018.

[95] H Palmans, P Andreo, K Christaki, MS Huq, and J Seuntjens. Trs-483: Dosimetry of small static fields used in external beam radiotherapy: an international code of practice for reference and relative dose determination. *International Atomic Energy Agency Vienna*, 2017.

[96] H Bouchard, J Seuntjens, JF Carrier, and I Kawrakow. Ionization chamber gradient effects in nonstandard beam configurations. *Medical physics*, 36(10):4654–4663, 2009.

[97] A J D Scott, S Kumar, A E Nahum, and J D Fenwick. Characterizing the influence of detector density on dosimeter response in non-equilibrium small photon fields. *Physics in Medicine and Biology*, 57(14):4461–4476, 2012.

[98] J D Fenwick, S Kumar, AJD Scott, and AE Nahum. Using cavity theory to describe the dependence on detector density of dosimeter response in non-equilibrium small fields. *Physics in Medicine and Biology*, 58(9):2901, 2013.

[99] H Bouchard, J Seuntjens, S Duane, Y Kamio, and H Palmans. Detector dose response in megavoltage small photon beams. i. theoretical concepts. *Medical physics*, 42(10):6033–6047, 2015.

[100] P Andreo. The physics of small megavoltage photon beam dosimetry. *Radiotherapy and oncology : journal of the European Society for Therapeutic Radiology and Oncology*, 126(2):205–213, 2018.

[101] H Bouchard and J Seuntjens. *Monte Carlo Techniques in Radiation Therapy, Ch. 4: Applications of Monte Carlo to Radiation Dosimetry*. Ed J Seco and F Verhaegen, CRC Press, Taylor and Francis Group, Boca Raton, FL, 2013.

[102] D Burns. An analysis of existing data for w_{air}, i_c and the product $w_{\text{airsc, air}}$. *Metrologia*, 49(4):507, 2012.

[103] P Andreo, J Wulff, D T Burns, and H Palmans. Consistency in reference radiotherapy dosimetry: resolution of an apparent conundrum when 60co

is the reference quality for charged-particle and photon beams. *Physics in Medicine and Biology*, 58(19):6593, 2013.

[104] I Billas, H Bouchard, U Oelfke, and S Duane. The effect of magnetic field strength on the response of Gafchromic EBT-3 film. *Physics in Medicine and Biology*, 64(6):06NT03, 2019.

[105] J. Wulff, K. Zink, and I. Kawrakow. Efficiency improvements for ion chamber calculations in high energy photon beams. *Medical Physics*, 35(4):1328–1336, 2008.

[106] Joint Committee for Guides in Metrology. Jcgm 100: Evaluation of measurement data - guide to the expression of uncertainty in measurement. Technical report, JCGM, 2008.

[107] J Wulff, JT Heverhagen, K Zink, and I Kawrakow. Investigation of systematic uncertainties in monte carlo-calculated beam quality correction factors. *Physics in Medicine and Biology*, 55(16):4481, 2010.

[108] H Bouchard. *Accurate Dosimetry of Intensity Modulated Radiation Therapy Beams Using Thimble Ionization Chambers*. PhD thesis, McGill University, 2003.

[109] F Crop, N Reynaert, G Pittomvils, L Paelinck, C De Wagter, and H Thierens. The influence of small field sizes, penumbra, spot size and measurement depth on perturbation factors for microionization chambers. *Physics in Medicine & Biology*, 54(9):2951–69, 2009.

[110] H Bouchard, J Seuntjens, JF Carrier, and I Kawrakow. Ionization chamber gradient effects in nonstandard beam configurations. *Medical Physics*, 36(10):4654–4663, 2009.

[111] Y Kamio and H Bouchard. Correction-less dosimetry of nonstandard photon fields: a new criterion to determine the usability of radiation detectors. *Physics in Medicine and Biology*, 59(17):4973, 2014.

[112] H Bouchard, J Seuntjens, S Duane, Y Kamio, and H Palmans. Detector dose response in megavoltage small photon beams. I. Theoretical concepts. *Medical Physics*, 42(10):6033–6047, 2015.

[113] H Bouchard, Y Kamio, H Palmans, J Seuntjens, and S Duane. Detector dose response in megavoltage small photon beams. II. Pencil beam perturbation effects. *Medical Physics*, 42(10):6048–6061, 2015.

[114] Y. Cervantes, J. Duchaine, I. Billas, S. Duane, and H. Bouchard. Monte carlo calculation of detector perturbation and quality correction factors in a 1.5 t magnetic resonance guided radiation therapy small photon beams. *Physics in Medicine & Biology*, 66:225004, 2021.

[115] Vimal K Desai, Zacariah E Labby, Megan A Hyun, Larry A DeWerd, and Wesley S Culberson. VMAT and IMRT plan-specific correction factors for linac-based ionization chamber dosimetry. *Medical physics*, 46(2):913–924, 2019.

[116] T S A Underwood, H C Winter, M A Hill, and J D Fenwick. Detector density and small field dosimetry: Integral versus point dose measurement schemes. *Medical Physics*, 40(8):082102, 2013.

[117] C Kurz, G Buizza, G Landry, F Kamp, M Rabe, C Paganelli, G Baroni, M Reiner, P J Keall, Cornelis AT van den B, et al. Medical physics challenges in clinical mr-guided radiotherapy. *Radiation Oncology*, 15:1–16, 2020.

[118] V N Malkov and D. W. O. Rogers. Monte Carlo study of ionization chamber magnetic field correction factors as a function of angle and beam quality. *Medical Physics*, 45(2):908–925, 2018.

[119] David A Roberts, Carlos Sandin, Panu T Vesanen, Hannah Lee, Ian M Hanson, Simeon Nill, Thijs Perik, Seng Boh Lim, Sastry Vedam, Jinzhong Yang, et al. Machine qa for the elekta unity system: A report from the elekta mr-linac consortium. *Medical physics*, 2021.

[120] S Woodings, J Wolthaus, B Van Asselen, J De Vries, J Kok, J Lagendijk, and B Raaymakers. Performance of a ptw 60019 microdiamond detector in a 1.5 t mri-linac phys. *Med. Biol*, 63, 2018.

[121] I Billas and S Duane. Report on dose measurements on the mr-linac at christie hospital performed by npl. 2018.

[122] D Shipley, I Billas, and S Duane. Experimental benchmarking of monte carlo based detector response simulations in magnetic field. 2019. 2nd International Conference on Monte Carlo Techniques for Medical Applications, Montreal, Canada.

[123] Tuba Tekin, Isabel Blum, Björn Delfs, Ann-Britt Schönfeld, Ralf-Peter Kapsch, Björn Poppe, and Hui Khee Looe. The dose response of high-resolution diode-type detectors and the role of their structural components in strong magnetic field. *Medical Physics*, 47(12):6509–6518, 2020.

[124] Ilias Billas, Hugo Bouchard, Uwe Oelfke, and Simon Duane. Traceable reference dosimetry in mri guided radiotherapy using alanine: calibration and magnetic field correction factors of ionisation chambers. *Physics in Medicine & Biology*, 2021.

[125] P Andreo and Anders Brahme. Stopping power data for high-energy photon beams. *Physics in Medicine and Biology*, 31(8):839, 1986.

[126] F Sánchez-Doblado, P Andreo, R Capote, A Leal, M Perucha, R Arráns, L Nunez, E Mainegra, JI Lagares, and E Carrasco. Ionization chamber dosimetry of small photon fields: a monte carlo study on stopping-power ratios for radiosurgery and imrt beams. *Physics in Medicine & Biology*, 48(14):2081, 2003.

[127] Alison JD Scott, Alan E Nahum, and John D Fenwick. Using a monte carlo model to predict dosimetric properties of small radiotherapy photon fields. *Medical physics*, 35(10):4671–4684, 2008.

[128] Hamza Benmakhlouf and Pedro Andreo. Spectral distribution of particle fluence in small field detectors and its implication on small field dosimetry. *Medical physics*, 44(2):713–724, 2017.

[129] Y. Cervantes, S. Duane, and H. Bouchard. Monte carlo investigation of electron fluence perturbation in mr-guided radiotherapy beams using six commercial radiation detectors.

[130] Björn Delfs, Isabel Blum, Tuba Tekin, Ann-Britt Schönfeld, Rafael Kranzer, Daniela Poppinga, Ulrich Giesen, Frank Langner, Ralf-Peter Kapsch, Björn Poppe, et al. The role of the construction and sensitive volume of compact ionization chambers on the magnetic field-dependent dose response. *Medical Physics*, 2021.